
Magnetic nanostructures with structural inversion asymmetry

Dissertation
zur Erlangung des Grades
Doktor der Naturwissenschaften (Dr. rer. nat.)
am Fachbereich Physik
der Johannes Gutenberg–Universität Mainz

von:
Roberto Lo Conte
geboren in Ariano Irpino (Italien)
Mainz, 2015



JOHANNES GUTENBERG
UNIVERSITÄT MAINZ

Roberto Lo Conte

Magnetic nanostructures with structural inversion asymmetry

Prüfung: 09 Dezember, 2015

Johannes Gutenberg–Universität Mainz

AG Kläui

Institut für Physik

Staudingerweg 7

55128, Mainz

Eidesstattliche Erklärung

Hiermit erkläre ich an Eides statt, dass ich meine Dissertation selbständig und ohne fremde Hilfe verfasst und keine anderen als die von mir angegebenen Quellen und Hilfsmittel zur Erstellung meiner Dissertation verwendet habe. Die Arbeit ist in vorliegender oder ähnlicher Form bei keiner anderen Prüfungsbehörde zur Erlangung eines Doktorgrades eingereicht worden.

Mainz, den

Roberto Lo Conte

I used to wonder how it comes about that the electron is negative. Negative-positive—these are perfectly symmetric in physics. There is no reason whatever to prefer one to the other. Then why is the electron negative? I thought about this for a long time and at last all I could think was “It won the fight!”

Albert Einstein

“Daddy,” she says, “which came first, the chicken or the egg?”
Steadfastly, even desperately, we have been refusing to commit ourselves. But our questioner is insistent. The truth alone will satisfy her. Nothing less. At long last we gather up courage and issue our solemn pronouncement on the subject: “Yes!”
So it is here.
“Daddy, is it a wave or a particle?” “Yes.”
“Daddy, is the electron here or is it there?”
“Yes.”
“Daddy, do scientists really know what they are talking about?”
“Yes!”

Banesh Hoffmann

Abstract

In the attempt of proposing new concepts for more efficient magnetic memories and logic devices, an intense scientific research is conducted in the field of Nanomagnetism and Spintronics. Accordingly, in the recent years a new discovery, going under the name of spin-orbit torques (SOTs), has attracted the attention of the scientific community. SOTs are expected to play a key role in the design of novel and more efficient spintronic devices based on the manipulation of the magnetic texture in ferromagnetic systems by electric currents. The origin of the SOTs is the strong spin-orbit interaction (SOI) in the material systems where such novel torques been observed, i.e. magnetic multilayers of the type: heavy metal\ferromagnet\oxide. Moreover, the structural inversion asymmetry (SIA) characterizing those magnetic heterostructures is the second key factor in the generation of the SOTs.

This thesis reports on the observed SOT-driven magnetization manipulation in two different magnetic multilayers: Ta\CoFeB\MgO and Pt\Co\AlOx, employing Kerr microscopy. The two materials systems have an ultra-thin ferromagnetic layer (1 nm for the CoFeB layer, 0.9-1.4 nm for the Co layer) and a spontaneous magnetization pointing out-of-plane. All the investigated material stacks were patterned into 1-1.5 μm -wide, 8-28 μm -long magnetic nanowires (NWs).

First, a deterministic current-induced magnetization switching effect is observed in Ta\CoFeB\MgO NWs. The symmetry and the efficiency of the magnetization reversal, due to the injection of current pulses of different lengths and amplitudes, are investigated. The experimental observations are in agreement with the presence of a strong SOT acting on the ferromagnet's magnetization, which originates from the large spin-Hall effect (SHE) in the Ta layer.

Second, current-induced magnetic domain wall motion (CIDWM) is studied in NWs made of Ta\CoFeB\MgO. The observed CIDWM along the conventional current (j) points to SOTs as the driving mechanism. The material system is found to exhibit a positive Dzyaloshinskii-Moriya interaction (DMI), generated at the Ta\CoFeB interface. The observed dependence of the CIDWM velocity on an applied longitudinal magnetic

field (H_L) is in agreement with the scenario of a SHE–SOT–driven motion of DMI–stabilized right–handed homo–chiral DWs. Furthermore, the Boron is found to play a key role in the definition of the sign of the observed DMI.

Finally, fast CIDWM is observed in Pt\Co\AlOx NWs. Here, the influence of the Co thickness (t_{Co}) on the DW motion is at the center of the study. The general dependence of the DW velocity on j and on H_L is in agreement with the interpretation based on DW moved by the SOT originating from the SHE in the Pt layer. A decrease in the magnitude of the effective negative DMI with an increasing t_{Co} is extracted, justifying the interpretation based on an interfacial origin for the DMI in our system. Finally, the DW width is observed to play a key role in the definition of the DW velocity dependence on the longitudinal field.

Kurzfassung

Die Suche nach neuen Konzepten effizienterer magnetischer Speicher und elektronischer Logikbausteine inspiriert schon lange die wissenschaftliche Forschung im Bereich des Nanomagnetismus und der Spintronik. In Folge dessen zieht die Entdeckung der Spin-Bahn-Drehmomente (SBD) seit einigen Jahren große Aufmerksamkeit auf sich. Allen Erwartungen nach werden SBD eine Schlüsselrolle in der Entwicklung neuartiger und effizienterer Spintronikbausteine spielen, die auf der Manipulation magnetischer Texturen in ferromagnetischen Systemen durch elektrische Ströme basieren. Der Ursprung dieser neuartigen SBD ist die Spin-Bahn-Kopplung (SBK) in Materialsystemen wie z.B. magnetische Multilagensysteme der Form Schwermetall\Ferromagnet\Oxid. Die zweite Hauptvoraussetzung zur Erzeugung der SBD ist eine strukturelle Inversionsasymmetrie (SIA) in solchen magnetischen Heterostrukturen.

Diese Doktorarbeit befasst sich mit der Manipulation der Magnetisierung in zwei verschiedenen magnetischen Multilagensystemen durch die SBD: Ta\CoFeB\MgO und Pt\Co\AlOx, gemessen und abgebildet mit der Technik der Kerr-Mikroskopie. Beide Materialsysteme besitzen eine ultradünne ferromagnetische Schicht (1 nm im Falle von CoFeB, 0.9-1.4 nm im Falle von reinem Co), welche spontan senkrecht zur Ebene magnetisiert ist. Die untersuchten Multilagensysteme wurden so strukturiert, dass magnetische Nano-drähte (ND) erhalten wurden mit Breiten von 1-1.5 μm und Längen von 8-28 μm .

Zunächst wurde beobachtet, dass sich die Magnetisierung in Ta\CoFeB\MgO ND mit Hilfe eines elektrischen Stroms deterministisch schalten lässt. Die Symmetrie und die Effizienz der Magnetisierungsumkehr wurden als Funktion von Strompulslänge und –amplitude untersucht. Die experimentellen Beobachtungen sind in Übereinstimmung mit der Anwesenheit eines starken SBK-Effektes, welcher auf einem großen Spin–Hall Effekt innerhalb der Ta–Schicht basiert und auf die Magnetisierung des Ferromagnets einwirkt.

Darüber hinaus wurde die durch den elektrischen Strom induzierte Bewegung magnetischer Domänenwände (DW) in ND aus Ta\CoFeB\MgO untersucht. Die beobachtete Domänenwandbewegung entlang konventioneller Stromrichtung (j) deutet auf SBD als treibenden Mechanismus hin. Das Materialsystem zeigt zudem eine positive Dzyaloshin-

skii-Moriya Wechselwirkung (DMWW), die durch die Ta\CoFeB-Grenzfläche entsteht. Die festgestellte Abhängigkeit der Domänenwandgeschwindigkeit vom longitudinal zu den ND angelegten Magnetfeld (H_L) kann erklärt werden durch die Annahme, dass rechtshändige, homo-chirale, DMWW-stabilisierte Domänenwände vorliegen, deren Bewegung durch SHE-SBD hervorgerufen wird. Darüber hinaus, wurde festgestellt, dass Bor eine Schlüsselrolle für das Vorzeichen der beobachteten DMWW spielt. Schließlich wurde eine sehr schnelle Domänenwandbewegung in Pt\Co\AlOx ND beobachtet. In diesem Fall ist der Einfluss der Co-Schichtdicke (t_{Co}) der zentrale Gegenstand der Untersuchung. Die generelle Abhängigkeit der DW-Geschwindigkeit von j und H_L ist in Übereinstimmung mit der Interpretation, dass die DW durch die SBD aufgrund des SHE in der Pt-Schicht angetrieben werden. Eine Verringerung der Stärke der effektiven, negativen DMWW mit zunehmendem t_{Co} konnte extrahiert werden, wodurch die Interpretation des Ursprunges der DMWW an der Schichtgrenzfläche untermauert wird. Schließlich spielt die DW-Breite eine Schlüsselrolle für die Abhängigkeit der DW-Geschwindigkeit vom longitudinal angelegten Feld.

Dedicated to

my parents C. and D.

and my brothers O. and D.

Dedicato a

i miei genitori C. e D.

e i miei fratelli O. e D.

Contents

Eidesstattliche Erklärung	iii
Abstract	vii
Kurzfassung	ix
Contents	xiii
List of Figures	xvii
List of Tables	xxi
Abbreviations	xxiii
1 Introduction	1
2 Theoretical background	3
2.1 Microscopic origins of magnetism	3
2.1.1 Atomic magnetism	3
2.1.2 Microscopic origin of magnetism in solids: the exchange interaction	6
2.1.2.1 Heisenberg–exchange interaction	6
2.1.2.2 Dzyaloshinskii–Moriya interaction	7
2.1.3 Magnetism in itinerant electron systems	9
2.1.4 Microscopic origin of the interfacial Dzyaloshinskii–Moriya interaction	11
2.2 Thermodynamical description of magnetism in the micromagnetic approximation	12
2.2.1 Exchange energy	12
2.2.2 Zeeman energy	13
2.2.3 Magnetic dipolar energy	13
2.2.4 Anisotropy energy	15
2.2.5 Induced perpendicular magnetic anisotropy	16
2.2.6 Energy minimization: magnetic domains and domain walls	18
2.3 Néel–Brown model of magnetization reversal	20
2.4 Interfacial DMI in PMA magnetic nanowires: chiral Néel domain walls	21
2.5 Field–induced magnetization dynamics: the Landau–Lifshitz–Gilbert equation	22

2.6	Current-induced magnetization dynamics in metallic ferromagnets	25
2.6.1	Spin-dependent transport	25
2.6.2	Spin-transfer torque: a toy model	26
2.6.3	Landau-Lifshitz-Gilbert equation with STT	28
2.6.4	STT-driven domain wall motion	29
2.6.5	Current-induced magnetization reversal: generalized Néel-Brown model	33
2.7	Spin-orbit torques	34
2.7.1	Inverse spin-galvanic effect	35
2.7.1.1	Rashba spin-orbit interaction	35
2.7.1.2	Inverse spin-galvanic effect	37
2.7.2	Spin-Hall effect: magnetization manipulation by a pure spin-current	40
2.7.2.1	Spin-Hall effect	40
2.7.2.2	Magnetization manipulation by the SHE-spin current	43
2.8	Beyond the spin-orbit torques: chiral damping	46
2.9	Magnetic nanostructures with structural inversion asymmetry: new effects for Spintronics	47
3	Experimental techniques	49
3.1	Introduction	49
3.2	Sample characterization	49
3.2.1	Superconducting quantum interference device magnetometry	49
3.3	Device fabrication	51
3.4	Kerr Microscopy	54
3.4.1	Magneto-optic Kerr effect	55
3.4.2	The Kerr microscope	59
3.4.3	Imaging domain wall motion at the Kerr microscope	63
3.5	Photo-emission electron microscopy (PEEM)	67
3.5.1	X-ray magnetic circular dichroism (XMCD)	68
4	Spin-orbit torque-driven magnetization switching in Ta\CoFeB\MgO	71
4.1	Introduction	71
4.2	Material stack: Ta\CoFeB\MgO	72
4.3	Experimental set-up	75
4.4	Magnetization switching by spin-orbit torques	76
4.4.1	Measuring the magnetization switching	76
4.4.2	Discussion	79
4.5	Thermal effects in the magnetization switching process	81
4.5.1	Discussion	85
4.6	Conclusion and outlook	89
5	Spin-orbit torque-induced domain wall motion in Ta\CoFeB\MgO	91
5.1	Introduction	91
5.2	Experimental set-up	92
5.3	Current-induced domain wall motion	94
5.3.1	Moving domain walls with current	94
5.3.2	Discussion	95
5.4	Chiral domain walls in motion	97

5.4.1	Effect of an external magnetic field on the domain wall motion . . .	97
5.4.2	Discussion	101
5.5	Extraction of the Dzyaloshinskii–Moriya interaction in Ta\CoFeB\MgO .	103
5.5.1	An alternative method for the extraction of the DMI	106
5.6	Chiral DWs in Ta\CoFeB\MgO moved by SOT	108
5.7	1D modeling of chiral domain wall motion: extraction of the spin–Hall effect efficiency	111
5.8	The role of B in the material stack	112
5.8.1	Observation of B diffusion	112
5.8.2	Discussion	114
5.9	Conclusion and outlook	115
6	Spin–orbit torque–induced domain wall motion in Pt\Co\AlO_x	119
6.1	Introduction	119
6.2	Material stack: Pt\Co(<i>t</i> _{Co})\AlO _x	120
6.3	Experimental set–up	122
6.4	Current–induced domain wall motion in Pt\Co\AlO _x NWs	124
6.4.1	Moving domain walls with current	124
6.4.2	Discussion	125
6.5	Chiral domain walls moving in Pt\Co\AlO _x NWs	129
6.5.1	Effect of an external magnetic field on the domain wall motion . .	129
6.5.2	Discussion	130
6.6	Dzyaloshinskii–Moriya interaction in Pt\Co(<i>t</i>)\AlO _x	133
6.7	Chiral DWs in Pt\Co\AlO _x moved by SOT	141
6.8	Conclusion and outlook	148
7	General conclusion and outlook	151
A	Temperature calibration during current pulse injection	155
B	Current–induced domain wall motion in Pt\CoFeB\MgO nanowires	159
	Bibliography	163
	Acknowledgements	179
	Curriculum Vitae	181
	Publications List	183

List of Figures

2.1	Atomic magnetism	4
2.2	Dzyaloshinskii–Moriya interaction at the interface	8
2.3	DOS of itinerant ferromagnets	10
2.4	Magnetic shape anisotropy	15
2.5	PMA material system	17
2.6	Atomic $2p$ and $3d$ electronic orbitals	18
2.7	Magnetic domain wall	19
2.8	Néel–Brown model	21
2.9	An $\uparrow\downarrow$ -DW’s magnetic configuration as a function of the DMI	23
2.10	Chiral domain walls	24
2.11	Magnetization dynamics as described by the LLG equation	24
2.12	STT mechanism	27
2.13	STT at a magnetic DW	28
2.14	Magnetization dynamics in the presence of STT	29
2.15	Domain walls magnetization configuration in the 1D model for PMA systems	32
2.16	Orientation of the Rashba spin–orbit field in the k -space	36
2.17	Fermi contours for a Rashba 2DEG	38
2.18	ISGE in a magnetic multilayer	38
2.19	Spin–Hall effect in heavy transition metals	40
2.20	SHE–spin current in the HM\FM bilayer	44
2.21	Symmetry of the SHE effective field	45
3.1	DC–SQUID	51
3.2	Hysteresis loops	52
3.3	Device patterning	54
3.4	Light beam reflection at a magnetic surface	56
3.5	MOKE configurations	57
3.6	Polar MOKE	58
3.7	MOKE set–up	60
3.8	Kerr microscope – Schematic	61
3.9	Maltese cross	62
3.10	Kerr image formation	62
3.11	<i>Evico</i> wide–field Kerr microscope	64
3.12	Schematic experimental set–up	65
3.13	Protocol for measuring DW motion at the Kerr microscope	66
3.14	PEEM	68
3.15	XMCD	70

4.1	Ta\CoFeB\MgO stack	72
4.2	TEM image of the cross-section of the Ta\CoFeB\MgO stack	74
4.3	Polar-MOKE hysteresis loop of the Ta\CoFeB\MgO multilayer for an applied out-of-plane field	74
4.4	Experimental set-up for the CIMS experiment	76
4.5	Magnetization reversal events	77
4.6	Current-induced magnetization switching	78
4.7	Symmetry of current-induced magnetization switching in Ta\CoFeB\MgO nanostructures	81
4.8	Magnetization switching probability at constant in-plane field	83
4.9	Magnetization switching with a 50% probability	84
4.10	Thermal effects in current-induced magnetization switching	85
4.11	Switching probability	86
5.1	Experimental set-up for CIDWM	93
5.2	CIDWM in Ta(5.0)\Co ₂₀ Fe ₆₀ B ₂₀ (1.0)\MgO(2.0) NWs	96
5.3	Extraction of the CIDWM velocity in Ta(5.0)\Co ₂₀ Fe ₆₀ B ₂₀ (1.0)\MgO(2.0) NWs	98
5.4	Nucleation and motion of chiral DWs in Ta(5.0)\Co ₂₀ Fe ₆₀ B ₂₀ (1.0)\MgO(2.0) NWs	99
5.5	Chiral DWs' velocity in Ta(5.0)\Co ₂₀ Fe ₆₀ B ₂₀ (1.0)\MgO(2.0) NWs	100
5.6	Symmetry of chiral DWs' velocity in Ta(5.0)\Co ₂₀ Fe ₆₀ B ₂₀ (1.0)\MgO(2.0) NWs	101
5.7	Chiral domain walls	104
5.8	Extraction of DMI effective field from CIDWM in Ta\CoFeB\MgO	105
5.9	Chiral DWs in Ta\CoFeB\MgO moved by the SOT	110
5.10	Chemical depth profiling of the Ta(5.0)\Co ₂₀ Fe ₆₀ B ₂₀ (1.0)\MgO(2.0) stack	113
5.11	Principle of operation of a Ta\CoFeB\MgO racetrack	117
6.1	Pt\Co(<i>t_{Co}</i>)\AlO _{<i>x</i>} stack	120
6.2	Polar-MOKE hysteresis loops of the Pt\Co(<i>t_{Co}</i>)\AlO _{<i>x</i>} multilayer for an applied out-of-plane field	121
6.3	Devices' positions on the Pt\Co(<i>t_{Co}</i>)\AlO _{<i>x</i>} sample	123
6.4	Experimental set-up for CIDWM in Pt\Co(<i>t_{Co}</i>)\AlO _{<i>x</i>} NWs	124
6.5	Pulse's waveform in the experimental set-up for CIDWM in Pt\Co(<i>t_{Co}</i>)\AlO _{<i>x</i>} NWs	125
6.6	CIDWM velocity in Pt(4)\Co(<i>t_{Co}</i>)\AlO _{<i>x</i>} (2) NWs	126
6.7	Comparing the CIDWM velocities in the five Pt\Co(<i>t_{Co}</i>)\AlO _{<i>x</i>} devices	128
6.8	Motion of chiral DWs in Pt\Co\AlO _{<i>x</i>} NWs in presence of an in-plane longitudinal field	130
6.9	Symmetry of chiral DWs' velocity in Pt(4)\Co(<i>t_{Co}</i>)\AlO _{<i>x</i>} (2) NWs	131
6.10	Extracted DMI effective values for Pt\Co(<i>t_{Co}</i>)\AlO _{<i>x</i>}	136
6.11	Chiral domain walls in Pt\Co(<i>t_{Co}</i>)\AlO _{<i>x</i>}	140
6.12	Chiral DWs in Pt\Co\AlO _{<i>x</i>} moved by the SOT	142
6.13	Tilting of chiral DWs in Pt\Co\AlO _{<i>x</i>} NWs in the presence of an in-plane longitudinal field	145
6.14	DW width in the presence of an in-plane longitudinal field	146

6.15	DW velocity increase in Pt\Co(t_{Co})\AlO _x NWs in the presence of an in-plane longitudinal field	147
6.16	DW velocity dependence on longitudinal field as a function of the Co thickness in Pt\Co(t_{Co})\AlO _x NWs	147
A.1	Sample resistance calibration during current pulse injection	156
A.2	Sample resistance and temperature as a function of current density	157
B.1	Layout of the sample used for PEEM imaging	160
B.2	XMCD-PEEM images of current-induced DW motion in Pt\Co ₆₈ Fe ₂₂ B ₁₀ \MgO nanowires	161

List of Tables

4.1	Magnetometry data for the Ta\CoFeB\MgO material stack	73
4.2	Stable magnetization configurations for Ta\CoFeB\MgO	78
5.1	Extracted DMI values for Ta\CoFeB\MgO for different current densities .	108
6.1	Magnetometry data for Pt\Co(t_{Co})\AlO _x from BLS measurements	122
6.2	DMI effective values for Pt\Co(t_{Co})\AlO _x	137
6.3	Critical DMI values for the Pt\Co(t_{Co})\AlO _x devices	138

Abbreviations

CCD	charge coupled device
CIDWM	current-induced domain wall motion
CIMS	current-induced magnetization switching
DC	direct current
DL	damping-like
DMI	Dzyaloshinskii-Moriya interaction
DOS	density of states
DW	domain wall
EBL	electron-beam lithography
FL	field-like
FM	ferromagnet
HF	high frequency
HM	heavy metal
HRTEM	high resolution transmission electron microscopy
ISGE	inverse spin-galvanic effect
LED	light emitting diode
LLG	Landau-Lifshitz-Gilbert
MMA	methyl methacrylate
MO	magneto-optic
MOKE	magneto-optic Kerr effect
NM	normal metal
NW	nanowire
OOP	out-of-plane
Ox	oxide
PCB	printed circuit board

PEEM	photoemission electron microscopy
PMA	perpendicular magnetic anisotropy
PMMA	polymethyl methacrylate
R	resistance
RF	radio-frequency
SEM	scanning electron microscopy
SGE	spin-galvanic effect
SHA	spin-Hall angle
SHE	spin-Hall effect
SIA	structural inversion asymmetry
SIMS	secondary ion mass spectrometry
SOC	spin-orbit coupling
SOI	spin-orbit interaction
SOT	spin-orbit torque
SQUID	superconducting quantum interference device
STT	spin-transfer torque
TEM	transmission electron microscopy
XMCD	x-ray magnetic circular dichroism

Chapter 1

Introduction

The storage of digital information, which can be read and processed electronically, started over half a century ago [1]. For many years the magnetic hard disc drive (HDD) has been one of the main forms of information storage. The success of magnetic HDD originates in its low cost/bit ratio, which is hundred times smaller than the one of the solid-state Random Access Memory (RAM) [2], and its ability to keep the digital data stored for years passively, i.e. without the need to actively refresh it.

The reason is that, in a magnetic memory a data-bit corresponds to a particular magnetic state. After a bit is written no electric currents or magnetic fields are required to avoid that the magnetic state of the bit changes. This makes magnetic HDDs very efficient from an energetic point of view, so that keeping information stored in magnetic memories is cheaper than with many other technologies. All these features makes magnetic storage devices very attractive, and justify the huge effort put in the development of a ferromagnetic-based technology that could be exploited in order to design magnetic RAMs [1–4].

The main limitation of HDDs is the long time needed to retrieve the stored information (in the order of ms), due to the relative mechanical movement between the magnetic disk and the read/write head in order to reach the position where the required information is stored. In solid-state RAMs this access time is 10^6 times smaller than in HDDs [3]. In the attempt to overcome this obstacle, new concepts of magnetic memories have been proposed. One of them is the magnetic Racetrack Memory (RM), proposed by Parkin et al. [1, 2]. The basic concept of the magnetic RM is that the information is stored in magnetic nanotracks, in the form of aligned magnetic domains separated by

magnetic domain walls (DWs). Each domain is a bit, which can be read or written by a read/write device, e.g. a magnetic tunnel junction [3, 5]. However, the revolutionary idea in RM is the way how information is retrieved. The different magnetic bits are displaced by electric current pulses, due to DW motion in the nanotrack, exploiting the spin-transfer torque (STT) mechanism [6–8]. In this way the magnetic bits reach the read/write device without any mechanical movement. By properly engineering the magnetic system that the racetrack is made of, it is possible to reach DW motion velocities larger than 100 m/s [9, 10]. This could allow to design magnetic memories where: first, no parts are moving relatively to each others, avoiding mechanical failures typical of magnetic HDDs; second, the writing and reading times would be compatible with the ones in present RAM.

The goal of this work is to investigate potentially promising material systems for current-induced magnetization manipulation. The investigation is focused on magnetic heterostructures where an ultra-thin ferromagnetic layer is sandwiched between a heavy metal and an oxide. Due to the presence of interfaces, such systems are characterized by a structural inversion asymmetry (SIA). The lack of symmetry inversion is a crucial point, since it is at the origin of brand-new effects, named *spin-orbit torques* (SOTs) [11]. The SOTs are expected to allow a more effective current-driven magnetization manipulation than STT, and are at the center of this scientific work.

An overview of the main theoretical concepts necessary to understand the present experimental results is reported in Chapter 2. A description of the experimental methodologies employed for this study is presented in Chapter 3. Chapter 4 and 5 report on the experimental results obtained from the investigation of the first material system investigated in this work: Ta\CoFeB\MgO. Chapter 4 is dedicated to the description of the observed current-induced magnetization reversal, while Chapter 5 reports on current-induced DW motion. The experimental results concerning current-induced domain wall motion in Pt\Co\AlO_x, the other investigated material system, are described in Chapter 6. A general conclusion and outlook are given in Chapter 7.

Chapter 2

Theoretical background

2.1 Microscopic origins of magnetism

2.1.1 Atomic magnetism

The primary origin of magnetism in matter, in any of its possible phases is one single particle: the electron. The electron is an elementary particle that can be characterized by three main properties: its electric charge $-e$, its mass m_e and its intrinsic angular momentum, or spin S . The first two properties have a possible interpretation in the classical sense, while the spin–angular momentum is an intrinsic quantum mechanical property of the electron [12].

Considering an atom in its classical view (see Fig. 2.1), the electron has an orbital magnetic moment μ and an angular momentum L . The relation between the orbital angular momentum and the corresponding magnetic moment is described by the equation:

$$\boldsymbol{\mu} = \frac{-e}{2m_e} \mathbf{L}, \quad (2.1)$$

where the ratio $\gamma = \frac{-e}{2m_e}$ is defined as the *electron gyromagnetic ratio* [12, 13]. The corresponding quantum mechanical quantity for the classical angular momentum L is defined by the quantization rules [12]:

$$L = \sqrt{l(l+1)}\hbar; L_z = m_l\hbar, \quad (2.2)$$

where $l = 0, 1, 2, \dots$ is the *orbital quantum number* and $m_l = 0, \pm 1, \dots, \pm l$ is the *magnetic quantum number*. Equations 2.2 define the *orbital angular momentum* of the electron.

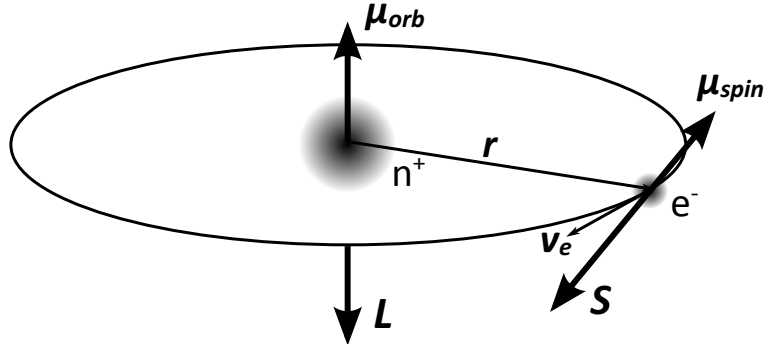


FIGURE 2.1: **Atomic magnetism.** Classical picture of an atom with the nucleus and an electron orbiting around it. The electron has two different angular momenta: the orbital angular momentum \mathbf{L} and the spin angular momentum \mathbf{S} . The two of them correspond to two different magnetic moments: the orbital magnetic moment $\boldsymbol{\mu}_{orb}$ and the spin magnetic moment $\boldsymbol{\mu}_{spin}$.

This angular momentum can attain only some specific quantized values, both in its magnitude (L) and in its component along a specific symmetry breaking direction (L_z). Due to the direct connection to the angular momentum, also the corresponding magnetic moment is quantized. Using the definition of the Bohr magneton, $\mu_B = \frac{e\hbar}{2m_e}$ [13], the z -component of the electron magnetic moment can be described by the following equation:

$$\mu_z = -\mu_B m_l. \quad (2.3)$$

The spinning electron as a classical picture of the *spin angular momentum* has no physical meaning. The spin angular momentum is an intrinsic quantum mechanical property of the electron, with a corresponding spin magnetic moment (see Fig. 2.1). The quantization rules apply also for the spin angular momentum:

$$S = \sqrt{s(s+1)}\hbar; S_z = m_s\hbar. \quad (2.4)$$

For the spin quantum number there is only one possible value: $s = \frac{1}{2}$, which results in only two possible values for the corresponding magnetic moment $m_s = \pm\frac{1}{2}$. When the electron is in the spin state $S_z = +\frac{1}{2}$ or $S_z = -\frac{1}{2}$, it is referred to as “spin-up” or “spin-down”, respectively.

As a result, the total magnetic moment of an electron is given by the sum of the orbital

and the spin contribution. This can be expressed in a classical way by:

$$\boldsymbol{\mu} = \boldsymbol{\mu}_{orb} + \boldsymbol{\mu}_{spin} = \frac{-e}{2m_e}(\mathbf{L} + g\mathbf{S}), \quad (2.5)$$

where g is the so-called *Landé g -factor*, which is circa 2 for the electron spin [12].

These two momenta interact in the so-called *spin-orbit interaction* (SOI), which can be interpreted classically as the spin magnetic moment of the electron interacting with the magnetic field in the rest frame of the electron, which is a result of the orbital motion of the electron itself in the electric field generated by the positive charge of the atomic nucleus [12, 13].

The energy associated to the SOI can be calculated as a *Zeeman energy*, which is the magnetostatic energy of a magnetic moment $\boldsymbol{\mu}$ interacting with a magnetic field \mathbf{B} . The Zeeman energy is given by: $E_Z = -\boldsymbol{\mu} \cdot \mathbf{B}$, and it is minimized when $\boldsymbol{\mu}$ is aligned parallel to \mathbf{B} . Analogously, the SOI energy is given by:

$$E_{SO} = -\boldsymbol{\mu}_{spin} \cdot \mathbf{B}_{SO} = \lambda_{SO}\mathbf{S} \cdot \mathbf{L}, \quad (2.6)$$

where λ_{SO} is the spin-orbit coupling constant. The relation between the relativistic magnetic field \mathbf{B}_{SO} and the electron orbital angular momentum \mathbf{L} can be expressed by $\mathbf{B}_{SO} = \frac{m_e\lambda_{SO}}{e}\mathbf{L}$.

In the presence of the SOI, the new Hamiltonian of the atom's electron contains not only the Coulomb interaction but also the spin-orbit interaction. For the new Hamiltonian, the conservation rules do not hold any longer separately for the orbital and the spin angular momentum. They sum up in order to form the *total angular momentum* \mathbf{J} , which gives the new eigenvalues of the electronic Hamiltonian and is the new quantity that is conserved [12]:

$$J = \sqrt{j(j+1)}\hbar; J_z = m_j\hbar, \quad (2.7)$$

where $j = l \pm s$ and $m_j = j, j-1, \dots, -j+1, -j$ are the new good quantum numbers, instead of m_l and m_s .

In the process of formation of atoms, the reason why electrons occupy the different atomic orbitals is described by the *Pauli exclusion principle*. However, the way that the electrons occupy the corresponding energy shells of an atom, resulting in the atomic

minimum energy state, can be described by the so-called *Hund's rules* [12, 13]. The main interaction to be minimized is the Coulomb repulsion between the electrons, causing them to occupy the available states in a way to maximize the occupation of the space at their disposal.

As a consequence of the minimization of the Coulomb energy in atoms according to Hund's rules, elements like Fe, Co and Ni (the *itinerant ferromagnets*) with not completely filled $3d$ -sub shells are generated. This results in a non-zero atomic magnetic moment, which is one of the requirements for obtaining ferromagnetism in solid systems.

2.1.2 Microscopic origin of magnetism in solids: the exchange interaction

2.1.2.1 Heisenberg-exchange interaction

When magnetic atoms join to form condensed matter, a long-range ferromagnetic order can be generated. Ferromagnetism is observed when the atomic magnetic moments align parallel to each other. The origin of the parallel alignment of the atomic moments is the *exchange interaction* [12], a pure quantum-mechanical effect which describes the Coulomb repulsion between electrons belonging to two neighboring atoms, jointly with the Pauli principle, which forbids two electrons to occupy the same quantum state. The strength of the interaction is directly connected to the overlap of the electronic wave-functions, justifying the definition of the exchange interaction as a short-range interaction.

A possible model for the description of ferromagnetism is the *Heisenberg model* [13]. In solid systems, due to the presence of a crystal electric field the "quenching" of the orbital angular momentum is commonly observed (mainly for itinerant ferromagnets) [12, 13]. This results in an effective magnetic moment for ferromagnetic materials arising solely from the atomic spin magnetic moment. Accordingly, the Heisenberg Hamiltonian for the exchange interaction can be written as [13]:

$$\mathcal{H}_{ex} = \sum_{i < j} -J_{ex} \mathbf{S}_i \cdot \mathbf{S}_j, \quad (2.8)$$

where J_{ex} is the inter-atomic exchange interaction strength between the two neighboring atoms i and j in the solid, S_i and S_j are the spins of the two atoms and the sum is over

all neighboring atoms. In order to minimize the Heisenberg energy, two neighboring spins will align parallel for $J_{ex} > 0$. This is the case of ferromagnetic materials like Fe, Co and Ni. While, in case $J_{ex} < 0$, the spins will align anti-parallel, generating an anti-ferromagnetic ordering [13].

The strength of the exchange interaction defines the Curie temperature, $T_C \propto \frac{J_{ex}}{k_B}$, of the ferromagnetic material, above which the material is in the *paramagnetic* phase. When $T > T_C$ the spontaneous magnetization of the system is lost, due to large thermal excitations; while for $T < T_C$ the exchange interaction dominates and the spontaneous ordered ferromagnetic phase is restored. A typical example for an itinerant ferromagnet is Fe, with a $T_C \approx 1000$ K [13].

The Heisenberg exchange interaction is also defined as a *symmetric exchange*. This is due to the scalar product between the two spin vectors in the Hamiltonian in Eq. 2.8. The definition of symmetric exchange is also used to distinguish the Heisenberg exchange from the so-called *anti-symmetric exchange interactions*. One of those is the Dzyaloshinskii–Moriya interaction [14], which is defined anti-symmetric since in the corresponding Hamiltonian the two spin vectors are multiplied by a vector product (see next section). As a consequence, the energetically favorable alignment of the two spins is perpendicular to each other. This is typical for systems with low symmetry, as it will be discussed in more details further below.

2.1.2.2 Dzyaloshinskii–Moriya interaction

The Dzyaloshinskii–Moriya interaction (DMI) is an anti-symmetric exchange interaction. It was first proposed by Dzyaloshinskii [14] in 1958 and shortly after by Moriya [15, 16] in 1960, in the attempt of describing the “weak ferromagnetism in antiferromagnets” and the “anisotropic super-exchange interaction” in bulk magnetic crystals characterized by a low symmetry. Dzyaloshinskii was first in understanding that there was a direct connection between the crystallographic symmetry and the magnetic configuration of solid systems. A lack of symmetry was at the origin of the small spontaneous magnetization in antiferromagnetic crystals, e.g. α -Fe₂O₃ or MnCO₃ [14]. Moriya [15, 16] was first in showing that, taking into account the spin-orbit coupling (SOC) $\lambda_{SO} \mathbf{S} \cdot \mathbf{L}$ and expanding it in powers of λ_{SO} , the effective Hamiltonian describing the interaction

between two spins, \mathbf{S}_i and \mathbf{S}_j , contains a term linear in the SOC which reads:

$$\mathcal{H}_{DMI} = \sum_{i < j} -\mathbf{D}_{ij} \cdot [\mathbf{S}_i \times \mathbf{S}_j], \quad (2.9)$$

where \mathbf{D}_{ij} is the DMI vector, whose modulus D_{ij} is proportional to the SOC (but not only, as it will be explained later) in the magnetic system. As it is shown in Fig. 2.2, the two spin magnetic moments need to be orthogonal to each other in order to minimize the DMI energy, resulting in a non-collinear spin configuration.

In magnetic systems, where the Heisenberg exchange interaction and a finite DMI are both present, the total Hamiltonian of the system contains both energy terms. Including also the effect of an external magnetic field, the ground state of the ferromagnetic system can change from a ferromagnetic state (Heisenberg exchange-dominated) to DMI-dominated states, like *chiral spin spirals* and *magnetic skyrmions* [17, 18].

Beside the bulk systems with low symmetry discussed by Dzyaloshinskii and Moriya in their early papers, in the last years a great interest has been growing around magnetic multilayers with interfacial DMI [19, 20]. In this case, the broken symmetry needed for the generation of the anti-symmetric exchange interaction is given by the interfaces of the material stacks [21, 22]. Considering an heterostructure where a thin FM layer is sandwiched between two different non-magnetic layers, a broken inversion symmetry is generated at each interface of the FM. As it is shown in Fig. 2.2, when a (3d) ferromag-

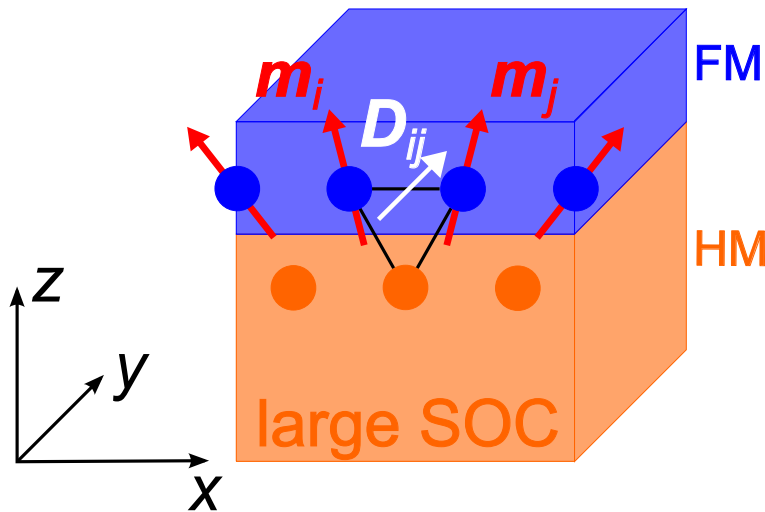


FIGURE 2.2: **Dzyaloshinskii–Moriya interaction at the interface.** Magnetization configuration at the HM\FM interface with DMI. The bottom heavy atoms mediate, via their strong SOC, the anti-symmetric exchange interaction between the magnetic atoms on top of them. The magnetic moments \mathbf{m}_i and \mathbf{m}_j have a finite angle in between, resulting in the minimization of the DMI. The rotation of the magnetic moment is dictated by the direction and the sign of the DMI vector \mathbf{D}_{ij} .

netic layer is in direct contact with an ($5d$) heavy metal layer with strong SOC, a DMI is generated between the ferromagnetic atoms and the heavy atoms directly at the interface, with the DMI vector \mathbf{D}_{ij} lying in the plane of the interface. As it has been shown by Yang et al. [22] with their first principles calculations for a Pt\Co interface, only the atoms right at the interface are mostly contributing to the generation of the DMI. Thus, the term “interfacial DMI” has been coined for such a new effect. A more detailed description of the microscopic origin of the interfacial DMI in metallic heterostructures will follow next, in the section focused on magnetism in metallic systems, where the concept of electronic energy bands will be introduced.

2.1.3 Magnetism in itinerant electron systems

On moving from single atoms to larger condensed matter systems, the description of the electronic states needs to be adjusted. In atomic systems, electrons occupy electronic orbitals, which are localized around the atomic nucleus. However, in solids electrons are contained in electronic energy bands [23]. Such energy bands are generated as a result of the overlapping of the electronic orbitals of the atoms present in the solid. This is mainly the case for the electrons residing in the outer shells, which are furthest from the atomic nucleus, while the inner shells’ electron states tend to remain localized around the nucleus. The outer electrons occupy the energy bands at their disposal up to the *Fermi Energy*, E_F . For metallic systems, E_F is in one (or more than one) of the energy bands, defined as *conduction band*. The electrons present at the Fermi energy can be shared among atoms, making them itinerant electrons. Those electrons are responsible for the conduction of the electric current in metals [23]. In the case of $3d$ itinerant ferromagnets (Fe, Co and Ni), the conduction energy band originates from the $3d$ and $4s$ atomic orbitals. This means that the charge carriers in these metals are $3d$ – $4s$ hybridized electrons.

A simple model for the description of ferromagnetism in metals was proposed by Stoner, based on a free–electron approximation [13]. The Stoner’s model describes the two spin–polarized (spin– \uparrow and spin– \downarrow) energy bands of a metallic ferromagnet as spontaneously shifted in energy. This split of the two energy bands occurs when the *Stoner criterion* is fulfilled:

$$I * N_{\uparrow,\downarrow}(E_F) > 1. \quad (2.10)$$

I is the Stoner exchange parameter; while $N_{\uparrow,\downarrow}(E_F) = \frac{D(E_F)}{2n}$ is the density of states per atom for each spin state (\uparrow or \downarrow), with $D(E_F)$ being the total density of states (DOS) at the Fermi level and n the number of atoms per unit volume. In Fig. 2.3 the DOS of an itinerant ferromagnet, with two spin-polarized sub-bands, is illustrated.

In a *molecular field* approach, the energy split between the two sub-bands can be explained as due to the presence of the internal exchange field, $\mathbf{H}_{ex} = n_S \mathbf{M}$, where n_S is a coefficient which describes the strength of the exchange field. The exchange field adds a Zeeman-like energy term to the conduction electrons energy due to their spin magnetic moment. The electrons with their magnetic moment parallel with \mathbf{H}_{ex} will be

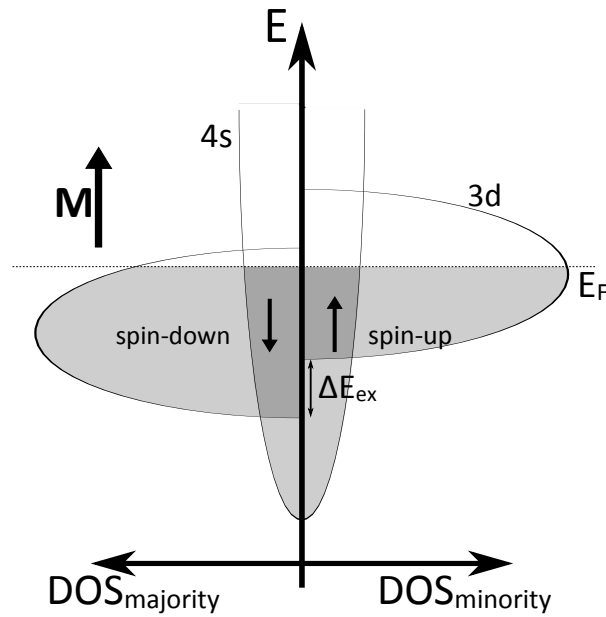


FIGURE 2.3: **DOS of itinerant ferromagnets.** Schematic of the DOS for the two spin-polarized sub-bands of an itinerant ferromagnet close to the Fermi level. The conduction electrons are contained in the overlapping $3d$ and $4s$ energy bands. The \downarrow -electrons are the majority electrons, while the \uparrow -electrons are the minority ones. The net magnetization is parallel to the magnetic moment of the majority electrons.

at lower energy compared to the electrons with the magnetic moment anti-parallel to \mathbf{H}_{ex} . The energy difference between the two spin states is $\Delta E_{ex} = 2\mu_0 \mu_e \cdot \mathbf{H}_{ex}$. The net magnetization is in turn generated by the difference between spin-down and spin-up electrons contained in the metal. Considering the case in Fig. 2.3, due to the larger number of spin-down electrons present in the system compared to spin-up electrons, a net magnetization pointing in the direction of the magnetic moments of the spin-down electrons is obtained.

2.1.4 Microscopic origin of the interfacial Dzyaloshinskii–Moriya interaction

Recently, different interpretations have been proposed for the microscopic origin of the DMI at [heavy metals]\[3d–ferromagnets] interfaces. On one side, new first principles calculations based on density functional theory [24] have highlighted the SOI, the hybridization between the 3d and the 5d orbitals, and the position of the Fermi level with respect to the center of the 5d electronic energy band as the key terms in the definition of the strength and the sign of the effective DMI.

The SOI is observed to affect strongly the electronic energy due to the hybridization of the 3d and 5d states. The electronic energy is observed to be increased or decreased by the SOI across the 5d band, generating an oscillating DMI as a function of the electronic energy. A change of the heavy metal, which means to change the number of electrons occupying the 5d energy band, generates a shift of the Fermi level in the 5d band. Accordingly, the Fermi level moves from positive DMI energies to negative DMI energies and vice versa, justifying the observed different signs and strengths of the DMI for different 5d metals [20, 25]. Furthermore, calculations based on a tight–binding model for a system consisting of two 3d ferromagnetic atoms and one 5d metal atom [24] confirm the linear proportionality of the DMI strength with respect the strength of the SOC at the 5d atom.

An alternative interpretation for the origin of the interfacial DMI has been proposed by Ryu et al. [26]. Studying the effect of an applied in–plane field on the current–induced domain wall motion in [heavy metals]\[3d–ferromagnets] nanowires, they extracted larger effective DMI values for the material systems with a larger magnetization induced at the interface in the heavy metal layer. According to the observed correlation between the strength of the induced magnetization and of the effective DMI, Ryu and co–authors propose the origin of the DMI to be closely related to the proximity–induced magnetization. However, this interpretation is not able to explain the origin of the sign of the effective DMI.

Finally, it has also been proposed the possibility of tailoring the strength and the sign of the DMI by doping the bottom heavy metal layer with light atoms characterized by a large electronegativity. This is the case discussed by Torrejon et al. [27], where they attributed the appearing of a positive DMI at the interface between Ta and CoFeB due to a doping of the heavy metal with N. The argument is that, the larger electronegativity of

the N atoms ([He]2s²2p³, 3.0 Pauling) compared to the one of Ta atoms ([Xe]4f¹⁴5d³6s², 1.5 Pauling) [28] gives a change of the electronic configuration at the interface due to the 2p–5d hybridization of the electronic orbitals. Such modification of the electronic states at the TaN\CoFeB interface is expected to influence directly or indirectly the DMI in the material system.

2.2 Thermodynamical description of magnetism in the micromagnetic approximation

In order to describe macroscopic magnetic systems, the atomistic description based on the Heisenberg Hamiltonian needs to be replaced by a thermodynamical description based on the *micromagnetic* approximation. In the micromagnetic approximation, the atomic magnetic moments are replaced by a continuous magnetization function, $\mathbf{M}(\mathbf{r})$ [13, 29, 30], which describes the magnetization locally in the system. The magnetization, \mathbf{M} , is the vector field that describes the density of the magnetic dipole moments in a magnetic material.

What defines the final magnetization configuration of a ferromagnetic sample is the minimization of its *magnetic free energy*, corresponding to either a local or a global energy minimum. It is possible to express the magnetic free energy as [13, 31]:

$$F = \int f(\mathbf{r})d^3r = \int [f_{ex}(\mathbf{r}) + f_Z(\mathbf{r}) + f_{str}(\mathbf{r}) + f_{ani}(\mathbf{r}) + \dots]d^3r, \quad (2.11)$$

where the terms in the volumetric integral are the contributions to the local free energy density, $f(\mathbf{r})$, respectively from the *exchange interaction*, the *Zeeman interaction*, the *dipolar stray field* generated by the magnetic moments, the *magnetic anisotropy*, and other contributions not relevant in the present discussion. In the following, each term will be described in more detail.

2.2.1 Exchange energy

The first term in Eq. 2.11 is the exchange energy. It reads [13]:

$$F_{ex} = \int f_{ex}(\mathbf{r})d^3r = \int A|\nabla\mathbf{e}_M|^2d^3r, \quad (2.12)$$

where $\mathbf{e}_M = \mathbf{M}(\mathbf{r})/M_s$ is a unit vector in the local magnetization direction. M_s is the saturation magnetization of the magnetic sample. A is the *exchange stiffness*. For crystallographic systems, the exchange stiffness can be defined as $A \approx \frac{J_{ex}S^2Z_c}{a}$ [13], with Z_c the number of atoms per unit cell and a the lattice parameter.

The exchange interaction does not define any preferential direction in space for the alignment of the spins. In other words, the exchange interaction is isotropic. The energy minimum is reached when all the spins are aligned to each other.

2.2.2 Zeeman energy

The second term in Eq. 2.11 is the Zeeman energy, which is the magnetostatic energy of the system due to the presence of an external magnetic field, $\mathbf{H}_{ext}(\mathbf{r})$. The effect of the presence of this external magnetic field is the tendency for the local magnetization, $\mathbf{M}(\mathbf{r})$, to align itself parallel to \mathbf{H}_{ext} . The corresponding energy can be expressed as [13]:

$$F_Z = \int f_Z(\mathbf{r})d^3r = -\mu_0 \int \mathbf{M}(\mathbf{r}) \cdot \mathbf{H}_{ext}(\mathbf{r})d^3r. \quad (2.13)$$

The Zeeman energy of the system is minimized when $\mathbf{M}(\mathbf{r})$ is aligned parallel to $\mathbf{H}_{ext}(\mathbf{r})$ everywhere in the magnetic sample.

2.2.3 Magnetic dipolar energy

The single magnetic moments inside the sample generate a dipolar magnetic stray field, which interacts with all the other magnetic moments present in the sample. Such dipolar interaction gives rise to another energy contribution to the total magnetic free energy. In the micromagnetic approximation the stray field, $\mathbf{H}_{str}(\mathbf{r})$, can be calculated by the 2nd Maxwell's equation [13]:

$$\nabla \cdot \mathbf{B} = \mu_0 \nabla \cdot (\mathbf{H} + \mathbf{M}) = 0. \quad (2.14)$$

Indeed, in the absence of an applied external magnetic field, Eq. 2.14 turns into $\mu_0 \nabla \cdot (\mathbf{H}_{str} + \mathbf{M}) = 0$, which implies:

$$\nabla \cdot \mathbf{H}_{str} = -\nabla \cdot \mathbf{M}. \quad (2.15)$$

It is possible to define the stray field as generated by an effective magnetic charge density $\rho_M(\mathbf{r}) = \nabla \cdot \mathbf{M}(\mathbf{r})$, using the Gauss's theorem for a vector field [13]. Accordingly, the energy contribution to the free energy due to the dipolar interaction reads [30]:

$$F_{str} = \int_V f_{str}(\mathbf{r}) d^3r = \frac{1}{2} \mu_0 \int_{\mathfrak{R}^3} |\mathbf{H}_{str}(\mathbf{r})|^2 d^3r, \quad (2.16)$$

where V is the magnetic volume and \mathfrak{R}^3 indicates the real three-dimensional space.

The shape of the sample strongly influences the stray field energy, which is often referred to as *shape anisotropy*. The stray field inside the magnetic sample is also referred to as *demagnetizing field*, \mathbf{H}_d [13]. To understand better why the name *shape anisotropy* is employed to describe the dipolar magnetic energy, let us consider the case of a thin film nanostructure, where the length l and the width w of the system are much larger than the thickness t ($l > w \gg t$, as shown in Fig. 2.4). The magnetization $\mathbf{M}(\mathbf{r})$ is finite inside the sample, and zero outside. This makes the divergence of the magnetization large at the sample surfaces if the component of $\mathbf{M}(\mathbf{r})$ normal to the surface is non-zero. In a phenomenological description, the magnetization component normal to the surface of the sample acts as a source of “magnetic charges”, which in turn generate the demagnetizing field, as described above.

Considering the magnetic nanostructure shown in Fig. 2.4, the magnetization can lie along three main directions: (a) along the length, (b) along the width or (c) along the thickness of the sample. For all the three cases, the demagnetizing field can be expressed as [13]:

$$\mathbf{H}_{d,i} = -N_{d,i} \mathbf{M}_i, \quad (2.17)$$

where $i = x, y, z$ and $N_{d,x} + N_{d,y} + N_{d,z} = 1$. The $N_{d,i}$ are defined as *demagnetizing coefficients*. For the chosen geometry, where $t \ll w < l$, it is possible to obtain the following expressions for the demagnetizing coefficients [32]:

$$N_{dx} \approx \frac{t}{2\pi^2 l}, N_{dy} \approx \frac{t}{2\pi^2 w}, N_{dz} \approx 1. \quad (2.18)$$

The shape anisotropy can be phenomenologically described as an effective magnetic field produced in the sample when the magnetization moves away from the minimum H_d direction. For \mathbf{M} moving away from the x -direction towards the y -direction in Fig. 2.4, the anisotropy field can be expressed as $\mathbf{H}_{shape} = \mathbf{M}(N_{d,x} - N_{d,y}) = \mathbf{M} \frac{t}{2\pi^2} (\frac{1}{l} - \frac{1}{w})$

[32]. The corresponding magnetostatic energy density is:

$$\epsilon_{shape} = -\frac{1}{2}\mu_0\mathbf{M}\cdot\mathbf{H}_{shape} = K_{shape}\cos^2(\alpha) = K_{shape} - K_{shape}\cos^2(\theta), \quad (2.19)$$

where $K_{shape} = \frac{t}{4\pi^2}\mu_0(\frac{1}{w} - \frac{1}{l})M_s^2 > 0$ is the shape anisotropy constant, α defines the tilting of \mathbf{M} with respect to the y -axis and θ is the angle between \mathbf{M} and the x -axis (the axis of minimum energy density). According to Eq. 2.18 and 2.19, in absence of any other magnetic anisotropy, the magnetization would spontaneously lie along the long side of the sample, since this would minimize the demagnetizing field and thus the magnetostatic energy of the system.

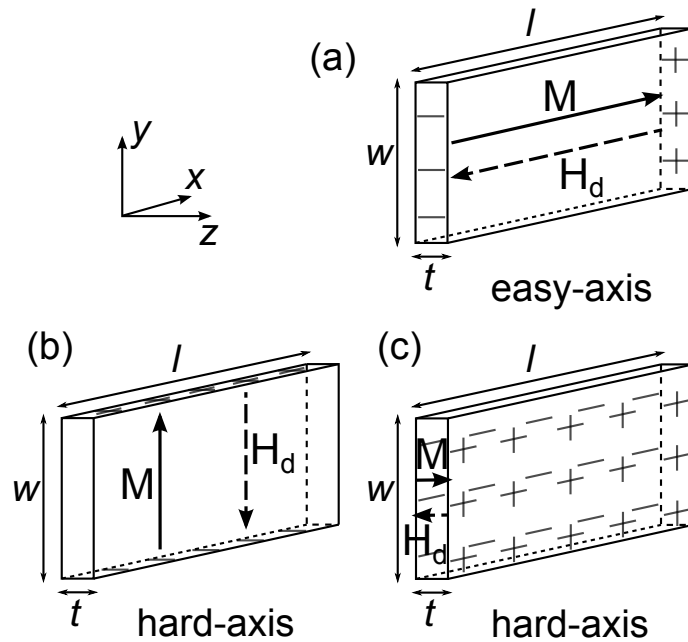


FIGURE 2.4: **Magnetic shape anisotropy.** The magnetization and the corresponding demagnetizing field, for the three main magnetization configuration. The “+” and “-” represent the “magnetic charges” at the sample surfaces. The more charges are produced, the larger the demagnetizing field will be.

2.2.4 Anisotropy energy

It is common to observe in crystalline ferromagnets that the spontaneous magnetization prefers to lie along some specific crystallographic directions. For example, in Fe, which exhibits a body centered cubic crystallographic structure, the magnetization prefers to align itself spontaneously along the sides of the cube [13]. This results in anisotropic magnetic systems, where the magnetization prefers to align only along specific crystallographic axes, defined as *easy-axes*.

The origin of such anisotropy is linked to the crystal electric field, due to the crystallographic structure. Due to the spin–orbit interaction (see Eq. 2.6), the spins \mathbf{S} of the atoms are not free to point in any direction, but only in those ones that minimize the SOI. Since this anisotropy originates directly from the crystal, it is defined as *magnetocrystalline anisotropy*.

In the micromagnetic approximation, the uniaxial anisotropy energy can be described as:

$$F_{ani} = \int f_{ani}(\mathbf{r})d^3r = \int K \sin^2(\theta)d^3r, \quad (2.20)$$

where K is the first order magnetocrystalline anisotropy constant and θ is the angle between the magnetic easy–axis and the magnetization direction. From Eq. 2.20, it is clear that the energy is minimized when the magnetization is collinear to the easy–axis ($\theta = 0^\circ, 180^\circ$), while it is maximized when the magnetization lies in the plane perpendicular to the easy–axis ($\theta = 90^\circ, 270^\circ$). As a result, in a ferromagnetic system characterized by a uni–axial magnetic anisotropy, the anisotropy energy is minimized when the spontaneous magnetization lies along the easy–axis.

2.2.5 Induced perpendicular magnetic anisotropy

The investigation of magnetic nanostructures characterized by a strong perpendicular magnetic anisotropy (PMA) has been of great interest in the last few years [25, 33–36]. The general material system where the PMA has been observed is a multilayer consisting of:

- A few nm–thick bottom heavy metal (HM) layer (Pt, Ta).
- An ultra–thin (a few Å to 1 nm) ferromagnetic (FM) layer in the middle (Co, CoNi, CoFe, CoFeB).
- An oxide (Ox) top layer (AlO_x , MgO).

A general PMA material stack is schematically shown in Fig. 2.5. According to what is reported above concerning the shape anisotropy, the magnetization in such ultra–thin FM is expected to lie in the plane of the sample. So, a possible explanation for the observed PMA could be a large crystal anisotropy with an easy–axis pointing perpendicular to the film surface. However, those systems are characterized by polycrystalline

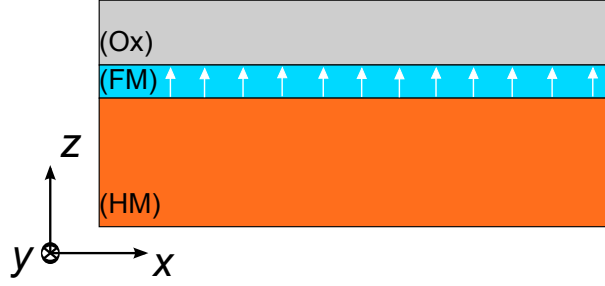


FIGURE 2.5: **PMA material system.** The PMA has been observed in material systems consisting of: a bottom heavy metal (HM) layer; an ultra-thin ($\leq 1\text{nm}$ thick) ferromagnetic (FM) layer; a top Oxide (Ox) layer. The two interfaces of the FM with the HM and the Ox is where the PMA is originated, due to strong SOI and electronic orbitals overlaps.

ferromagnetic layers, which consist of nanometer-size grains separated by grain boundaries, or by amorphous ferromagnetic materials. There is no long range crystallographic order to justify a macroscopic crystal anisotropy. As a consequence, another anisotropy term has to be taken into account to explain the observed out-of-plane (OOP) spontaneous magnetization.

The origin of this OOP easy-axis has been shown to be at both the HM\FM-interface and the FM\Ox-interface, from which the name of *magnetic interface anisotropy*. At the HM\FM-interface the induced PMA is attributed to the HM $5d$ -FM $3d$ -hybridization of the electronic orbitals [37]. Due to the strong SOI present in the system, the electronic orbitals with their magnetic moment pointing OOP are energetically favorable compared to the others. An example is the observed enhancement of the orbital magnetic moment μ_{orb} in Co at the Pt\Co interface [37], which drives the PMA in the system.

A second origin for the PMA in the magnetic thin film is at the FM\Ox-interface. As shown by first principles calculations [38] for the Fe\MgO and Co\MgO interfaces, there are two main mechanisms which generate the PMA in such magnetic bilayers. First, there is the overlap between the Ox- p_z -like and the transition metal FM- d_{z^2} -like electronic states (see electronic orbitals in Fig. 2.6), which results in hybridized $p-d$ -like electronic states at the interface. Second, there is the hybridization between the d_{z^2} -like and the $d_{xz,yz}$ -like electronic states in the ferromagnet. Due to the SOI, the hybridized electronic states close to the Fermi edge carrying an OOP magnetic moment, are energetically favorable in comparison to the ones with an in-plane magnetic moment.

The two interface anisotropy contributions sum up resulting in a net PMA for the material stack. The total effective anisotropy of the system due to the co-existence of the interface anisotropy, the bulk (crystal) anisotropy, and the shape anisotropy can be

phenomenologically described by [39]:

$$K_{eff} = K_b + \frac{K_i}{t_{FM}} - \frac{1}{2}\mu_0 M_s^2. \quad (2.21)$$

Here, K_b is the bulk anisotropy energy density, that, for non-textured and amorphous FM layers, is zero. K_i is the interface anisotropy energy per unit area. The last term represents the shape anisotropy energy density due to the demagnetizing field. Since the latter contribution to the effective anisotropy is constant with respect to the thickness of the ferromagnetic layer, t_{FM} (assuming no change of M_s with respect to t_{FM}), K_{eff} can be positive or negative depending on t_{FM} . In the case of a large K_i , for a very thin FM layer K_{eff} will be positive and the system will exhibit a PMA. On the other hand, if t_{FM} is large enough, K_{eff} will be negative, resulting in an in-plane effective anisotropy.

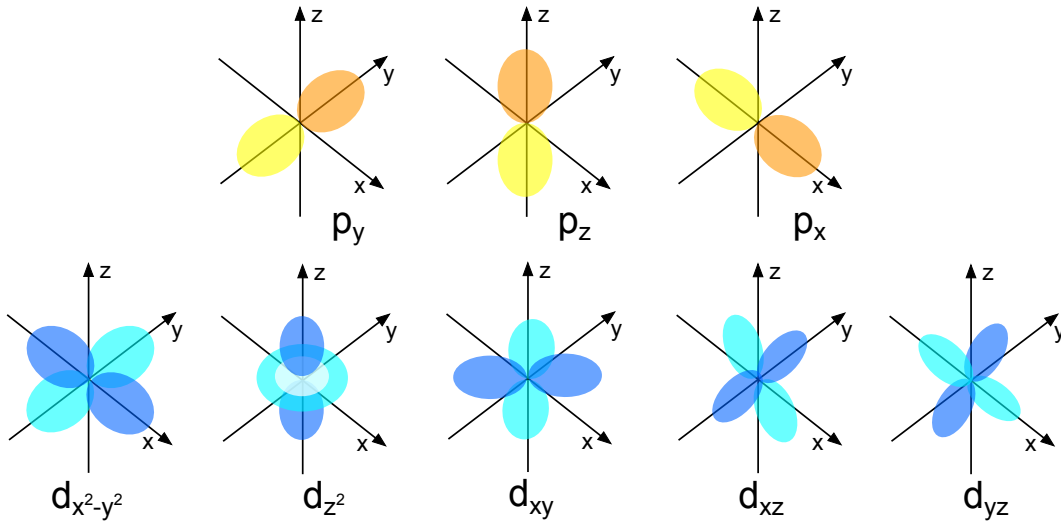


FIGURE 2.6: **Atomic 2p and 3d electronic orbitals.** Angular distribution of the electronic density of the 2p and 3d atomic orbitals [13].

2.2.6 Energy minimization: magnetic domains and domain walls

The final magnetic texture in a magnetic sample is the one which minimizes the sum of all the energy terms contributing to the magnetic free energy, and it can reflect a local or an absolute energy minimum, depending on the specific energy minimization path followed by the system. Considering only the exchange energy and the magnetic anisotropy, it would be expected to observe macroscopic ferromagnetic systems fully magnetized in one direction, corresponding to one of the magnetic easy-axis. However,

it is of common knowledge that usual macroscopic ferromagnetic systems have no net magnetization, due to the presence of *magnetic domains* separated by thin *magnetic domain walls*.

According to Weiss's theory [13], macroscopic ferromagnetic systems split up into many microscopic magnetic domains in order to minimize their total dipolar energy F_{str} , due to the dipolar stray field (or demagnetizing field) [13]. However, the formation of a domain wall (DW) in between two magnetic domains is also energetically expensive. This means that a DW is generated only if the total energy of the system is reduced after its formation.

Considering the case of a ferromagnetic system characterized by a uni-axial anisotropy along the x -axis (see Fig. 2.7), the dimension of a DW (proportional to the number N of spins contained in the DW along its width) is determined by the minimization of the sum $F_{ex} + F_{ani}$ (assuming no other contributions to the total free energy, beside these two). The magnetization rotates continuously over many inter-atomic distances, moving from one uniformly magnetized area to the next. The minimization of the sum of exchange and anisotropy energy will define the width of the DW. An expression for the width of the DW is given by [13]:

$$\lambda_{DW} = N * a \approx \sqrt{\frac{A}{K}}, \quad (2.22)$$

where A is the exchange stiffness, K is the uni-axial anisotropy energy density constant, and a is the lattice parameter.

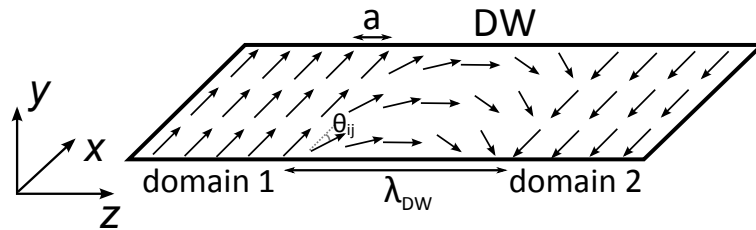


FIGURE 2.7: **Magnetic domain wall.** Two magnetic domains separated by a DW. The magnetization in the DW rotates continuously from *domain 1*'s magnetization direction to *domain 2*'s magnetization direction. Both domains have their magnetization pointing along the easy-axis, but anti-parallel with respect to each other. The DW width, λ_{DW} , is given by the lattice parameter, a , times the number of spins, N , needed to move from *domain 1* to *domain 2*. θ_{ij} defines the angle between two consecutive spins in the DW.

2.3 Néel–Brown model of magnetization reversal

The theory of magnetism in the micromagnetic approximation presented in the previous section refers to the case $T = 0$ K, where the effects of thermal fluctuations are not considered. However, in real systems the temperature is finite, and the $T = 0$ magnetization stable state obtained by the minimization of the magnetic free energy in Eq. 2.11 is continuously perturbed by thermal agitation.

A description of thermal fluctuations of magnetic moments in a single-domain magnetic particle was, for the first time, proposed by Néel [40] and Brown [41]. Considering a magnetic particle whose internal magnetization can be described by a single macrospin (being all the magnetic moments aligned), with a uni-axial magnetic anisotropy, its magnetization will lie along the magnetic easy-axis, in one of the two stable states (see Fig. 2.8). The two stable states are separated by a single energy barrier, $E_b(H)$, which is a function of the applied magnetic field, H . The magnetization changes from one state to the other by overcoming the energy barrier E_b . The energy barrier between the two stable states can be lowered by applying H in the opposite direction of the particle's magnetization. When the field is large enough, the thermal fluctuations will allow the system to reverse its magnetization. An simple analytical approximation for the dependence of E_b on H is [42]:

$$E_b(H) = E_0 \left(1 - \frac{H}{H_{sw}^0}\right)^\chi, \quad (2.23)$$

where E_0 is the energy barrier at zero field, H_{sw}^0 is the switching field at zero temperature, and χ is a coefficient that is usually equal to 1.5. The probability that the magnetization in the magnetic particle has not switched after a time t is give by [42]:

$$P(t) = \exp\left(-\frac{t}{\tau}\right), \quad (2.24)$$

where τ here represent the inverse of the switching rate, also known as *relaxation time*, and can be expressed as [42]:

$$\tau(T, H) = \tau_0 \exp\left(\frac{E_b(H)}{k_B T}\right), \quad (2.25)$$

with τ_0 being the inverse of the attempt frequency, f_0 . Here, τ_0 represents the time during which the thermal fluctuations of the magnetization occur, which is in the order

of 1 ns.

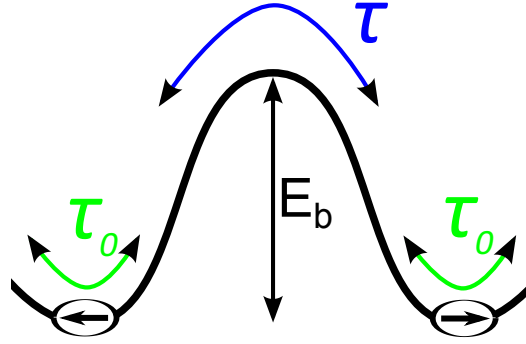


FIGURE 2.8: **Néel–Brown model.** Schematic of the thermal activated magnetization reversal described by the Néel–Brown model. The probability of transition between the two magnetization states is defined by the single energy barrier, E_b , separating the two states. When E_b is sufficiently small, due to the application of an external magnetic field for example, the particle’s magnetization can switch due to thermal fluctuations. The switching time (or relaxation time) and the fluctuation time are indicated by τ and τ_0 , respectively.

2.4 Interfacial DMI in PMA magnetic nanowires: chiral Néel domain walls

Let us consider now the effect of the interfacial DMI discussed before on the magnetic texture in magnetic nanowires. As shown in Fig. 2.9, for PMA materials with large values of the magnetic anisotropy DW widths, λ_{DW} , of the order of a few nm are expected [43]. Accordingly, in thin films ($t_{FM} \leq 1$ nm) and in the commonly investigated nanostructures [25, 35, 44] with a width w ranging between a few 100 nm and a few μm , Bloch–type DWs are expected, for magnetostatic reasons (see Fig. 2.9(a)). However, as shown by Thiaville et al. [45], in the presence of DMI at the HM\FM interface, a Néel–type DW can be generated. Increasing the strength of the DMI, the DW magnetic moments can be rotated from the full Bloch configuration to the full Néel configuration, as shown in Figs 2.9(b) and 2.9(c). This is due to the minimization of the DW energy density, where the magnetostatic energy and the DMI are competing in the definition of the DW final state. As calculated by Thiaville et al. [45], when $D \geq D_c = 4\lambda_{DW}K/\pi$, the DW will assume the Néel configuration (where K is the shape anisotropy density of the DW), while for $D < D_c$ the DW’s moments reorient to the Bloch configuration with decreasing D .

In PMA systems two different types of DWs can be obtained: $\uparrow\downarrow$ -DW and $\downarrow\uparrow$ -DW; as

shown in Fig. 2.10. In the presence of DMI at the interface, the Néel component of the DW magnetic moment $\mathbf{m}_{DW,x}$ will have opposite sign for the two DWs, forming “chiral” domain walls. This means that, moving from one magnetic domain to the other, the magnetic moments in the DW will rotate with the same winding (either clockwise or counterclockwise) around the direction of \mathbf{D} . When the winding occurs *clockwise* the DWs are referred to as *right-handed* and the DMI is said to be positive; while for counterclockwise winding the DWs are referred to as *left-handed* and the DMI is said to be negative.

Phenomenologically, the action of the DMI on the DW magnetic configuration can be described as an effective magnetic field \mathbf{H}_{DMI} localized at the DW [25, 35, 45]. Such effective field points along the longitudinal direction (x -axis) and has opposite sign for $\uparrow\downarrow$ - and $\downarrow\uparrow$ -DW, generating the Néel component of the DW in Fig. 2.10. The expression of the effective DMI field reads [45]:

$$H_{DMI} = \frac{D}{\mu_0 M_s \lambda_{DW}}, \quad (2.26)$$

with \mathbf{H}_{DMI} pointing along $+x$ -direction ($-x$ -direction) when \mathbf{D} points along the $+y$ -direction ($-y$ -direction), for an $\uparrow\downarrow$ -DW. The same symmetry, but with opposite sign, holds for a $\downarrow\uparrow$ -DW.

2.5 Field-induced magnetization dynamics: the Landau–Lifshitz–Gilbert equation

Formally, the dynamics of magnetization in ferromagnetic materials is described by the phenomenological *Landau–Lifshitz–Gilbert* (LLG) equation [46]. The LLG equation can be expressed as [46]:

$$\frac{\partial \mathbf{M}}{\partial t} = -\gamma \mu_0 \mathbf{M} \times \mathbf{H}_{\text{eff}} + \frac{\alpha}{M_S} \mathbf{M} \times \frac{\partial \mathbf{M}}{\partial t}, \quad (2.27)$$

where γ is the gyromagnetic ratio, μ_0 is the permeability of free space, \mathbf{H}_{eff} is the total effective field acting on the magnetization \mathbf{M} , and α is the Gilbert damping constant. The effective field is the sum of all the magnetic fields acting on the magnetization: external field, anisotropy field and other possible effective fields that could be interacting with \mathbf{M} .

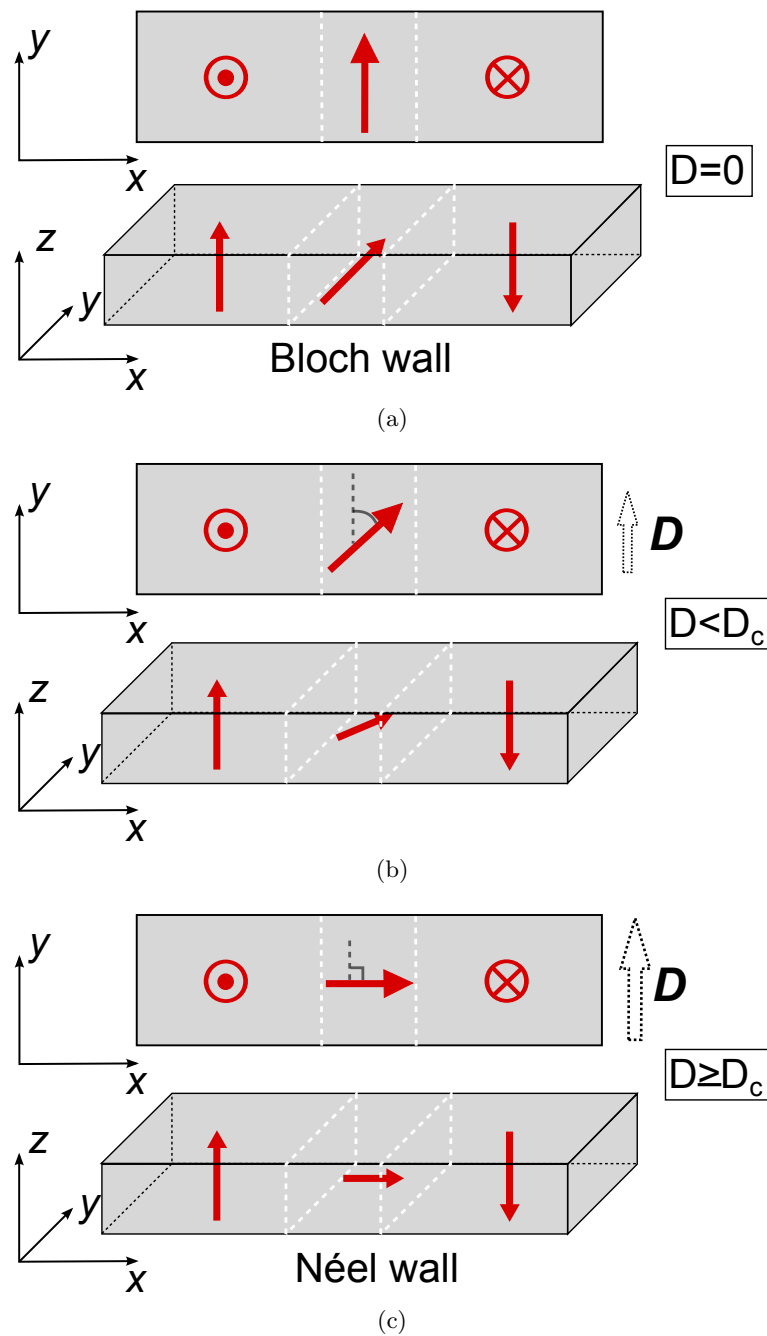


FIGURE 2.9: An $\uparrow\downarrow$ -DW's magnetic configuration as a function of the DMI. (a) In the absence of DMI, in PMA magnetic nanowires with $w \gg \lambda_{DW}$, DWs are expected to be of the Bloch-type, due to the strong shape anisotropy of the DW. (b) In the presence of a moderate DMI, with $D < D_c$, the DW is between the Bloch and the Néel configuration. (c) When the DMI is strong enough, with $D \geq D_c$, the DW is fully Néel-type. The case reported here refers to a positive DMI, which induces right-handed DWs.

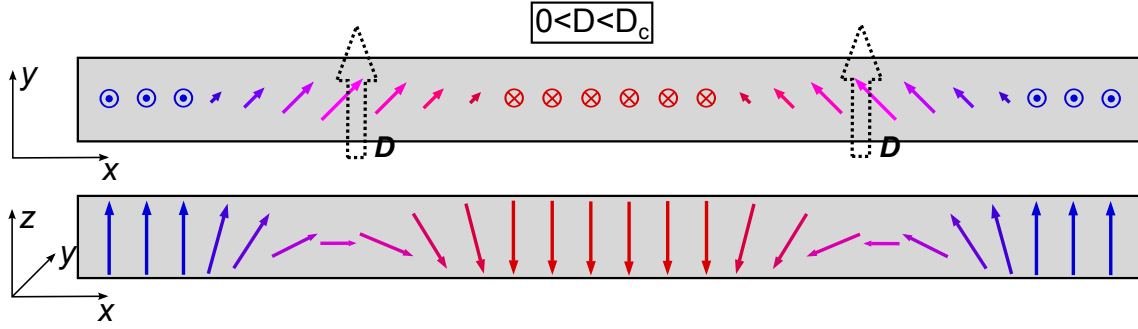


FIGURE 2.10: **Chiral domain walls.** Top-view and side-view of an $\uparrow\downarrow$ -DW (left) and a $\downarrow\uparrow$ -DW (right), in a material system with a positive interfacial DMI. The DMI strength is finite and lower than the saturation value D_c , generating right-handed DWs with a finite Néel component $\mathbf{m}_{DW,x}$ that is positive (negative) for the $\uparrow\downarrow$ -DW ($\downarrow\uparrow$ -DW).

The first term on the right side of Eq. 2.27 describes the precession of the magnetic moment around the effective field, as indicated by the violet arrow in Fig. 2.11. Without any dissipation term, the magnetic moment would precess around the effective field continuously. Accordingly, the second term is introduced in order to account for the energy dissipation effects [47]. The corresponding damping torque is indicated by the red arrow in Fig. 2.11. Such a torque tends to align the magnetic moment with the effective field.

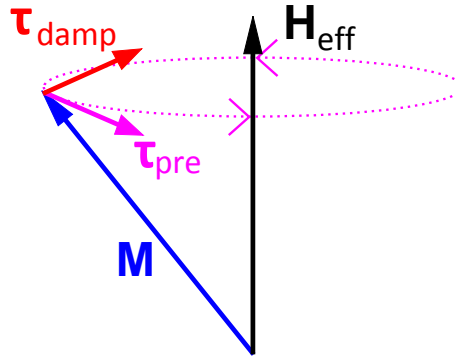


FIGURE 2.11: **Magnetization dynamics as described by the LLG equation.** Schematic of the magnetization dynamics in the presence of a net effective magnetic field, \mathbf{H}_{eff} . When the magnetization vector is non collinear with \mathbf{H}_{eff} , a precessional torque, τ_{pre} , causes precession of \mathbf{M} around the effective field, while a damping torque, τ_{damp} , aligns \mathbf{M} with the field.

2.6 Current-induced magnetization dynamics in metallic ferromagnets

2.6.1 Spin-dependent transport

Referring to Fig. 2.3, the overlapping of the $3d$ and the $4s$ energy bands at the Fermi level results in spin-dependent transport properties. The presence of a net magnetization introduces a spin-dependent scattering process, which is characterized by two different momentum scattering mean free path for spin-up and spin-down electrons, $\lambda^{\uparrow,\downarrow}$, associated to two different momentum scattering times, $\tau^{\uparrow,\downarrow}$. As a consequence, the injection of an electric current into an itinerant ferromagnet results in the generation of a spin-polarized current.

Referring to Fig. 2.3, the spin-down electrons are defined as *majority electrons*, while the spin-up electrons are the *minority electrons*. The majority and minority electrons populate the majority and the minority band, respectively. Due to the spin-dependent scattering characteristic of metallic ferromagnets, the two types of electrons have different conductivities [13, 48]. This can be expressed by [49]:

$$\sigma^{\uparrow,\downarrow} = \frac{1}{\rho^{\uparrow,\downarrow}} = \frac{e^2 \tau^{\uparrow,\downarrow} D^{\uparrow,\downarrow}(E_F)}{m_e^*}, \quad (2.28)$$

where \uparrow and \downarrow refer to spin-up and spin-down electrons, $D(E_F)$ is the DOS at the Fermi level, m_e^* is the effective mass of the conduction electrons and $\tau^{\uparrow,\downarrow}$ is the spin-dependent momentum scattering time. A two-channel model can be developed for itinerant ferromagnets [50], where the metallic system consists of two half-metals (a half-metal is a metallic system where only electrons of one type of spin contribute to the conductivity). In such a model, considering also the possibility of inter-channels scattering events, the ferromagnet resistivity can be expressed in the following way [50]:

$$\rho = \frac{\rho^\downarrow \rho^\uparrow + \rho^{\downarrow\uparrow}(\rho^\downarrow + \rho^\uparrow)}{\rho^\downarrow + \rho^\uparrow + 4\rho^{\downarrow\uparrow}}, \quad (2.29)$$

where $\rho^{\downarrow\uparrow}$ is the resistivity contribution due to the inter-channel scattering processes (also known as *spin-flip* scattering events). It is easy to see from Eq. 2.29 that, when $\rho^{\downarrow\uparrow} \ll \rho^\downarrow, \rho^\uparrow$, the total resistivity $\rho = \frac{\rho^\downarrow \rho^\uparrow}{\rho^\downarrow + \rho^\uparrow}$ is equivalent to that resulting from \uparrow -spin \downarrow -spin half-metals connected in parallel.

The electrical resistivity of the two spin-channels are usually different [50]. The probability of scattering in the s - d band is a function of the available states at the Fermi level. More available states means a higher probability for the “itinerant” (small m_e^*) s -like electrons to be scattered into the more “localized” (large m_e^*) d -like states, which results in a higher resistivity, in accordance with Eq. 2.28. On the other hand, the DOS at the Fermi level is also usually different for the two spin-channels. As a consequence, the two contributions I^\downarrow and I^\uparrow to the total current ($I = I^\downarrow + I^\uparrow$) are different, resulting in the generation of a spin-polarized current, $I_{diff} = I^\downarrow - I^\uparrow$. The degree of polarization of the electric current is referred to as *spin-polarization* (P) [13, 48], and can be defined as [13]:

$$P = \frac{I_{diff}}{I} = \frac{v_{F,\downarrow}^n D^\downarrow(E_F) - v_{F,\uparrow}^n D^\uparrow(E_F)}{v_{F,\downarrow}^n D^\downarrow(E_F) + v_{F,\uparrow}^n D^\uparrow(E_F)}, \quad (2.30)$$

where $v_{F,\uparrow,\downarrow}$ is the spin dependent Fermi velocity of the electrons and $n = 0, 1, 2$ for spin-polarized photoemission, ballistic transport or diffusive transport, respectively. According to the definition of spin-polarization, the commonly used itinerant ferromagnets Fe, Co, and Ni have $P > 0$ under diffusive transport conditions, with the major contribution to the total electric current originating from their majority band electrons [13].

2.6.2 Spin-transfer torque: a toy model

Let us consider a system consisting of two ferromagnetic thin films, FM1 and FM2, separated by a non-magnetic metallic layer, NM, as shown in Fig. 2.12. Such a magnetic system is known as a *spin valve* [48]. If an electric current is injected from the left to the right of the spin valve in Fig. 2.12, the conduction electrons are spin-polarized in FM1, with their magnetic moments aligned with the magnetization \mathbf{M}_1 (neglecting the orbital moments, a reasonable approximation at this basic level of description for transition-metal ferromagnets, due to the quenching of the angular moments [46]). Moving towards FM2, the spin-polarized electrons cross the thin NM layer without losing their spin polarization, if t_{NM} is smaller than the spin diffusion length, λ_{spin} , in the NM (λ_{spin} is the distance over which the electron travels with a fixed spin, defined by the scattering probability of the electron in the metal [48]). At this point, the spin-polarized electrons reach FM2, where the magnetization \mathbf{M}_2 is not collinear to \mathbf{M}_1 . Right at the interface NM/FM2 there are spin magnetic moments aligned with \mathbf{M}_1 , entering the second ferromagnet. The misalignment between the itinerant magnetization, \mathbf{M}'_1 , and

\mathbf{M}_2 generates a torque (actually, a change of the magnetization in time) on the local magnetization in FM2 (STT–arrow in Fig. 2.12), due to $s - d$ –exchange interaction. The itinerant s –spin, \mathbf{s} , and the localized d –spin, \mathbf{S} , interact locally at the d –electron’s position. The $s - d$ –exchange can be described by $\mathcal{H}_{ex}^{s-d} = -J_{ex}^{s-d}\Omega|\psi|^2\mathbf{S}_i \cdot \mathbf{S}_j$ [13], where J_{ex}^{s-d} is the $s - d$ –exchange constant, Ω is the volume of the core d shell and $|\psi|^2$ the s –electron probability density. Reciprocally, the spin–polarized electrons entering FM2 will be forced to align along \mathbf{M}_2 due to the internal exchange field $\mathbf{H}_{ex,2}$. This is the so–called *spin–transfer torque* (STT) effect, described for the first time by J. C. Slonczewski [6, 7, 51] and L. Berger [8, 52]. The torque acting on \mathbf{M}_2 due to the spin–polarized electrons coming from FM1 is directed along the line joining the two magnetization vectors, as shown in Fig. 2.12.

The STT is not generated only between two FMs separated by a thin NM layer. Anytime

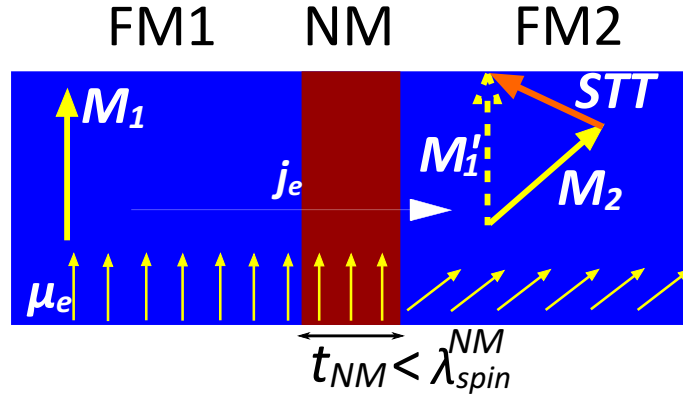


FIGURE 2.12: **STT mechanism.** Schematic description of the STT effect. The spin–polarized current generated in FM1 is able to exert a torque on the magnetization in FM2 if it is not collinear with \mathbf{M}_2 . The resulting torque is along the line joining the two vectors \mathbf{M}_2 and \mathbf{M}'_1 , with the latter representing the itinerant magnetization at the interface NM/FM2. The big yellow arrows represent the magnetization vectors in the two FMs, while the small yellow arrows are the magnetic moments of the itinerant electrons. The electron flow is from left to right.

a spin–polarized current enters a differently magnetized region in a ferromagnet, a torque is applied on the local magnetization. This is the case of a ferromagnetic nanostructure containing magnetic domains separated by DWs. Each time that the conduction electrons move from one magnetic domain to the next, crossing the DW in between, a similar case to the one described here is realized. This time the torque is exerted on the DW’s internal magnetization, as depicted in Fig. 2.13.

In the case of DWs, the STT mechanism can be described as follows: the spin–polarized electrons coming from domain D1 (see Fig. 2.13) cross the DW on their way to D2. In the magnetic DW, the magnetic moments of the conduction electrons and the ones

of the local magnetization are non-collinear. Due to the $s - d$ -exchange interaction, the non-collinearity between the two spins results in a torque acting on the local spin, which makes it to rotate towards the itinerant spin-polarization. However, due to the conservation of the total angular momentum in the exchange interaction, the spins of the conduction electrons experience an opposite torque which reorients them parallel to the local spins. As a result, a net motion of the DW in the direction of the electron flow occurs. This is the underlying mechanism in current-induced DW motion (CIDWM) based on the STT effect. However, as will be explained in more details later, it is possible to have different types of STT-driven DW motion.

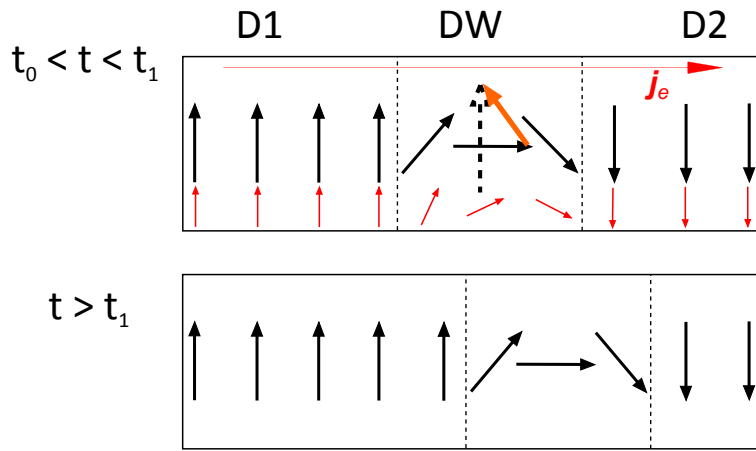


FIGURE 2.13: **STT at a magnetic DW.** The STT can be generated also at magnetic DWs. The spin-polarized current from domain D1 exerts a torque on the DW's internal magnetization. In return, the electrons crossing the DW experience an opposite torque which aligns their magnetic moments (small red arrows) with the local magnetization (black arrows). This generates a motion of the DW in the direction of the electron-flow, during the application of an electric current between time t_0 and t_1 . The red horizontal arrow indicates the electron flow.

2.6.3 Landau–Lifshitz–Gilbert equation with STT

In the presence of a spin-polarized electric current, a STT is expected to influence the magnetization together with the effective field. In the LLG equation, the effect of the STT can be included by adding a third term on the right side of Eq. 2.27, as in the following:

$$\frac{\partial \mathbf{M}}{\partial t} = -\gamma \mu_0 \mathbf{M} \times \mathbf{H}_{\text{eff}} + \frac{\alpha}{M_S} \mathbf{M} \times \frac{\partial \mathbf{M}}{\partial t} + \left(\frac{\partial \mathbf{M}}{\partial t} \right)_{STT}, \quad (2.31)$$

where the last term on the right side assumes a different expression for different experimental situations. In Fig. 2.14 the orange arrow indicates the STT, which points in

the opposite direction with respect to the damping torque. However, the STT would be parallel to $\boldsymbol{\tau}_{damp}$ if the current sign was changed. Considering the direction of the applied magnetic field, the STT has the symmetry of a damping torque, justifying the definition of *damping-like* torque. However, this holds if only the so-called *adiabatic* STT is considered (see below). Indeed, as it will be explained in more details in the following, this is not the only type of STT which can be generated.

The STT can be used for inducing magnetization dynamics in ferromagnets, such as stable precessions or reversal of the magnetization in the ferromagnet [46], as well as for displacing magnetic domain walls [43]. In the next section the case of STT-driven domain wall motion will be presented.

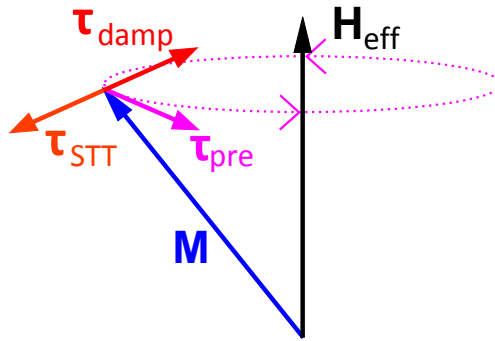


FIGURE 2.14: **Magnetization dynamics in the presence of STT.** Schematic of the magnetization dynamics in the presence of a net effective magnetic field, \mathbf{H}_{eff} and of STT. When the magnetization vector is non collinear with \mathbf{H}_{eff} , a precessional torque, $\boldsymbol{\tau}_{pre}$, causes precession of \mathbf{M} around the effective field, while a damping torque, $\boldsymbol{\tau}_{damp}$, aligns \mathbf{M} with the field. On the other hand, in the presence of an electric current a damping-like STT, $\boldsymbol{\tau}_{STT}$, is generated. The $\boldsymbol{\tau}_{STT}$ will increase or decrease the misalignment between \mathbf{M} and \mathbf{H}_{eff} , depending on the sign of the current.

2.6.4 STT-driven domain wall motion

Of particular interest for this thesis is the concept of domain wall motion driven by a spin-polarized current. Accordingly, a description of the STT-driven DW motion in nanowires is presented in the following.

In the description of current induced torques at a DW, it is possible to distinguish between two different limiting cases [43]. One is the *adiabatic limit*, within which the spins of the conduction electrons are always perfectly aligned with the local magnetization due to the exchange interaction J_{ex}^{s-d} . This is the case for the wide DWs, where the gradient of the magnetization in the direction of the drift motion of the electrons is much smaller than the spin precession length (which is the length that the electron

travels during the time of one precession of its spin around the exchange field) or than the Fermi wave–packet’s dimension (which is of the order of the inverse of the Fermi wave–vector). Typically, this is valid for low anisotropy materials, like Permalloy (Py), having DW widths around 100 nm [43]. In this case the electrons crossing the DW have enough time to exchange their angular momentum with the local magnetization, reorienting their spins continuously. Due to the conservation of angular momentum, this results in a torque on the local magnetization which tries to align the magnetization with the spin polarization of the electric current. The STT acting on the DW can be expressed as [43]:

$$\boldsymbol{\tau}_{STT,ad} = \frac{jP\hbar}{2e} \frac{\partial \mathbf{m}}{\partial x}, \quad (2.32)$$

where P is the spin–polarization of the current, j the current density for a current flowing along the x –direction.

Due to the STT, the time derivative of the magnetization unit vector reads as:

$$\left(\frac{\partial \mathbf{m}}{\partial t}\right)_{STT,ad} = -(\mathbf{u} \cdot \nabla) \mathbf{m}, \quad (2.33)$$

where $\mathbf{u} = \mathbf{j}P\mu_B/2eM_S$ is generally called the *spin drift velocity*. The velocity, u , is the maximum velocity at which a DW can move under the action of the $\boldsymbol{\tau}_{STT,ad}$. This is obtained when all of the changes in the angular momentum of the conduction electrons are transferred to the local magnetization and eventually converted into DW displacement. For each electron moving from one domain to the next, the angular momentum transfer amounts to $1\hbar$, corresponding to a change of $2\mu_B$ in the magnetic moment.

The adiabatic torque is not the only STT term which can act on a DW. This became clear since the experimental observations of current–induced DW motion could not be fully explained by the adiabatic STT model. Accordingly, an additional *non–adiabatic* STT has been proposed, which takes into account other possible mechanisms for the change in the electron spin, besides the adiabatic exchange of angular momentum with the local magnetization.

The non–adiabatic torque was first proposed in 2004–2005 by different scientists [53–55], in an attempt to understand the experimental observations of DW motion in magnetic nanowires obtained at that time. Phenomenologically, the non–adiabatic torque can be

described by a dimensionless parameter, β [43]:

$$\left(\frac{\partial \mathbf{m}}{\partial t}\right)_{STT,nad} = \beta \mathbf{m} \times [(\mathbf{u} \cdot \nabla) \mathbf{m}]. \quad (2.34)$$

As can be seen by comparing Eq. 2.33 and Eq. 2.34, the new torque is perpendicular to the adiabatic torque. It has the symmetry of a torque generated by a magnetic field applied along the easy-axis of the system. Accordingly, the non-adiabatic torque is defined as *field-like torque*, while the adiabatic torque is defined as *damping-like torque*. There are several origins for the non-adiabatic torque, however they can be separated in two categories. The first type of $\boldsymbol{\tau}_{STT,nad}$ is due to spin-relaxation phenomena in the DW. The spin-relaxation can occur via spin-flip events at impurities or with phonons. Since these scattering events are driven by spin-orbit coupling [43], there is no conservation of the angular momentum, justifying the definition of “non-adiabatic” torque. This non-adiabatic STT can be interpreted as a dissipative term, since it has the same microscopic origin as the Gilbert damping effect [56].

The second type of non-adiabatic torque is linked to the internal magnetization of the DW. In the case of systems with a strong magnetic anisotropy, resulting in narrow DWs, the gradient of the magnetization is large. This makes the spin precession length comparable with the DW’s width, resulting in a non-adiabatic alignment of the electron spin with the local magnetization. This generates a non-adiabatic torque. As Tatara et al. [57] explained, this can be seen as a linear momentum transfer (in the one-dimensional model) from the conduction electrons to the DW, due to the scattering of the electrons at the spatially fast varying DW’s spin texture.

Adding the two STT terms reported above to the LLG equation, it is possible to phenomenologically describe the dynamics of DWs under the effect of electric currents. The corresponding form of the LLG equation results [43]:

$$\frac{\partial \mathbf{M}}{\partial t} = -\gamma \mu_0 \mathbf{M} \times \mathbf{H}_{\text{eff}} + \frac{\alpha}{M_S} \mathbf{M} \times \frac{\partial \mathbf{M}}{\partial t} - (\mathbf{u} \cdot \nabla) \mathbf{M} + \frac{\beta}{M_S} \mathbf{M} \times [(\mathbf{u} \cdot \nabla) \mathbf{M}], \quad (2.35)$$

where the last two terms indicate the adiabatic and the non-adiabatic STTs.

Equation 2.35 can be written in a simple analytical form, if a one-dimensional (1D) model is used for describing the magnetic DW [43]. In the 1D model, the DW dynamics are described by the dynamics of two independent variables: its position, q , and its

internal magnetization angle, ψ (see Fig. 2.15). The equations of motion resulting from the 1D model are [43]:

$$\frac{\partial \psi}{\partial t} + \frac{\alpha}{\lambda_{DW}} \frac{\partial q}{\partial t} = \gamma \mu_0 H + \frac{\beta u}{\lambda_{DW}} - \frac{\gamma}{2M_S} \frac{\partial V_{pin}}{\partial q} \quad (2.36)$$

$$\frac{1}{\lambda_{DW}} \frac{\partial q}{\partial t} - \alpha \frac{\partial \psi}{\partial t} = \frac{\gamma \mu_0 H_K}{2} \sin(2\psi) + \frac{u}{\lambda_{DW}}. \quad (2.37)$$

Here, H_K is the DW demagnetizing field ($H_K = 2K_d/(\mu_0 M_S)$, with K_d being the DW demagnetizing energy), H is the external field applied along the easy-axis, V_{pin} is the pinning potential of the DW due to the roughness, impurities or grain boundaries present in the system. In ideal nanowires, where no pinning is present, if the adiabatic STT is

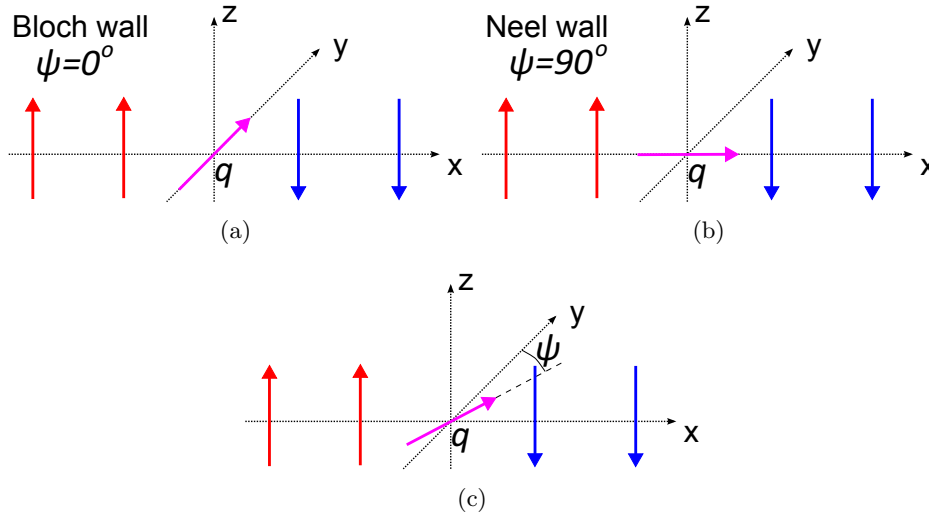


FIGURE 2.15: **Domain walls magnetization configuration in the 1D model for PMA systems.** Schematic representation of a magnetic DW in the 1D model framework, for PMA systems. The DW is described by its position q and its internal magnetization angle ψ . The color-code describes the macro-spins belonging to the two different magnetic domains and to the DW in between. (a) Bloch wall configuration. (b) Néel wall configuration. (c) Magnetic configuration of a general DW.

the only torque acting on the DW magnetization, an *intrinsic* critical current density $u_c = \gamma \mu_0 H_K \lambda_{DW} / 2$ needs to be reached in order to move the DW [43]. Indeed, the adiabatic torque generates a net displacement of the DW only if the critical torque needed to induce a continuous precession of the DW internal magnetization is reached. This happens when the current-induced torque is strong enough to overcome H_K , inducing the so-called *Walker breakdown* (WB) [58]. In the WB regime, the average velocity of the DW motion is described by $\langle v_{DW} \rangle = \frac{\sqrt{u^2 - u_c^2}}{1 + \alpha^2}$ [43].

On the other hand, in the presence of the non-adiabatic torque there is no longer an

intrinsic critical current density for ideal nanowires. However, in real systems with a finite DW pinning strength, an *extrinsic* critical current density is given by the strength of the pinning potential V_{pin} . In the steady state regime (even known as the *flow regime*), the velocity increases linearly with the current density as $v_{DW} = \frac{\beta}{\alpha}u$ [43]. The larger the non-adiabaticity parameter, the larger the final velocity of the DW. This justifies the enormous interest towards magnetic systems with large β , due to the possibility of using them for the design of new magnetic memories and logic devices based on fast DW motion [2, 59]. The final DW velocity changes linearly with the current until a critical value $u_W = u_c \frac{\alpha}{|\beta - \alpha|}$ is reached [43]. Above u_W the DW undergoes periodic oscillations as already described before and the average velocity drops if $\beta > \alpha$, or increases if $\beta < \alpha$, similarly to the adiabatic limit. Finally, for very large value of the current density (that means, large u) the final average velocity of the DW motion converges to the limit $\langle v_{DW} \rangle = \frac{1 + \alpha\beta}{1 + \alpha^2}u$ [43].

2.6.5 Current-induced magnetization reversal: generalized Néel–Brown model

The Néel–Brown model previously reported is useful in the description of thermal assisted magnetization reversal in single-domain magnetic structures when an external easy-axis magnetic field is applied. However, such a model is not able to describe the magnetization switching induced by a spin polarized current. This is the case for spin-valves (see Fig. 2.12) [60, 61] and magnetic tunnel junctions [62, 63], where the spin-polarized current generated in a magnetic *reference* layer is used to induce magnetization reversal, by STT, in a second magnetic *free* layer [62, 64]. When an electric current is injected through the magnetic system, an out-of-equilibrium situation is generated, which cannot be described anymore by the Boltzmann distribution function: $P_B \propto \exp(-E/k_B T)$ [65]. In the presence of a spin-transfer torque acting on the magnetization, the correct description is offered by the Fokker–Planck equation, which, numerically solved, allows to obtain the probability distribution that describes the system out-of-equilibrium [65, 66].

In the presence of an electric current, the energy barrier, E_b , which governs the magnetization reversal depends on the magnitude as well as the direction of the current [65]. However, even if the Néel–Brown formula (reported in Eq. 2.25) does not apply in the presence of STT, according to Li and Zhang [65] the out-of-equilibrium situation can

be described by a modified version of it. It is possible to define an effective temperature, T^* , or equivalently an effective energy barrier, E_b^* , so that a modified version of the Néel–Brown formula can be employed to describe the magnetization reversal in the presence of STT. The modified Néel–Brown formula for the switching rate will then read [65]:

$$\tau^{-1} = f_0 \exp\left(-\frac{E_b^*}{k_B T}\right), \quad (2.38)$$

with $E_b^* = E_0\left(1 - \frac{H}{H_{sw}^0}\right)^\beta\left(1 - \frac{a_j}{a_c}\right)$ being the effective energy barrier. Here, H is the applied field along the easy-axis, H_{sw}^0 is the switching field at zero temperature, β is a coefficient which can vary between 1.5 and 2, a_j describes the strength of the STT, and a_c represents a critical STT (linked to the minimum STT needed in order to switch the magnetization at zero temperature).

2.7 Spin–orbit torques

In the last 7 years a new kind of current–induced torque has been reported, whose origin has been attributed to the strong spin–orbit coupling (SOC) characterizing the material systems where they were observed [9, 25, 35, 36, 44, 67–69], from which originates the name *spin–orbit torques* (SOTs). Such observations have been obtained in the investigation of magnetic multilayers with structural inversion asymmetry (SIA). The general material stack where the new torque has been observed consists of a thin ferromagnetic layer sandwiched between two different non magnetic layers, where the bottom layer consist of a strong SOI and the top layer is usually an oxide, as the one reported in Fig. 2.5.

There are two main effects that have been proposed so far as playing a role in the generation of the SOT, namely: the inverse spin–galvanic effect (ISGE) [69–72], originating from the Rashba effect [73]; and the spin–Hall effect [74–77]. Both effects listed above have their origin in the SOI. Each one of them will be briefly presented, including a description of the role played by each one of these effects in the generation of SOTs.

2.7.1 Inverse spin–galvanic effect

2.7.1.1 Rashba spin–orbit interaction

As it was first shown by Bychkov and Rashba [73, 78], a crystal with a single high symmetry axis can generate an energy term in the spin–orbit Hamiltonian which is linear in the electron momentum $\mathbf{p} = \hbar\mathbf{k}$. This is also the case for magnetic multilayers with SIA [71]. Following the discussion in [71], the one–electron Rashba Hamiltonian reads:

$$\mathcal{H}_{SO} = \alpha_R(\mathbf{k} \times \hat{\mathbf{z}}) \cdot \boldsymbol{\sigma}, \quad (2.39)$$

where α_R is the Rashba coefficient (function of the SOI in the specific material), $\boldsymbol{\sigma} = (\sigma_x, \sigma_y, \sigma_z)$ represents the Pauli spin–matrices and $\hat{\mathbf{z}}$ is the out–of–plane unitary vector. For 2D systems, as for example surfaces or interfaces in multilayers, Eq. 2.39 can be simplified in the form:

$$\mathcal{H}_{SO} = \alpha_R(k_y\sigma_x - k_x\sigma_y), \quad (2.40)$$

where it is possible to see that there is a coupling between the electron direction of motion in the plane and the spin of the electron. The electron spin is locked to the electron momentum, being always orthogonal to it.

Equation 2.39 formally describes the Zeeman–like interaction between the electron spin and an effective spin–orbit magnetic field. This can be shown writing the Hamiltonian in the following way [71]:

$$\mathcal{H}_{SO} = \mu_B \boldsymbol{\sigma} \cdot \mathbf{B}_{SO}, \quad (2.41)$$

where \mathbf{B}_{SO} is the effective spin–orbit magnetic field. The orientation of $\mathbf{B}_{SO}(\mathbf{k})$ as a function of the wave–vector \mathbf{k} is shown in Fig. 2.16. The effective magnetic field is always perpendicular to the electron direction of motion.

One possible way to understand how SIA can generate a Zeeman–like interaction is to consider the motion of electrons in a non–symmetric crystal electric field potential V . In the electron’s rest frame, the electric field $\mathbf{E} = -\nabla V$ transforms in a magnetic field. When transformed back into the laboratory’s reference frame such a field results in $\mathbf{B}_{SO} = -(\mathbf{v}_e \times \mathbf{E})/2c^2 = (\hbar\mathbf{k} \times \nabla V)/2m_e c^2$ [71], where \mathbf{v}_e is the electron velocity and c is the light velocity in vacuum.

In the case of itinerant systems, the conduction electrons experience both the microscopic nuclear potential V_{nuc} due to the nuclear charge, and the macroscopic interface potential

V_{int} due to the presence of a surface or an interface between two different materials (SIA). This results in a spin-orbit Hamiltonian which contains both contributions [71]:

$$\mathcal{H}_{SO} = \frac{e\hbar^2}{4m_e c^2} \boldsymbol{\sigma} \cdot [\mathbf{k} \times \nabla(V_{nuc} + V_{int})]. \quad (2.42)$$

According to Eq. 2.42, there are two different degrees of freedom in the control of

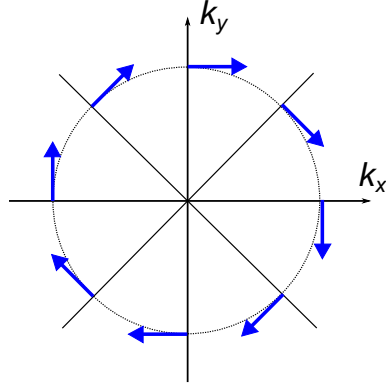


FIGURE 2.16: **Orientation of the Rashba spin-orbit field in the k -space.** Orientation of the spin-orbit magnetic field with respect the electron momentum k . The effective magnetic field (blue arrows) is always orthogonal to the momentum of the electron.

the Rashba effect: the nuclear charge and the interface potential. Considering the first one, it results that the Rashba Hamiltonian is proportional to Z^4 [71], where Z is the atomic number. This suggests that in systems containing heavy metals, with large Z , the Rashba effect will be large. On the other hand, concerning the potential at the interface, its contribution to the Rashba Hamiltonian is maximized for interfaces with a large electric potential gradient. This can be obtained at the interface between two materials with a huge mismatch in the respective work functions, justifying why the Rashba effect is expected to be present at interfaces between an heavy metal and an itinerant ferromagnet [36, 67, 71] or between a metal and an oxide [79, 80]. It is clear that a trilayer consisting of a bottom heavy metal, an ultra-thin itinerant ferromagnet and a top oxide layer like the one reported in Fig. 2.18 is a good candidate for the observation of a strong Rashba effect.

2.7.1.2 Inverse spin–galvanic effect

The Rashba effect presented above has possible consequences on the transport properties of conducting systems. Considering the model system consisting in a non magnetic two-dimensional electron gas (2DEG) with Rashba SOI, the electronic Hamiltonian reads [71]:

$$\mathcal{H} = \frac{\hbar^2 k^2}{2m_e^*} + \alpha_R (\mathbf{k} \times \hat{\mathbf{z}}) \cdot \boldsymbol{\sigma}, \quad (2.43)$$

m_e^* being the effective electron mass. The eigenvalues for this Hamiltonian result to be:

$$\epsilon_{\pm, \mathbf{k}} = \frac{\hbar^2 k^2}{2m_e^*} \pm \alpha_R |k|. \quad (2.44)$$

In Eq. 2.44, the term proportional to the Rashba coefficient adds a energy contribution linear in k , which has an opposite sign for spins parallel (+) or anti-parallel (-) to the spin-orbit field. A split in energy between the two spin-bands is obtained, resulting in different \mathbf{k}_F and so different iso-energetic contours for the two spin-states at the Fermi level, as shown in Fig. 2.17(a). In the absence of current, the total spin-polarization of the system averages out, since the average net electron momentum is $\langle \mathbf{k} \rangle = 0$. However, in case an electric current is injected into the system, it will generate a non equilibrium situation. As it is shown in Fig. 2.17(b), the application of an external electric field $\mathbf{E}_{ext} = E_{ext} \hat{\mathbf{x}}$ will displace the two Fermi discs of a different amount for the “+” and “-” spin-band. This results in the generation of a non-equilibrium spin polarization, which can be phenomenologically described as $\mathbf{S}_{SO} = \alpha_R m_e^* (\hat{\mathbf{z}} \times \mathbf{j}_c) / e\hbar$ [72], where α_R is the Rashba coefficient, m_e^* the effective electron mass. This is the so called *inverse spin-galvanic effect* (ISGE), also known as *Edelstein effect* [69–72], where an electric current induces a non equilibrium spin polarization due to SOI. This effect is the reciprocal of the spin-galvanic effect (SGE), where a non-equilibrium spin density $\mathbf{S}_{n.-e.}$ injected into a system with Rashba SOI gives rise to an electric current $\mathbf{j}_c = -e\alpha_R (\hat{\mathbf{z}} \times \mathbf{S}_{n.-e.})$ [72, 81]. Let us consider now the magnetic system reported in Fig. 2.18. The system consist of a thin ferromagnetic layer sandwiched between an heavy metal and an oxide. Due to the presence of the two interfaces at such a small distance ($t_{FM} \leq 1$ nm) a net intrinsic electric field is found in the ferromagnetic thin film, perpendicular to plane. If an in-plane electric current is injected through the conductive layers, a net “out-of-equilibrium” spin polarization of the current is generated in the direction $\mathbf{E} \times \langle \mathbf{k} \rangle$. Such a spin polarization will couple with the localized magnetic

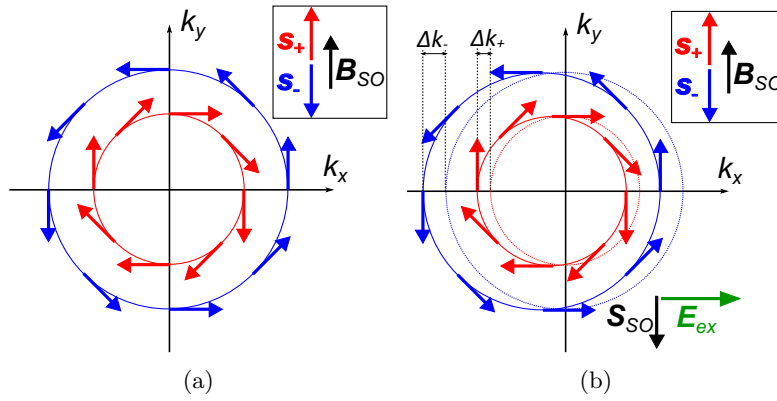


FIGURE 2.17: **Fermi contours for a Rashba 2DEG.** (a) The Fermi contours for the two spin-bands are different. The Fermi momentum k_F for the electrons with spin anti-parallel to the spin-orbit magnetic field (blue arrows) is larger than the one for the electrons having their spin parallel to it (red arrows). (b) In the presence of an external electric field, \mathbf{E}_{ext} , the two Fermi discs are displaced of a different amount Δk_{\pm} , generating a non-equilibrium spin-polarization, \mathbf{S}_{SO} , in the system. The insets describe the relative orientations of the electron spins and the spin-orbit field.

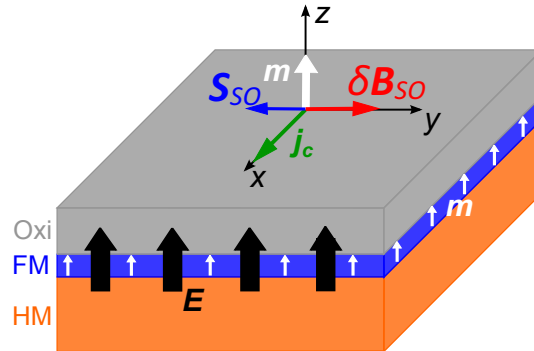


FIGURE 2.18: **ISGE in a magnetic multilayer.** Schematic of the inverse spin-galvanic effect in a ferromagnetic multilayer with PMA. Due to the presence of the two interfaces with a bottom heavy metal layer (HM) and a top Oxide layer (Ox), a built-in electric field \mathbf{E} in the ferromagnetic layer (FM) along the z -axis is generated. When an electric current \mathbf{j}_c is injected in the multilayer along the \hat{x} -direction, a non-equilibrium spin polarization \mathbf{S}_{SO} is generated in the ferromagnet along the \hat{y} direction. In turn, \mathbf{S}_{SO} acts on the local magnetization, \mathbf{m} , by exchange interaction. This is equivalent to the presence of an effective spin-orbit magnetic field, $\delta\mathbf{B}_{SO}$, in the ferromagnet. Eventually, the spin-orbit field will tilt the out-of-plane magnetization towards the in-plane direction, changing the magnetic configuration in the FM.

moments in the ferromagnet via the $s - d$ exchange interaction, J_{ex}^{s-d} . As a result, \mathbf{S}_{SO} will exert a torque on the magnetization, acting on the localized magnetic moments, equivalent to an effective magnetic field of the type $\delta\mathbf{B}_{SO} = -\delta B_{SO}\hat{\mathbf{s}}_{SO}$, where δB_{SO} is the magnitude of the non-equilibrium SO field and $\hat{\mathbf{s}}_{SO}$ is the non-equilibrium spin-polarization unit vector. The generated SOT reads [82]:

$$\boldsymbol{\tau}_{SO,FL} = -\mathbf{m} \times \delta\mathbf{B}_{SO} = \tau_{SO,FL}\mathbf{m} \times \hat{\mathbf{u}}_{SO}, \quad (2.45)$$

where $\tau_{SO,FL}$ is the magnitude of the torque, \mathbf{m} is the unitary magnetic moment and $\hat{\mathbf{u}}_{SO}$ is a unit vector parallel to the the non-equilibrium SO field [82]. The SOT in Eq. 2.45 is a *field-like* (FL) torque, being *odd* in the magnetization direction \mathbf{m} [82]. In the case of magnetic multilayers, like the one discussed here, the effective ISGE-torque acting on the whole magnetic layer is expected to be observable only in ultra-thin ferromagnetic layers, due to its intrinsic interface-like character.

So far, the ISGE has been discussed as a perfect interface-like effect, generated by a single free electron-like energy band. However, the magnetic multilayers investigated in the present thesis are far more complex than the single-band Rashba 2DEG system discussed above. A more advanced description of the real system is offered by Li et al. [82], where a multiband magnetic Rashba 2DEG is considered. Both the intra-band and the inter-band contributions to the current-induced spin-orbit torque are theoretically studied. According to Li and co-authors, the inter-band contribution to the SOT can generate an additional torque with the symmetry:

$$\boldsymbol{\tau}_{SO,DL} = \tau_{SO,DL}\mathbf{m} \times (\hat{\mathbf{u}}_{SO} \times \mathbf{m}), \quad (2.46)$$

with $\tau_{SO,DL}$ being the magnitude of the torque. The new torque is defined as an *damping-like* (DL) torque, *even* in the magnetization direction \mathbf{m} [82]. Accordingly, in magnetic multilayers with SIA, current-induced torques with both symmetries, field-like and damping-like, are expected to be originated due to a Rashba-like SOI.

Furthermore, the observation of a current induced ISGE-DL-torque has been reported by Kurebayashi et al. [83] for the ferromagnetic semiconductor (Ga,Mn)As with crystal inversion asymmetry. The origin of the DL-SOT is attributed to the intrinsic (impurity-independent) relativistic quantum-mechanical effect named *Berry curvature* [72, 84, 85].

Such intrinsic origin of the DL-SOT is actually the same proposed as origin of the intrinsic spin-Hall effect in paramagnetic heavy metals [76, 86]. As it will be discussed in the next section, the SHE is actually the other main effect considered as possible origin of the observed DL-torque in magnetic multilayers with SIA.

2.7.2 Spin-Hall effect: magnetization manipulation by a pure spin-current

2.7.2.1 Spin-Hall effect

The spin-Hall effect (SHE) was for the first time proposed by Dyakonov and Perel in 1971 [74, 75]. They predicted the possibility of producing a pure spin-current in solid-state systems due to spin-dependent scattering processes. More than thirty years later, a scattering independent SHE was theoretically proposed by Murakami et al. [87] and Sinova et al. [76]. The origin of such spin-dependent phenomena is the SOI [86, 88]. In the SHE, when an electric current \mathbf{j}_c is injected in a solid with SOI, electrons with opposite spins are deviated in opposite directions and a transverse spin current \mathbf{j}_s is generated. The spin of the deviated electrons is perpendicular to the plane containing \mathbf{j}_c and \mathbf{j}_s . As a result, spin with opposite signs accumulate at opposite interfaces of the sample, as shown in Fig. 2.19. The spin accumulation has an intrinsic chiral symmetry, where $\boldsymbol{\sigma}_s \propto \mathbf{j}_c \times \mathbf{j}_s$. Here, $\boldsymbol{\sigma}_s$ represents the spin accumulation vector. The SHE can be

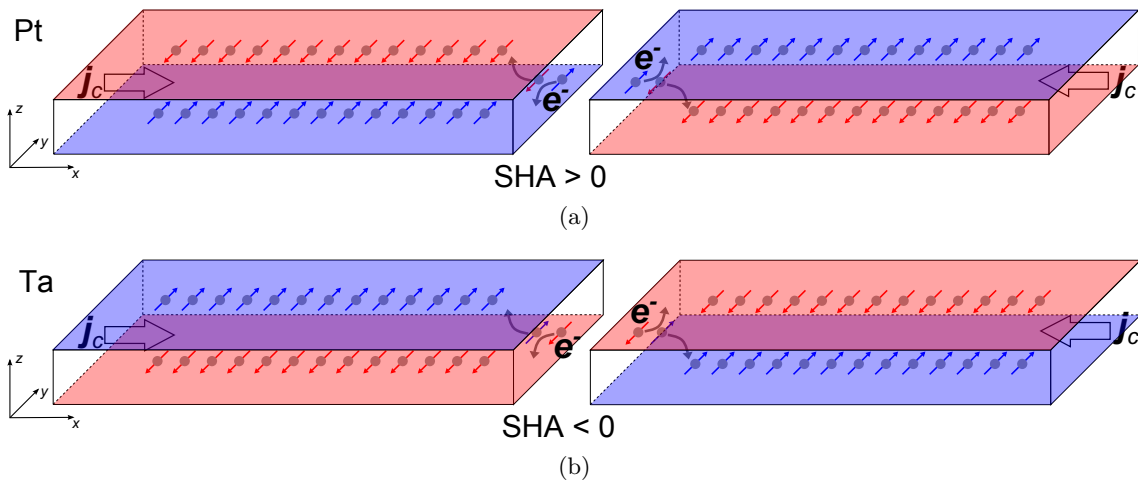


FIGURE 2.19: **Spin-Hall effect in heavy transition metals.** (a) Schematic of the spin accumulation generated at the top and bottom interfaces of a Platinum (Pt) layer due to the SHE. (b) As in (a), but for a Tantalum (Ta) layer. The arrows indicate the spin of the conduction electrons in the metal.

described by the transversal spin–Hall conductivity, σ_{xy}^H , resulting in $j_s = \sigma_{xy}^H E_x$, where E_x is the applied external electric field and j_s is in the orthogonal direction. Following the recent review paper about the SHE by Sinova et al. [86], three different microscopic contributions to σ_{xy}^H have been identified: the *intrinsic* contribution, σ_{xy}^{H-int} ; the *skew-scattering* contribution, σ_{xy}^{H-skew} ; and the *side-jump* contribution, σ_{xy}^{H-sj} . The sum of the three Hall conductivities defines the total spin–Hall conductivity of a certain material, $\sigma_{xy}^H = \sigma_{xy}^{H-int} + \sigma_{xy}^{H-skew} + \sigma_{xy}^{H-sj}$.

The *intrinsic* contribution to the spin–Hall conductivity is only dependent on the band structure of the perfect crystal. This results in a contribution which is directly linked to the topological properties of the Bloch states [86]. It is independent of the transport scattering life–time, τ_{sca} , resulting in $\sigma_{xy}^{H-int} \propto \tau_{sca}^0$. The intrinsic term is particularly relevant for systems with a strong SOI, as for heavy transition metals like Ta and Pt. In the case of such strong SOC materials, with relatively complex energy bands, the spin–Hall conductivity arises from the presence of SOC–connected bands near the Fermi level [77, 89]. Very relevant for the present thesis are the results presented by Tanaka et al. [77], where it is shown that the size and the sign of the intrinsic spin–Hall conductivity in 5*d*–transition metals is a function of the 5*d*–band filling. The largest values of σ_{xy}^{H-int} are predicted for Tungsten (W) ([Xe]4f¹⁴5d⁴6s²; almost half filled 5*d*–shell with 4 electrons) and Platinum (Pt) (Xe]4f¹⁴5d⁹6s¹; almost completely filled 5*d*–shell with 9 electrons), while the sign of σ_{xy}^{H-int} is predicted to change from negative to positive moving from Ta ([Xe]4f¹⁴5d³6s²; only 3 electrons in the 5*d*–shell) to Pt in the *period 6* of the periodic table of the elements. Such prediction have been experimentally verified, as reported by Wang et al. [90].

The *skew-scattering* contribution to the spin–Hall conductivity has an extrinsic origin. It originates from a spin–dependent scattering of electrons at the disorder potential into the crystal, where SOC is present [86, 91]. A chiral scattering is produced, resulting in the deviation of electrons with opposite spins in opposite directions, as depicted in Fig. 2.19. This extrinsic contribution to σ_{xy}^H depends on τ_{sca} , resulting in $\sigma_{xy}^{H-skew} \propto \tau_{sca}^1$, as for the longitudinal conductivity, σ_{xx} . Accordingly, the spin–Hall resistivity $\rho_{xy}^{H-skew} = \sigma_{xy}^{H-skew} \rho_{xx}^2$ is proportional to the longitudinal resistivity, ρ_{xx} , when this contribution is the dominant one [86]. However, such extrinsic contribution is expected to be less relevant than the intrinsic one in the case of heavy transition metals, as reported by Zimmerman et al. [91] in their theoretical study.

The third contribution comes from the *side-jump* mechanism, which can be defined as

the difference between the total Hall conductivity and the previously presented terms, giving $\sigma_{xy}^{H-sj} = \sigma_{xy}^H - (\sigma_{xy}^{H-int} + \sigma_{xy}^{H-skew})$. In the side-jump mechanism, the electrons with opposite spins are separated a certain distance (the side-jump) in the transverse direction, undergoing a scattering process with impurities present in the crystal. The side-jump mechanism is believed to have both an intrinsic and an extrinsic contribution, mainly when considering materials with a large SOC. As explained by Sinova et al. [86]: the extrinsic-side-jump refers to the non-spin-orbit coupled part of the electronic wave-packet (describing the conduction electron) scattering off the spin-orbit coupled disorder. On the other hand, the intrinsic-side-jump refers to the spin-orbit coupled part of the electronic wave-packet scattering off the scalar potential (of the impurity) without spin-orbit coupling. This second type of side-jump is expected to dominate in heavy metals like Ta and Pt. Both types of side-jump mechanisms generate a contribution to the Hall conductivity which is scattering independent, resulting in $\sigma_{xy}^{H-sj} \propto \tau_{sca}^0$. Accordingly, the skew-scattering term is the only real extrinsic contribution to the spin-Hall conductivity, being a function of the transport scattering life-time.

Considering a bilayer HM\FM as illustrated in Fig. 2.20, when an in-plane electric current, \mathbf{j}_c , is injected in the bottom layer an out-of-equilibrium situation is generated. Due to the sum of the different mechanisms of the SHE which are actually contributing in the specific material, a transverse pure spin current, \mathbf{j}_s^y , is generated along the out-of-plane direction. The superscript y indicates the direction along which the electron spins are aligned. The link between the injected charge current and the generated pure spin current is given by: $\mathbf{j}_s^y = \theta_{SHE} \frac{\hbar}{2e} \mathbf{j}_c \hat{z}$, which is the spin current generated by the SHE with an efficiency θ_{SHE} , flowing towards the positive z -direction with the electron spins aligned along the y -direction. The SHE efficiency is usually referred to as *spin-Hall angle* (SHA).

Each heavy transition metal is characterized by its own SHA, which can go from about zero to a few tens of percent, and can be positive or negative. For example, Pt is known for being characterized by a positive SHA, while β -Ta has a negative SHA [86, 92], as illustrated in Fig. 2.19. Furthermore, a spin-diffusion length, λ_{spin} , is defined to characterize the transverse length scale over which the spin accumulation decays.

Considering the HM\FM bilayer depicted in Fig. 2.20, the spin current propagating towards the top interface will eventually enter the top ferromagnetic layer. The actual

spin density entering the ferromagnet is a function of the SHE efficiency in the HM (defined by its SHA) and its thickness, t_{FM} , and of the properties of the HM\FM interface. The properties of the HM define the spin current density below the interface. For a HM layer with thickness much larger than its spin diffusion length, the spin current density close to the top interface is saturated, as described by $j_s(t_{HM}) = j_s(\infty)(1 - \text{sech}(\frac{t_{HM}}{\lambda_{spin}}))$, where $j_s(\infty)$ is the bulk value of the spin current density in the HM layer [93]. This equation is obtained using drift-diffusion theory [94] and describes the limit of a transparent HM\FM interface, where it is assumed no accumulation of spins transverse to the ferromagnet's magnetic moments at the interface. However, in real systems the interface between the HM and the FM is not transparent, and interface's transparencies of different values characterize different material systems [95, 96]. The spin-transparency of the system can be improved by appropriately engineering the interface [96]. In HM\FM systems the spin-transparency is believed to be a function of the *spin-mixing conductance* [96–98]. The spin-mixing conductance is a concept usually employed for describing the generation of a spin current at the HM\FM interface due to spin pumping from the ferromagnet [97, 98]. The same concept can be used also in the description of a pure spin current injected from a HM to a FM.

One more effect has been proposed in the attempt of describing the process of spin current transmission through a HM\FM interface. This effect is the so-called *spin-memory loss* [99], where the spin current pumped from the FM towards the HM layer experience a strong depolarization. The same effect is believed to play a key role in the transmission of a SHE-generated spin current into a ferromagnetic layer.

2.7.2.2 Magnetization manipulation by the SHE-spin current

It has been proposed theoretically [45, 100] and demonstrated experimentally that the SHE-spin current injected into a ferromagnetic layer through the HM\FM interface can be used for producing magnetization reversal [25, 34, 68, 101] or magnetic DW motion [25, 35] in the ferromagnetic layer. The component of the itinerant electron spins perpendicular to the magnetization can be absorbed by the ferromagnet due to exchange interaction, generating a spin-transfer torque acting on the local magnetization [101]. The spin torque generated by the SHE on the local magnetization has the form [101]:

$$\boldsymbol{\tau}_{SHE} = \tau_{SHE} \mathbf{m} \times (\hat{\boldsymbol{\sigma}}_s \times \mathbf{m}), \quad (2.47)$$

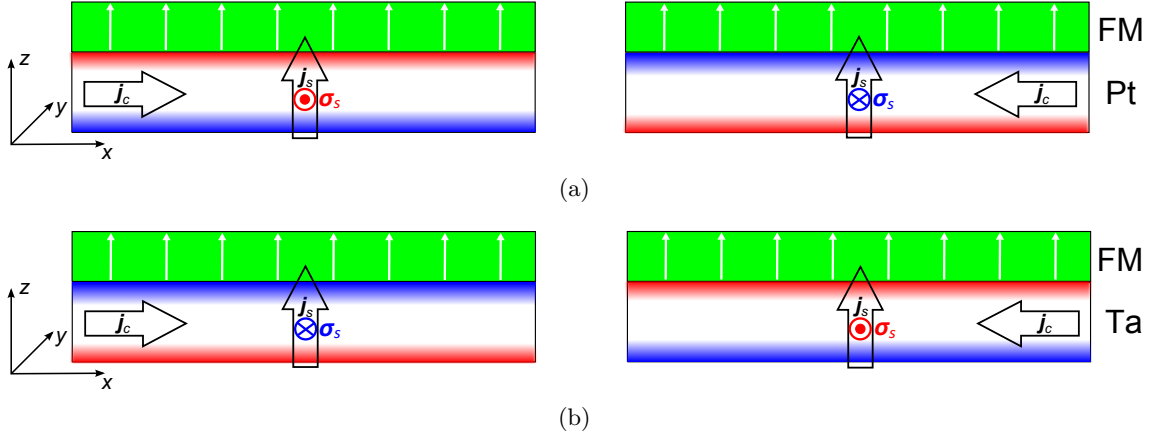


FIGURE 2.20: **SHE–spin current in the HM\FM bilayer.** (a) SHE–spin current in the Pt\FM bilayer. The spin polarization of the spin current injected into the FM is indicated by σ_s . (b) As in (a), for a Ta\FM bilayer. Note that the polarization of the pure spin current at the HM\FM interface changes sign for j_c with an opposite polarity.

with τ_{SHE} being the magnitude of the torque, \mathbf{m} the magnetization unit vector and $\hat{\sigma}_s$ the SHE–spin polarization unit vector. This torque has the symmetry of a DL–torque, since it is *even* in the magnetization direction \mathbf{m} .

Alternatively, the effect of the SHE–generated spin current onto the ferromagnet’s magnetization can be described by the presence of an effective magnetic field, \mathbf{H}_{SHE} . Such a field is defined by the following expression [25]:

$$\mathbf{H}_{SHE} = \frac{\hbar\theta_{SHE}|j_e|}{2\mu_0|e|M_s t_{FM}} \hat{\mathbf{m}} \times (\hat{\mathbf{z}} \times \hat{\mathbf{j}}_e), \quad (2.48)$$

with \mathbf{j}_e the electron–current density ($\mathbf{j}_e = -\mathbf{j}_c$) and $\hat{\mathbf{j}}_e$ the corresponding unit vector, M_s the saturation magnetization of the ferromagnetic material, t_{FM} the thickness of the FM layer and $\hat{\mathbf{m}}$ the magnetic moment unit. This expression for the SHE–effective field is valid only under three assumptions: (i) the HM layer where the SHE is generated is thick enough in order to saturate the spin current; (ii) the HM\FM interface is characterized by a 100% spin–transparency and no spin–memory loss; (iii) 100% of the spin angular momentum is transferred from the itinerant electrons to the local magnetization.

The precessional torque per magnetic moment unit acting on the local magnetization, due to the presence of an effective magnetic field like the one in Eq. 2.48, reads:

$$\boldsymbol{\tau}_{SHE} = -\gamma \hat{\mathbf{m}} \times \mu_0 \mathbf{H}_{SHE} = -\gamma \tau_{SHE}^0 \hat{\mathbf{m}} \times (\hat{\mathbf{m}} \times \hat{\sigma}_s), \quad (2.49)$$

with $\tau_{SHE}^0 = \frac{\hbar\theta_{SHE}|j_e|}{2|e|M_{st_{FM}}}$. Including the effective SHE-field in the LLG Eq. 2.35 it is possible to describe the magnetization dynamics in the presence of the SHE.

From Eq. 2.48 it is clear that the effective field is a function of the magnetization too. More precisely, the out-of-plane component of the effective field (which is collinear with the easy-axis for PMA materials), \mathbf{H}_{SHE}^z , and so the corresponding torque are maximized for $\hat{\mathbf{m}}$ being along the current direction. Accordingly, as shown by Khvalkovskiy et al. [100], Néel DWs ($\hat{\mathbf{m}} // x$ -axis & $\perp \hat{\sigma}_s$) maximize the SHE-torque, while for Bloch DWs ($\hat{\mathbf{m}} // y$ -axis & $// \hat{\sigma}_s$) the torque is zero. Furthermore, the sign of the effective field changes for $\uparrow\downarrow$ and $\downarrow\uparrow$ chiral DWs, making it possible to move both types of DW in the same direction [25, 35], as shown in Fig. 2.21(a). \mathbf{H}_{SHE}^z can also drive magnetization reversal processes in PMA materials. The symmetry of \mathbf{H}_{SHE} is described in Fig. 2.21(b).

It is interesting to report that a FL-torque can also be induced by the SHE, as it has been reported for example by Nan et al. [102]. By spin-torque ferromagnetic resonance

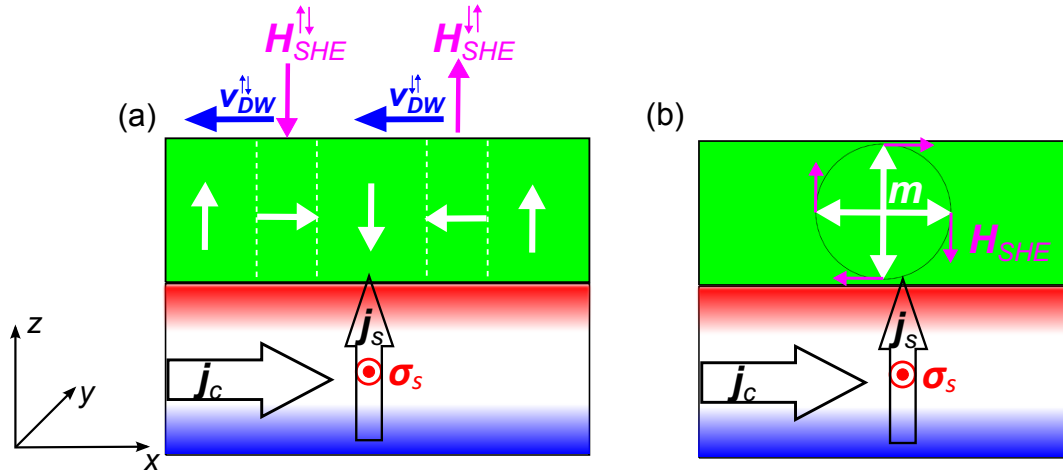


FIGURE 2.21: **Symmetry of the SHE effective field.** Schematic of the symmetry of \mathbf{H}_{SHE} generated in a PMA ferromagnetic layer. (a) The direction of the effective field at the DW is a function of its internal magnetic moment. Chiral Néel DWs are moved in the same direction by \mathbf{H}_{SHE} , since the field sign is opposite for the $\uparrow\downarrow$ - and $\downarrow\uparrow$ -DW. (b) The SHE-effective field can induce magnetization reversal.

measurements in Pt/NiFe bilayers, they could observe that both an DL-torque and a FL-torque were generated by the SHE in the heavy metal layer. This effect is mainly due to the presence of a non-zero imaginary part of the spin-mixing conductance at the interface between the HM and the FM [95]. As explained by Haney et al. [103] in their semiclassical modeling of the current induced SOTs, the generation of the FL-torque due to the SHE can be explained by the precession of the itinerant spins diffusing across the ferromagnetic layer. Indeed, during their diffusive motion across the ferromagnet,

the electron spins transversal to the local magnetization will experience a precession around the internal exchange field. This results in the generation of a spin polarization into the FM which is transversal to the injected spin polarization right at the interface. As a result a new field-like torque, $\boldsymbol{\tau}_{SHE,FL} = \tau_{SHE,FL} \mathbf{m} \times \hat{\boldsymbol{\sigma}}_s$, is generated in the FM. Note that $\hat{\boldsymbol{\sigma}}_s$ in the previous equation is in the direction of the spin polarization at the interface.

2.8 Beyond the spin-orbit torques: chiral damping

During the last year, the new concept of *chiral damping* has been proposed as an alternative explanation, to the SOTs, for the observed DW motion in material systems with SIA. Jué et al. [104] employed the new concept in the attempt of explaining the observed field-induced DW motion in OOP-magnetized Pt\Co\Pt trilayers. In their experiment, the DWs are moved by OOP magnetic field (H_z) pulses, in the presence of a static in-plane magnetic field (H_x). The DW motion is observed in the so-called *creep regime*, where the DW velocity is strongly affected by thermal excitations and can be expressed by [104]:

$$v_{DW,creep} = v_0 \cdot \exp\left[-\frac{U_c}{k_B T} \cdot \frac{H_p^{1/4}}{H_z^{1/4}}\right], \quad (2.50)$$

with U_c being the pinning energy barrier of the DW that has to be overcome in order to move the DW from its pinning site, T the temperature of the magnetic system, H_p the de-pinning field needed to move the DW, H_z the applied OOP field, and v_0 is a velocity pre-factor. As shown by Jué et al. [104], the velocity pre-factor is inversely proportional to the effective damping parameter, $v_0 = v_0(\alpha) \propto \frac{1}{\alpha}$, resulting in $v_{DW,creep} \propto \frac{1}{\alpha}$.

They observed that the velocity of the $\uparrow\downarrow$ -DW and the $\downarrow\uparrow$ -DW, equal for $H_x = 0$, were different in the presence of a finite H_x : $v_{DW}^{\uparrow\downarrow}(H_z, H_x) \neq v_{DW}^{\downarrow\uparrow}(H_z, H_x)$. Such observation has been attributed to different values of the effective damping for the two types of DW. Accordingly, the following expression for the effective damping influencing the DW motion has been proposed: $\alpha \propto \alpha_0 + \alpha_c(\mathbf{m} \cdot \nabla \mathbf{m})$. The effective damping is presented as the sum of an isotropic term, α_0 , and a chiral term, $\alpha_c(\mathbf{m} \cdot \nabla \mathbf{m})$ [104], where the latter is a function of the relative orientation between the magnetic moment in the DW and the gradient of the magnetization at the DW.

The theoretical concept of chiral damping has been presented by Akosa et al. [105] in a

phenomenological description. For ultra-thin magnetic systems with SIA, which is the relevant case for the presented work, the effective damping tensor takes the form:

$$\alpha^{ij} = \alpha_0^{ij} + \alpha_z^{ij} \Delta \mathbf{m} \cdot [(\hat{\mathbf{z}} \times \nabla) \times \mathbf{m}], \quad (2.51)$$

where α_0^{ij} are the isotropic damping terms, α_z^{ij} the chiral damping terms, Δ is the characteristic exchange length, $\hat{\mathbf{z}}$ the direction of symmetry breaking, and \mathbf{m} the magnetization unit vector. From Eq. 2.51 it is clear that the effective damping is a function of the direction of the magnetization, \mathbf{m} , and of its spacial gradients, $\nabla \mathbf{m}$. Including Eq. 2.51 in Eq. 2.50 with $v_{DW}^0 \propto \frac{1}{\alpha}$ makes DWs with different chirality move at different velocities during their creep motion.

In PMA systems, $\uparrow\downarrow$ and $\downarrow\uparrow$ DWs have opposite chirality when an in-plane field is applied parallel to the DW motion direction. This happens when the applied field is large enough to align the internal magnetic moments of the two types of DWs, parallel to each other. According to the new theory of chiral damping, if such a situation is generated, the two types of DWs are expected to move at different velocities. This is in agreement with findings of Jué et al. [104].

The chiral damping is only the latest proposed mechanism governing the complex and still not well understood dynamics of DWs in magnetic systems with SIA and strong SOI [104–106]. Furthermore, it is not clear yet which the limits of applicability of the new theory are in the interpretation of the multitude of observations of field-induced [19, 20, 104, 107] and current-induced [9, 25, 27, 35, 44] DW motion reported so far.

2.9 Magnetic nanostructures with structural inversion asymmetry: new effects for Spintronics

The observations of SOTs in ferromagnetic metal layer-based systems started only when the attention of several researchers in the field of nanomagnetism and spintronics fell on magnetic heterostructures with an ultra-thin FM layer in direct contact with a strong SOC material. The material system where the SOT have been observed experimentally for the first time was the trilayer Pt\Co\AlO_x, with a 0.6 nm thick Co layer [9, 44, 67]. The ultra-thin FM layer was the key to make the observation of SOTs in the system possible. Since the ISGE is expected to be a pure interfacial effect and the spin current

injected into the FM layer due to the SHE decays rapidly across the FM thickness, the thin Co layer made it possible to observe the effects of the new torques. The exciting novel effects observed in such multilayered material systems with SIA [9, 25, 35, 36, 44, 67, 68] inspired and motivated the experimental work presented in this thesis.

Chapter 3

Experimental techniques

3.1 Introduction

This chapter offers a description of the techniques employed for the characterization of the samples and for the fabrication of the devices analyzed in this thesis. Moreover, an introduction to the main experimental techniques used for the investigation of those devices will also be given in this chapter. The magnetic properties of the investigated material stacks were characterized by superconducting quantum interference device (SQUID) magnetometry. The device fabrication process was based on electron-beam lithography and Argon-ion milling. Finally, the magnetic domains and the current-induced domain wall motion (CIDWM) were imaged by Kerr microscopy and photo-emission electron microscopy (PEEM). The physical principle behind each of these techniques will be discussed in the following sections. Particular attention is paid to the magneto-optic Kerr effect (MOKE) and to Kerr microscopy, which is the main technique used for the present scientific work.

3.2 Sample characterization

3.2.1 Superconducting quantum interference device magnetometry

In order to pre-characterize the magnetic properties of the material stacks, SQUID magnetometry was used. Coercivity field, H_c , hard-axis saturation field, H_k , and saturation

magnetization, M_s , were determined for the material stacks used for device fabrication.

The SQUID is a device based on a quantum interference effect. As its name implies, it consists of superconducting elements, it involves quantum effects and it is mainly based on an interference effect [108]. The specific device used for obtaining the results here reported was a RF-SQUID. However, for simplicity, in the following the principle of operation of the DC-SQUID will be presented.

In Fig. 3.1(a) a schematic of the so-called DC-SQUID is shown, and the corresponding electric circuit is illustrated in Fig. 3.1(b). It consists of two superconductive elements separated by two Josephson junctions (two tunnel barriers). A bias current I is injected across the device, which splits in half at point A into two different conductive paths. After passing through the junctions, the two currents join again at point B. The two electronic wavefunctions will undergo a dephasing when traveling through the two tunnel barriers. Such dephasing is defined by the specific device properties. If a magnetic field \mathbf{B} is trying to enter the superconductive loop, an extra dephasing component will be added to the two wavefunctions. In particular, this extra phase exhibits the same magnitude but opposite sign for the two current paths. Thanks to this dephasing, an interference effect between the two wavefunctions will occur at point B. The so-generated interference pattern will depend on the magnetic field entering the superconducting loop. In particular, its maxima and minima will be periodic with respect to the magnitude of \mathbf{B} , with a period corresponding to one magnetic flux quantum $\Phi_0 = h/2e$, where h is the Planck's constant and e the electron charge. By measuring the voltage drop between point A and point B as a function of \mathbf{B} a sinusoidal signal will be obtained.

At this point, it is clear that a SQUID can be used for measuring magnetic fields. Furthermore, since the magnetic moments of a magnetic sample generate a stray field in the surrounding space, such a field can then be as well measured with SQUID magnetometry. Thus, by measuring the stray field of a magnetic sample, we can actually measure its total magnetic moment and extract its magnetization, that is its magnetic moment per unit volume. To measure H_c and M_s , the magnetic moment of each sample was measured as a function of an external magnetic field applied along the magnetic easy-axis of the sample. Sweeping the magnetic field back and forth between a minimum and a maximum value, an hysteresis loop such as the one sketched in Fig. 3.2(a) is obtained,

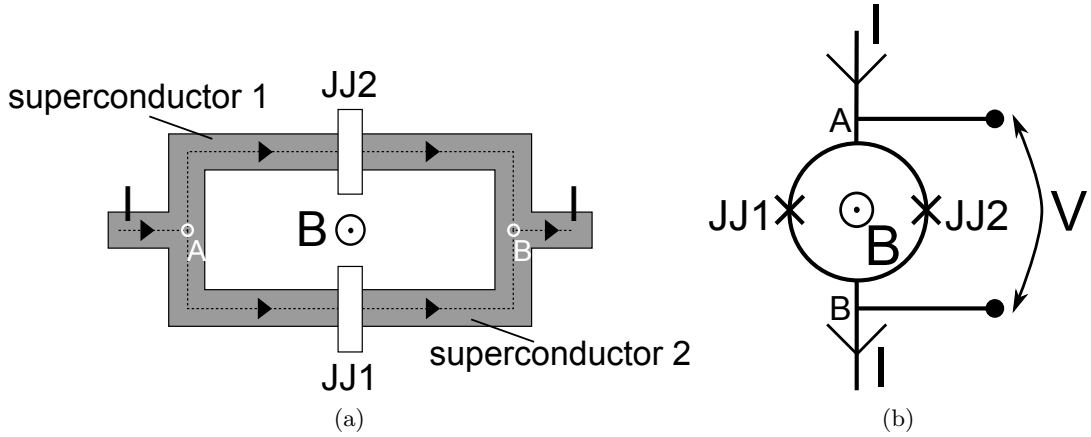


FIGURE 3.1: **DC-SQUID.** (a) Schematic of the device, consisting of two superconductive elements separated by the two tunnel barriers JJ1 and JJ2. (b) Corresponding electric circuit.

where actually the magnitude of the magnetization, M , as a function of the applied magnetic field is shown. However, as the magnetic moment is actually measured by the system, the value of the magnetization can be obtained by dividing the measured magnetic moment m by the magnetic volume $V_{FM} = t_{FM} * A_{FM}$, being t_{FM} the thickness of the magnetic film and A_{FM} its area.

On the other hand, to measure H_k the magnetic moment is measured as a function of an external magnetic field applied along the magnetic hard-axis of the sample. The resulting hysteresis loop appears as the one sketched in Fig. 3.2(b). However, before being able to extract the saturation field, the diamagnetic signal originating from the bulky substrate has to be subtracted from the total measured signal. This is explained in more details in the Master thesis works of Mr. G. V. Karnad [109] and Mr. T. N. Zake [110].

3.3 Device fabrication

After characterizing the magnetic properties of the material stacks, spintronic devices were lithographically fabricated on them. The patterning process, fully developed by the author as part of this experimental PhD project, consisted in two steps of electron-beam (e-beam) lithography (EBL) [111] and sputtering [112], plus one step of EBL and Argon-ion milling. At the end of the fabrication, each device consisted of several magnetic nanowires parallel to each other, where the effect of electric current on the

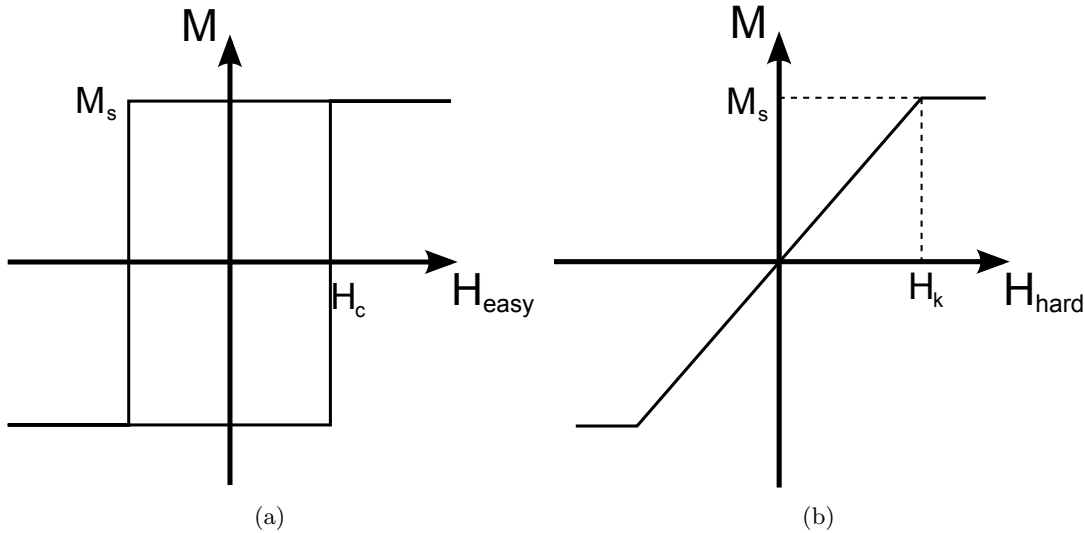


FIGURE 3.2: **Hysteresis loops.** (a) Magnetic hysteresis loop for external magnetic field along the easy-axis. The loop is squared. (b) Magnetic hysteresis loop for external magnetic field along the hard-axis. No hysteresis, the magnetization is a linear function of the applied field, up to its saturation value.

magnetic texture in all of them could be observed at the same time. The typical material stacks used in the present work consisted of a magnetic multilayer on top of a Si/SiO₂ substrate. A detailed description of the specific material stack used in each experiment will be offered in the corresponding chapters.

Electron-beam lithography is mainly based on the use of the highly focused electron beam of a scanning electron microscope (SEM) to define structures down to nanometric dimensions in an electron-sensitive polymeric resist [111]. The resist is spin-coated on the sample surface before the exposure to the electron beam. After a development step in an appropriate solvent, the regions of the polymer exposed to the e-beam are removed from/left on the sample surface in case of a positive/negative tone resist. As a result, a polymeric mask is defined on the sample surface. Such a mask can then be used either to deposit material on the free areas on the sample surface, or to pattern devices from the material stack with a specific shape.

Sputtering is a well developed technique for thin film deposition on the surface of a substrate [112]. Many different classes of materials can be deposited with this technique, among which metals and oxides. After that the substrate, which the thin film has to be deposited on, has been in a high vacuum chamber reaching a base pressure between 10^{-9} and 10^{-6} mbar (the lower the base pressure, the higher the purity of the deposited thin film), an Argon atmosphere with a pressure of about 10^{-2} mbar is

produced. Argon-plasma is subsequently generated in front of a target made of the material to be deposited by applying a high voltage (around 300 V in this case) between the target and an anode in front of it. The Ar-ions are accelerated towards the target and, by impacting against it, atoms of the target will be sputtered away from its surface. Those atoms are now free to move towards the substrate (situated in front of the target, at a certain distance usually in the range of a few-several cm) with a certain kinetic energy, and will be eventually absorbed on the substrate surface.

Ar-ion milling is a technique used to remove material from the surface of a substrate. Its functioning is very similar to the one described above regarding the sputtering deposition technique, with the difference that now the “target” is the thin film sample itself. Assuming to have a hard mask on the sample surface previously produced by EBL, the milling technique can be used to remove a desired amount (thickness) of material from the uncovered regions at the top surface. As a result, devices can be patterned on the sample surface, consisting of the material stack elsewhere removed.

In order to pattern the devices and electrically connect them to the rest of the experimental set-up, a multi-step lithographic process was implemented. Alignment markers were patterned first. They were obtained by transferring the lithographically defined mask on the bare sample. The mask consisted of the bi-layer *methyl methacrylate/polymethyl methacrylate* (MMA\PMMA), a positive tone electron-sensitive resist bi-layer [113]. The mask transfer consisted in depositing 10 nm of Cr (adhesion layer) followed by 100 nm of Au on the sample by sputtering technique and then lifting off the resist from the sample by immersion in Acetone. At the end of the process, an array of Cr\Au-markers was obtained.

Using the patterned markers as a reference framework, a new mask for the patterning of the devices was defined by a second step of lithography. This time, a negative tone electron-sensitive resist (AR-N 7520.073 [114]) was employed, so that a hard polymer mask was obtained with the same shape of the desired devices. By Ar-ion milling, all the material stack was removed from the uncovered regions of the sample, down to the Si\SiO₂ substrate. At the end of the milling process, the resist left at the top of the devices was removed with a very effective solvent (Remover AR 300-70 [115]). In this way, the desired magnetic devices were obtained on the initial sample.

Finally, bond pads were patterned on the sample with a second lift-off step. Those contacts, made of Cr(10 nm)\Au(100 nm), were patterned in a way to be directly in contact

with the devices. One of the patterned devices used for the experiments described in the following chapters is shown in Fig. 3.3.

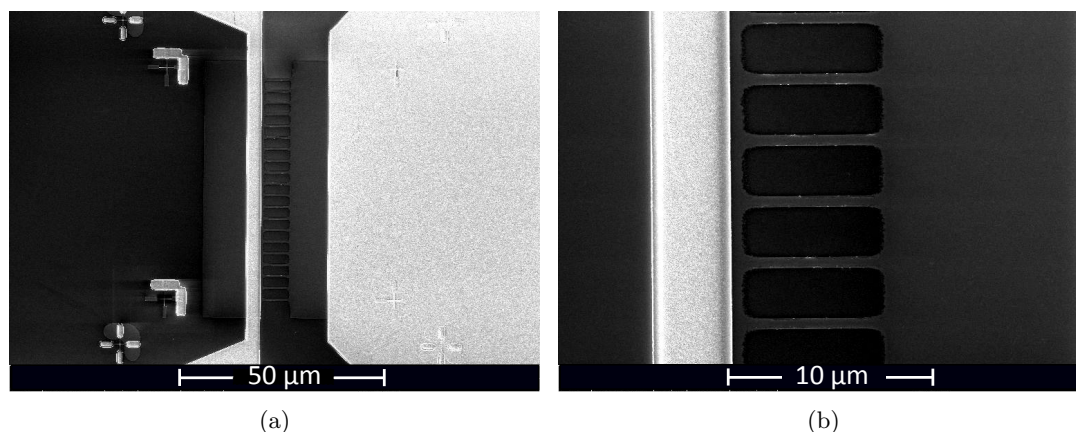


FIGURE 3.3: **Device patterning.** (a) SEM micrograph of a typical device used for current-induced domain wall motion experiments. In the center of the figure are the magnetic nanowires, while on the two sides are the two gold pads used for current injection. In this specific case, one gold pad consists in an Oersted-line. (b) Detail of the device in (a), showing the Oersted-line and some of the magnetic nanowires.

3.4 Kerr Microscopy

The principal experimental technique used for the imaging of the current-induced magnetization manipulation was Kerr microscopy. The Kerr microscope exploits the so-called *magneto-optic Kerr effect* (MOKE) to produce a magnetic contrast in the image of the sample. With this technique, a direct visualization of the magnetic domains structure at the sample surface is possible. Furthermore, by imaging the sample before and after the application of an external magnetic field or of current pulses through the structures, it is possible to directly visualize the motion of the magnetic domain walls. In the rest of this section, an introduction to MOKE is offered, in order to explain the basic physical phenomenon which Kerr microscopy relies on. Then, the general operating principles of the Kerr microscope will be described, together with some details about the actual device used for the experiments discussed in the following chapters.

3.4.1 Magneto–optic Kerr effect

The observation of the *magneto–optic Kerr effect* was for the first time reported by John Kerr, as described in his article published on the *Philosophical Magazine and Journal of Science* in 1877 [116]. The effect consists in the rotation of the plane of polarization of a light beam by reflection from the surface of a magnetic material. Given a linearly polarized light shining onto a magnetic surface, the reflected light will not be linearly polarized anymore. The beam reflected off the sample surface will be elliptically polarized, with the main polarization axes rotated of a certain angle compared to the initial linear polarization. The degree of ellipticity and the angle of rotation of the polarization plane are defined as *Kerr ellipticity*, ϵ_K , and *Kerr rotation*, θ_K , respectively. Together, they define the so–called *complex Kerr angle*: $\Phi_K = \theta_K + i\epsilon_K$ [117], which fully describes the reflection of the incoming beam at the magnetic surface.

In order to understand MOKE more in details, the quantum mechanical response of the matter to the electromagnetic field of the incoming light beam has to be taken into account. The microscopic origin of the Kerr effect seems to rely on the spin–orbit interaction present in the ferromagnetic materials [117, 118]. The MOKE can be described as a birefringence effect due to the magnetic properties of the sample, where the spin–orbit coupling and the exchange interaction act at the same time on the electronic states involved in the absorption/emission process [119]. However, a detailed discussion of the quantum mechanical origin of the Kerr effect is beyond the scope of the present thesis, and not crucial for the understanding of the experimental results here reported. To anyone who could be interested in going more in depth in that direction, the references [117, 118] are suggested as a starting point.

It is possible to describe the MOKE by a classical *dielectric tensor theory* [117, 120], where the reflectivity tensor is a function of the magnetization. Defining as \mathbf{E}^i and \mathbf{E}^r the electric field of respectively the incoming and reflected light beam, it is possible to write:

$$\begin{bmatrix} E_s^r \\ E_p^r \end{bmatrix} = \begin{bmatrix} r_{ss} & r_{sp} \\ r_{ps} & r_{pp} \end{bmatrix} \bullet \begin{bmatrix} E_s^i \\ E_p^i \end{bmatrix}. \quad (3.1)$$

Here, s and p define the component of the electric field perpendicular and parallel to the plane of incidence, as shown in Fig. 3.4. According to Eq. 3.1, when an incoming light beam is reflected off the magnetic surface the two orthogonal components of the electric field are mixed up. This is possible when the off–diagonal elements of the reflectivity

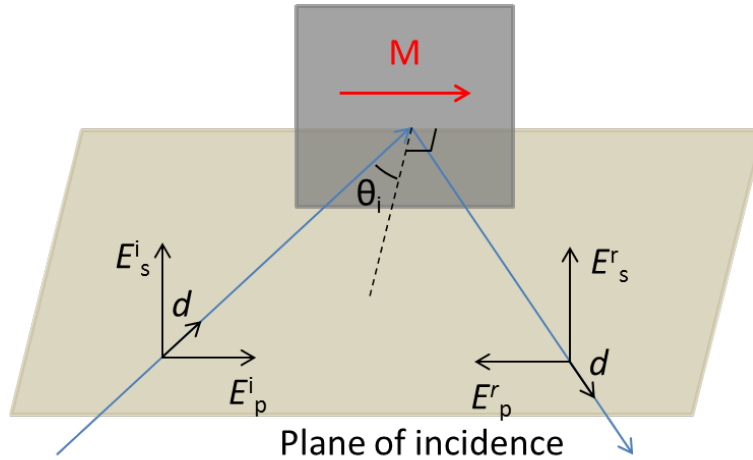


FIGURE 3.4: **Light beam reflection at a magnetic surface.** The incoming beam \mathbf{E}^i is reflected off the sample surface obtaining the reflected beam \mathbf{E}^r . The s - and p -component of the electric field are mixed at the reflection, due to non-zero off-diagonal elements of the magnetization-dependent reflectivity tensor. The vector \mathbf{d} indicates the light's propagation direction.

tensor are non-zero and a function of the sample magnetization. This means that, the reflectivity properties of the sample are a function of its magnetization state. Different magnetization magnitudes and directions correspond, for a fixed incoming beam, to a different reflected beam. Due to this coupling between the magnetic and optical properties of magnetic samples, it is possible to investigate the magnetization state of the sample or the effect of an external magnetic field on the magnetization looking at the reflected beam properties. This is the core of the MOKE technique used as a magnetometry tool [121].

Analogously to SQUID magnetometry, by MOKE magnetometry it is possible to characterize samples from a magnetic point of view. However, the SQUID is sensitive to bulk properties of the sample, due to the fact that it probes its total magnetic moment, while MOKE is only sensitive to the surface of the sample, where the reflection effect occurs. For metallic samples probed with visible light, the probing-depth of MOKE is in the order of 10-20 nm [121], making it more suitable for the investigation of magnetic thin films. This is the case of the magnetic systems studied in this work, which is focused on the investigation of magnetic multilayers containing an ultra-thin ferromagnetic layer ($t_{FM} \approx 1$ nm). Accordingly, MOKE magnetometry was also employed in the process of sample characterization, jointly to SQUID magnetometry.

Three main different MOKE configurations are typically defined. What distinguishes

these three different configurations is the relative orientation between the magnetization vector and the plane of incidence of the probing light beam. As shown in Fig. 3.5, when the magnetization lies in the plane of incidence, pointing perpendicular to the sample surface, the system operates in the so-called *polar-MOKE* configuration. Moreover, there are two other configurations in the case that the magnetization vector lies on the sample surface. It is common to distinguish between *longitudinal-MOKE* and *transverse-MOKE* in the case of \mathbf{M} being in the plane of incidence or perpendicular to it, respectively. As the focus of the work presented in this thesis was on magnetic thin

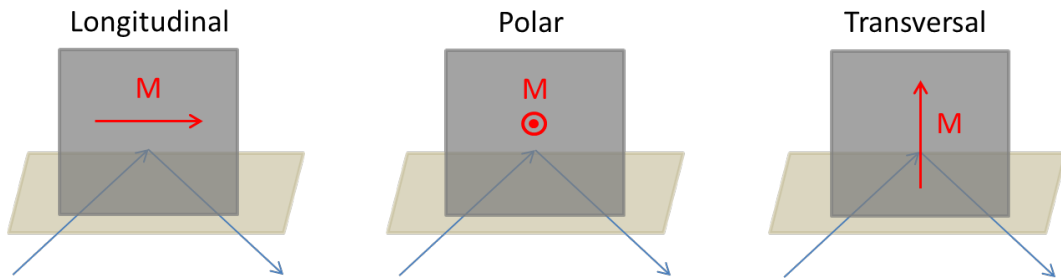


FIGURE 3.5: **MOKE configurations.** The three MOKE configurations: *longitudinal*, *polar* and *transverse*. In case of samples with the magnetization pointing out of the sample surface the polar configuration is the one to be used.

films with magnetization perpendicular to the sample surface, the polar configuration has been used, as it is the only one sensitive to the magnetization pointing perpendicularly to the sample surface. Accordingly, in the remaining part of the discussion about MOKE and Kerr microscopy, we will refer to the polar configuration.

The classical interpretation of the MOKE relies on the concept of the Lorentz force [121]. As shown in Fig. 3.6, when the incoming beam reaches the sample surface, the electrons at the sample surface start to oscillate with the incoming electric field \mathbf{E}^i , with a velocity \mathbf{v}_e . Due to this oscillation and as a consequence of the non-zero internal magnetic field \mathbf{H}_{int} of the magnetic sample, a Lorentz force of the form $\mathbf{F}_{\text{Lor}} = -e\mathbf{v}_e \times \mathbf{H}_{\text{int}}$ will influence the electrons motion. Such a Lorentz-oscillation (in Fig. 3.6 indicated by the dashed white arrows) causes the emission of electromagnetic radiation where the total electric field has a new component $\mathbf{E}_{\mathbf{K}}$, which is defined as the Kerr component. Due to the presence of $\mathbf{E}_{\mathbf{K}}$, the reflected beam will exhibit a different polarization state with respect to the incoming beam. The in-phase component of $\mathbf{E}_{\mathbf{K}}$, with respect to $\mathbf{E}_{\text{s,p}}^r$, generates the Kerr rotation θ_K , while the out-of-phase component of $\mathbf{E}_{\mathbf{K}}$ generates the Kerr ellipticity ϵ_K . In Fig. 3.6(a) and Fig. 3.6(b) the MOKE in the polar configuration

is pictorially described for an incoming beam with p and s polarization, respectively. Based on the argument of the Lorentz force, it is clear that the polar–Kerr effect is maximized for small incident angles ($\theta_i \approx 0^\circ$), when the angle between the incoming electric field and the magnetization is maximum (90°). According to what has been said

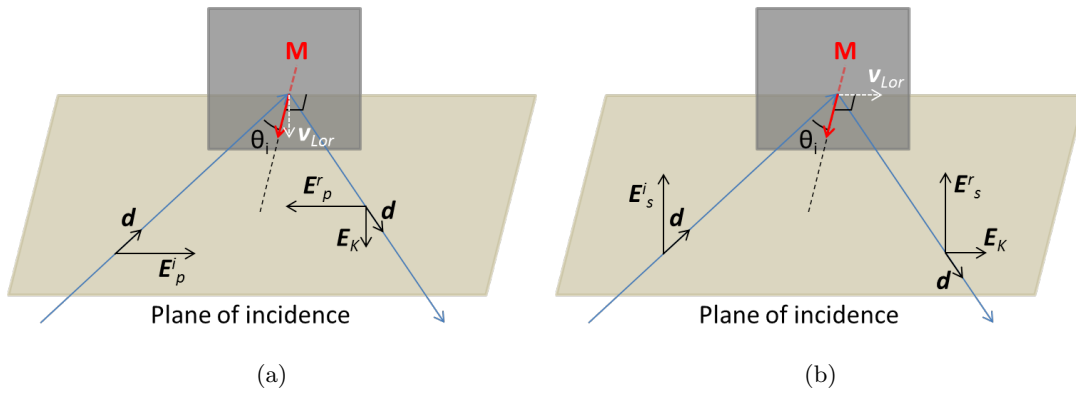


FIGURE 3.6: **Polar MOKE.** (a) The MO Kerr effect in the polar configuration is pictorially described, based on a Lorentz–force argument. In this particular case, a p -polarized incoming beam is considered. (b) The same as in (a), but for the case of an s -polarized incoming beam.

so far, by analyzing the polarization state of the reflected beam, it is possible to assess the magnetic properties of the analyzed samples. Then, let us consider now to build up an experimental set–up for the measuring of the MOKE. Such a set–up is schematically shown in Fig. 3.7. As it is reported in the schematic, the principal components of such a MOKE set–up are:

The light source, used for generating the probing radiation.

The polarizer, used for fixing the polarization state of the incoming beam.

The magnetic surface, which is at the center of investigation.

The analyzer (e.i. a second polarizer), used for filtering the reflected beam to measure the Kerr effect.

The detector, which is used for measuring the final light beam intensity.

First of all, a light beam is produced by a light source, which can be, for example, a laser, a mercury lamp or a light emitting diode (LED). After its generation, the incoming beam is polarized in the preferred state (s - or p -polarization) by a polarizer, before reaching the sample surface with an intensity I_i . After being reflected, the light beam leaves the

sample with intensity I_r and with a new polarization state, characterized by the Kerr rotation angle θ_K . Here it is filtered by an analyzer, which has a polarization direction tilted compared to the one of the reflected beam. Such an angle α_A can be considered also as the angle between the two polarization directions fixed by the polarizer and the analyzer, since the Kerr rotation is a very tiny effect. Finally, the reflected beam is absorbed by a photo-detector, used for measuring the beam intensity I_d .

The detected intensity is given by

$$I_d = I_r (\cos(\alpha_A))^2, \quad (3.2)$$

and the differential intensity with respect to the analyzer angle is

$$\frac{dI_d}{d\alpha_A} = 2I_r \cos(\alpha_A) \sin(\alpha_A). \quad (3.3)$$

According to Eq. 3.3, the maximum change of the total intensity due to a change of α_A is obtained for $\alpha_A = 45^\circ$. This means that, the change in the measured intensity due to the Kerr effect is

$$\Delta I_d = \frac{dI_d}{d\alpha_A} \theta_K, \quad (3.4)$$

resulting in the relative Kerr intensity or *Kerr sensitivity*

$$I_{Kerr} = \frac{\Delta I_d}{I_d} = 2\theta_K \tan(\alpha_A) = \frac{I_{max} - I_{min}}{I_{max}}, \quad (3.5)$$

where I_{max} and I_{min} are the maximum and minimum measured intensity. Equation 3.5 makes it clear that in order to have the highest sensitivity to the Kerr rotation the set-up has to be employed close to the so-called *extinction mode*, that means $\alpha_A \approx 90^\circ$ [122].

3.4.2 The Kerr microscope

In the previous section the MOKE has been described, using the concepts of magnetization-dependent reflectivity tensor and Lorentz force. In the following, it will be explained how such a magneto-optic effect can be exploited to directly image the magnetization state of magnetic surfaces and thin films. An optical microscope equipped with a polarizer and an analyzer is an efficient tool for imaging magnetic domains, as it will be

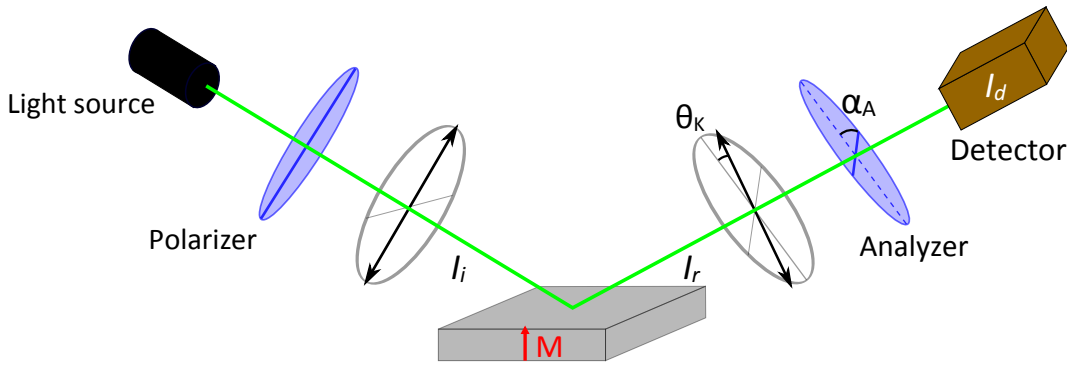


FIGURE 3.7: **MOKE set-up.** A schematic of a typical polar-MOKE set-up. The light beam is first generated by a light source and then polarized before impinging onto the sample surface. At the magnetic surface the light beam is reflected with a certain Kerr rotation θ_K . After that, the reflected beam is filtered by an analyzer before being detected at a photo-detector, where the intensity of the light is measured.

explained in the following.

In Fig. 3.8, the schematic of a wide-field Kerr microscope is reported. There is a light source (an LED), a series of lenses used for projecting/focusing the light beam, a few apertures for the lateral confinement of the beam, a beam splitter for deviating the light path, a polarizer/analyzer and a compensator for manipulating the light polarization state and a CCD camera used for collecting the reflected light and recording the sample image. In green and yellow are reported the illumination light path and the image-forming light path, respectively.

The *aperture diaphragm* (AD) is used to regulate the total intensity of the illumination light as well as the Kerr configuration. As it will be explained later, positioning the AD centered or off-centered allows to actually change the magnetization component probed by the microscope. After passing through the *field diaphragm* (FD), the light beam is linearly polarized by a *polarizer* (P) and then focused by the *focusing lens* (FL). The FL produces an image of the AD at the *back focal plane* (BFP), while the *objective lens* (OL) projects the light beam uniformly on the sample surface. This configuration of lenses is needed in order to generate the so-called *Köhler illumination*, which ensures an uniform illumination and the formation of no image of the light source on the sample surface [121]. The OL collects the reflected light coming from the sample, and after that the light passes through a *compensator* (C) and an *analyzer* (A) before being focused on the camera pupil in order to finally record the sample image.

As said before, the FL generates an image of the AD in the BFP. When the P and the A are in the extinction configuration, the image of the AD in the BFP appears as the

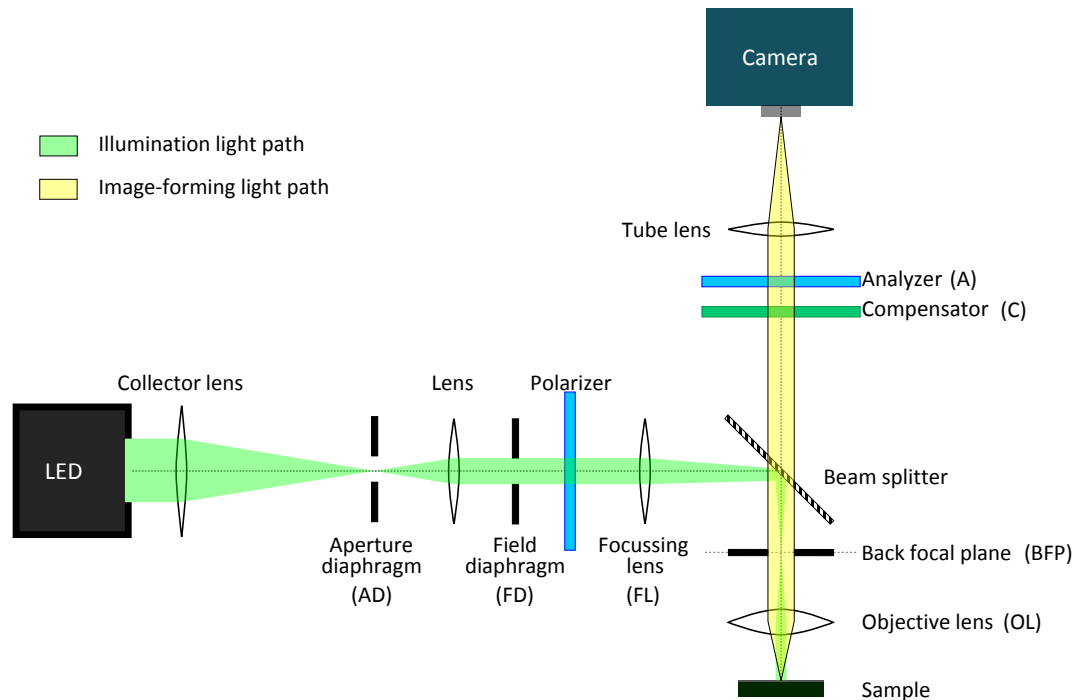


FIGURE 3.8: **Kerr microscope – Schematic.** Schematic of a wide-field Kerr microscope in the polar configuration. The illumination light path and the image-forming light path are separately shown. An LED is the commonly used light source in commercial devices. The sample images are recorder by a CCD camera, which allows for a digital image processing. All the rest is as previously discussed for the MOKE set-up.

one shown in Fig. 3.9. Such an image takes the name of *Maltese cross*, and it can be observed in the so-called conoscopical image of the microscope [121]. The black aperture in Fig. 3.9 is the AD. As it can be seen, the selection of different specific areas of the Maltese cross corresponds to set the microscope in different Kerr configurations. So, in case the operator is interested in probing the out-of-plane component of the sample magnetization (PMA materials, for example) the AD has to be positioned centered. On the other hand, if the magnetization of the sample is in-plane, the AD has to be positioned off-centered in order to operate the microscope in the longitudinal or transverse mode. Due to the fact that in this project the attention was focused on out-of-plane magnetized thin films, the microscope was operated in the polar-Kerr configuration, i.e. the AD was kept centered.

Once that the Kerr configuration is selected, the microscope can be employed to image the magnetic state of the sample. In Fig. 3.10 the process of magnetic imaging acquisition is schematically illustrated. The linearly polarized incoming beam is reflected with a different polarization state from differently magnetized magnetic domains. After the analyzer, the intensity of the light coming from the different domains will thus



FIGURE 3.9: **Maltese cross.** Image of the Aperture diaphragm in the back focal plane, in the extinction condition, for the three different Kerr configurations. The positioning of the aperture selects the Kerr configuration. In order to probe magnetization pointing perpendicularly to the sample surface, the aperture has to be centered. The black areas indicate where the light is transmitted through the AD.

have different intensities. Once the light is collected by the CCD camera, an image of the sample is obtained, where different domains will appear as areas with high or low intensity.

Since the Kerr effect gives rise to a small variation of the light polarization, the magnetic image is enhanced electronically. This is possible by using the so-called *differential imaging mode*, where a background image is subtracted from a second image with a different magnetization state. The change in the magnetization state between the background image and the second image will be strongly enhanced by subtracting the two images. This will remove all the non magnetic information from the final image (in an ideal case, with no mechanical vibrations), leaving it with only an enhanced magnetic contrast [121].

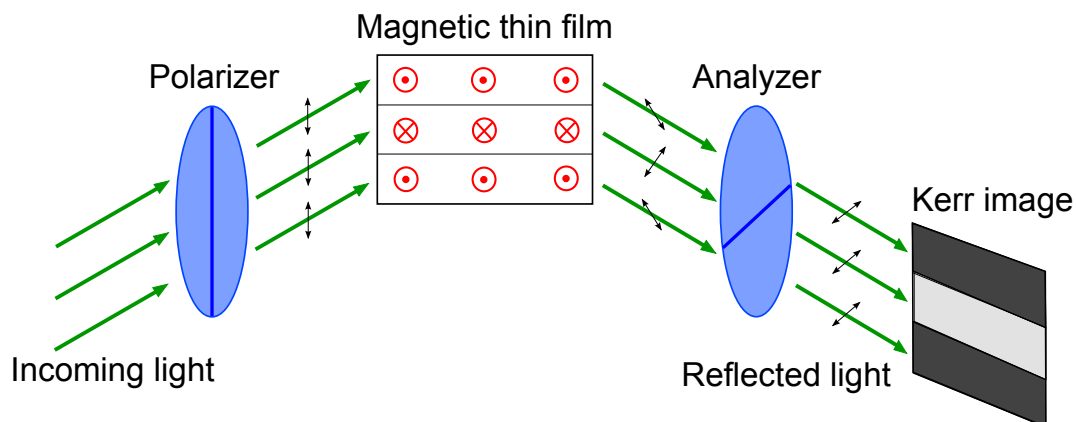


FIGURE 3.10: **Kerr image formation.** The process of Kerr imaging is described. The magnetic contrast is generated by the analyzer, which is differently transparent to the light coming from different magnetic domains. As a consequence, in the sample image the areas corresponding to different domains will appear brighter or darker.

3.4.3 Imaging domain wall motion at the Kerr microscope

For the measurements here reported, a commercial *Evico* wide-field Kerr microscope was employed. The light source of the microscope is a high stability white LED positioned at the back of the microscope, while the sample images are recorded by a CCD camera located at the top of it, as shown in Fig. 3.11. The electronic image acquisition process is controlled by a commercial Lab-View-based software, which allows also the control of the magnetic coils. Moreover, it is also the software used for the generation of the magnetic contrast by differential imaging.

For the employed microscope, two different objective lenses were available, with magnification factors of 20x and 50x. Furthermore, the microscope itself contains an extra lens-system which allows for an additional magnification of either: 1x, 1.6x, 2.5x or 4x. This means that the maximum magnification available is 200x, which is more than enough in order to observe domain wall motion in the patterned micrometer-wide nanowires like the ones shown in Fig. 3.3. The lateral resolution of the Kerr microscope can be heuristically assumed as given by the diffraction limit, where the minimum resolvable distance between two points is given by [121]

$$D_{min} = \frac{0.5\lambda}{NA}, \quad (3.6)$$

where λ is the light wavelength and $NA = n * \sin(\alpha)$ is the numerical aperture of the objective lens (n is the refractive index of the material at the interface with the sample surface and α is the acceptance angle of the objective lens). For the actual imaging of the DW motion, the employed objective lens is an *Olympus LCPLFLN50xLCD*, with a magnification of 50x and a numerical aperture of $NA = 0.7$. Accordingly, the ratio $\frac{0.5}{NA}$ is in the order of the unity, resulting in a lateral resolution of the microscope fixed by the light wavelength, which for the visible light is between 380 nm and 750 nm. Such a lateral resolution allows us to image the patterned micrometer-wide nanostructures, like the ones reported in Fig. 3.3. However, even if the effects of the diffraction start to be visible in the imaging of narrower structures, resulting in blurred images, the magnetic contrast can actually still be visible (in the actual set-up it was possible to observe a magnetic contrast in nanostructures with a width down to 250 nm). Furthermore, when the differential imaging technique is used, mechanical drift is occurring between the acquisition of the background image and of the second image. Such a drift reduces

the possibility of observing a clear magnetic contrast in the nanostructures. However, in order to minimize the drift effect due to vibrations of the microscope, an anti-vibration table is employed.

The experimental set-up needed to carry out the imaging of *current-induced domain wall motion* and *magnetization switching* is schematically depicted in Fig. 3.12. A *pulse*

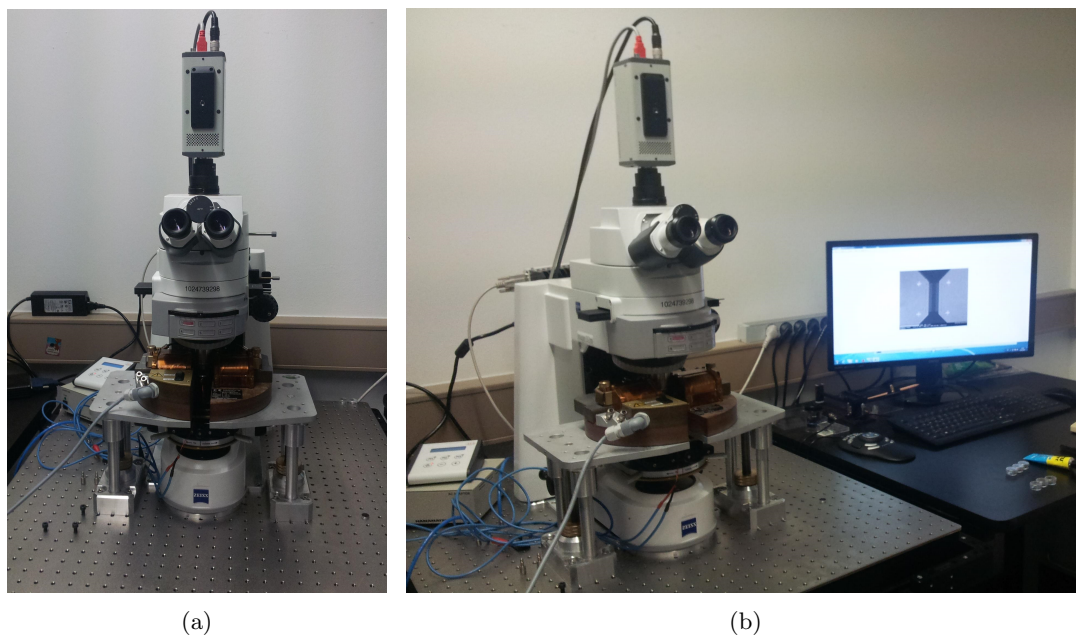


FIGURE 3.11: **Evico wide-field Kerr microscope.** (a) A picture of the front side of the Kerr microscope used during the experiments here reported. (b) A second picture of the front side of the microscope, where the imaged structure is visible at the computer screen. The electronic imaging can be exploited in order to increase the signal-to-noise ratio and the magnetic contrast.

generator is used for injecting the desired current pulses in the device. Sometimes a *power amplifier* was needed in order to generate the desired amplitudes of the current pulses. The sample is connected to the pulse generator on one side and to a $50\ \Omega$ -resistor termination on the other. The sample is also glued on a custom-designed high frequencies printed circuit board (HF-PCB), and connected electrically to it by two bonded aluminum wires. Finally, the injection of current pulses through the devices is made possible by HF SMA-end launchers. All the circuit, except the Al wires, is designed in a way to be $50\ \Omega$ -impedance matched. The devices are patterned in a way to be as close as possible to such condition. The PCB is plugged in a custom-designed Kerr microscope sample stage, and the imaging of current-induced magnetization manipulation in magnetic nanostructures is made possible.

Protocol for DW motion measurement. The protocol used for current-induced domain wall motion measurement using a device like the one shown in Fig. 3.3 is described in Fig. 3.13. First of all, the NWs are saturated in one of the two possible directions (up or down) by an external out-of-plane magnetic field. After that, a background image of the device is saved and subtracted (electronically) to the real time image acquisition, resulting in a no-contrast image as shown in Fig. 3.13(a). Second, reversed magnetic domains are nucleated in the NWs, in this case by a current pulse through the Oersted-line. At this point the reversed areas will generate an intensity contrast in the image, as shown in Fig. 3.13(b). This new image is now used as background image and subtracted from the real time image acquisition, resulting in the new no-contrast image shown in Fig. 3.13(c). Finally, current pulses are injected through the NWs, generating DW displacements. The motion of the DWs in the NWs result in the intensity contrast in Fig. 3.13(d). The last image containing the displacements of the DWs is analyzed employing the software *Image J*. The line-profile (integrated over the width on the NW) of the light intensity signal along the NWs length is acquired, from each area delimited by the red rectangles shown in Fig. 3.13(d). The result is shown in Fig. 3.13(e). Calibrating the length-scale of the line-profile graph with the scale contained in the picture, it is possible to measure the displacement Δx of the DW as the full width at half maximum of the obtained profile.

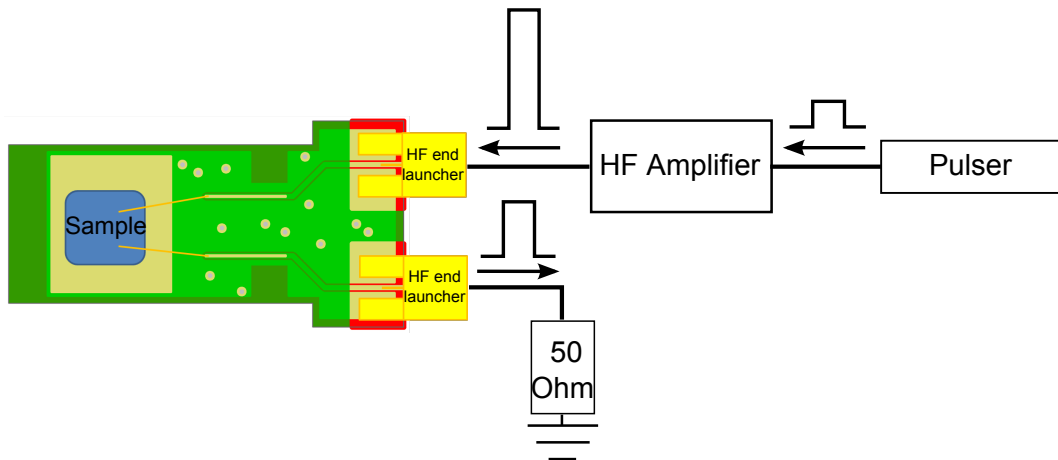


FIGURE 3.12: **Schematic experimental set-up.** A pulser and a power amplifier are used in order to generate the desired current pulses to be injected in the device. The sample is connected to a custom-designed HF-PCB and through it to the electronic device, so that the injection of current pulses is made possible. All the circuit is designed (where possible) in a way to be 50 Ω -impedance matched.

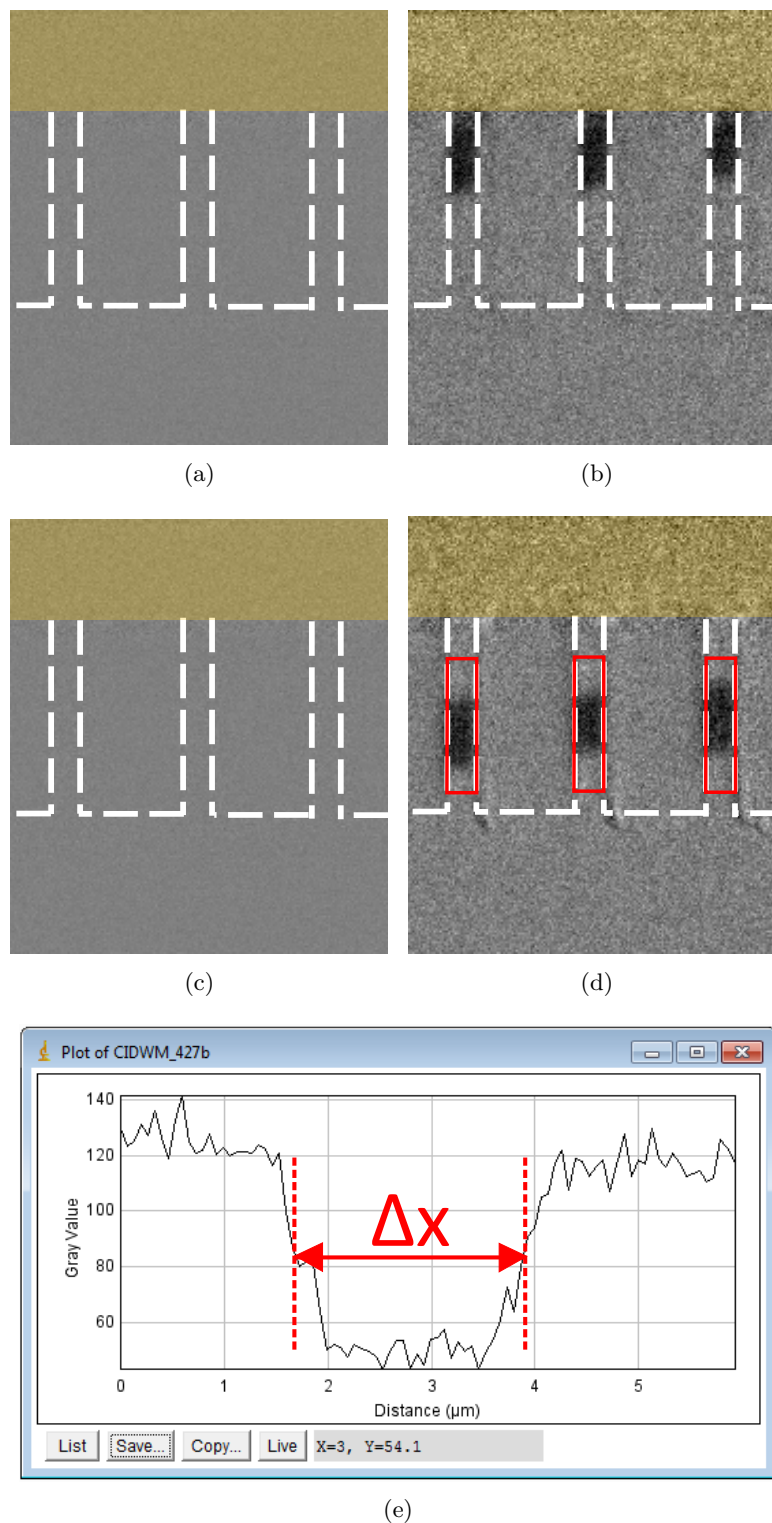


FIGURE 3.13: **Protocol for measuring DW motion at the Kerr microscope.** (a) **-Saturation-** The NWs are saturated by an external magnetic field, and a background image is acquired. (b) **-Nucleation-** Reversed domains are nucleated, resulting in dark areas in the NWs. (c) **-Background subtraction-** Image in (b) is used as new background image, resulting in a new no-contrast image. (d) **-Motion-** The nucleated DWs are moved by current pulses, generating a new magnetic contrast. (e) **-Measuring DW motion-** The DW displacement is measured by a software for image analysis.

3.5 Photo-emission electron microscopy (PEEM)

The second experimental technique used for the investigation of the patterned samples is photo-emission electron microscopy (PEEM). This is a hybrid microscopy technique, since it is based on the absorption of light (UV or soft X-rays) from the sample (as in a spectroscopy technique) and it collects the photo-emitted secondary electrons in order to generate an electron image of the sample (as in an ordinary electron microscope) [119]. Nowadays, most of the magnetism-related PEEM experiments are done at synchrotron radiation sources, where it is possible to obtain monochromatic soft x-ray radiation with a specific polarization (linear or circular) and a high brilliance [119]. This makes it possible to investigate samples made of different materials with elemental selectivity, due to the possibility of tuning the x-ray energy on a specific absorption edge. Furthermore, selecting the specific element by x-ray tuning gives the opportunity to investigate not only materials present on the sample surface, but also buried materials up to a depth of circa 5-6 nm. A later space resolution down to 20 nm can be obtained [119].

The schematic of a PEEM is shown in Fig. 3.14, where its main parts are illustrated. The sample is mounted on a sample stage, which is in some cases piezomotor-driven in the x and y directions, into an ultra high vacuum chamber (working pressure of the order of $\leq 10^{-9}$ mbar). This allows the user to move the sample horizontally, so that different areas of the sample surface can be imaged. Generally, the electron-optics present in the microscope are of the electrostatic type. The reason is the need of avoiding any magnetic stray field produced by magnetic lenses close to the sample surface, since it could influence the magnetization of the sample under investigation. However, the employed Elmitec PEEM at the Nanoscience beamline IO6 in DIAMOND (the synchrotron light source in Didcot, UK) had actually a magnetic objective lens, where the small stray field generated close to the sample was actively compensated. In the specific case of the Elmitec microscope employed during the measurements reported in this thesis, the objective lens consists of a magnetic lens surrounded by an electrostatic cathode, which is put at a different electrostatic potential with respect to the sample (sample is at ground). The secondary electrons emitted from the sample surface after the x-rays absorption are accelerated by the objective lens cathode due to the existing potential difference, usually of 15–20 kV. The accelerated electrons are then processed by all the electron-optic components present after the objective lens, eventually reaching the electron-sensitive screen. On their way to the screen, the electrons are processed

in order to reduce the spherical and chromatic aberrations (by the contrast aperture), astigmatism (by the stigmator) and to define the field of view (FoV, by the Iris aperture and the projective lenses). Finally, the optimized image formed on the screen is captured by a CCD camera [119].

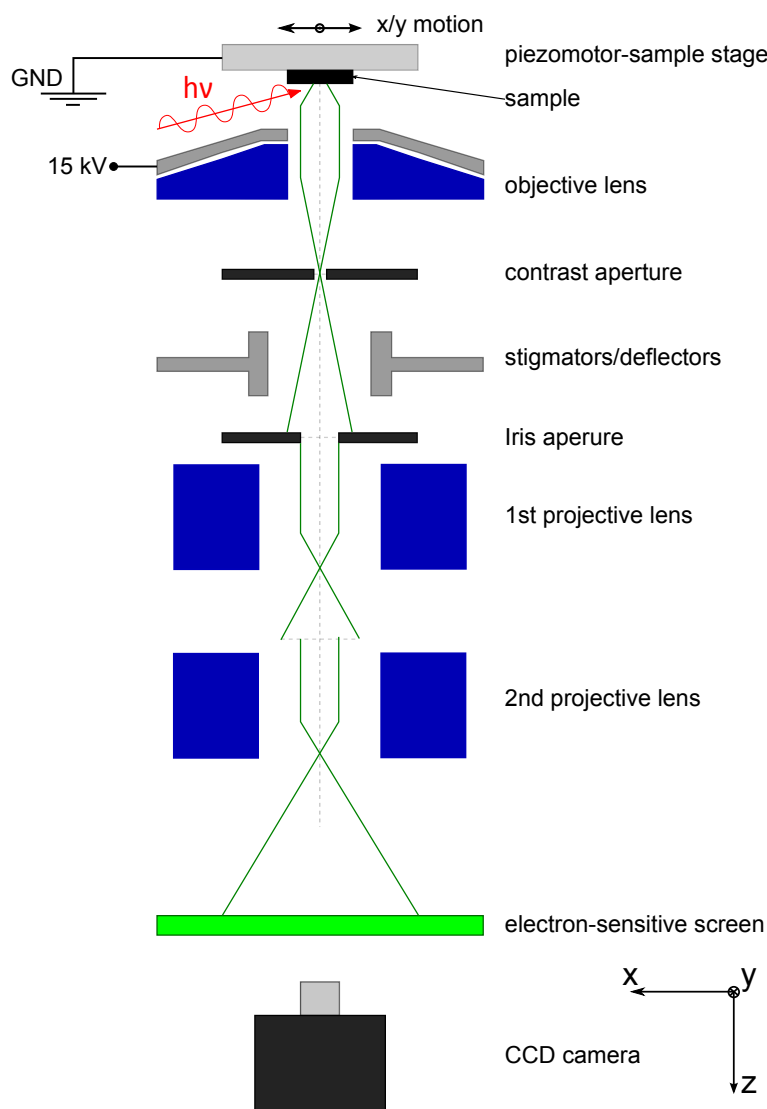


FIGURE 3.14: **PEEM**. Schematic of a photo-emission electron microscope. The sample absorbs the incident radiation and emits secondary electrons. Those electrons are collected by the objective lens and processed by all the electron-optics till the reaching of an electron-sensitive screen. A CCD camera generates an electronic image of the sample.

3.5.1 X-ray magnetic circular dichroism (XMCD)

Since the primary interest is to image the magnetic texture present in the patterned nanostructures, the x-ray magnetic circular dichroism (XMCD) [123, 124] has been

exploited for magnetic contrast formation. At the core of the technique there is the difference in the absorption of right and left circularly polarized x-rays at the inner shell absorption edges of magnetic materials (see Fig. 3.15). More precisely, the absorption matrix element depends on the relative orientation between the incoming light spin direction \mathbf{s}_γ and the local magnetization \mathbf{M} direction in the magnetic material (or the corresponding electrons spin \mathbf{s}).

Considering the L_3 absorption edge process for transition metals (Fe, Co, Ni) as shown in Fig. 3.15, the XMCD effect can be explained as a three-step process, even if it is actually a quantum mechanical one-step process [119]. First, the circularly polarized x-rays are resonantly absorbed by the $2p_{3/2}$ shell electrons, which are excited to the empty electron states just above the Fermi level E_F . The probability of absorption is a function of the density of states (DOS) at the Fermi edge. For the specific case discussed in Fig. 3.15, the minority electrons have more available states at E_F . Accordingly, more minority than majority electrons can be excited due to photon absorption. This defines an asymmetry in the absorption probability between minority and majority electrons. Second, the generated holes decay by filling the empty core states with electrons coming from higher energy states. Third, the energy conservation allows for the emission of Auger electrons. The asymmetry in the photon absorption is kept in the Auger electrons emission. Finally, on their way to the sample surface the emitted electrons experience inelastic scattering events, ending in the emission of secondary electrons with a certain energy distribution from the sample surface. This explains how the difference in photon absorption probability for different magnetized areas of the samples can be measured by collecting the emitted secondary electrons.

For a fixed circular light polarization (left, with $s_\gamma = -1$ or right, with $s_\gamma = +1$) the probability of absorption is different in different magnetic domains. On the other hand, for a fixed magnetic configuration, the absorption of right and left polarized x-rays is different. By taking two images of the sample with right and left polarized x-rays and then subtracting one from the other, a clear image of the magnetic configuration with a strong magnetic contrast can be achieved. This is described by the XMCD asymmetry A_{XMCD} as

$$A_{XMCD} = \frac{I_R - I_L}{I_R + I_L},$$

where I_R (I_L) is the measured intensity for right- (left-) circularly polarized x-rays [119].

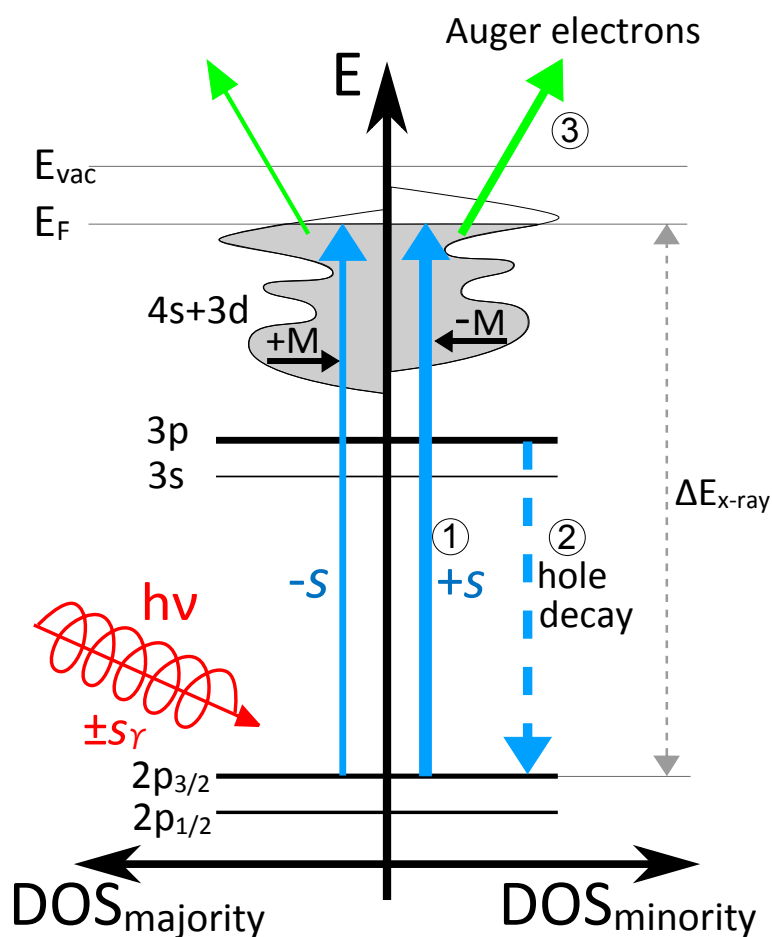


FIGURE 3.15: **XMCD**. Three-step model of x-ray magnetic circular dichroism for the L_3 absorption edge. 1) Photon absorption; 2) hole decay; 3) emission of Auger electrons. The different probability for the absorption of circularly polarized x-rays by majority and minority electrons is at the core of the magnetic contrast formation in the PEEM image. This is due to the fact that the asymmetry in the photon absorption is conserved in the emission of secondary electrons, which are then used for the formation of the sample image. The thickness of the different arrows is a visual indication of the probability of the represented transition/emission.

Chapter 4

Spin–orbit torque–driven magnetization switching in Ta\CoFeB\MgO

4.1 Introduction

Spin–orbit torques (SOTs) are at the center of this scientific work. The main goal is to measure the strength and sign of such torques, in order to learn more about their physical origin. One of the material stacks chosen for this investigation is Ta\CoFeB\MgO. There are two reasons at the basis of this choice. First, Ta\CoFeB\MgO is a material system widely used in the fabrication of magnetic tunnel junctions, an important component in present spintronic devices [3, 5]. Any new discovery regarding this system would be very interesting from an application point of view, due to the compatibility of the stack with the present technology. Second, the material stack consists of a few nm–thick heavy metal bottom layer, an ultra–thin ferromagnetic layer and an oxide layer at the top. All these ingredients make it a good candidate for the observation of SOTs, due to the strong spin–orbit coupling in the heavy metal and the structural inversion asymmetry which are present in the system [25, 68].

The first experiment discussed here is the magnetization switching by current pulses injected through magnetic nanowires. The purpose of the experiment was to verify if the magnetization switching was governed by SOTs, which would also provide information

on the symmetry of the torques. The effect of thermal excitations on the switching process was also studied. The topic discussed in this chapter has been already presented in a manuscript published in the journal *Applied Physics Letters* in 2014 [125].

4.2 Material stack: Ta\CoFeB\MgO

The material system employed for the patterning of the magnetic devices was the multilayer: Ta(5.0)\Co₂₀Fe₆₀B₂₀(1.0)\MgO(2.0)\Ta(5.0) (all thicknesses in nm). The stack was deposited at the *Singulus Nanotechnologies AG* by magnetron sputtering technique (a Singulus TIMARIS/ROTARIS tool was employed) on a Si/SiO₂ substrate. The deposition process was followed by an annealing step at 300 °C for 2 hours in vacuum, in order to obtain a large perpendicular magnetic anisotropy (PMA) [110, 126]. From growth studies carried out at *Singulus Nanotechnologies AG* it is known that the Ta bottom layer grows largely in the β -phase (tetragonal unit cell for single-crystal [127]), for the specific deposition conditions and thicknesses. This is confirmed by its high measured resistivity (180 $\mu\Omega\text{cm}$, while typical resistivity values for the bcc-phase are around 25–50 $\mu\Omega\text{cm}$ [127]), which is a hallmark of this specific crystallographic phase [68, 127]. A schematic of the stack is reported in Fig. 4.1. A high resolution tunneling electron

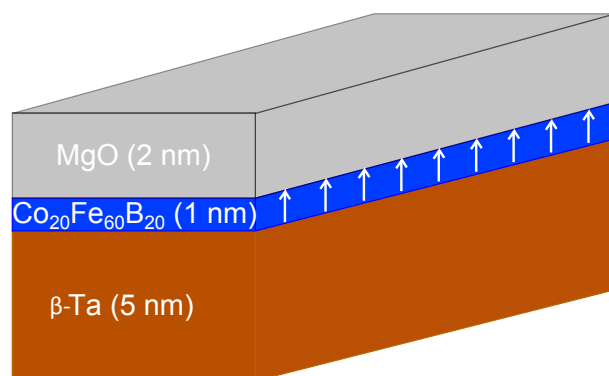


FIGURE 4.1: **Ta\CoFeB\MgO stack.** Schematic of the Ta\CoFeB\MgO stack used for magnetic nanowires patterning. The arrows indicate the magnetic moments in the ferromagnet, which is characterized by PMA. The bottom Ta layer is mainly in its crystallographic β -phase [127].

microscopy (HRTEM) image of the cross-section of the material stack¹ is reported in Fig. 4.2 [128]. The TEM micrograph in Fig. 4.2 shows a sharp CoFeB\MgO interface, a less sharp Ta\CoFeB interface and provides evidence for the presence of a top Ta-oxide

¹The HRTEM micrograph has been taken by our collaborators L. Nasi and L. Lazzarini from the IMEM-CNR of Parma, Italy.

layer due to the natural Ta oxidation in air. It is also visible the presence of crystalline MgO and CoFeB layers around the top interface. Finally, the image confirms the nominal thicknesses of the different layers.

During the annealing process, the B is expected to diffuse out of the ferromagnetic layer, mainly towards the bottom Ta layer (as also confirmed by the chemical depth profiling measurements reported in Chapter 5). As a consequence of that, at the CoFeB\MgO interface a larger number of Fe–O bonds are expected to occur compared to the case of the as-deposited stack. Since part of the origin of the PMA is believed to rise from the hybridization between the Fe- d_{z^2} and the O- p_z orbitals [38], as explained in the Theory chapter, the annealing is expected to increase the out-of-plane anisotropy in the material stack. The effect of the annealing process on the out-of-plane magnetic anisotropy has been experimentally observed also by other groups [129].

The material stack was pre-characterized by SQUID and MOKE magnetometry, where M_s , H_c and H_K were measured. An out-of-plane hysteresis loop obtained by MOKE magnetometry is reported in Fig. 4.3 . It can be observed that the loop is very square, confirming the presence of a strong uni-axial PMA, with a coercive field of $H_c \approx 2.5$ mT. As reported in the Diploma Thesis of Mr. Tim Zacke² [110], SQUID magnetometry measurements confirmed the strong PMA characterizing the material system, with a measured in-plane saturation field of $H_K = 400$ mT. This demonstrates that the interfacial uni-axial anisotropy energy density, $K_u = \frac{K_i}{t_{FM}} = K_{eff} + \frac{1}{2}\mu_0 M_s^2$, is strong enough in order to generate an out-of-plane magnetized thin film ($K_{eff} > 0$), for such a thickness of the magnetic layer ($t_{FM} = 1$ nm). All the values of the magnetic parameters of the material stack are listed in Tab. 4.1.

\mathbf{M}_s (A/m)	$\mu_0 \mathbf{H}_c$ (mT)	$\mu_0 \mathbf{H}_k$ (mT)	\mathbf{K}_u (J/m ³)	\mathbf{K}_{eff} (J/m ³)
$1.1 * 10^6$	2.5	400	$9.8 * 10^5$	$2.2 * 10^5$

TABLE 4.1: **Magnetometry data for the Ta\CoFeB\MgO material stack.** Magnetometry values for the material stack used for current-induced magnetization switching experiments. All the values contained in the table but the coercive field are extracted from Ref. [110], where they have been obtained by SQUID magnetometry.

²Tim Zacke was a diploma student at the Kläui Lab in 2012, who also investigated Ta\CoFeB\MgO thin films and nanostructures.

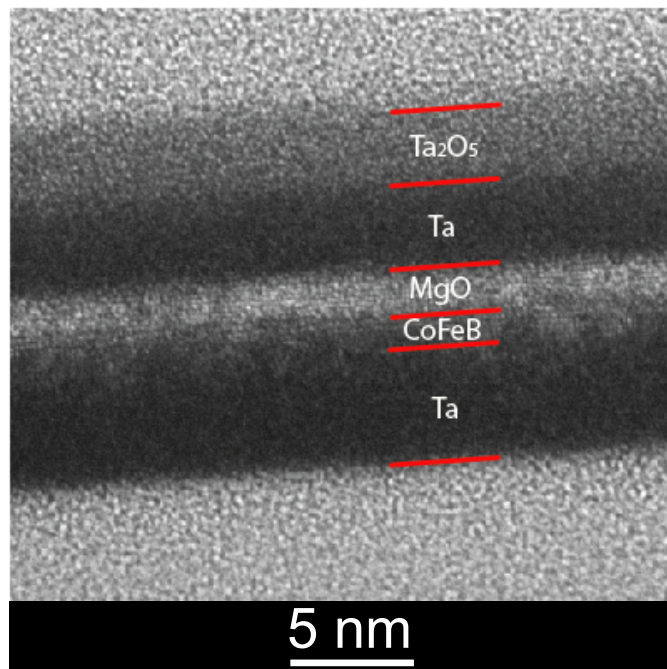


FIGURE 4.2: **TEM image of the cross-section of the Ta/CoFeB/MgO stack.** High resolution TEM micrograph of the cross-section of the Ta/CoFeB/MgO stack used for magnetic nanowires patterning. A sharp CoFeB/MgO interface is visible, suggesting that the B diffused out of the FM towards the bottom Ta layer. This is also confirmed by less sharp Ta/CoFeB interface, where the two layers appear more intermixed. Data from [128]. (Image taken by L. Nasi and L. Lazzarini from the IMEM-CNR of Parma, Italy.)

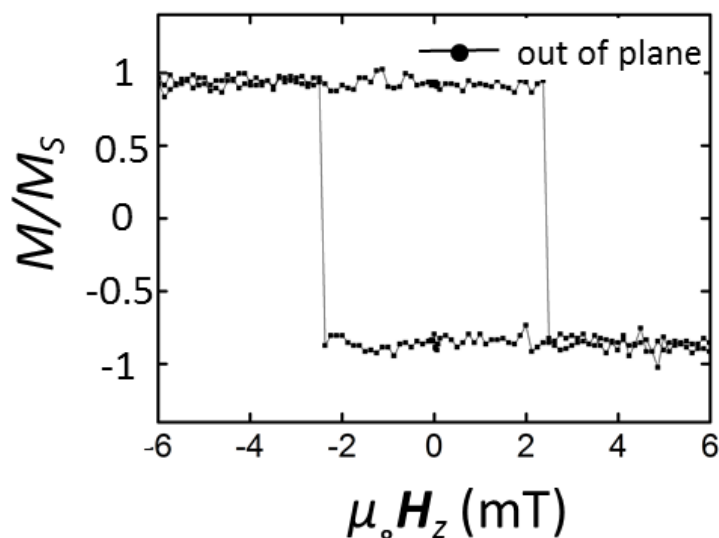


FIGURE 4.3: **Polar-MOKE hysteresis loop of the Ta/CoFeB/MgO multilayer for an applied out-of-plane field.** MOKE magnetometry hysteresis loop for the Ta/CoFeB/MgO stack used for magnetic nanowires patterning. The external magnetic field was applied perpendicular to the sample surface, with the MOKE system operating in the polar configuration. The experiment was carried out at room temperature ($T \approx 300$ K). The loop is square, indicating a strong PMA, with a coercive field of 2.5 mT. (Measurement carried out by T. Schulz, T. Zacke and Dr. S.-J. Noh at the Johannes Gutenberg Universität Mainz.)

4.3 Experimental set-up

In order to carry out the desired current-induced magnetization switching (CIMS) experiments, the material stack described above is patterned into an array of 20 nanowires in a parallel configuration (see top part of Fig. 4.4) by e-beam lithography and Ar-ion milling [125]. Each nanowire is 1 μm wide and 8 μm long. At both ends of the nanowires there are two magnetic pads, directly connected to two gold pads made in a second lithography step. As depicted in Fig. 4.4, during the measurements the device is electrically connected in series to a pulse generator on one side, and an oscilloscope on the other. A voltage pulse is applied to the sample and the pulse waveform is measured by the oscilloscope across its 50 Ω -internal resistance (R_o). The current flowing through the system is obtained by the measured voltage V_o across R_o . The Ta-capping layer at the top of the stack is assumed to have no influence on the current-induced magnetization dynamics generated in the magnetic layer, since it is electrically isolated from the rest of the conductive part of the stack. However, some of the current injected in the device is shunted by the conductive part of such a layer. Only about 3 nm of the total 5 nm of the capping layer are still conductive, due to natural surface oxidation when exposed to air [128]. Accordingly, the total current density through the device is calculated as in the following: 1 V dropping across R_o (corresponding to a total current of 20 mA) corresponds to a current density $j_a = 1.1 * 10^{11}$ A/m² flowing through the nanowires.

As explained in Chapter 3, the magnetization state of the nanowires during the experiments is imaged by differential Kerr microscopy in the polar configuration. For the specific experiments discussed here, the microscope is equipped with a magnetic coil for the generation of an external in-plane magnetic field \mathbf{H}_x . All the experiments are carried out at T=300 K.

In order to observe CIMS, first of all the magnetic nanowires are saturated in the “up”(+z) or “down”(-z) magnetization state in an external out-of-plane field (see bottom left in Fig. 4.4). After that, a constant and uniform in-plane magnetic field, \mathbf{H}_x , is applied along the nanowires. Injecting a current pulse through the device, the magnetization of the nanowires is switched for appropriately chosen field amplitude and current density. Each magnetization switching event is observed and recorded by the Kerr microscope, after the current pulse injection (bottom-right in Fig. 4.4). Part of the measurements reported here were carried out in collaboration with Dr. A. Hrabec.

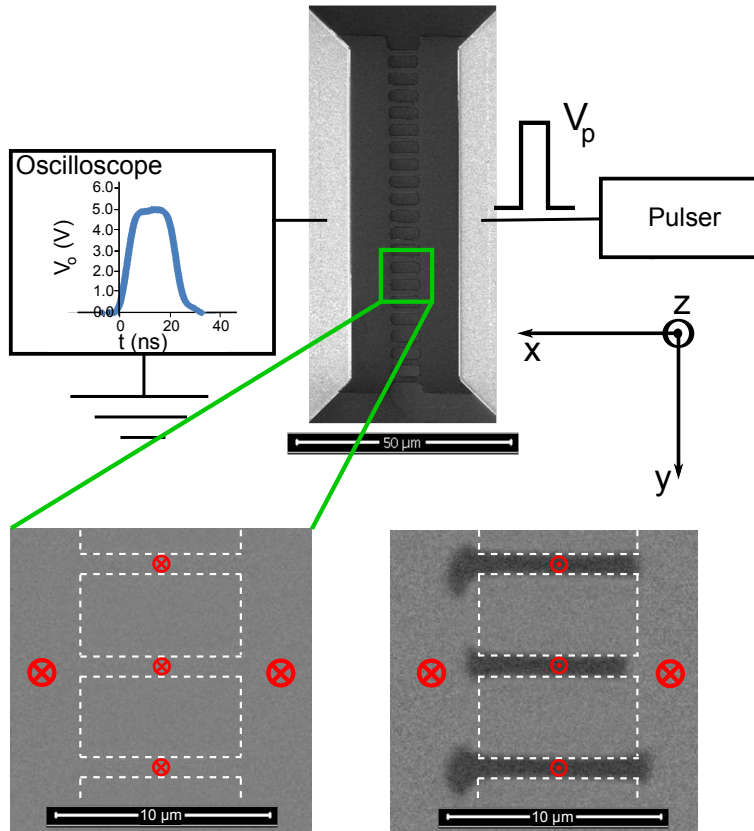


FIGURE 4.4: **Experimental set-up for the CIMS experiment.** At the top, it is shown a schematic of the experimental set-up for current pulse injection, including an SEM micrograph of the Ta\CoFeB\MgO nanowires. The shape of one of the voltage pulses applied to the device is shown in the inset. It was measured with an oscilloscope (across the $50\ \Omega$ internal resistance). At the bottom-left, a differential Kerr microscopy image of the initialized nanowires with the magnetization pointing “down” ($-z$) everywhere. At the bottom-right, a differential Kerr microscopy image of the same nanowires, after their magnetization has been switched “up” ($+z$) by a current pulse in the presence of an in-plane magnetic field collinear with the current-flow. The red symbols represent the magnetization state in the magnetic device. Data from [125].

4.4 Magnetization switching by spin-orbit torques

4.4.1 Measuring the magnetization switching

Firstly, it is observed which combination (if any) of current density and magnetic field could produce a certain switching event. In Fig. 4.5 switching events for different current-field combinations are shown. The condition for the observation of a successful magnetization switching event, for the specific experiment here described, is defined as switching in at least half of the total number of pre-saturated nanowires. Successful switching events for all the four possible combinations of current and field are illustrated.

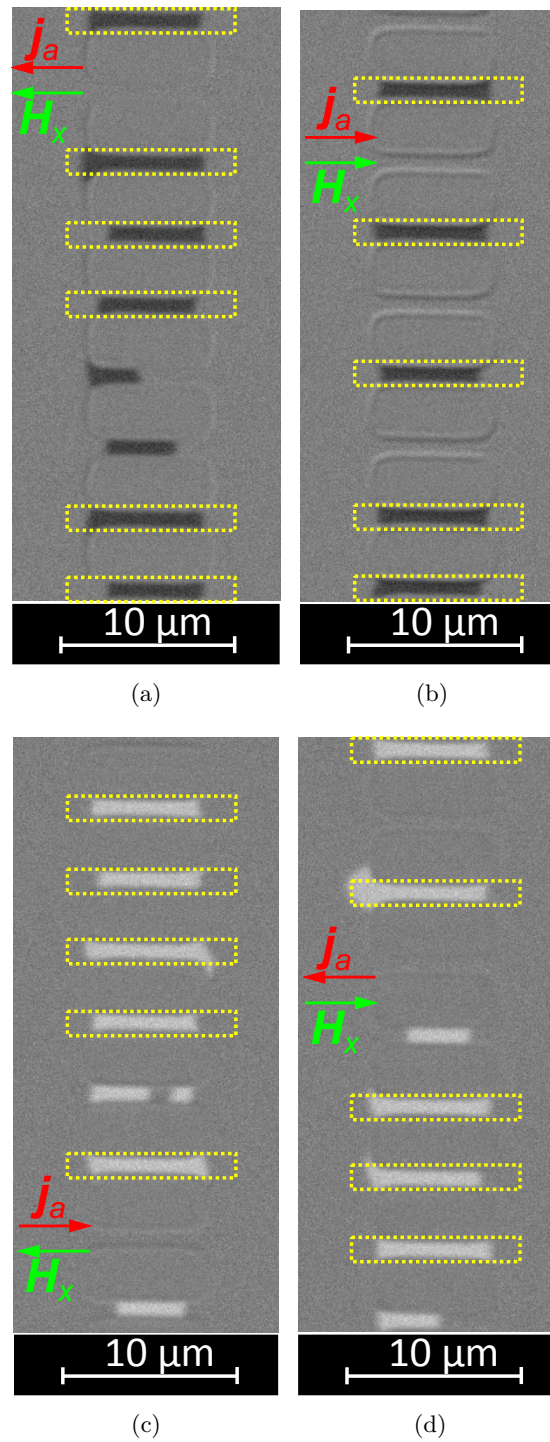


FIGURE 4.5: **Magnetization reversal events.** Successful magnetization reversal events for all the four possible combinations of current and field. (a) Switching for $j_a > 0$ and $H_x > 0$. (b) Switching for $j_a < 0$ and $H_x < 0$. (c) Switching for $j_a < 0$ and $H_x > 0$. (d) Switching for $j_a > 0$ and $H_x < 0$. In (a) and (b) two examples of down→up switching events are reported, while (c) and (d) refer to up→down switching events. Black (white) contrast indicates an “up”(“down”) magnetization state. The yellow rectangles indicate the fully switched NWs. Five or more fully switched NWs indicate a successful magnetization reversal event.

Figures 4.5(a) and 4.5(b) report down→up switching events for \mathbf{j}_a parallel to \mathbf{H}_x , while Figs 4.5(c) and 4.5(d) show up→down switching for \mathbf{j}_a anti-parallel to \mathbf{H}_x . The successful switching is indicated by the fact that at least half of the imaged nanowires are fully switched (as indicated by the yellow rectangles), where “fully” means that at least a 90% of the total NW’s area is switched.

Figure 4.6 reports about the magnetization switching for 100 ns- (closed symbols) and 100 ms- (open symbols) long current pulses, when a constant and uniform external magnetic field, \mathbf{H}_x , is applied along the nanowire direction. For both the 100 ns- and

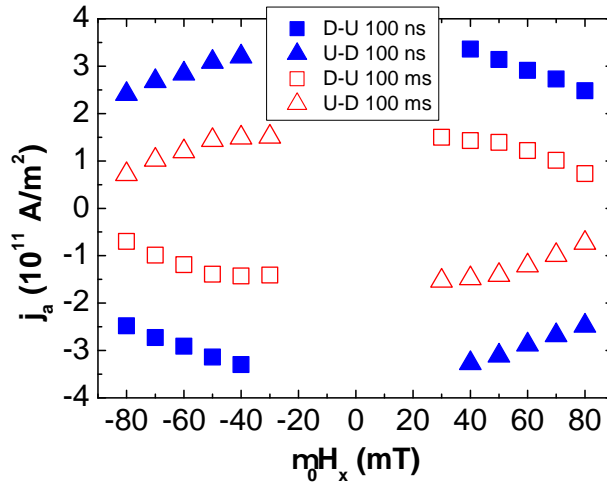


FIGURE 4.6: **Current-induced magnetization switching.** Minimum current density j_a needed to switch the magnetization in at least half of the nanowires (5 of 10) for a fixed longitudinal in-plane magnetic field $\mu_0 H_x$. The closed (open) symbols show the switching events due to 100 ns- (100 ms-) long current pulses. The squares (triangles) show the down→up (up→down) switching events. For the long pulses it can be observed a saturation in the current density needed to obtain the switching event, for small H_x . Data from [125].

	$\mathbf{I} > \mathbf{0}$	$\mathbf{I} < \mathbf{0}$
$\mathbf{H}_x > \mathbf{0}$	$+M_z$	$-M_z$
$\mathbf{H}_x < \mathbf{0}$	$-M_z$	$+M_z$

TABLE 4.2: **Stable magnetization configurations for Ta/CoFeB/MgO.** Stable magnetization states for the four different field-current combinations: $+M_z$ ($+z$ -direction), $-M_z$ ($-z$ -direction).

100 ms-long pulses, it is determined the minimum current amplitude j_a needed to obtain successful magnetization switching in combination with a fixed external magnetic field value (see Fig.4.6). In Fig. 4.6 it is possible to see that there is a clear link between the current density needed for the switching to occur and the applied in-plane field. The

lower is the in-plane field, the larger is the necessary amplitude of the current pulse to satisfy the switching condition. Secondly, for larger durations of the current pulses the needed switching current density amplitude is smaller. Finally, as reported in Tab. 4.2, the final stable magnetization state is found to be a function of the specific combination of the sign of \mathbf{j}_a and of \mathbf{H}_x (see also Fig. 4.5). When j_a and H_x are both either positive or negative, the observed stable magnetization state is in the $+z$ -direction. While, if j_a and H_x are of opposite sign, the stable magnetization state is in the $-z$ -direction.

The switching event is observed only in the case that the initial magnetization state of the nanowires was different from the stable state corresponding to the particular current-field combination under use. For example: in case the initial magnetization state is “down”, the switching event towards the “up”-state is observed only if the current density and the field are both positive or negative (Figs 4.5(a) and 4.5(b)), that means both current and magnetic field pointing in the positive or negative x -direction (squares in Fig. 4.6). On the other hand, starting from an “up” initial state, the switching toward the “down”-state (Figs 4.5(a) and 4.5(b)) is observed only in case current and field have opposite signs (triangles in Fig. 4.6).

4.4.2 Discussion

The results reported above are qualitatively in agreement with the model of the spin-orbit effective field reported by Liu et al. [68] and Emori et al. [25]. According to the model, an effective magnetic field is produced when an electric current is injected through the material stack, parallel to the sample surface. Such a field is defined by the following expression [25]:

$$\mathbf{H}_{SHE} = \frac{\hbar\theta_{SHE}|j_e|}{2\mu_0|e|M_s t_{FM}} \hat{\mathbf{m}} \times (\hat{\mathbf{z}} \times \hat{\mathbf{j}}_e), \quad (4.1)$$

where θ_{SHE} is the spin-Hall angle (SHA), \mathbf{j}_e the electron-current density ($\mathbf{j}_e = -\mathbf{j}_a$) and $\hat{\mathbf{j}}_e$ the corresponding unit vector, M_s the saturation magnetization of the ferromagnetic material, t_{FM} the thickness of the ferromagnetic layer and $\hat{\mathbf{m}}$ the magnetic moment unit vector (see Fig. 4.7). As already explained in the Theory chapter, such a model is valid only under three assumptions: (i) the HM layer where the SHE is generated is thick enough in order to saturate the spin current [93]; (ii) the HM\FM interface is characterized by a 100% spin-transparency [96] and no spin-memory loss [99]; (iii)

100% of the spin angular momentum (transverse to the magnetization) is transferred from the itinerant electrons to the local magnetization. Due to the thickness of 5 nm of the Ta bottom layer present in the investigated device, and the spin diffusion length in Ta which has been reported to be $\lambda_{spin}^{Ta} = 1-2$ nm [130–132], the first assumption can be considered fulfilled (see Chapter 5 for more details, where the SHA of Ta for the same materials stack will be extracted). While, the second and the third assumptions represent the real approximation adopted in the present work, since neither the spin-transparency/spin-memory loss at the Ta\CoFB interface nor the efficiency of the spin angular momentum transfer in the ferromagnet are known.

As it can be seen in Eq. 4.1, the effective spin-orbit field is expected to be a linear function of the electron current density \mathbf{j}_e . This is due to the fact that, in this particular model, the origin of the spin-orbit field is attributed to the spin-Hall effect (SHE) [74–77] in the Ta bottom layer. As explained in Chapter 2, due to the SHE a pure spin current is generated, which flows from the HM towards the FM. The spin polarization of the generated spin current is oriented along the y -direction, with the sign being fixed by the current polarity and the sign of the SHA. Such a spin current, diffusing into the ferromagnet, exerts a torque on the magnetic texture.

The second main point about the strength and the sign of \mathbf{H}_{SHE} is that: the effective field is parallel to the vector product between the magnetic moment in the ferromagnet, \mathbf{m} , and the direction $\hat{\mathbf{z}} \times \hat{\mathbf{j}}_e$ (which is collinear with the y -axis). Accordingly: first, the larger is the x -component of \mathbf{m} , the stronger is the z -component of the effective field, which is the one needed to switch the magnetization from “up” to “down” and vice versa; second, the sign of \mathbf{H}_{SHE}^z is a function of the relative orientation between \mathbf{j}_e and \mathbf{m} .

The first point explains why the current density needed for switching is observed to decrease with increasing magnetic fields. The strength of the switching effective field is fixed. Since for larger H_x larger m_x are obtained, in order to keep the strength of \mathbf{H}_{SHE}^z constant, j_a has to be reduced with increasing H_x . This is in agreement with what is reported in Fig. 4.6. The second point concerning the sign of \mathbf{H}_{SHE} offers a possible explanation for the symmetry of the graph shown in Fig. 4.6 and for what is reported in Tab. 4.2. According to Eq. 4.1, the sign of \mathbf{H}_{SHE}^z is fixed by \mathbf{j}_a , \mathbf{m}_x and θ_{SHE} . For conventional current and magnetic field both positive or negative (that means \mathbf{m}_x pointing along the same direction of \mathbf{j}_a), \mathbf{H}_{SHE}^z results pointing “up” (“down”) in case θ_{SHE} is negative (positive). On the other hand, when the current and the field are anti-parallel, \mathbf{H}_{SHE}^z results pointing “down” (“up”) when θ_{SHE} is negative (positive).

Interpreting the experimental observations according to that, a negative sign for the SHA is extracted. This is in agreement with previous experimental observations, where the Ta layer was reported to be in its crystallographic β -phase and its SHA being negative [25, 68]. The conclusion is that the main effect at the origin of the observed magnetization reversal is indeed the SHE effective field due to the Ta bottom layer, as illustrated in Fig. 4.7. In the presence of $H_x > 0$ (Fig. 4.7(a)), the generated SHE-field stabilizes the magnetization “up” (“down”) for $j_a > 0$ ($j_a < 0$). While, in the presence of $H_x < 0$ (Fig. 4.7(b)), the generated SHE-field stabilizes the magnetization “down” (“up”) for $j_a > 0$ ($j_a < 0$).

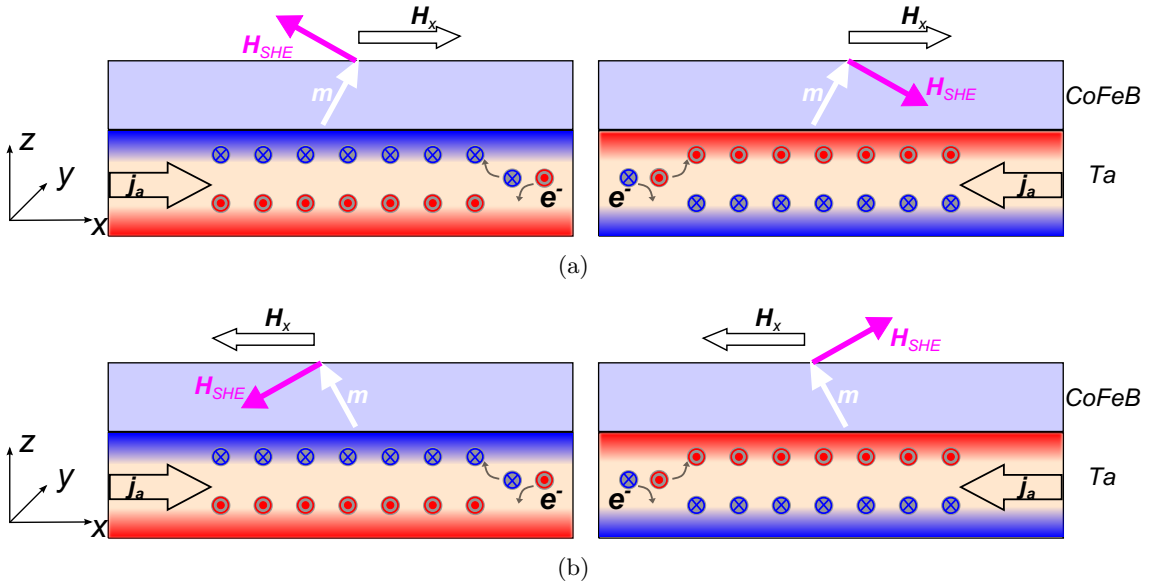


FIGURE 4.7: **Symmetry of current-induced magnetization switching in Ta\CoFeB\MgO nanostructures.** Schematic of SHE effective field-driven magnetization reversal in Ta\CoFeB\MgO. (a) The generated effective field, \mathbf{H}_{SHE} , in the presence of an applied $H_x > 0$. For $j_a > 0$ ($j_a < 0$), the stable magnetization configuration is $m_z > 0$ ($m_z < 0$). (b) The generated effective field, \mathbf{H}_{SHE} , in the presence of an applied $H_x < 0$. For $j_a > 0$ ($j_a < 0$), the stable magnetization configuration is $m_z < 0$ ($m_z > 0$). The symbols in the Ta bottom layer indicate the direction of the conduction electrons' spins.

4.5 Thermal effects in the magnetization switching process

A second main observation obtained during the switching experiment is the difference in the switching current density for the two different pulse lengths, as reported in Fig. 4.6. First of all, the amplitude of the short current pulses required for switching is about 3 times larger than what it is in the case of long pulses, for a fixed value of H_x .

Furthermore, the switching current for the long pulses saturates for values of $\mu_0 H_x$ lower than 50 mT. This is not expected according to the SHE-SOT model, where the current density needed for the switching process to occur is always increasing with decreasing in-plane fields. These observations clearly point to thermal effects playing a crucial role, as it will be explained in the following.

To study the observed thermally activated switching process in more detail, a second experiment is carried out. Using a fixed current density amplitude of $7 * 10^{11}$ A/m², for fixed applied in-plane magnetic fields the probability of switching is measured as a function of the length of the current pulse, Δt_p . The measurement is repeated 5 times for each $\mu_0 H_x - \Delta t_p$ combination, in order to obtain an average probability, P , and a statistical error on it. For each single switching event (recorded in each single Kerr microscopy image), the switching probability is defined as the switched fraction of the total switchable area in the observed NWs. Accordingly, if all the NWs are completely switched a $P = 100\%$ switching event is observed, as explained in Figs 4.8 and 4.9 (the two figures will be analyzed in more details in the following Discussion section). In Fig. 4.10, the Δt_p needed to switch the magnetization in the system, with a certain probability P , is reported as a function of the applied $\mu_0 H_x$. While, in Figs 4.11(a) and 4.11(b) the switching probability is reported as a function of $\mu_0 H_x$ (for certain values of Δt_p) and as a function of Δt_p (for certain values of $\mu_0 H_x$), respectively (the two graphs will be analyzed in more details in the following Discussion section). These measurements were done on a second device, made of the same material stack and with the same thicknesses reported above. This second nominally identical device was used since the previous device was damaged during the experiment.

In Fig. 4.10 the minimum Δt_p needed for a 10%, 30% and 50% (actually 49% for the zero field case, since the 50% is the asymptotic limit in that case) probability of switching is reported. According to the graph, Δt_p seems to be an exponential function of the external magnetic field \mathbf{H}_x , for all the three different switching probabilities here reported (blue dots, green diamonds and red stars refer to a 10%, 30% and 49% switching probability, respectively). The smaller is the applied in-plane field, the longer is the current pulse needed for switching. For $\mu_0 H_x = 0$ mT we observe a 10%, 30% and $\geq 49\%$ magnetization switching starting from a pulse length of 17 ns, 18 ns and 23 ns, respectively.

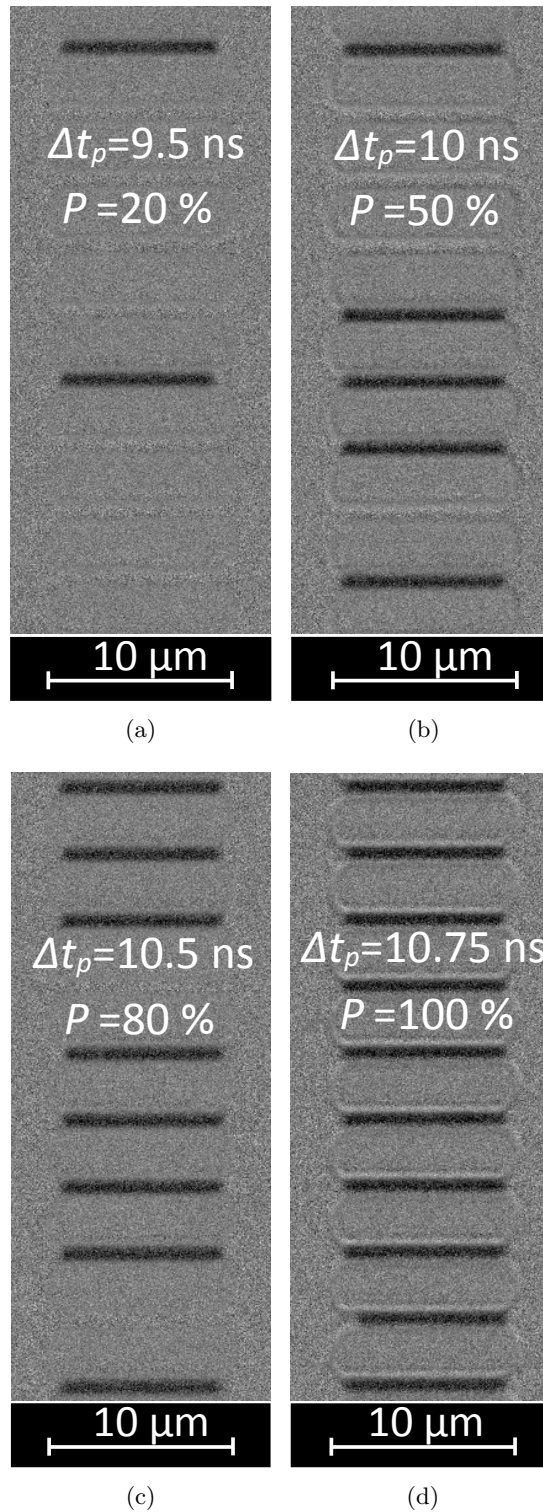


FIGURE 4.8: **Magnetization switching probability at constant in-plane field.** Illustration of single switching events at a fixed applied in-plane field of $\mu_0 H_x = 7.5$ mT. (a) Switching with $\Delta t_p = 9.5$ ns, resulting in a probability of $P = 20\%$. (b) Switching with $\Delta t_p = 10$ ns, resulting in a probability of $P = 50\%$. (c) Switching with $\Delta t_p = 10.5$ ns, resulting in a probability of $P = 80\%$. (d) Switching with $\Delta t_p = 10.75$ ns, resulting in a probability of $P = 100\%$. The probability is defined as the ration between the switched area and the total switchable area (NWs) times 100. The pulse current density is $j_a = 7 * 10^{11}$ A/m².

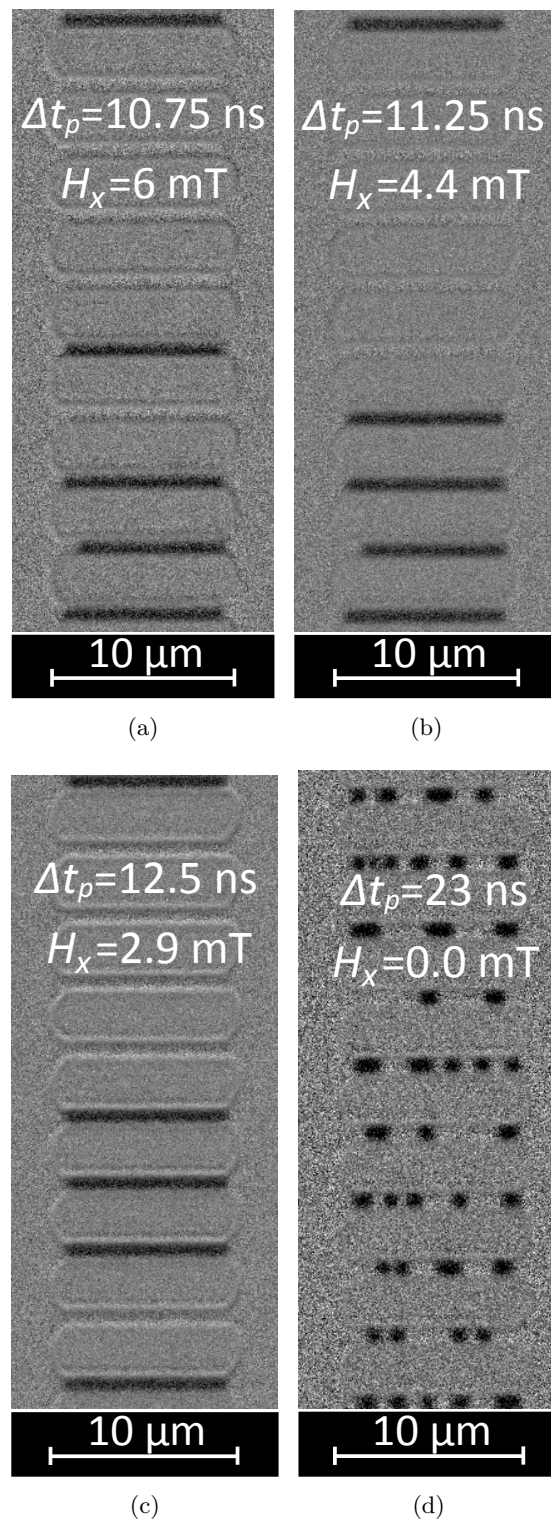


FIGURE 4.9: **Magnetization switching with a 50% probability.** Illustration of single switching events with a switching probability of 50%. (a) Switching with $\Delta t_p = 10.75$ ns and $\mu_0 H_x = 6$ mT. (b) Switching with $\Delta t_p = 11.25$ ns and $\mu_0 H_x = 4.4$ mT. (c) Switching with $\Delta t_p = 12.5$ ns and $\mu_0 H_x = 2.9$ mT. (d) Switching with $\Delta t_p = 23$ ns and $\mu_0 H_x = 0$ mT. The probability is defined as the ratio between the switched area and the total switchable area (NWs) times 100. The pulse current density is $j_a = 7 \cdot 10^{11}$ A/m².

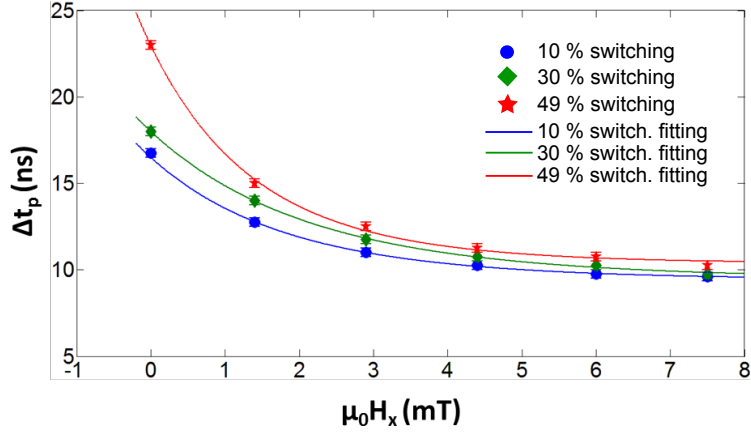
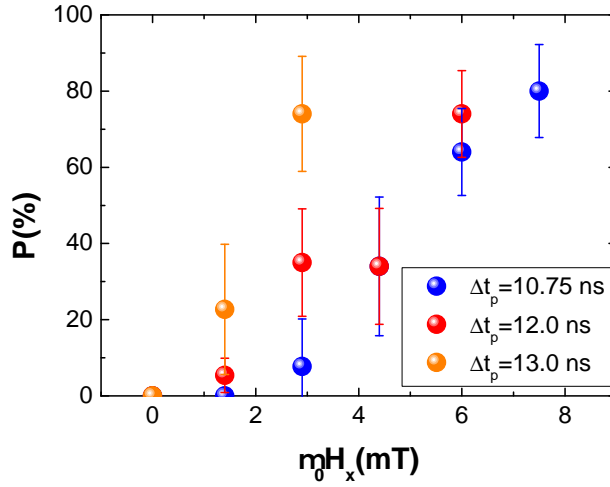


FIGURE 4.10: **Thermal effects in current-induced magnetization switching.** Minimum length of the current pulse Δt_p needed to switch the magnetization in the NWs of the sample with a probability of at least 10% (blue dots), 30% (green diamonds) and 49% (red stars), as a function of the longitudinal magnetic field $\mu_0 H_x$. The pulse current density is $j_a = 7 \cdot 10^{11}$ A/m². The error bar corresponds to 0.25 ns, which is the difference between two consecutive pulse lengths used during the measurements. The solid lines are the corresponding fitting curves, based on the generalized Néel-Brown model for thermal-assisted current-induced magnetization switching. Data from [125].

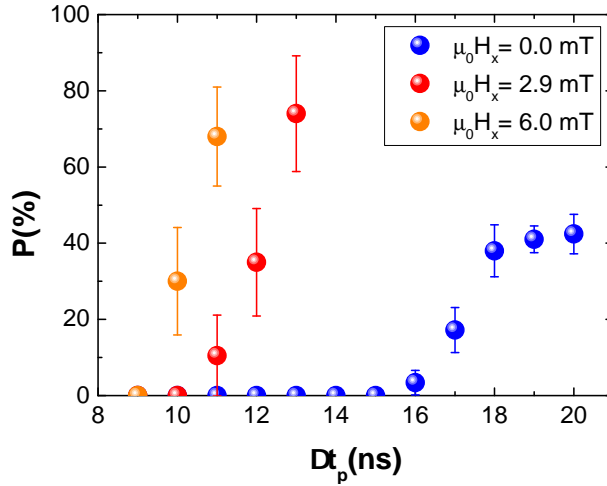
4.5.1 Discussion

The origin of the observations reported above can be attributed to thermal fluctuations of the magnetization in the device. For large enough current density amplitudes, the thermal fluctuations of the magnetization, \mathbf{M} , due to Joule heating generate an in-plane component, \mathbf{M}_x , which is comparable to that generated by a finite external magnetic field. When a large enough \mathbf{M}_x is eventually thermally generated in the appropriate direction, the spin-orbit effective field acts on it, yielding local magnetization switching events in different parts of the nanowire. This would explain the observed switching at zero-field. Furthermore, during the injection of long pulses there is much more time for the thermally induced switching to occur than in the case of short pulses, increasing the switching probability and thus reducing the necessary in-plane current. This explains why, even for large pulse amplitudes, there is no observation of the saturation effect for short pulses in Fig. 4.6.

To obtain the key parameters of the thermally activated switching, we fit our experimental data reported in Fig. 4.10 with a *generalized Néel-Brown model* [65]. As explained in the Theory chapter, this model describes the role of the thermal fluctuations in magnetization switching processes, in the presence of a spin-transfer torque. It relies on the introduction of an effective temperature (or an effective energy barrier) based on a



(a)



(b)

FIGURE 4.11: **Switching probability.** (a) The average switching probability P as a function of the applied field $\mu_0 H_x$, for three different values of the pulse length. (b) The average switching probability P as a function of the pulse length Δt_p , for three different values of the applied magnetic field. The pulse current density is $j_a = 7 * 10^{11}$ A/m².

stationary solution of the Fokker-Planck equation [65]. In our experiment we have a similar situation, with an electric current flowing in the system and a spin-current entering the magnetic layer due to the SHE. The equation that describes our experiment is the following [65]:

$$\Delta t_p = -\ln(1 - P) f_0^{-1} * \exp^{\frac{E_0^*}{k_B T} (1 - \frac{H_z}{H_{sw}^0})^{1.5}}, \quad (4.2)$$

where P is the switching probability, f_0 is the attempt frequency, $E_0^* = E_0(1 - \alpha I)$ is the zero-field effective energy barrier at the given current (I is the current flowing in the system, α is a coefficient), $\mu_0 H_{sw}^0$ is the switching field at 0 K, and $\mu_0 H_z$ is the effective field along the easy axis. In this case, assuming to have no contribution to the current-induced effective field originating from the ISGE [82, 83], 100% spin transparency and no spin-memory loss at the HM\FM interface, the field along the z -direction is the effective SHE-field, $H_z = \frac{\hbar\theta_{SHE}|j_e|}{2\mu_0|e|M_{stFM}} m_x \approx \frac{\hbar\theta_{SHE}|j_e|}{2\mu_0|e|M_{stFM}} \frac{H_x}{H_x^{sat}}$, where H_x^{sat} is the longitudinal field needed for aligning all the magnetization in the x -direction (≈ 400 mT in our system). As can be seen in Fig. 4.10, the model (solid lines) fits the data for a value of the effective energy barrier $E_0^* \approx 90$ meV. The extracted average attempt frequency is $f_0 \approx 1.4$ GHz.

The value reported above for E_0^* is a lower boundary of the actual energy barrier E_0 . This is because the electric current flowing in the multilayer lowers the effective energy barrier separating the two magnetization stable states, due mainly to the increase in temperature generated in the system. In Appendix A, the measurement of the sample resistance as a function of the temperature and of the current density, during current injection [133], is discussed. From this measurement, the actual temperature in the nanowires during the injection of 1 ms-long pulses is found to be $T \approx 1070 \pm 80$ K at a current density of $7 * 10^{11}$ A/m². This value is close to the expected Curie temperature of our magnetic material, that is $T_C \approx 1030$ K (for annealed $Co_{20}Fe_{60}B_{20}$) as reported by M. Yamanouchi et al. [134]. However, for the experiment reported in Fig. 4.10 the actual length of the injected pulse is in the order of a few tens of ns. Accordingly, the temperature in the NWs during the experiment is much lower than that, allowing us to interpret the experiment in the condition $T \ll T_C$.

The fitting curves in Fig. 4.10 have an off-set of 10 ns which can be explained as the sum of two potential contributions. One contribution is due to the actual shape of the pulses we were able to apply with the set-up at our disposal at the time the experiment was carried out. For this specific experiment, we have a rise- and a fall-time of about 2 ns each. Accordingly, the current density is actually at its maximum value for at least 4 ns less than the nominal duration of the pulse. Secondly, we assume an 100% switching in each NW when the magnetization is reversed throughout its length. For a switching mechanism based on domain nucleation followed by domain wall motion [135], part of the minimum time obtained from the fitting curve could also be due to the fact that the nucleated domain walls need some time to move and reach the end of the nanowires (this

can be seen in Fig. 4.5). The calculated domain wall speed is in the order of 100 m/s, which is in line with the velocities measured for similar materials stacks [9, 25, 44, 67] as well as for the very same one [128] (see also next chapter).

Figure 4.11 shows that the probability of switching increases with both increasing H_x (4.11(a)) and increasing Δt_p (4.11(b)). This is again in support of the interpretation of the experimental data based on a thermal-assisted SHE-field-driven magnetization reversal. An increasing H_x corresponds to a stronger SHE-field, which makes the switching probability higher. While, a longer Δt_p increases the chance of having a switching event due to two main reasons: first, the system has a longer time to switch; second, the Joule heating produced in the system increases, giving place to stronger thermal excitations and so an higher probability of switching.

In Fig. 4.11(b) it is possible to observe that in case of a finite in-plane field (red and orange dots), the probability P always increases with increasing Δt_p (eventually reaching 100%). However, for the zero-field case (blue dots) the switching probability does saturate for long pulses to the value $P = 50\%$. This is also visible in Fig. 4.9(d), where the total switched area is almost the 50% of the total one, but not more than that. The switching event in the zero-field case consists of many small reversed areas in each NW of the device, confirming that the switching is a local event assisted by the Joule heating. Due to the absence of a longitudinal magnetic field which would break the in-plane symmetry of the system, the switching is not deterministic. As a consequence, after that the switching in the pre-saturated NWs has occurred, the reversed areas can eventually switch back to their initial magnetic state (during the pulsing time). This results in a lower value for the measured switching probability. However, in the present analysis the back switching event is not considered. Moreover, in the absence of an external magnetic field, after the local domains are nucleated they do not expand. This is due to the fact that both types of domain wall ($\uparrow\downarrow$ and $\downarrow\uparrow$) are moved in the same direction (see next chapter), resulting in a net zero expansion of the nucleated domains. As a result, the switching process moves from a *fully switched NWs* case, in the presence of H_x (see Figs 4.9(a), 4.9(b), 4.9(c)), to a *locally switched NWs* case, in the absence of H_x (see Fig. 4.9(d)).

These observations give the possibility to understand the real mechanism at the basis of the magnetization reversal. After local nucleations randomly occurring in the NWs, the nucleated domains expand due to fast motion of the two types of domain walls in

opposite directions (see next chapter), as also explained by Garello et al. [135]. This means that, after that several domains are nucleated, they merge by DWs annihilation, resulting in fully switched NWs as shown in Figs 4.9(a), 4.9(b), 4.9(c). However, this is not the case when no field is present, due to the fact that the domains do not expand and the back switching probability is not zero. Accordingly, a saturation of P around 50% for long pulses at zero-field is expected, as observed here.

4.6 Conclusion and outlook

Current-induced magnetization switching in magnetic NWs made of Ta\CoFeB\MgO was reported. The switching effect was observed for 100 ns- and 100 ms-long current pulses, and current densities values of the order of 10^{11} A/m². The symmetry of the switching process was found to be consistent with the model of the SHE effective field, suggesting that the main driving force in the observed effect was indeed the SHE-spin current injected in the ferromagnet through the HM\FM interface, with a negative SHA. Furthermore, the process was also found to be dependent on the length of the pulse, mainly due to thermal effects. The experimental data could be reproduced by employing a generalized Néel-Brown model for thermally-assisted current-induced magnetization switching, enabling the extraction of the attempt frequency and the effective energy barrier for the specific switching process taking place locally in the system.

The observed SOT-induced switching process is a good candidate for the design of actual spintronic devices. The most promising application of switching by SOTs is a three-terminal magnetic tunnel junction, where only the reading current would go through the MgO-tunnel barrier, while the writing current pulse would flow in the bottom Ta\CoFeB bilayer [68, 101]. This would ensure a more durable and efficient device. However, the thermally activated switching is not unidirectional. In the absence of the magnetic field, the spin-orbit torque, assisted by the thermal fluctuations, would destabilize the magnetization configuration every time a current pulse is injected in the system. This means that, it is possible to obtain switching in both directions using the same current pulse polarity. For applications, this would require a reading step after each writing step, in order to verify the switching event. For the sake of completeness, it has to be added that there have been new suggestions on how to obtain a unidirectional SOT-driven switching at zero field [33, 34]. They are based on an engineered magnetic anisotropy,

which breaks the symmetry of the system in the plane of the sample and fixes the torque direction in the absence of any external magnetic field.

Chapter 5

Spin–orbit torque–induced domain wall motion in Ta\CoFeB\MgO

5.1 Introduction

As discussed in the previous chapter, by the current–induced magnetization switching experiment it is possible to gain information about the symmetry of the torques acting in the Ta\CoFeB\MgO nanostructures. However, in order to understand more about the origin of the torques it is necessary to investigate the motion of domain walls (DWs) when an electric current flows perpendicular to them. Looking at the displacement of DWs generated by current injection, it is possible to extract not only the symmetry, but also the strength of the acting torque.

This chapter reports current–induced DW motion in Ta\Co₂₀Fe₆₀B₂₀\MgO nanowires. The observed DW motion is not explicable by the standard spin–transfer torque–model [6–8, 43, 51, 52]. The interpretation offered here relies on the action of spin–orbit torques [25, 35, 45]. In the framework of the spin–orbit torque model, the measurement of the current–induced DW motion gives the possibility to extract the sign and the strength of the spin–Hall effect [74–76, 87] and of the Dzyaloshinskii–Moriya interaction [21, 136] present in the material system. Most of what is discussed in this chapter is contained in a manuscript published in the journal *Physical Review B* in 2015 [128].

5.2 Experimental set-up

The main results presented and discussed in this chapter were obtained with a sample made of the same material stack used for the switching experiment reported in Chapter 4 (see Tab. 4.1 for magnetic parameters values). Accordingly, the sample consists of NWs made of the materials stack: Ta(5.0)/Co₂₀Fe₆₀B₂₀(1.0)/MgO(2.0)/Ta(5.0) (all thicknesses in nm). As reported in Chapter 4, the entire material stack was deposited on a thermally oxidized Si/SiO₂-wafer by sputtering (using a Singulus TIMARIS/ROTARIS tool), and then annealed at 300 °C for 2 hours in vacuum so that a large PMA was obtained. From growth studies carried out at *Singulus Nanotechnologies AG* it is known that the Ta bottom layer grows largely in the β -phase (tetragonal unit cell for single-crystal [127]), for the specific deposition conditions and thicknesses. This is confirmed by its high measured resistivity (180 $\mu\Omega\text{cm}$, while typical resistivity values for the bcc-phase are around 25–50 $\mu\Omega\text{cm}$ [127]), which is a hallmark of this specific crystallographic phase [68, 127]. For a measured in-plane magnetization saturation field $\mu_0 H_k = 400$ mT and a saturation magnetization $M_s = (1.1 \pm 0.1) * 10^6$ A/m (measured by SQUID [110]), we obtain an effective anisotropy $K_{eff} = \mu_0 H_k M_s / 2 = 2.2 * 10^5$ J/m³. More details about the material stack can be found in the dedicated section in Chapter 4.

By e-beam lithography and Ar-ion milling the sample was patterned into an array of 20 nanowires in a parallel geometry (see Fig. 5.1). The dimensions of each wire is 1 $\mu\text{m} \times 8 \mu\text{m}$. At the ends of the wires there are magnetic pads, directly connected to two gold contact pads made in a second patterning step by lift-off technique. One of the two gold pads consists of an Oersted-line (3 μm wide, 150 nm thick), used for the nucleation of reversed magnetic domains in pre-saturated wires, by the injection of 20 ns-long current pulses ($j_a \approx 10^{12}$ A/m²).

As shown in Fig. 5.1, a pulse generator is used for injecting current through either the Oersted-line or the magnetic wires. An oscilloscope is used for measuring the pulse waveform, across its 50 Ω -internal resistance (R_o). The total current flowing through the system is obtained by the measured voltage V_o across R_o . Taking into account the oxidation of the top 2 nm of the Ta capping layer (see the section on the materials stack's description at the beginning of Chapter 4), a current density of $1.1 * 10^{11}$ A/m² is estimated to flow through the nanowires when 1 V drops across R_o (corresponding to a total current of 20 mA). The conventional current density \mathbf{j}_a is assumed to be positive

when it flows in the $+x$ -direction (see Fig. 5.1), corresponding to an electron current density \mathbf{j}_e flowing in the $-x$ -direction.

The magnetization configuration of the wires is imaged by polar Kerr microscopy in differential mode, and the analysis of the images is carried out following the protocol described in Chapter 3. A magnetic coil is used for the generation of an external in-plane

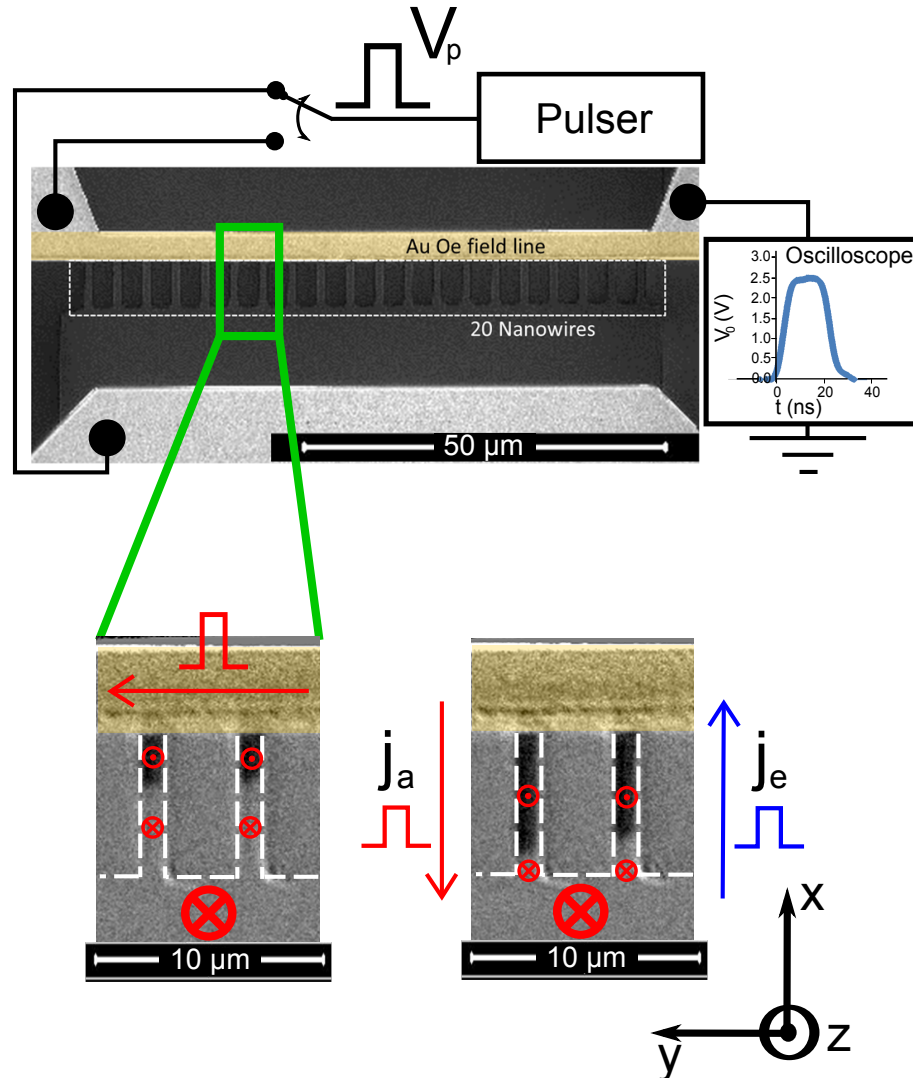


FIGURE 5.1: **Experimental set-up for CIDWM.** At the top, it is shown the experimental set-up for current pulse injection, including an SEM micrograph of the sample used during the experiment. The inset shows the shape of one of the pulses applied to the device, measured with the oscilloscope (across the $50\ \Omega$ -internal resistance). At the bottom-left, a differential Kerr microscopy image of nucleated magnetic domains by Oersted-field in initialized nanowires. The magnetization in the reversed domains is pointing “up” ($+z$, black areas). At the bottom-right, a differential Kerr microscopy image of the same wires on the left, after domain walls motion obtained by injecting a burst of 50 current pulses ($\Delta t = 25\ \text{ns}$, $j_a = -2.75 \times 10^{11}\ \text{A/m}^2$, $j_a > 0$ in the $+x$ -direction) through the nanowires. The flowing direction of the conventional current density, \mathbf{j}_a , and of the electron current density, \mathbf{j}_e , is indicated by the red and blue arrow, respectively. The red symbols represent the magnetization state in the magnetic device. Data from [128].

magnetic field. The experiments are carried out at $T=300$ K. First, the magnetic wires are saturated in the “up” ($+z$) or “down” ($-z$) magnetization state by an out-of-plane magnetic field. Second, reversed domains are nucleated in the NWs, in order to have DWs useful for the current-induced DW motion (CIDWM) experiment. The nucleation is obtained by the Oersted-line when only one type of DW is required for the experiment, either “up-down” ($\uparrow\downarrow$) or “down-up” ($\downarrow\uparrow$) DWs. While, when both types of DWs are required to be present in the NWs at the same time, a current pulse is injected through the wires, which generates current-induced magnetization switching locally in the NWs [125] (see also Chapter 4). As a consequence of that, both types of DWs are generated in the nanostructures at the same time. At the bottom-right and bottom-left of Fig. 5.1, controlled domain nucleation by a single current pulse through the Oersted-line and DW displacement by the injection of a burst of negative current pulses ($j_a < 0$) in the wires are shown, respectively. Most of the measurements reported here were carried out in collaboration with Dr. A. Hrabec.

5.3 Current-induced domain wall motion

5.3.1 Moving domain walls with current

Figure 5.2 reports the average velocity of the DW as a function of the current density \mathbf{j}_a flowing through the magnetic wires. For each current density the measurement is repeated three times, yielding a total of 30 DW displacements (10 nanowires are imaged at a time). This made it possible to obtain sufficient statistics for the extraction of average velocities with respectively small error bars. Bursts of several (n) current pulses with a time duration $\Delta t_p=10, 15, 20$ and 25 ns are used for the current-induced domain wall motion (see Fig. 5.2(a)). The time between two consecutive pulses is $100 \mu\text{s}$ and the number of pulses in a burst ranges from $n=20$ to $n=400$.

The velocity of the DW is calculated as the ratio between the average displacement of the domain wall due to the injected pulses and the total pulsing time, $t_{tot} = n * \Delta t_p$. In Fig. 5.2(a) the average velocity of the DW, v_{DW} , is reported as a function of the current density, j_a , for 4 different lengths of the pulse. Different v_{DW} for different Δt_p are obtained. This is due to the particular shape of the current pulses used during the experiment, as it will be explained more in detail in the following “Discussion” section.

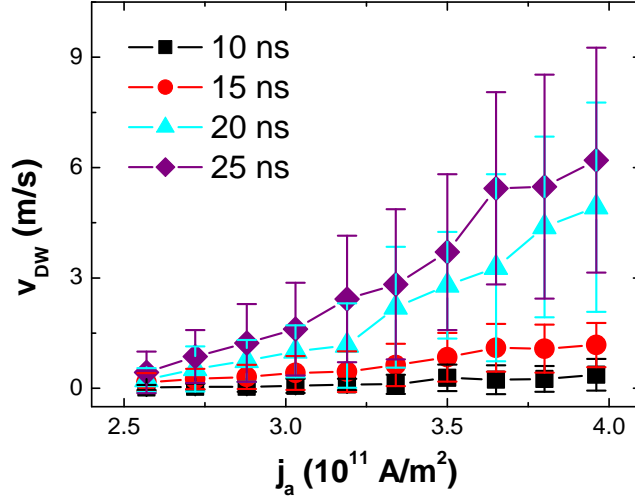
While, in Fig. 5.2(b) the resulting average DW velocity free of the influence of the pulse shape is reported. One of the key pieces of information in Fig. 5.2 is the direction of the DW velocity: the DWs move against the electron flow (e-flow). Furthermore, the DWs start moving with $j_a \approx 2.5 * 10^{11}$ A/m², at increasing speed with an increasing current density.

5.3.2 Discussion

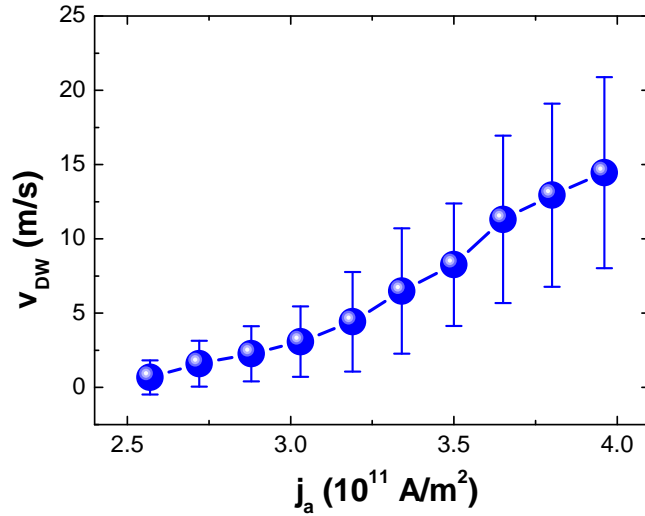
First of all, we explain the different velocities of the DW reported in Fig. 5.2(a) when different lengths of the current pulse are employed. The actual current pulses injected with the experimental set-up employed during the experiment are affected by a rise- and fall-time of 5 ns. Accordingly, for about 10 ns of the total (nominal) pulse length, Δt_p , the current amplitude is actually not at its maximum value. Indeed, as shown in Fig. 5.2(a), higher velocities are measured for longer pulse lengths at a fixed current density. This is because the rise/fall-time takes up a smaller proportion of the overall pulse length in the case of longer pulses, enabling the torque acting on the DW to be maximum for a larger fraction of Δt_p . This is something to take always into account when comparing results for different Δt_p .

Carrying out measurements with different pulse lengths it is possible to rule out the effect of the rise- and fall-time. In Fig. 5.3(a), the average DW's displacement due to a single pulse, $\langle \Delta x \rangle$, for a fixed j_a is reported as a function of Δt_p . As it can be seen in the graph, the DW displacement is almost null for the shortest pulse, with $\Delta t_p = 10$ ns. This is not surprising, since such a pulse length is identical to the sum of the rise- and fall-time, making it impossible for the current to reach its full amplitude. On the other hand, for longer pulses $\langle \Delta x \rangle$ starts to increase linearly with increasing pulse length. By linear fitting the experimental data point for the three largest Δt_p (solid line in Fig. 5.3(b)), it is possible to extract the DW velocity free of the influence of the pulse shape. The result of this process, done for all the used current density's amplitudes, is what is shown in Fig. 5.2(b).

The observed CIDWM reported above cannot be explained solely by the conventional STT [6, 43], since it would result in a DW motion with the e-flow. Theoretically, it is actually possible to obtain a STT-driven DW motion against the e-flow, but this would require a negative non-adiabaticity parameter for the magnetic system [137]. However, there is no experimental evidence that this is the case for CoFeB. Furthermore, as it will



(a)



(b)

FIGURE 5.2: **CIDWM in Ta(5.0)\Co₂₀Fe₆₀B₂₀(1.0)\MgO(2.0) NWs.** (a) Average velocity of the DW, v_{DW} , as a function of the current density, j_a , injected in the magnetic wires, for different durations of the current pulse, Δt_p . The DW velocity increases with the pulse duration, due to the fact that the 5 ns rise- and fall-time of the injected pulses have less influence on the measured domain wall velocity during longer pulses. The DW moves with the conventional current j_a (against the electron flow j_e). The average velocities and the error bars (standard deviations) are calculated from 30 different DW motions, at each current density. (b) Average velocity of the DW as a function of j_a , corrected for the rise- and fall-time influence. Data from [128].

be discussed later in the chapter, other experimental observations support even stronger the idea that STT is not the leading mechanism in the observed CIDWM. Accordingly, a new interpretation is needed to explain the reported observations.

A possible alternative interpretation is based on the SOT-model [25, 35, 45]. The same approach was used in the interpretation of the observations obtained for Pt\CoFe\MgO and Ta\CoFe\MgO systems [25], where the authors claimed that the DW motion was due to the SHE-effective field $\mathbf{H}_{\text{SHE}} = \frac{\hbar\theta_{\text{SHE}}|j_e|}{2\mu_0|e|M_s t_{\text{FM}}} \hat{\mathbf{m}} \times (\hat{\mathbf{z}} \times \hat{\mathbf{j}}_e)$, where θ_{SHE} is the spin-Hall angle (SHA), j_e is the electron current density, M_s is the saturation magnetization of the ferromagnetic material and t_{FM} is the thickness of the ferromagnetic layer. However, in the experiment here reported the DW motion is in the opposite direction to that observed in Ta\CoFe\MgO.

The main difference between the material system in [25] and the one here discussed is the presence of Boron (B) in the ferromagnetic layer. This suggests an interpretation of the present observations based on the effect of the B contained in the material stack. In order to support such interpretation, a structural and chemical analysis of the material stack has been carried out, as it will be discussed in Section 5.6.

5.4 Chiral domain walls in motion

5.4.1 Effect of an external magnetic field on the domain wall motion

To understand the surprising observed CIDWM against the electron flow, a deeper investigation of the phenomenon is needed. Accordingly, the effect of magnetic fields on the current-driven DW motion is studied. More precisely, the DW velocity is measured as a function of an applied magnetic field along the wire axis (x -direction) for fixed current densities.

First of all, both types of DW ($\uparrow\downarrow$ and $\downarrow\uparrow$) are nucleated in pre-saturated nanostructures by current-induced magnetization switching (left side of Fig. 5.4). Typical nucleation pulses used in the experiment have a current density's amplitude of $j_a \approx 10^{12}$ A/m² and a duration of $\Delta t_p = 20$ ns. Once the DWs are generated, they are displaced by the injection of a burst ($n=1-20$) of 20 ns-long current pulses with lower current densities ($j_a = 1.8 - 3.6 * 10^{11}$ A/m²) as shown in the right side of Fig. 5.4. In order to calculate the DW velocity, the full width at half maximum of the current pulse is used as the time

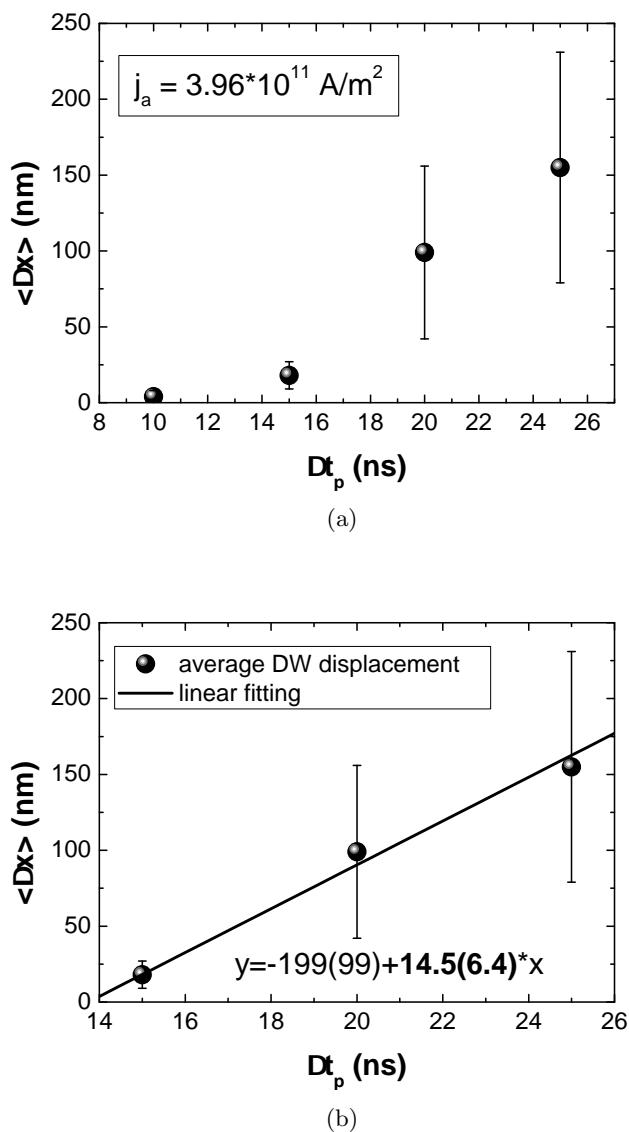


FIGURE 5.3: Extraction of the CIDWM velocity in Ta(5.0)\Co₂₀Fe₆₀B₂₀(1.0)\MgO(2.0) NWs. (a) Average displacement for single pulse, $\langle \Delta x \rangle$, as a function of the pulse length, Δt_p . (b) Linear fitting (solid line) of the three data points in (a) with largest $\langle \Delta x \rangle$. The slope of the fitting line (equation in the inset) is the average velocity of the DW, independent of the pulse's shape.

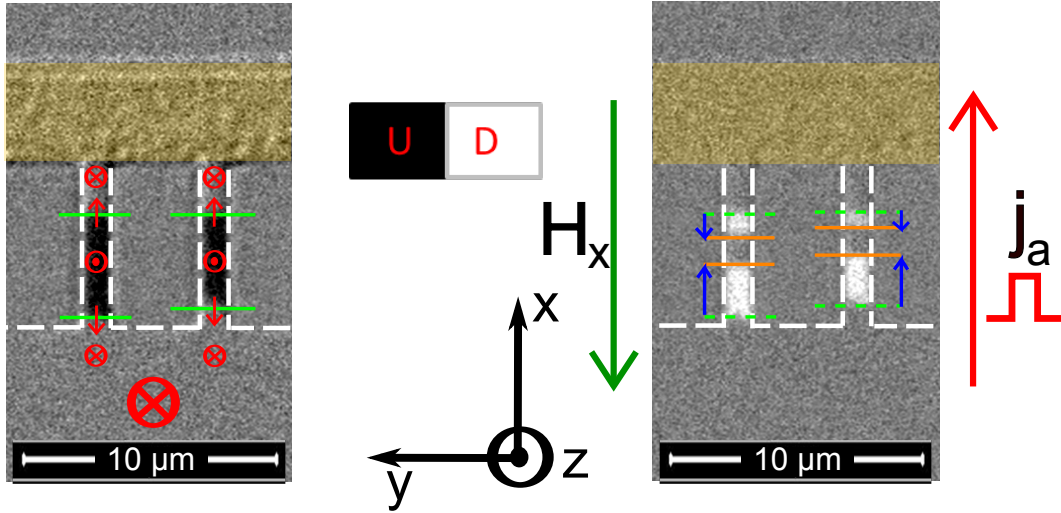
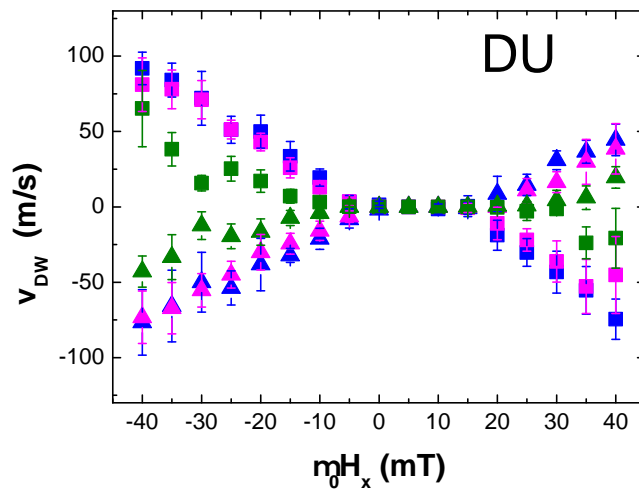
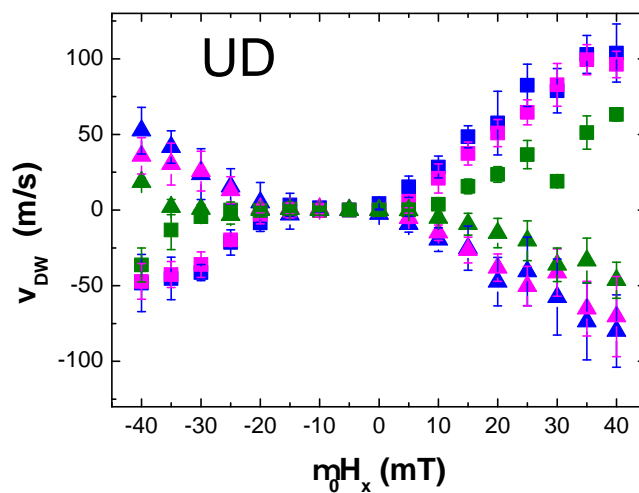


FIGURE 5.4: Nucleation and motion of chiral DWs in Ta(5.0)\Co₂₀Fe₆₀B₂₀(1.0)\MgO(2.0) NWs. On the left side, differential Kerr microscopy image of nucleated magnetic domains in pre-saturated nanowires. The magnetization in the reversed domains points in the $+z$ -direction (black areas). The green lines indicate the position of the DWs. The red arrows describe the Néel-component of the DWs' magnetization configuration. Observing the NWs' magnetization texture from small x values towards large x values, two $\downarrow\uparrow$ -DWs are followed by two $\uparrow\downarrow$ -DWs. On the right side, differential Kerr microscopy image of the domain walls motion due to current pulse injection ($j_a = +3.6 \times 10^{11} \text{ A/m}^2$), when a longitudinal field is applied ($\mu_0 H_x = -35 \text{ mT}$). The dashed green lines indicate the starting position of the DWs, while the solid orange lines indicate their final position. The blue arrows show the DW motion. DU ($\downarrow\uparrow$) DWs move fast and with the conventional current-flow, while UD ($\uparrow\downarrow$) DWs move slower and with the electron-flow. Data from [128].

duration of a single pulse. For each current density-field amplitude combination the measurement is repeated five times. The DW velocity as a function of the longitudinal field, $\mu_0 \mathbf{H}_x$, is shown in Fig. 5.5(a) and 5.5(b) (symbols) for the $\downarrow\uparrow$ - and $\uparrow\downarrow$ -DWs, respectively. It is clear from the graphs that the DW's velocity is strongly influenced by the presence of the longitudinal field. While at zero-field the velocity of both types of DWs is the same, in the presence of the field the two DWs move at different velocities. The change in the field amplitude affects differently the velocity of the two types of DW, making it possible to obtain $\uparrow\downarrow$ - and $\downarrow\uparrow$ -DWs moving in opposite directions, when the field's amplitude is large enough. A symmetric behavior is observed for the velocity of the two DW types with respect to \mathbf{H}_x , as shown in Fig. 5.6 (red symbols for the $\uparrow\downarrow$ -DW, blue symbols for the $\downarrow\uparrow$ -DW).



(a)



(b)

FIGURE 5.5: **Chiral DWs' velocity in Ta(5.0)\Co₂₀Fe₆₀B₂₀(1.0)\MgO(2.0) NWs.** (a) Average velocity of $\downarrow\uparrow$ -DW as a function of the longitudinal field, $\mu_0\mathbf{H}_x$, for three different current densities. *Blue* symbols refer to $j_a = 3.6 \times 10^{11}$ A/m², *magenta* to $j_a = 2.8 \times 10^{11}$ A/m² and *green* to $j_a = 1.8 \times 10^{11}$ A/m². Squares refer to $j_a > 0$, while triangles refer to $j_a < 0$. (b) As in (a), for $\uparrow\downarrow$ -DWs. Data from [128].

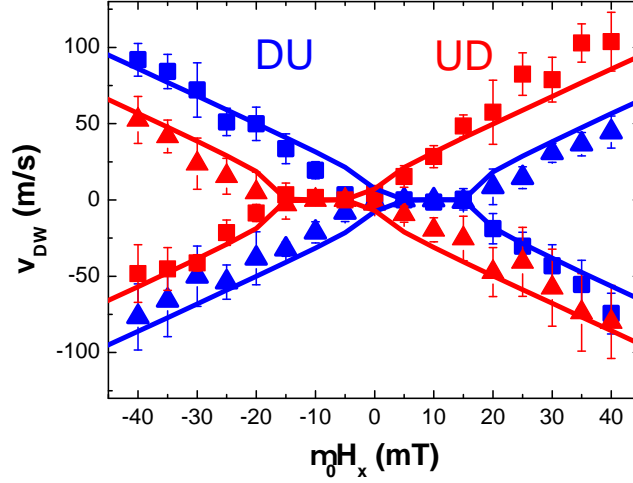


FIGURE 5.6: **Symmetry of chiral DWs' velocity in Ta(5.0)\Co₂₀Fe₆₀B₂₀(1.0)\MgO(2.0) NWs.** Average velocity of $\uparrow\downarrow$ (red symbols) and $\downarrow\uparrow$ (blue symbols) DWs as a function of $\mu_0\mathbf{H}_x$, for a current density of $j_a = +3.6 \times 10^{11}$ A/m² (squares), and $j_a = -3.6 \times 10^{11}$ A/m² (triangles). Lines represent the 1D-model fitting-curves (by E. Martinez, University of Salamanca). Data from [128].

5.4.2 Discussion

In order to understand the observations reported above, including the motion of DWs against the e-flow, the interplay of different mechanisms has to be considered. According to the standard STT-model [43] the DWs are expected to move always with the electron flow, since the spin-polarized conduction electrons tend to expand the magnetic domain where they “come from”. Unless the magnetic layer exhibits a negative spin polarization or a negative non-adiabaticity parameter [137], it is impossible for the STT to move domain walls against the drift motion of the conduction electrons. However, it seems that neither a negative spin-polarization nor a negative non-adiabaticity parameter has been reported experimentally, so far, for this material stack. Secondly, such a strong effect of a longitudinal magnetic field on a STT-driven DW motion is not expected. Furthermore, the STT cannot explain why for some specific longitudinal fields the DW stops moving or even changes its direction of motion. All this suggests that a different interpretation has to be found for the present experimental data.

Let us consider now the scenario where spin-orbit torques originating from the SHE are the main driving force of the DW dynamics [25, 35, 45]. In the SHE-SOT-model, the

magnetic DW can move with or against the e-flow. The direction of motion depends on the sign of the SHE and on the domain wall's internal spin-structure. Assuming to have a predominant contribution to the total SOT from the SHE in the Ta bottom layer, the driving force for the DW motion is the pure spin-current induced by the SHE during the pulse injection. Furthermore, as discussed already in the Theory chapter (Chapter 2), one more ingredient has to be taken into account here: the Dzyaloshinskii-Moriya interaction (DMI) [21, 24, 136]. In the presence of a non-zero DMI, the DMI at the interface between the heavy metal and the ferromagnetic layer is responsible for the initial magnetic configuration and in particular the chirality of the DW [20, 45], which is one of the two key factors governing the DW motion. As a consequence, the direction of motion of the DW depends on both the sign of the SHA and the sign of the DMI, where the latter fixes the chirality (left- or right-handed) of the Néel-component of the DW's magnetization.

The SHE of β -Ta is known to have a negative sign, as reported in the literature by other groups for different materials stacks [25, 27, 68] as well as in the previous chapter of this thesis and in [125]. While, an extensive study of DMI in [heavy metal]\CoFeB\MgO systems is still missing, apart from a few reports contained in the literature [27], where a strong dependence of the measured DMI on the material and the thickness of the underlayer was found. Accordingly, an analysis of the present data within the SOT-model framework is reported in the following.

As previously reported in the Theory chapter, the interfacial DMI acts on the magnetic texture as a longitudinal effective field localized at the domain wall position [45]. This field is known as the DMI effective field and is defined (in the 1D model framework) as $\mu_0\mathbf{H}_{DMI} = \mathbf{D}/(M_s\lambda_{DW})$ [45, 138], where \mathbf{D} is the DMI vector (D its modulus, the DMI coefficient) and λ_{DW} is the DW's width. Theoretically [45, 139], it is predicted the existence of a particular value of the applied external longitudinal field at which the SOT is minimized (stopping field), resulting in a stationary DW. Such stopping field is of the same amplitude as and with opposite sign respect to \mathbf{H}_{DMI} , (assuming that there is no significant STT). However, Fig.s 5.5(a), 5.5(b) and 5.6 show that there is a range of in-plane longitudinal fields where the DW remains stationary (with zero or very small DW's velocity compared to the velocities measured for larger longitudinal fields). This zero-motion field's range is not expected in the simple SOT-model based on perfect nanostructures, where the pinning of the DW due to the edge roughness

and the imperfections of the crystal lattice is not considered. Accordingly, to properly analyze the experimental data a more accurate model is needed, where the pinning of the DW is taken into account [26, 139, 140].

5.5 Extraction of the Dzyaloshinskii–Moriya interaction in Ta\CoFeB\MgO

In order to extract the DMI coefficient from the observed CIDWM, the approach presented in the manuscript by K.-S. Ryu et al. [26] is followed. There is a particular magnetic field amplitude which is able to suppress the Néel-component of the DW due to the DMI. Such a field is the so-called stopping field, and it has the same amplitude and the opposite sign of the effective DMI-field localized at the DW position, as illustrated in Fig. 5.7. In the actual experiment, such a stopping field is contained in the pinning range, that is the range of longitudinal magnetic fields where there is no motion of the DW (as reported in Fig. 5.5). In order to extract the value of the stopping field, it is required to fit, for each DW type, the experimental data for the positive and the negative current density by two linear functions, as shown in Fig. 5.8. The fitting is done considering only the “high” velocity points (data points in the two graphs in Fig. 5.8, between the vertical dashed lines and the graphs vertical axis), since they are least influenced by the pinning effect and so very close to the ideal flow regime, which is the one assumed in the 1D-model where no pinning is present. The point where the two fitting curves are crossing each other indicates the stopping field. This is done for both $\uparrow\downarrow$ - and $\downarrow\uparrow$ -DWs, as shown in Figs 5.8(a) and 5.8(b), respectively.

For the $\uparrow\downarrow$ -DW the extracted stopping field is $\mu_0\mathbf{H}_x^{\uparrow\downarrow} = -8.5 \pm 1.8$ mT, which corresponds to a DMI effective field $\mu_0\mathbf{H}_{DMI}^{\uparrow\downarrow} = +8.5 \pm 1.8$ mT. On the other hand, for the $\downarrow\uparrow$ -DW the extracted value is $\mu_0\mathbf{H}_x^{\downarrow\uparrow} = +7.0 \pm 1.5$ mT, which corresponds to $\mu_0\mathbf{H}_{DMI}^{\downarrow\uparrow} = -7.0 \pm 1.5$ mT. The errors on the DMI-fields are obtained from the accuracy of the fitting curves, which are a function of the errors of the experimental data used for the fitting procedure. Finally, the value of the DMI effective field is calculated as the average of the two extracted values (in absolute value) for $\uparrow\downarrow$ - and $\downarrow\uparrow$ -DWs. This results in $\mu_0\mathbf{H}_{DMI} = +7.8 \pm 1.2$ mT, since by convention the DMI field refers to the case of the $\uparrow\downarrow$ -DW.

As reported before, the definition of the DMI field is [45, 138]: $\mu_0\mathbf{H}_{DMI} = \mathbf{D}/(M_s\lambda_{DW})$,

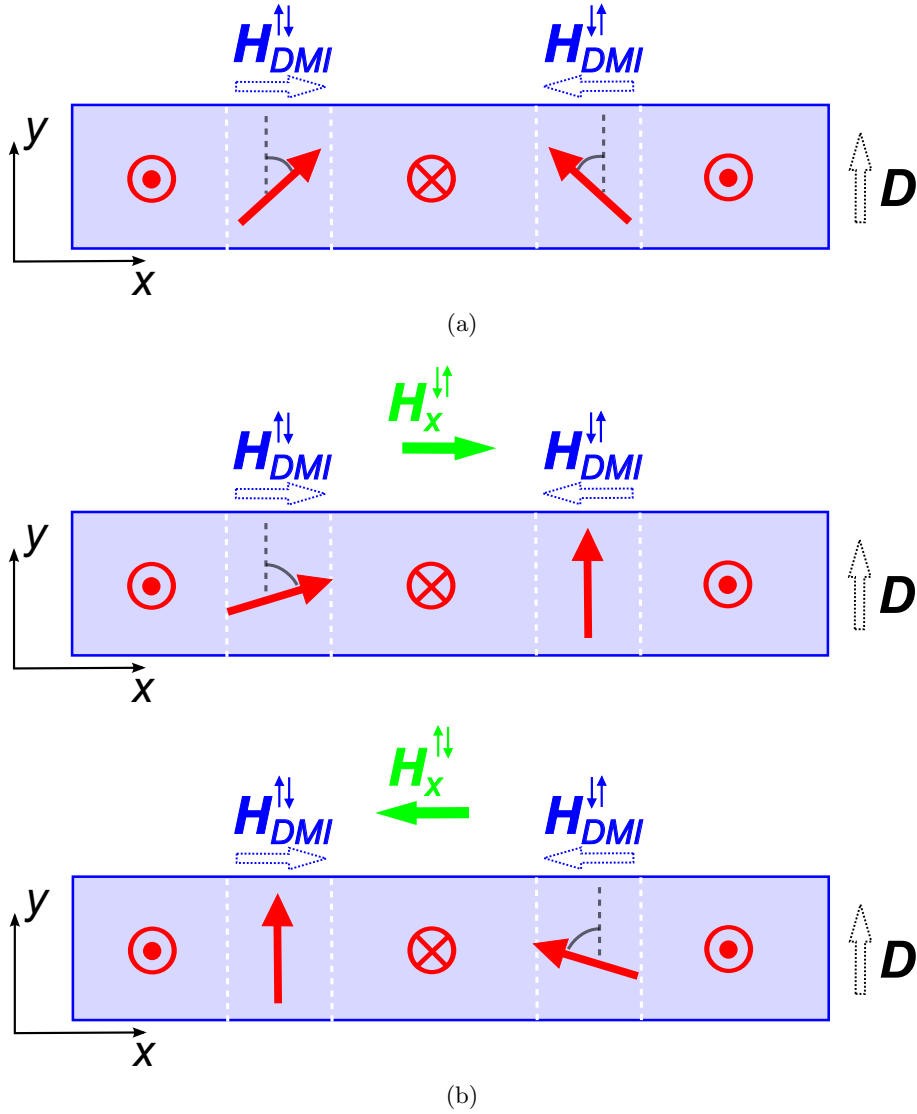
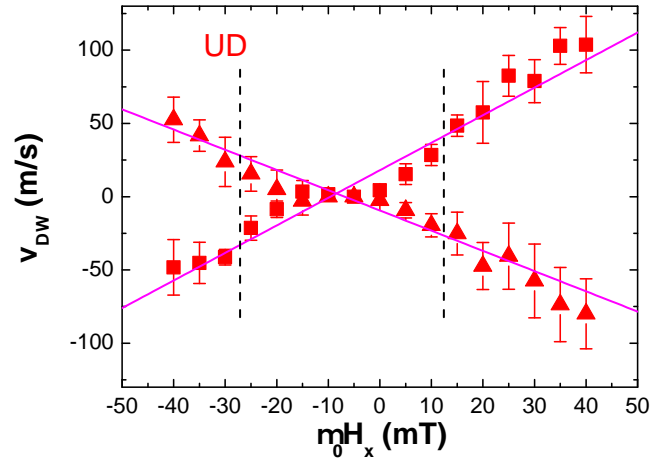


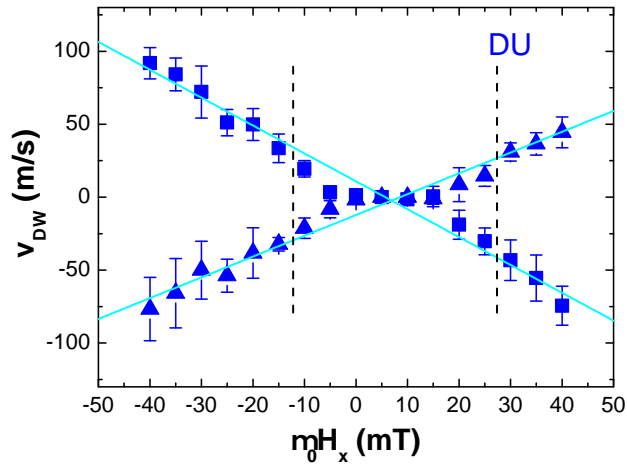
FIGURE 5.7: **Chiral domain walls.** (a) Chiral DWs stabilized by a positive DMI at the bottom interface. The blue arrows indicate the built-in DMI effective fields at the DWs' location. (b) Re-orientation of the DWs' magnetization by an external longitudinal field, H_x . At the top (bottom), the magnetic configuration during the application of the stopping field for the $\downarrow\uparrow$ ($\uparrow\downarrow$) DW is illustrated. The SOT acting on the DW in the Bloch-configuration is expected to be null.

where the DW's width is calculated to be $\lambda_{DW} = \sqrt{\frac{A}{K_{eff}}} = 7 \text{ nm}$ ($A = 10^{-11} \text{ J/m}$ from [138]), and the saturation magnetization is $M_s = 1.1 * 10^6 \text{ A/m}$ (values reported in Chapter 4). The resulting DMI coefficient for the investigated Ta\Co₂₀Fe₆₀B₂₀\MgO system is $D = +0.06 \pm 0.01 \text{ mJ/m}^2$. Such a value is close to the one measured for the Ta\CoFe interface [138], but of opposite sign. This indicates the presence of right-handed DWs in the present material stack (see Fig. 5.7(a)), while left-handed DWs were reported for Ta\CoFe\MgO nanowires [138].

Using the definition of DW's anisotropy energy density reported in [140], for the DWs



(a)



(b)

FIGURE 5.8: **Extraction of DMI effective field from CIDWM in Ta\CoFeB\MgO.** (a) The symbols are the experimental values of the DW's velocity as a function of the longitudinal field for $\uparrow\downarrow$ -DWs. Squares (triangles) refer to positive (negative) j_a . The solid lines are the fitting curves for the fast DW motion points (which are the data points between the dashed line and the graph's vertical axis, for both positive and negative fields). The crossing point between the fitting curves defines the stopping field. (b) The same as in (a), for $\downarrow\uparrow$ -DWs. The current density amplitude is $j_a = 3.6 \times 10^{11}$ A/m².

in the present system it is possible to calculate an effective shape anisotropy field of $H_{\perp} = N_x M_s = \frac{\ln(2)t_{FM}}{\pi\lambda_{DW}} M_s = 0.032 M_s = 3.52 * 10^4$ A/m, corresponding to an induction field of $\mu_0 H_{\perp} = 44$ mT. The corresponding anisotropy energy density is $K_{\perp} = \frac{1}{2} \mu_0 H_{\perp} M_s = 2.4 * 10^4$ J/m³, resulting in a critical DMI constant of $D_c = \frac{4\lambda_{DW} K_{\perp}}{\pi} = 0.21$ mJ/m² [45]. The critical DMI constant, D_c , is the DMI value above which the DW, in the investigated system, has its energy minimized when it assumes the Néel configuration. In this case, the calculated value of D_c is 3.5 times larger than the extracted DMI coefficient, resulting in $D < D_c$. Accordingly, the DMI-stabilized DWs in the studied system are expected to be in a hybrid configuration, with a small chiral Néel component, as shown in Fig. 5.9(a).

5.5.1 An alternative method for the extraction of the DMI

Here, an alternative method for the extraction of the DMI is proposed. The experimental data used for the following analysis are the ones presented in Fig. 5.5. The criterion at the basis of this alternative procedure for the extraction of the DMI is the following.

First, as discussed in the literature [25, 35, 128, 139], and according to the symmetry of the SHE-effective field reported above, the stopping field, $\mathbf{H}_x^{\uparrow\downarrow,\downarrow\uparrow}$, is the field at which the torque acting on the DW's magnetic moments is zero, and around which the torque changes sign. Assuming the STT being much smaller than the SHE-SOT [25, 35, 128, 139], $|\mathbf{H}_x^{\uparrow\downarrow,\downarrow\uparrow}| = |\mathbf{H}_{DMI}^{\uparrow\downarrow,\downarrow\uparrow}|$. Second, reducing ($H_x < H_x^{\uparrow\downarrow,\downarrow\uparrow}$) or increasing ($H_x > H_x^{\uparrow\downarrow,\downarrow\uparrow}$) the applied H_x with respect to $H_x^{\uparrow\downarrow,\downarrow\uparrow}$, the torque acting on the DW increases in magnitude, in both cases, due to the rotation of the DW's internal magnetization towards the Néel-configuration. The torque increases of the same amount and with opposite sign in the two cases, for the same change in magnitude of H_x ($H_x = H_x^{\uparrow\downarrow,\downarrow\uparrow} - \Delta H_x$ or $H_x = H_x^{\uparrow\downarrow,\downarrow\uparrow} + \Delta H_x$), for symmetry reasons [139]. The depinning of the DW occurs when a critical strength of the torque is reached, that corresponds to a specific ΔH_x^{dep} . According to the discussion above, the range of in-plane magnetic fields where the DWs are observed to be pinned (or moving at low velocities) is expected to be centered around the DMI effective field. The pinning range can thus be expressed as: $[H_{DMI}^{\uparrow\downarrow,\downarrow\uparrow} - \Delta H_x^{dep}, H_{DMI}^{\uparrow\downarrow,\downarrow\uparrow} + \Delta H_x^{dep}]$. Accordingly, the DMI effective field can be extracted as the center of the observed pinning regions in H_x . Finally the strength of the DMI can be obtained by the equation $D = \mu_0 H_{DMI} M_s \lambda_{DW}$ [45, 138].

The protocol used for the extraction of the two stopping fields, $\mathbf{H}_x^{\uparrow\downarrow}$ and $\mathbf{H}_x^{\downarrow\uparrow}$, is described in the following. This is done for each type of domain wall, for both positive and negative currents. First of all, it is taken note of the magnetic field values \mathbf{H}_1 and \mathbf{H}_2 at which the threshold condition $|v_{DW}| \geq \tilde{v}_{DW}$, is obtained. Here, \tilde{v}_{DW} is a chosen value of the velocity of the DW just outside the pinning region, which defines the border between low-velocity regime and high-velocity regime. For this specific experiment, $\tilde{v}_{DW} = 10$ m/s is chosen. The values of \mathbf{H}_1 and \mathbf{H}_2 are used as the extremes of the pinning range, and the corresponding stopping field, $\mathbf{H}_{stop}^{+,-}$, is calculated as the arithmetic mean of the two. Two stopping fields are calculated for each type of DW, corresponding to $j_a > 0$ (\mathbf{H}_{stop}^+) and $j_a < 0$ (\mathbf{H}_{stop}^-), and the average stopping field for each DW's type is obtained as $\mathbf{H}_x^{\downarrow\uparrow, \uparrow\downarrow} = \frac{\mathbf{H}_{stop}^+ + \mathbf{H}_{stop}^-}{2}$.

Let us consider the case of $j_a = 3.6 * 10^{11}$ A/m², reported in Fig. 5.5 (blue symbols) and Fig. 5.6. For $\uparrow\downarrow$ -DWs, it is obtained: $\mu_0 H_1 = 5 \pm 1$ mT (the error on the magnetic field comes from the accuracy of the measurement by the Gauss-meter) and $\mu_0 H_2 = -25 \pm 1$ mT, resulting in $\mu_0 H_{stop}^+ = -10 \pm 1$ mT for $j_a > 0$; $\mu_0 H_1 = 10 \pm 1$ mT and $\mu_0 H_2 = -25 \pm 1$ mT, resulting in $\mu_0 H_{stop}^- = -7.5 \pm 1.0$ mT for $j_a < 0$. As a result, the extracted stopping field for the $\uparrow\downarrow$ -DW is $\mu_0 H_x^{\uparrow\downarrow} = \frac{\mu_0 H_{stop}^+ + \mu_0 H_{stop}^-}{2} = -8.8 \pm 1.0$ mT. On the other hand, for the $\downarrow\uparrow$ -DW it is obtained: $\mu_0 H_1 = 20 \pm 1$ mT and $\mu_0 H_2 = -10 \pm 1$ mT, resulting in $\mu_0 H_{stop}^+ = 5 \pm 1$ mT for $j_a > 0$; $\mu_0 H_1 = 25 \pm 1$ mT and $\mu_0 H_2 = -10 \pm 1$ mT, resulting in $\mu_0 H_{stop}^- = 7.5 \pm 1.0$ mT for $j_a < 0$. As a result, the extracted stopping field for the $\downarrow\uparrow$ -DW is $\mu_0 H_x^{\downarrow\uparrow} = \frac{\mu_0 H_{stop}^+ + \mu_0 H_{stop}^-}{2} = 6.3 \pm 1.0$ mT. To these stopping fields correspond: $\mu_0 H_{DMI}^{\uparrow\downarrow} = 8.8 \pm 1.0$ mT and $\mu_0 H_{DMI}^{\downarrow\uparrow} = -6.3 \pm 1.0$ mT; resulting in an effective DMI field of $\mu_0 H_{DMI} = \frac{\mu_0 H_{DMI}^{\uparrow\downarrow} - \mu_0 H_{DMI}^{\downarrow\uparrow}}{2} = +7.6 \pm 1.0$ mT.

In order to extract the effective DMI coefficient, D , the values of the DW width, $\lambda_{DW} = 7$ nm, and of the saturation magnetization, $M_s = 1.1 * 10^6$ A/m, are used. Accordingly, the effective DMI results to be $D = \mu_0 H_{DMI} M_s \lambda_{DW} = +0.06 \pm 0.01$ mJ/m².

The extracted DMI value is equal to the one extracted in the previous section, by the linear fitting of the high velocity data points, according to Ryu et al. [26]. This result suggests the method here presented as an alternative method for the extraction of the effective DMI from CIDWM measurements.

Finally, the new procedure has been used for the extraction of the DMI from the data points corresponding to the other two current densities reported in Fig. 5.5 (magenta for $j_a = 2.8 * 10^{11}$ A/m², and green for $j_a = 1.8 * 10^{11}$ A/m²). The extracted DMI

strengths are in line (equal in the limits of the error) with the one obtained for the high current density, as reported in Tab. 5.1. No clear influence of the current density on the extracted DMI is observed, for the range of j_a employed in the measurement.

j_a ($10^{11} A/m^2$)	$\mu_0 H_{DMI}$ (mT)	D (mJ/m ²)
1.8	+9.4(1)	+0.07(0.01)
2.8	+6.9(1)	+0.05(0.01)
3.6	+7.6(1)	+0.06(0.01)

TABLE 5.1: **Extracted DMI values for Ta\CoFeB\MgO for different current densities.** Values of the effective DMI field, H_{DMI} , and of the effective DMI coefficient, D , for each of the three current densities employed for the investigation of the velocity of the DW, v_{DW} , as a function of the longitudinal magnetic field, H_x . In parentheses are the values of the error.

5.6 Chiral DWs in Ta\CoFeB\MgO moved by SOT

Interpreting the experimental observations in the framework of the SHE-SOT model, the answer to why DWs are observed moving against the e-flow can be found. The observed CIDWM can be interpreted as due to the presence of a positive interfacial DMI and a negative SHE in the investigated material system. When an electric current is injected through the material stack, parallel to the sample's surface, an effective magnetic field, $\mathbf{H}_{SHE} = \frac{\hbar\theta_{SHE}|j_e|}{2\mu_0|e|M_s t_{FM}} \hat{\mathbf{m}} \times (\hat{\mathbf{z}} \times \hat{\mathbf{j}}_e)$, is generated at the DW's location. Such a SHE effective field, in the present material system and with no applied external field, results to be parallel to the magnetization of the domain from which the conventional current, j_a , is coming from (see Fig. 5.9(a)).

As already explained in the Theory section and in Chapter 4, such a model is valid only under three assumptions: (i) the HM layer where the SHE is generated is thick enough in order to saturate the spin current [93]; (ii) the HM\FM interface is characterized by a 100% spin-transparency [95, 96] and no spin-memory loss [99]; (iii) 100% of the spin angular momentum (transverse to the magnetization) is transferred from the itinerant electrons to the local magnetization. The reported values for the spin-diffusion length in Ta are in the range $\lambda_{spin}^{Ta} \approx 1-2$ nm [130-132]. Due to the thickness of 5 nm of the Ta bottom layer present in the investigated device, the amplitude of the spin current density, j_s , crossing the Ta\CoFeB interface is expected to be lower than the bulk value, $j_s(\infty)$. According to Liu et al. [93], the fraction of the bulk spin current density at the

Ta\CoFeB interface is given by: $\frac{j_s(t_{Ta})}{j_s(\infty)} = (1 - \text{sech}(\frac{t_{Ta}}{\lambda_{spin}^{Ta}})) = 0.99-0.84$, with $\lambda_{spin}^{Ta} = 1-2$ nm. Accordingly, between the 84% and 99% of the bulk spin current is generated right below the HM\FM interface, due to the 5 nm-thick Ta layer present in our sample.

Concerning the second and the third assumptions, neither the spin-transparency/spin-memory loss at the Ta\CoFeB interface nor the efficiency of the spin angular momentum transfer in the ferromagnet are known. As reported by Kim et al. [141], the Ta\CoFeB interface is characterized by a spin-transparency which is less than 1. However, due to the lack of quantitative information, the approximation of 100% spin-transparency will be used in the following. The same approximation is employed concerning the efficiency of the spin angular momentum transfer between the SHE-spin current and the magnetization in the ferromagnet, according to what has been done previously by other groups [25, 27]. A possible approach to improve the present analysis would consist in measuring the spin-transparency at the Ta\CoFeB interface, for example by spin-torque ferromagnetic resonance measurements as reported by Zhang and co-authors [96].

The SHE-effective field above contributes to the total effective field acting on the DW's magnetic moments, generating an additional precessional torque, $\boldsymbol{\tau}_{SHE,1} \propto -\hat{\mathbf{m}} \times \mathbf{H}_{SHE}$, and an additional dissipative torque, $\boldsymbol{\tau}_{SHE,2} \propto -\hat{\mathbf{m}} \times (\hat{\mathbf{m}} \times \mathbf{H}_{SHE})$, which result in the motion of DWs along the direction of the conventional current, in the zero-field case (see Fig. 5.9(a)). However, when a finite longitudinal field is applied, the internal structure of the DW is changed. If the Néel-component of the DW, \mathbf{m}_x , points in the same direction of the applied field, the \mathbf{H}_{SHE} acting on it will become larger and the velocity of the DW will be increased. While, in case \mathbf{m}_x is initially anti-parallel to the applied field, the magnetization will rotate to the Bloch-configuration and then eventually reverse in the opposite direction along the longitudinal direction. In turn, H_{SHE} is reduced to zero and then changed in sign. This results in the stopping and then in the reversal of the DW's velocity for increasing H_x , as reported in Fig. 5.5 and illustrated in Fig. 5.9(b). If on one side the negative SHE is in agreement with previous observations by other scientific groups [25, 27, 68], on the other the observation of a positive DMI at the Ta\CoFeB interface is new, and it has still to be understood. Regarding this second point, later in the chapter it will be proposed a possible explanation for the extracted positive DMI, based on the outcomes of a structural and chemical characterization of the material stack.

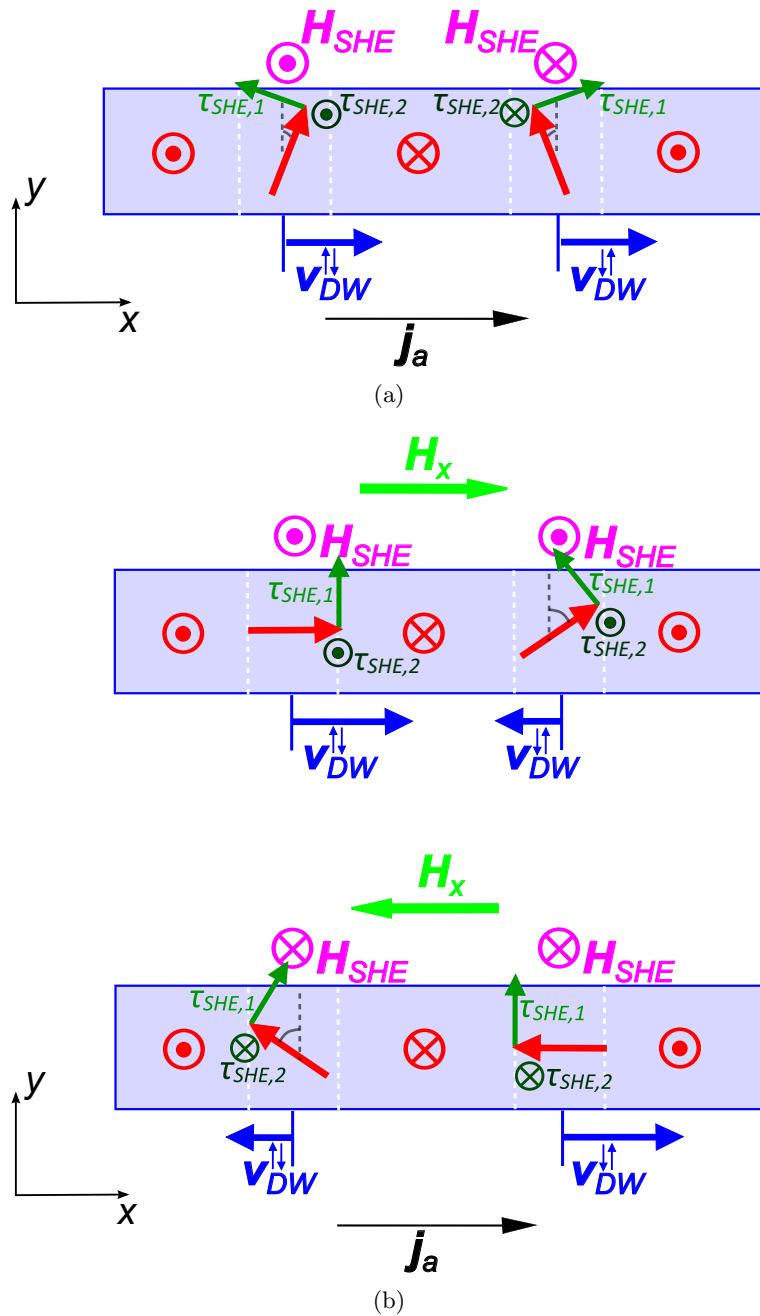


FIGURE 5.9: **Chiral DWs in Ta\CoFeB\MgO moved by the SOT.** (a) DW motion driven by SOT in Ta\CoFeB\MgO NWs, at zero-field. DWs are stabilized by the DMI in a chiral state, with a small Néel-component. The effective SHE-field acts locally on the DWs, pointing in opposite directions for $\uparrow\downarrow$ and $\downarrow\uparrow$ DWs. The result, due to the action of the precessional torque, $\tau_{SHE,1}$, and of the dissipative torque, $\tau_{SHE,2}$, on the DW's magnetic moments, is the motion of both DWs with \mathbf{j}_a in lock-steps. (b) Applying an external magnetic field along the NW's length, the DW's internal magnetization is rotated. The velocity of DWs with intrinsic \mathbf{m}_x parallel to the field is increased, while for DWs with intrinsic \mathbf{m}_x anti-parallel to the field the velocity is reduced. In case the applied field is stronger than the DMI effective field the DW's velocity can be reversed. This sketch tries to explain the experimental observations reported in Fig.s 5.5(a), 5.5(b) and 5.6.

5.7 1D modeling of chiral domain wall motion: extraction of the spin-Hall effect efficiency

The strength of the SHE in the investigated sample is quantified by reproducing the observed CIDWM reported in Fig. 5.5 with a 1-dimensional (1D) model. As reported in the Theory chapter, the 1D-model describes the entire DW dynamics by two degrees of freedom: the DW position q along the NW (assumed to be a 1D object) and the angle ϕ between its magnetization vector (in plane) and the NW's axis. In the used 1D-model¹ [139, 140, 142], the thermal fluctuations and the DW pinning due to the edge roughness are taken into consideration, in order to simulate more accurately the experimentally observed DW motion in the actual sample. The results of the simulations are reported in the shared manuscript [128], which contains also the main experimental findings reported in the present chapter. A summary of the simulation outcomes is presented in the following.

The experimental data reported in Figs. 5.5(a), 5.5(b) and 5.6 are reproduced by 1D simulations, where the effective pinning landscape (strength V_0 and periodicity p), the SHA and the DMI coefficient are the three main fitting parameters. The pinning potential parameter, $V_0 = 7 * 10^{-20}$ J, is chosen to be the one corresponding to the experimentally observed depinning field (at zero-current), $\mu_0 H_p \approx 0.5$ mT. The value of the DMI coefficient is also chosen to be the same as the average value experimentally obtained, that is: $D = +0.06 \pm 0.01$ mJ/m² (in the actual simulations, the value of $D = +0.06$ mJ/m² is employed as exact parameter). The best fitting of the experimental results reported in Figs. 5.5(a), 5.5(b) and Fig. 5.6 allow to extract a SHA of $\theta_{SHE} = -0.11$ (and a pinning potential periodicity $p = 21$ nm). Such a value of the SHA is very close to others previously reported in literature for similar material systems where Ta was the bottom layer [68, 138]. However, the extracted effective value of the SHA, $\theta_{SHE} = -0.11$, is influenced by the thickness of the Ta bottom layer. Accordingly, this is not the bulk value of the SHE efficiency. The extracted SHA is a function of the t_{Ta} , as reported above [93]: $\theta_{SHE} = \theta_{SHE}^0 (1 - \text{sech}(\frac{t_{Ta}}{\lambda_{spin}^{Ta}}))$. Assuming to have $\lambda_{spin}^{Ta} = 1-2$ nm [130-132], this results in an extracted $|\theta_{SHE}^0| = 0.11-0.13$ for the SHA in bulk Ta.

It is important to underline that those fitting parameters can reproduce, with a good accuracy, the experimental values for $j_a = 3.6 * 10^{11}$ A/m² and $j_a = 2.8 * 10^{11}$ A/m²,

¹The simulation work has been carried out by our collaborator Prof. E. Martinez from the *University of Salamanca* (Spain).

but not the ones obtained for the lowest current density $j_a = 1.8 * 10^{11}$ A/m². The reason seems to be that the lowest current density used for the experiments reported in Figs 5.5(a) and 5.5(b) is actually smaller than the critical current density needed to start moving the DWs in the NWs (at zero-field). This can be seen in Fig. 5.2(b), where it is clear that for $j_a < 2.5 * 10^{11}$ A/m² the DWs are not displaced by current injection. Accordingly, since the 1D-model for the extraction of the SHE applies only to the case of DW motion in the flow regime [139] (where the DW pinning and the thermal activations play a little role in the DW motion process), the fitting is meaningful only for the two “high” current density cases. In Fig. 5.6, the solid lines are the fitting curves obtained for the highest current density case. The red (blue) solid symbols in the figure show the experimental data for $\uparrow\downarrow$ -DWs ($\downarrow\uparrow$ -DWs).

5.8 The role of B in the material stack

5.8.1 Observation of B diffusion

According to what has been discussed above, the observed motion of DWs against the e-flow at zero-field seems to be connected with the presence of a positive DMI at the Ta\CoFeB interface. According to the sign and the small absolute value of the extracted DMI coefficient, the DWs are in an intermediate state between Néel and Bloch, with a right-handed chiral Néel-component. However, the origin of this positive DMI is still not clear.

For explaining the observed positive DMI coefficient, it is important to note that the material stack was annealed at 300 °C for 2 h in vacuum. Since the DMI and the SOTs depend strongly on the interfaces’ conditions [20, 26, 96, 143], a structural characterization of the material stack is carried out in order to gain more information about them. High resolution transmission electron microscopy (HRTEM) imaging of the cross section of the material stack (see Fig. 4.2), and chemical depth profiling measurements by secondary ion mass spectrometry (SIMS)² are carried out in order to characterize more in depth the material system. As already discussed in the previous chapter, the TEM

²The chemical depth profiling measurements and relative analysis were carried out by our collaborators, Dr. A. Lamperti and Mr. R. Mantovan at the *Laboratorio MDM, IMM-CNR of Agrate Brianza* (Italy).

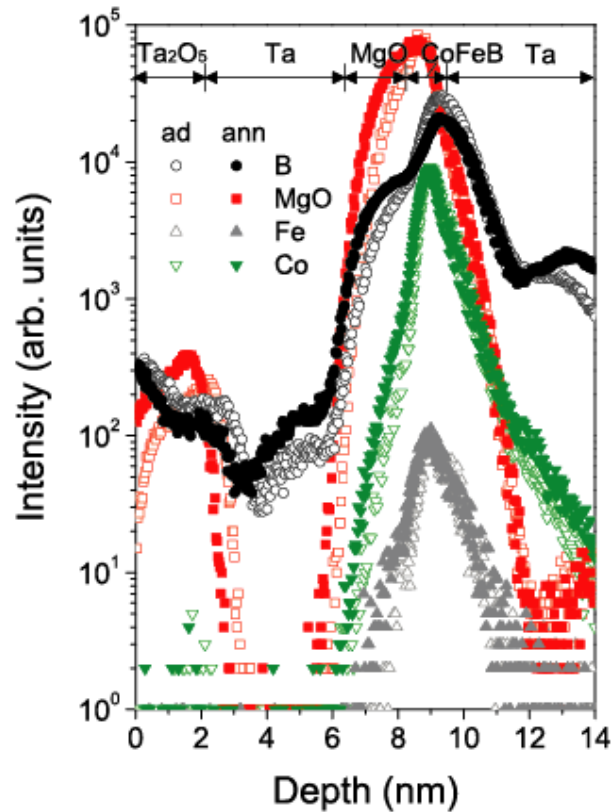


FIGURE 5.10: **Chemical depth profiling of the Ta(5.0)\Co₂₀Fe₆₀B₂₀(1.0)\MgO(2.0) stack.** SIMS depth profiles of as-deposited (ad) and annealed (ann) (300 °C, 2h) structures. Signals related to B (dots), MgO (squares), Fe (up-triangles) and Co (down-triangles) are shown. Following the B profile, the presence of B diffusion from the CoFeB layer towards the Ta layer (and partially the MgO layer) is evidenced. For the sake of clarity profiles are aligned at Ta\Co₂₀Fe₆₀B₂₀ interface. Secondary ions are collected in negative mode, and the measurement parameters are as reported in [144]. This image and the related analysis were performed by Dr. A. Lamperti and Mr. R. Mantovan from the *Laboratorio MDM, IMM-CNR of Agrate Brianza* (Italy). Data from [128].

cross-section confirms the nominal thickness of each layer composing the stack, and provides evidence for the presence of a top Ta-oxide layer due to the natural Ta oxidation in air. The top MgO\Ta interface shows sub-nanometer topographical roughness after the crystallization of the MgO and the CoFeB layers upon annealing, in agreement with other reported results [145]. Furthermore, the bottom Ta\CoFeB interface results to be not sharp, revealing a strong intermixing between the two layers.

The results obtained from the time-of-flight SIMS depth profiling measurements are shown in Fig. 5.10. The figure reports about the distribution of the different elements as a function of the stack's depth, starting from the top surface, for the material stack before the annealing (*ad*, open symbols) and after the annealing (*ann*, solid symbols). Comparing the open black dots with the solid black ones in Fig. 5.10, it is possible to

deduce that B diffuses out of the CoFeB-layer towards the MgO and the bottom Ta-layer during the annealing process. Summarizing the SIMS observations for the material stack before and after annealing: (i) the B intensity in the CoFeB layer is reduced after annealing; (ii) the B intensity increases in the region corresponding to the underneath Ta layer after annealing; (iii) a different intensity close to the CoFeB\MgO interface is observed after annealing. All these observations suggest that the B diffuses from the ferromagnetic layer to the adjacent layers during the annealing process, thus affecting in particular the Ta\CoFeB interface, where the B is expected to segregate [146].

5.8.2 Discussion

As stated before, the DMI is expected to depend on the material structure of the system, particularly the atomic arrangement at the [heavy metal]\ferromagnet interface [20, 24, 27, 136]. Accordingly, the B accumulation at the Ta\CoFeB interface can play a major role in the generation of the positive DMI, in particular due to the fact that the B is the key difference compared to CoFe-based material stacks, which have been reported to exhibit negative DMI. Furthermore, the idea that a strong accumulation of B in the bottom Ta-layer could be responsible for the character of the DMI is supported by previous works where it was reported that a N-doped Ta bottom layer can change the DMI sign compared to the case of a pure Ta\CoFeB system [27]. The larger electronegativity of the N atoms ([He]2s²2p³, 3.0 Pauling) compared to the one of Ta atoms ([Xe]4f¹⁴5d³6s², 1.5 Pauling) [28] is expected to change the electronic configuration at the interface due to the 2*p*-5*d* hybridization of the electronic orbitals. Such modification of the electronic states at the TaN\CoFeB interface is expected to influence directly or indirectly the DMI in the material system.

Relying on the interpretation offered by Torrejon et al. [27], it is possible to interpret the role of the observed concentration of B near the Ta\CoFeB interface and inside the Ta layer similarly to the one of N in N-doped Ta. The accumulation of B in Ta (as observed in our material system, after the annealing process) and the larger electronegativity of B ([He]2s²2p¹, 2.0 Pauling [28]) with respect to Ta can lead to a change in the electronic configuration at the Ta\CoFeB interface due to the 2*p*-5*d* hybridization of the electronic orbitals. Accordingly, the observation of a positive DMI in our system could be due to a rearrangement of the electronic configuration at the interface during the annealing step.

It is important to underline that the interpretation offered for the observed positive DMI in Ta\CoFeB\MgO NWs is the latest interpretation proposed at the time when this thesis was written. More investigation is required from both the theoretical and the experimental side in order to clarify whether this is the real origin of the positive DMI experimentally observed. However, it is also important to add that observations of right-handed chiral DWs in Ta\CoFeB\TaO_x systems have been recently reported [147]. This supports the findings here presented, adding one more experimental evidence to the interpretation based on the presence of a positive DMI in Ta\CoFeB systems. Finally, CIDWM was also investigated in Pt\CoFeB\MgO NWs. PEEM images of the DW displacements shows motion with the e-flow (for more details see Appendix B). This result is again in disagreement with what has been reported so far about Pt\CoFe\MgO systems, where DW motion against the e-flow was observed, attributing it to a negative DMI [25]. Another indication that systems containing B could show different results compared to very similar material systems where no B is present. However, this is not a complete study, and a more detailed investigation of the Pt\CoFeB\MgO system is needed in order to clarify the preliminary results reported in this thesis.

5.9 Conclusion and outlook

In the present chapter, the observed current-induced domain wall motion in magnetic nanowires made of Ta\Co₂₀Fe₆₀B₂₀\MgO is reported. First of all, the velocity of the DWs is measured as a function of the current density flowing into the nanostructures. The DWs are observed to move against the direction of motion of the conduction electrons, at a velocity that increases with an increasing current density. Such a DW motion is interpreted as due to the spin-orbit torque generated by the spin-Hall effect in the Ta bottom layer. Secondly, the effect of a longitudinal magnetic field on the CIDWM is investigated. The DW's velocity is strongly dependent on the applied magnetic field, and such a dependence is found to be symmetric for $\uparrow\downarrow$ - and $\downarrow\uparrow$ -DWs. This is interpreted as the presence of an interfacial Dzyaloshinskii-Moriya interaction in the investigated system. Such a spin-orbit interaction at the interface between the heavy metal layer and the ferromagnetic layer is the origin of a chiral Néel-component of the DW internal magnetization. A positive DMI with a strength of $D = (+0.06 \pm 0.01)$ mJ/m² is extracted, indicating the presence of homo-chiral right-handed DWs. Such a positive DMI

seems to be connected with the presence of the B in the material stack. Furthermore, reproducing the experimental results by 1D-model simulations, an effective spin-Hall angle value of $\theta_{SHE} = -0.11$ is obtained. The extracted positive DMI joined with the negative SHE of Ta emerge as the key factors at the basis of the observed DW motion. The obtained results have a certain relevance from both a scientific and a technological point of view. From the scientific point of view, it is very interesting to discover the presence of such new phenomena in a material system which has already been investigated for decades. The presence of a DMI in Ta/CoFeB/MgO systems is a new observation, with very few publications reporting on it. Probably this is due to the fact that the measured DMI is small (if compared, for example, to the much higher value of DMI reported for Pt/Co/AlO_x systems [148]), making it harder to be detected. Furthermore, these observations can help in the understanding of the real origin of spin-orbit torques, shedding new light on the problem. Second, these findings are very important from a technological point of view, since Ta/CoFeB/MgO is a material system already used in the fabrication of present magnetic storage devices. The new findings can be used for the design of novel spintronic devices, where a more effective manipulation of the DW motion by spin-orbit torques could be the key factor for their success. An example of the basic functioning of a racetrack memory [2] based on spin-orbit torque-driven DW motion is shown in Fig. 5.11, where the principle of operation of a Ta/CoFeB/MgO racetrack is illustrated. Starting with pre-initialized racetracks, magnetic bits can be written by a current pulse injected in the Oersted-line. After that, the written information can be transported by current pulses injected through the racetracks. Opposite magnetic bits can be written in the racetracks by a second current pulse through the Oersted-line, but in the opposite direction compared to before. Finally, both types of magnetic bits can be transported through the racetracks by the SOT.

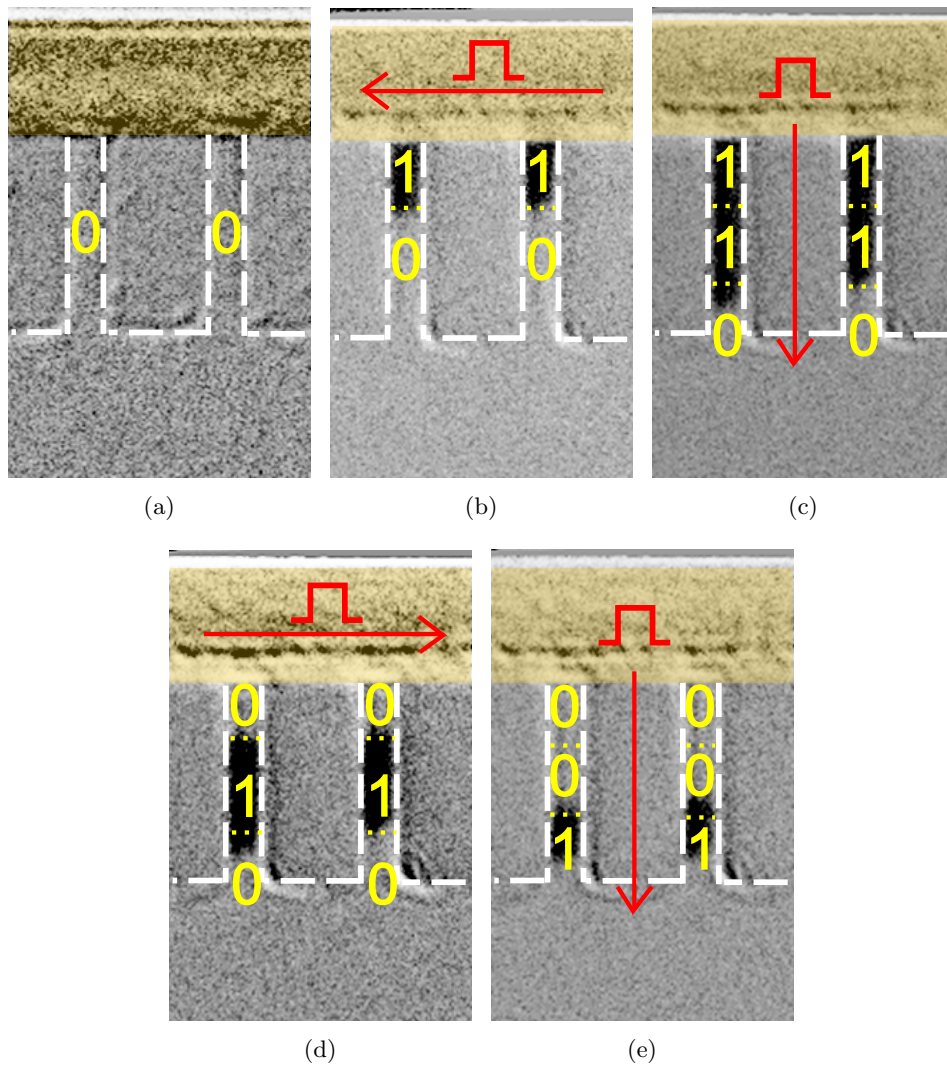


FIGURE 5.11: **Principle of operation of a Ta\CoFeB\MgO racetrack.** (a) **Initialization:** the two racetracks are pre-initialized in the “down” state. (b) **Information writing:** by a current pulse injection through the Oersted-line, two magnetic bits (1s) are written in the racetracks. (c) **Information transport:** by a train of current pulses through the nanostructures, the magnetic bits are displaced in the racetracks. (d) **New information writing:** two new bits (0s) are written in the racetracks. (e) **Information transport:** the magnetic bits are again displaced in the racetracks. The black contrast indicate magnetization “up” (or “1” as memory-bit state), while gray indicates magnetization “down” (“0” memory-bit state). The red arrows indicate the direction of the conventional current, j_a .

Chapter 6

Spin-orbit torque-induced domain wall motion in Pt\Co\AlO_x

6.1 Introduction

In the previous chapter, it was reported about the experimental observation of SOTs acting on DWs in a system characterized by a weak DMI. In the present chapter, the focus is on a different material system, which has a much larger DMI [138, 148]. SOTs are investigated in nanowires made of Pt\Co(t_{Co})\AlO_x¹, for different thicknesses of the ferromagnetic layer, by a systematic current-induced DW motion study. The main interest is on the investigation of the effect of t_{Co} on the measured DW motion, trying to learn about the effective SOT acting in the material stack. Furthermore, the effect of the ferromagnetic layer's thickness on the measured DMI is also investigated. A direct comparison between the results here presented and the outcomes of the investigation of the weak DMI system is conducted along all the chapter, trying to highlight the main differences between the two cases. The experimental methodology developed and presented in Chapter 5 is employed for the investigation of this new material stack.

¹The material stack used for the patterning of the devices presented here was grown by Dr. J.-S. Kim and Dr. D.-S. Han from the *Eindhoven University of Technology* (The Netherlands).

6.2 Material stack: Pt\Co(t_{Co})\AlO_x

The material system employed for the patterning of the magnetic devices is the multilayer: Ta(4.0)\Pt(4.0)\Co(0.8–1.8)\AlO_x(2.0) (all thicknesses in nm). The stack was deposited by magnetron sputtering technique² on a Si\SiO₂ substrate. The Ta buffer layer is used in order to induce a growth of the Pt layer with a smooth surface, with a strong (111) texture [149]. A schematic of the stack is reported in Fig. 6.1.

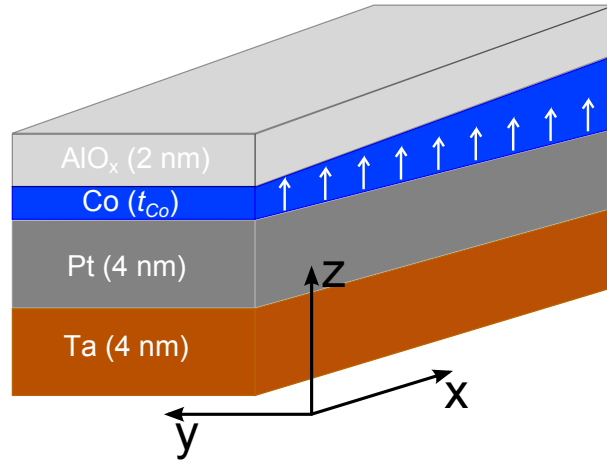


FIGURE 6.1: **Pt\Co(t_{Co})\AlO_x stack.** Schematic of the Pt\Co(t_{Co})\AlO_x stack used for magnetic nanowires patterning. The arrows indicate the magnetic moments in the ferromagnet, which is characterized by PMA. The Co layer is a wedge layer, with a nominal change in thickness of 1 nm (from 0.8 nm to 1.8 nm) over a 2 cm length. The Ta buffer layer is used to improve the crystallographic properties of the Pt layer.

The material stack is characterized by a wedge Co layer, with a nominal increase in thickness of 1 nm over 2 cm in the horizontal direction (x -direction in Fig. 6.1). The wedge Co layer is obtained by an *in-situ* moving shadow mask [150]. MOKE magnetometry hysteresis loops for an applied out-of-plane magnetic field are measured at different t_{Co} positions of the material stack's surface, as reported in Fig. 6.2. The stack results to be characterized by an out-of-plane magnetic easy-axis, with a spontaneous magnetization pointing along the z -axis. The coercive field is observed to decrease with increasing t_{Co} , together with a reduction of the squareness of the loops, in agreement with previous observations [148]. The observed perpendicular magnetic anisotropy (PMA) is induced by a strong interface anisotropy at the Pt\Co interface [37, 148, 151]. The interface-like

²The material stack used for the patterning of the devices presented here was grown by Dr. J.-S. Kim and Dr. D.-S. Han from the *Eindhoven University of Technology* (The Netherlands).

origin of the observed PMA is confirmed by Brillouin Light Scattering (BLS) measurements³. The effective anisotropy energy density, $K_{eff} = \frac{K_i}{t_{Co}} - \frac{1}{2}\mu_0 M_s^2$, is found to decrease with an increasing Co thickness, consistent with the presence of an interface anisotropy of $K_i = 3.48 \pm 0.1$ mJ/m². This explains the reducing coercive field as a function of an increasing Co thickness observed by MOKE magnetometry (Fig. 6.2). All the values of the magnetic parameters for the five devices used in the investigation of CIDWM are reported in Tab. 6.1.

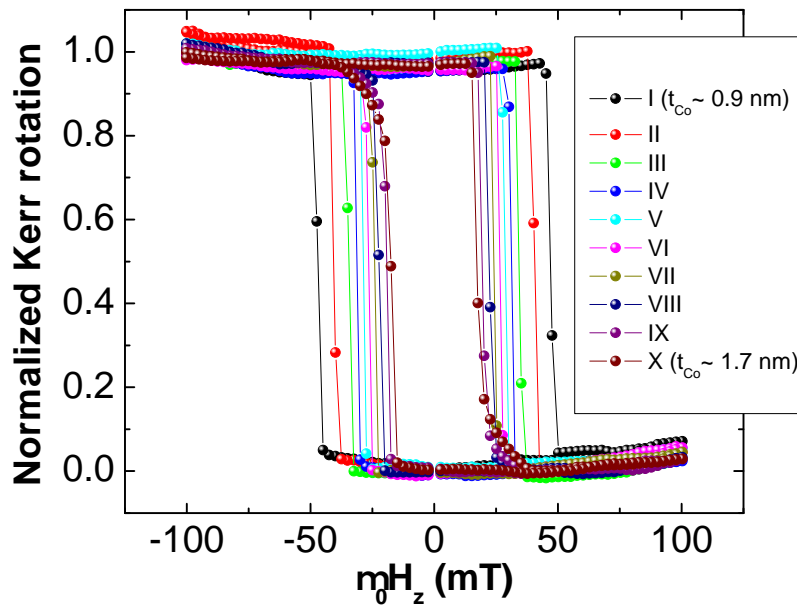


FIGURE 6.2: **Polar-MOKE hysteresis loops of the Pt/Co(t_{Co})/AlO_x multilayer for an applied out-of-plane field.** MOKE magnetometry hysteresis loops for the Pt/Co/AlO_x stack used for magnetic nanowires patterning. The external magnetic field is applied perpendicular to the sample surface, with the MOKE system operating in the polar configuration. The experiment is carried out at room temperature ($T = 300$ K), probing 10 equidistant areas on the stack's surface along the increasing Co thickness direction. (I) refers to an area of the sample with a nominal thickness of the Co layer of $t_{Co} = 0.9$ nm, (X) to $t_{Co} = 1.7$ nm. The Co thickness for each of the probed areas of the sample is given by: $t_{Co}^i = t_{Co}^I + \frac{t_{Co}^X - t_{Co}^I}{9}i$, with $i = 0, 1, 2, \dots, 8, 9$ ($i = 0 \rightarrow I, i = 1 \rightarrow II, \dots, i = 9 \rightarrow X$). Both the coercive field and the squareness of the loops decrease with increasing t_{Co} . (Measurements carried out together with Mr. Nam-Hui Kim.)

³The BLS measurements were carried out by our collaborator Mr. N.-H. Kim, from *Inha University* (Korea).

Device#	t_{Co} (nm)	M_s (A/m)	$K_u = \frac{K_1}{t_{\text{Co}}} (J/m^3)$	$K_{\text{eff}} (J/m^3)$
1	0.93	$1.8 * 10^6 (3 * 10^4)$	$3.7 * 10^6 (5 * 10^4)$	$1.7 * 10^6 (0.1 * 10^6)$
2	0.99	$1.8 * 10^6 (3 * 10^4)$	$3.5 * 10^6 (5 * 10^4)$	$1.5 * 10^6 (0.1 * 10^6)$
3	1.31	$1.8 * 10^6 (3 * 10^4)$	$2.7 * 10^6 (4 * 10^4)$	$6.4 * 10^5 (0.8 * 10^5)$
4	1.37	$1.8 * 10^6 (3 * 10^4)$	$2.5 * 10^6 (4 * 10^4)$	$5.3 * 10^5 (0.7 * 10^5)$
5	1.43	$1.8 * 10^6 (3 * 10^4)$	$2.4 * 10^6 (3 * 10^4)$	$4.2 * 10^5 (0.7 * 10^5)$

TABLE 6.1: **Magnetometry data for Pt\Co(t_{Co})\AlO_x from BLS measurements.** Values of the main magnetic parameters for the five devices used in the CIDWM experiments. All the values contained in the table are extracted by BLS-based spin-waves spectroscopy measurements (see [150]), by our collaborator, Mr. N.-H. Kim from Inha University (Korea). The t_{Co} values are the nominal values. In parentheses are the values of the error.

6.3 Experimental set-up

The results presented and discussed in this chapter are obtained from CIDWM measurements in five different devices, patterned on the material stack presented above. The nominal thickness of the Co layer in the different devices ranges between 0.93 and 1.43 nm, as reported in Tab. 6.1. The magnetic devices are patterned by e-beam lithography and Ar-ion milling, at 5 different t_{Co} -positions on the sample surface, as schematically shown in Fig. 6.3. Each device consists of an array of several NWs in parallel. The dimensions of a single wire is $(1.5-2) \mu\text{m} \times (25-28) \mu\text{m}$. At the ends of the wires there are magnetic pads, directly connected to two gold contact pads made in a second patterning step by lift-off technique. An SEM micrograph of one of the devices used for the CIDWM experiment is reported in Fig. 6.4.

As shown in Fig. 6.4, a pulse generator together with a power amplifier (nominal amplification in power of +40 dB) are employed for injecting the desired current pulses through the magnetic wires. The net pulse's rise-time and fall-time for the experimental set-up employed during the experiment here discussed are around 2 ns each, as reported in Fig. 6.5. A 50 Ω -termination is used to drive the injected pulse to ground after flowing across the device. In a second time, an oscilloscope is used for measuring the pulse waveform, across its 50 Ω -internal resistance (R_o). The total current flowing through the system is obtained by the measured voltage V_o across R_o (see Fig. 6.5). For the evaluation of the current density, j_a , the nominal thicknesses of the layers are used. The resistivity of the Ta layer is expected to be around 4-5 times larger than that of Pt [25], while the Co layer and the Pt layer are assumed to have a similar resistivity value.

Accordingly, considering the case of a device with 28 NWs in parallel, with a width for

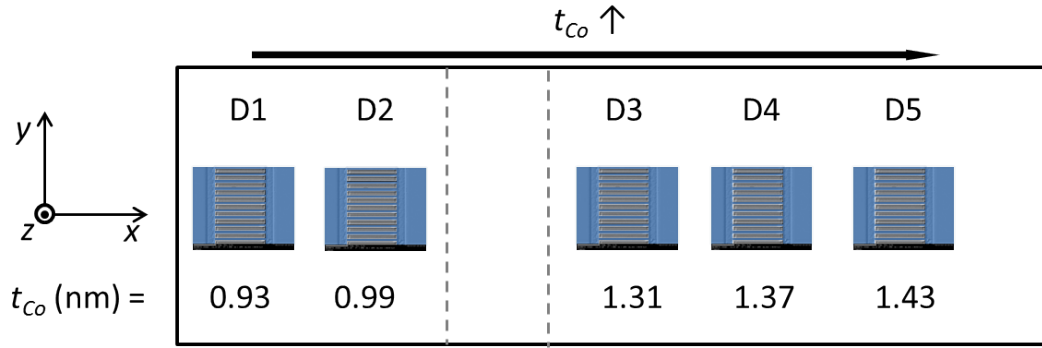


FIGURE 6.3: **Devices' positions on the Pt/Co(t_{Co})/AlO_x sample.** Schematic of the five devices patterned on the Pt/Co(t_{Co})/AlO_x sample, at positions with different Co thickness. Device 1 (D1) is the thinnest one, with $t_{Co} = 0.93$ nm, while device 5 (D5) is the thickest one, with $t_{Co} = 1.43$ nm. The other three devices have intermediate Co thicknesses, as indicated in the sketch. All the thicknesses are nominal values, obtained by the growth's conditions and calibration's data. The insets are small SEM micrographs of one of the devices actually used for the experiments. The image is not to scale.

the single NW of $1.5 \mu\text{m}$ and a nominal $t_{Co} = 1$ nm, a current density of 7.9×10^{10} A/m² is estimated to flow through the nanowires when 1 V drops across R_o . The conventional current density \mathbf{j}_a is assumed to be positive when it flows in the $+x$ -direction (see Fig. 6.4), corresponding to an electron current density \mathbf{j}_e flowing in the $-x$ -direction.

The magnetization configuration of the wires is imaged by polar Kerr microscopy in differential mode, as explained in Chapter 3. A magnetic coil is used for the generation of an external in-plane magnetic field. The experiments are carried out at $T=300$ K. First, the magnetic wires are saturated in the “up” ($+z$) or “down” ($-z$) magnetization state by an out-of-plane magnetic field. Second, the magnetization is reversed in all the NWs by the switching process presented in Chapter 4, this time by the SHE induced in the Pt layer. As a result, a DW ready to be displaced in each NW is obtained.

At the bottom left (right) of Fig. 6.4 the CIDWM experiment for $\uparrow\downarrow-$ ($\downarrow\uparrow-$) DWs in pre-saturated NWs is shown. At $t = t_0$ the DWs are nucleated. At $t = t_1$ the DWs are moved by the injection of a train of current pulses. At $t = t_2$ the DWs are moved again by the injection of a second train of current pulses. All the DW displacements are captured by Kerr microscopy in differential mode. The analysis of the images is carried out following the protocol described in Chapter 3. However, in this case the measurement of DWs' motion is performed with the help of a Python-based software⁴. It automatically recognizes and evaluates the DWs' displacements contained in the acquired images.

⁴The software for the automatic recognition and evaluation of DWs' displacement was entirely developed by Mr. K. Litzius, a colleague PhD student in Physics at the Johannes Gutenberg-Universität Mainz, in collaboration with the author.

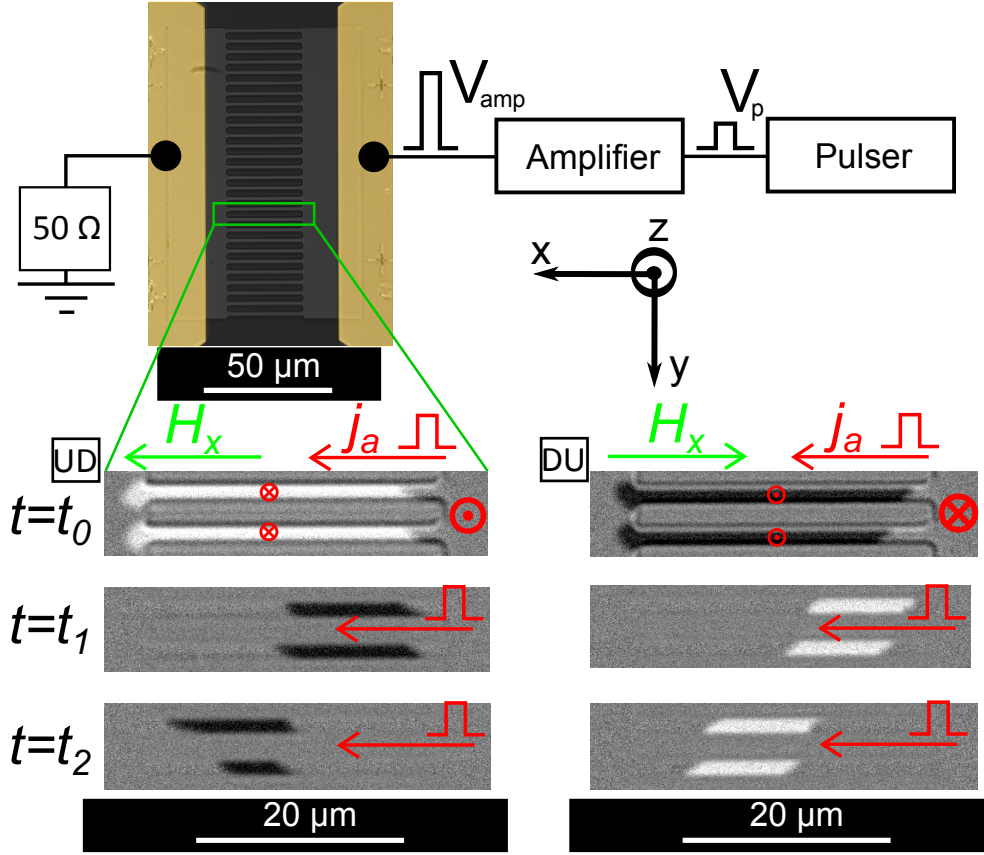


FIGURE 6.4: **Experimental set-up for CIDWM in Pt/Co(t_{Co})/AlO_x NWs.** At the top, it is shown the experimental set-up for current pulse injection, including an SEM micrograph of one of the devices used during the experiment. At the bottom, a series of differential Kerr microscopy images show the CIDWM measurement protocol. At $t = t_0$ the DWs are nucleated by the application of a fixed external magnetic field (50–100 mT) and a current pulse (high 10^{11} A/m², 50 ns). At $t = t_1$ the DWs are moved by the injection of a train of current pulses (8×10^{11} A/m², 10 ns). At $t = t_2$ the DWs are moved again by the injection of a second train of current pulses. The procedure is shown for $\uparrow\downarrow$ -DWs (left side) and $\downarrow\uparrow$ -DWs (right side). The red symbols represent the magnetization state in the magnetic device. The tilt of the DWs visible in the Kerr microscopy images will be discussed in the following.

6.4 Current-induced domain wall motion in Pt/Co/AlO_x NWs

6.4.1 Moving domain walls with current

Figure 6.6 reports the DW's average velocity, v_{DW} , as a function of the current density, j_a , flowing through the magnetic wires, for all the five devices. The measurement is done for both $\uparrow\downarrow$ -DWs (red dots) and $\downarrow\uparrow$ -DWs (blue dots), for positive and negative j_a . Bursts of several (n) current pulses with a time duration Δt_p (full width at half maximum) are used for the current-induced domain wall motion. The time between

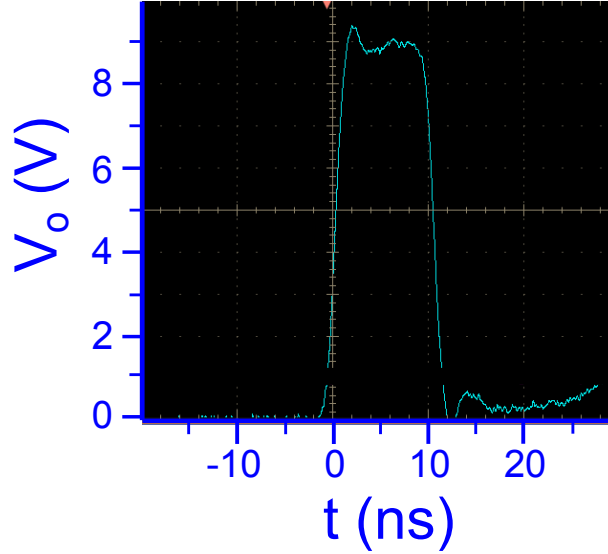


FIGURE 6.5: **Pulse's waveform in the experimental set-up for CIDWM in Pt/Co(t_{Co})/AlO_x NWs.** Typical waveform of a pulse transmitted through the studied devices. The transmitted voltage, V_o , is measured across the 50 Ω -internal resistance of an oscilloscope, R_o . The illustrated waveform corresponds to an injected pulse with a nominal time duration $\Delta t_p = 10$ ns and an amplitude $V_p = 200$ mV, amplified by a +40 dB power amplifier.

two consecutive pulses is 1 ms. The number of pulses in a burst ranges from $n=5$ to $n=50$.

The velocity of the DW is calculated as the ratio between the average displacement of the domain wall due to the injected pulses and the total pulsing time, $t_{tot} = n * \Delta t_p$. The DWs, both $\uparrow\downarrow$ and $\downarrow\uparrow$, are observed moving with the current flow, like in the case of the Ta/CoFeB/MgO NWs presented in the previous chapter. This points again to SOTs as the leading mechanism in the DW's motion. The critical current density, in all the devices, is found to be in the range $j_a \approx 6.0 - 8.5 * 10^{11}$ A/m². In all cases, the DW's velocity increases rapidly with increasing j_a for current densities just above the depinning condition.

6.4.2 Discussion

In all the five devices, $\uparrow\downarrow$ - and $\downarrow\uparrow$ -DWs are observed moving in the same direction (with the conventional current \mathbf{j}_a), at approximately the same speed (within the error bars). The critical current density for inducing a measurable DW motion in each device is observed as being in the range $j_a \approx 6.0 - 8.5 * 10^{11}$ A/m², in line with what has been reported in literature [9, 44]. Such a value is 2.5–3.5 times larger than what has been

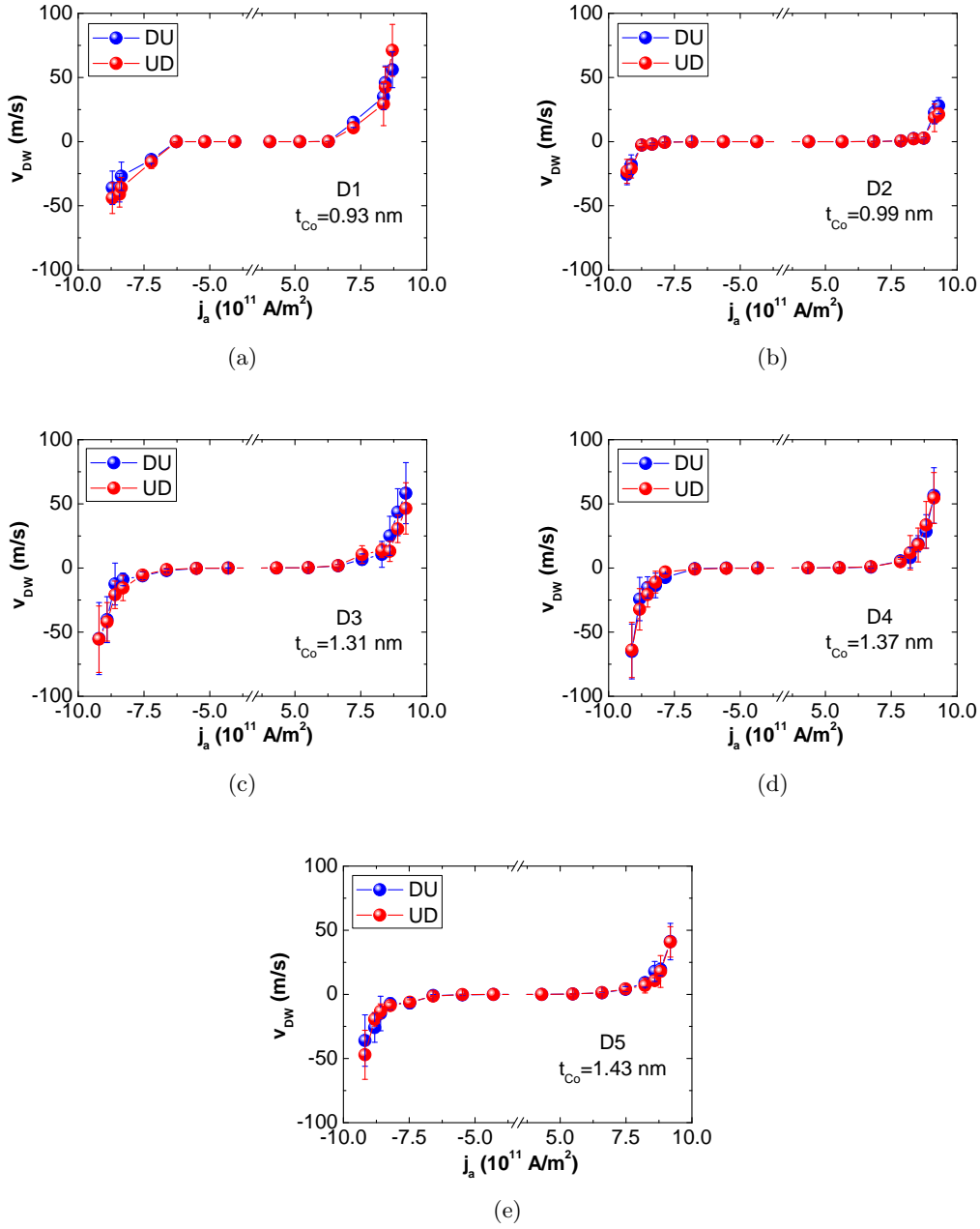


FIGURE 6.6: **CIDWM velocity in $Pt(4)/Co(t_{Co})/AlO_x(2)$ NWs.** Average DW's velocity, v_{DW} , as a function of the current density, j_a , injected in the magnetic wires, for 5 different devices. The DW's velocity is reported for both $\uparrow\downarrow$ -DWs (red dots) and $\downarrow\uparrow$ -DWs (blue dots). The DW moves with the conventional current j_a (against the electron flow j_e). The average velocities and the error bars (standard deviations) are calculated from several DW's motions, for each current density. (a) CIDWM data for D1, with $t_{Co} = 0.93$ nm. (b) CIDWM data for D2, with $t_{Co} = 0.99$ nm. (c) CIDWM data for D3, with $t_{Co} = 1.31$ nm. (d) CIDWM data for D4, with $t_{Co} = 1.37$ nm. (e) CIDWM data for D5, with $t_{Co} = 1.43$ nm.

reported for the Ta/CoFeB/MgO NWs. The reason for the observation of an higher critical value in Pt/Co/AlO_x is mainly due to the expected polycrystalline character of the Co layer. Indeed, CoFeB is an amorphous material due to the presence of B that prevents the formation of a crystalline structure [146]. However, reducing the B concentration the CoFe-alloy tends to become crystalline (as also reported in Chapter 4 and 5). The presence of grains and grain boundaries in the Co layer are expected to increase the effective pinning of the DW, resulting in a higher depinning current density for the Pt/Co/AlO_x sample compared to the Ta/CoFeB/MgO sample, as reported here.

In the reported experiments, DWs are observed moving against the electron-flow (e-flow). This cannot be explained if the STT [6, 43] alone is considered to be the driving mechanism. Accordingly, the reported observations are here analyzed employing the recently discovered spin-orbit torques [25, 35, 45, 151]. Considering the SHE-based SOT [25, 35, 45], a pure spin-current produced by the SHE in the Pt bottom layer diffuses into the Co layer, where it generates a torque on the local magnetization. The interaction between the SHE-spin current and the magnetization in the ferromagnet can be interpreted as the interaction between the magnetization and an effective magnetic field, \mathbf{H}_{SHE} (see Chapter 2). The SHE-effective field is defined as: $\mathbf{H}_{SHE} = \frac{\hbar\theta_{SHE}|j_e|}{2\mu_0|e|M_s t_{FM}} \hat{\mathbf{m}} \times (\hat{\mathbf{z}} \times \hat{\mathbf{j}}_e)$; where θ_{SHE} is the effective spin-Hall angle (SHA) of Pt, j_e is the electron current density, M_s is the saturation magnetization of the ferromagnetic material, t_{FM} is the thickness of the ferromagnetic layer and $\hat{\mathbf{z}}$ is a unit vector indicating the $+z$ -direction (the symmetry breaking direction). The limitations of such approach and the assumptions at the basis of it have been already discussed in Ch. 2. Some more details are also reported in the last part of this chapter, where the motion of DWs under the action of the SHE-SOT in large DMI-systems is discussed in more detail.

In Fig. 6.7, the DW velocities measured in the five devices are compared. As shown in Fig. 6.7(a), the “ v_{DW} vs j_a ” curves (ideally obtained by joining the data points) are similar to each other, from a qualitative point of view. However, the observed DW velocities in D2 are clearly smaller than in all the other devices, and it is not clear why at the moment. Further investigation is required in order to clarify the origin of such difference between the observations obtained for D2 and the ones obtained for the other four devices. On the other hand, Fig. 6.7(b) reports the normalized DW velocities, $v_{DW}/v_{DW,max}$, for the five devices. In this graph, it is possible to see that the five

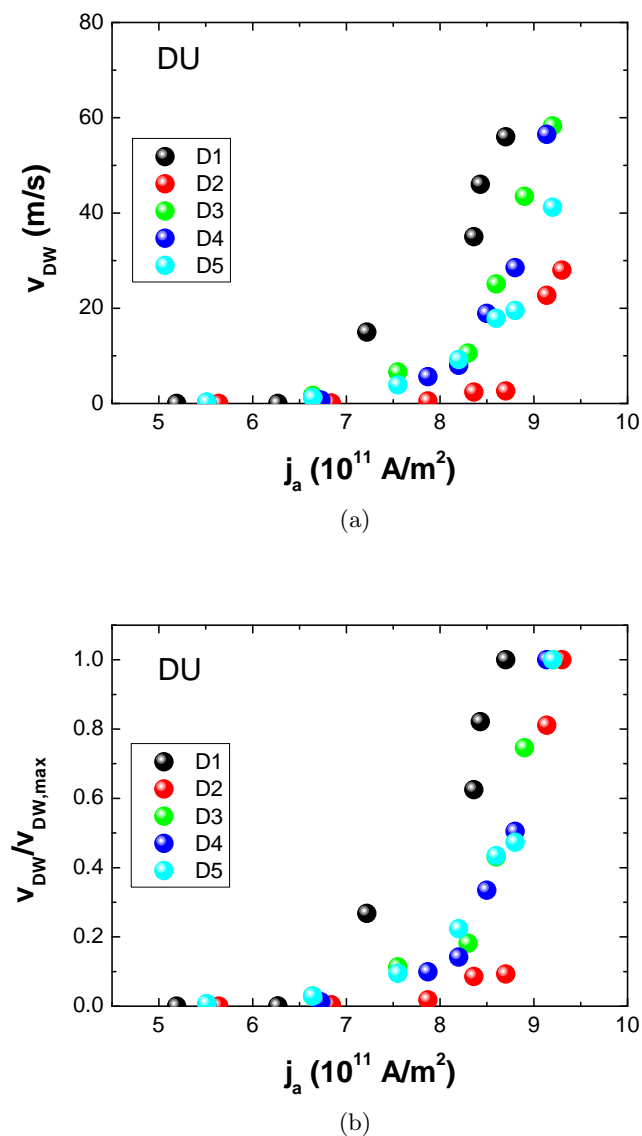


FIGURE 6.7: **Comparing the CIDWM velocities in the five Pt\Co(t_{Co})\AlO_x devices.** (a) Average DW velocity, v_{DW} , as a function of the current density, j_a , for the 5 different devices. The DW velocity is reported for the $\downarrow\uparrow$ -DW. *Black* dots refer to D1, with $t_{Co} = 0.93$ nm; *red* to D2, with $t_{Co} = 0.99$ nm; *green* to D3, with $t_{Co} = 1.31$ nm; *blue* to D4, with $t_{Co} = 1.37$ nm; *cyan* to D5, with $t_{Co} = 1.43$ nm. (b) Normalized average DW velocity, $v_{DW}/v_{DW,max}$, as a function of the current density, j_a , for the 5 different devices. Error bars are removed in order to make the graphs more understandable.

curves are both qualitatively and quantitatively similar, showing a general trend for $v_{DW}/v_{DW,max}$ as a function of j_a . The normalized DW velocity values for D2 are now observed to be similar to the data points referring to the other devices. This seems to indicate that the observed CIDWM in all the devices has a common origin, even if it is not possible, at this stage, to say if there is more than one origin behind the observed DW motion.

6.5 Chiral domain walls moving in Pt\Co\AlO_x NWs

6.5.1 Effect of an external magnetic field on the domain wall motion

Following the same approach used in the investigation of Ta\CoFeB\MgO NWs, the effect of magnetic fields on the DW motion is studied here as well. For each device, the DW velocity is measured as a function of an applied magnetic field along the wire axis (x -direction) for fixed current densities.

For each device, the measuring protocol is the following. First, one type of DW ($\uparrow\downarrow$ or $\downarrow\uparrow$) is nucleated in each pre-saturated NW by current-induced magnetization switching [36, 101, 125] (as described in Fig. 6.4). A typical switching pulse used in the experiment has a current density amplitude of $j_a \approx 8 * 10^{11}$ A/m² and a time duration of $\Delta t_p = 40 - 50$ ns, assisted in the switching process by an external longitudinal field of about 50 mT. Once the DWs are generated, they are displaced by the injection of a burst ($n=1-50$) of current pulses with a nominal duration of 10 ns. In Fig. 6.8, the motion of $\uparrow\downarrow$ -DWs in the presence of an applied longitudinal field is illustrated. The total DW's displacement is strongly affected by the presence of a finite \mathbf{H}_x . In order to calculate the DW velocity, the full width at half maximum of the current pulse (see Fig. 6.5) is used as the time duration of a single pulse. The measured average DW velocity as a function of the longitudinal field, $\mu_0\mathbf{H}_x$, for each device is reported in Fig. 6.9. Red (blue) symbols refer to $\uparrow\downarrow$ ($\downarrow\uparrow$) DWs, while squares (stars) refer to $j_a > 0$ ($j_a < 0$). It is clear from the graphs that the DW velocity is strongly influenced by the presence of the longitudinal field, in a similar way to what has been reported before about the Ta\CoFeB\MgO system. While at zero-field the velocity of both types of DWs is the same, in the presence of a finite longitudinal field the two types of DW move at different velocities. The change in the field amplitude affects differently the velocity of the two types of DW,

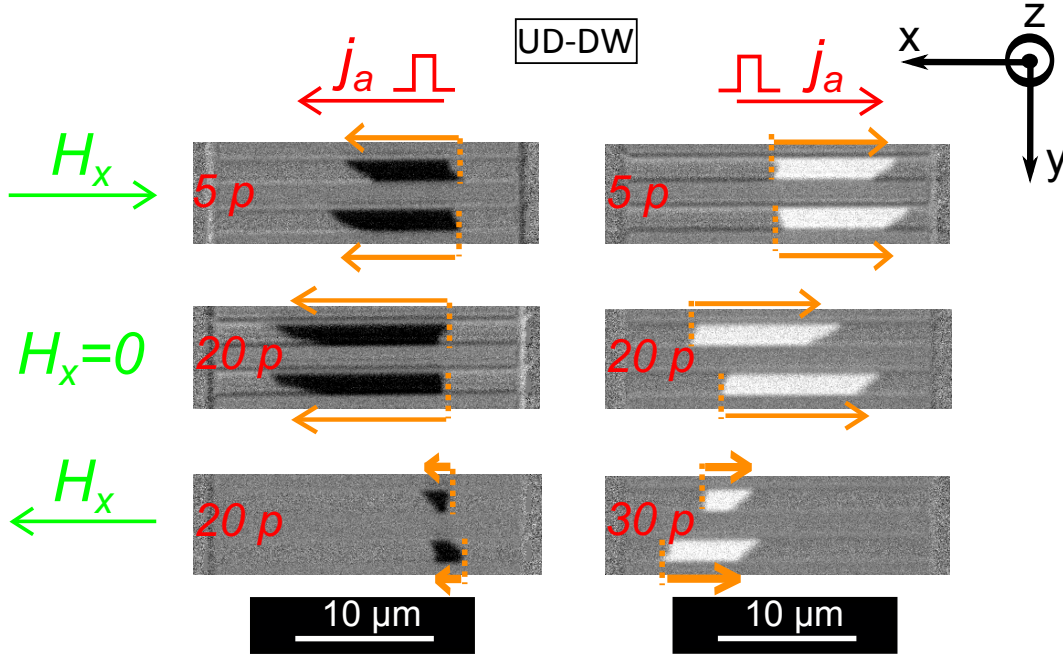


FIGURE 6.8: Motion of chiral DWs in Pt/Co/AlO_x NWs in presence of an in-plane longitudinal field. Effect of an applied in-plane longitudinal magnetic field, \mathbf{H}_x , on the current-induced motion of $\uparrow\downarrow$ -DWs. The velocity of the DWs reduces for $H_x > 0$ and increases for $H_x < 0$, for both $j_a > 0$ and $j_a < 0$. The gold dashed lines indicate the initial position of the DWs. The gold arrows indicate the DWs' direction of motion. The injected current density is $j_a = 8.7 \times 10^{11} \text{ A/m}^2$, while the longitudinal field amplitudes are: $\mu_0 H_x = -58 \text{ mT}$, $\mu_0 H_x = 0 \text{ mT}$, $\mu_0 H_x = +58 \text{ mT}$. The red numbers indicate how many pulses are used to generate the illustrated DWs' displacements. The images refer to Device 1.

making it possible to obtain $\uparrow\downarrow$ - and $\downarrow\uparrow$ -DWs moving in opposite directions, when the field's amplitude is large enough. A symmetric behavior is observed for the velocity of the two DW types with respect to \mathbf{H}_x , of the type: $v_{DW}^{\uparrow\downarrow}(j_a, H_x) = v_{DW}^{\downarrow\uparrow}(j_a, -H_x)$.

6.5.2 Discussion

As extensively discussed in the previous chapter, the observed motion of DWs against the e-flow at zero-field and the strong effect of a longitudinal field on the DW's velocity cannot be explained considering the STT as the main mechanism behind the DW's dynamics. An alternative interpretation for such observations has to be found. The interpretation relies on the presence of SOTs in the material stacks under investigation. Accordingly, the following analysis will be conducted in the SOT-model framework [25, 35, 45].

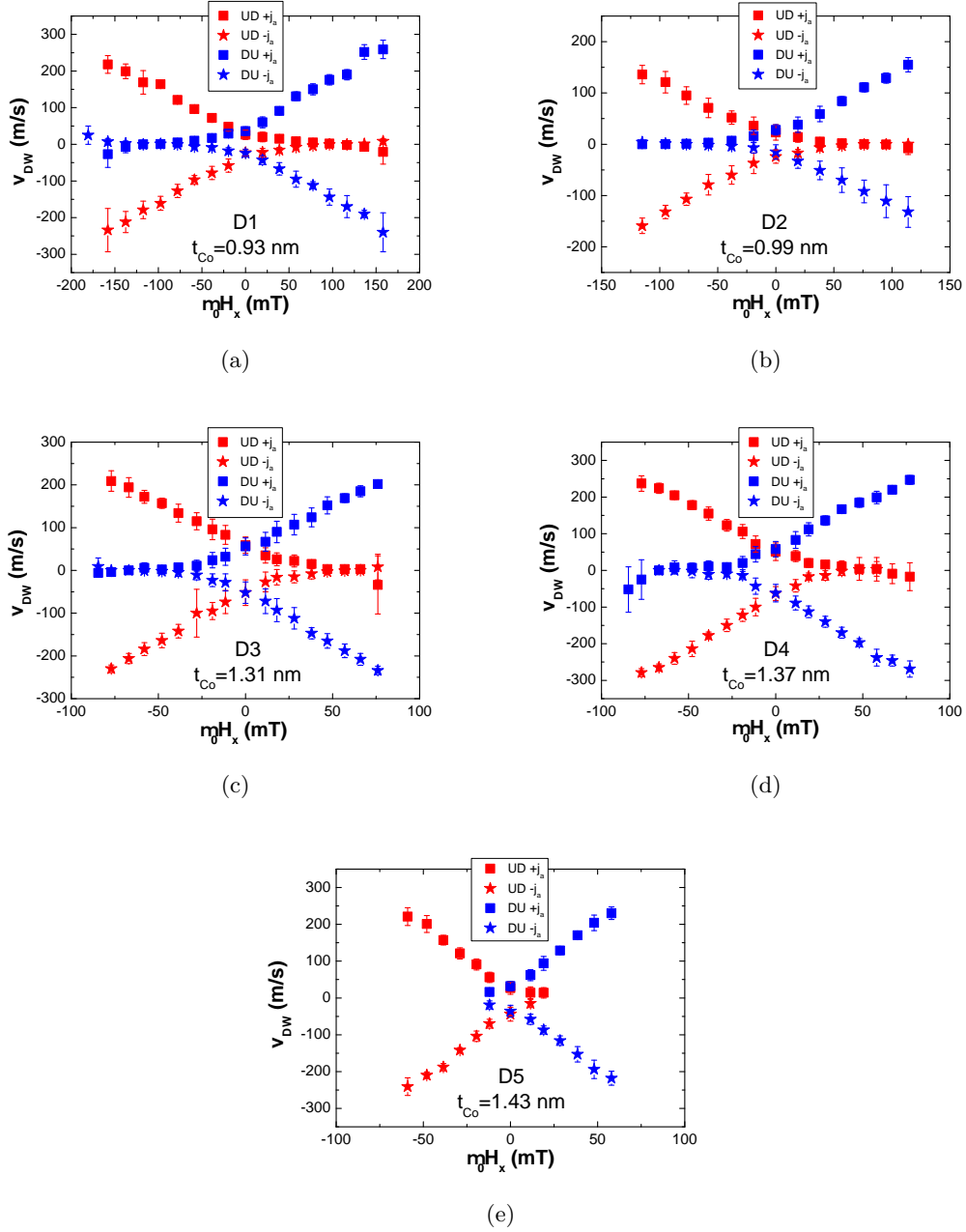


FIGURE 6.9: **Symmetry of chiral DWs' velocity in Pt(4)\Co(t_{Co})\AlO_x(2) NWs.** Average velocity, v_{DW} , of $\uparrow\downarrow$ (red symbols) and $\downarrow\uparrow$ (blue symbols) DWs as a function of $\mu_0 H_x$, for all the five devices, with both $j_a > 0$ (squares) and $j_a < 0$ (stars). The average velocities and the error bars (standard deviations) are calculated from several DW's motions, for each magnetic field value. (a) Data for D1, with $t_{Co} = 0.93$ nm; $j_a = 8.7 \times 10^{11}$ A/m². (b) Data for D2, with $t_{Co} = 0.99$ nm; $j_a = 9.5 \times 10^{11}$ A/m². (c) Data for D3, with $t_{Co} = 1.31$ nm; $j_a = 9.2 \times 10^{11}$ A/m². (d) Data for D4, with $t_{Co} = 1.37$ nm; $j_a = 9.1 \times 10^{11}$ A/m². (e) Data for D5, with $t_{Co} = 1.43$ nm; $j_a = 9 \times 10^{11}$ A/m².

Assuming the SHE-SOT as the main driving force behind the DW motion, the direction of motion depends on the sign of the SHE and on the domain wall's internal spin-structure. The reported values for the spin-diffusion length in Pt are in the range $\lambda_{spin}^{Pt} \approx 0.5-4$ nm [93, 99, 130, 131, 152, 153]. The bottom Pt layer has a nominal thickness of $t_{Pt} = 4$ nm, which is comparable or larger than λ_{spin}^{Pt} . Accordingly, it is reasonable to assume that the spin current crossing the Pt/Co interface is not influenced by the SHE in the Ta buffer layer. This is also supported by the fact that the Ta layer is expected to be several times more resistive than the Pt layer [25, 154], resulting in the shunting of the current through the Pt layer. Accordingly, the predominant contribution to the total SHE-SOT is expected to rise from the SHE in the Pt bottom layer, for which a positive SHA has been reported [25, 35, 93, 96, 131].

The DW motion is activated by the pure spin-current generated in the Pt layer during the current pulse injection. According to Liu et al. [93], the fraction of the bulk spin current density at the Pt/Co interface is given by: $\frac{j_s(t_{Pt})}{j_s(\infty)} = (1 - \text{sech}(\frac{t_{Pt}}{\lambda_{spin}^{Pt}})) = 1-0.35$, with $\lambda_{spin}^{Pt} = 0.5-4$ nm. Accordingly, between the 35% and 100% of the bulk spin current is generated right below the Pt/Co interface, in the investigated devices.

On the other hand, as already discussed in Chapter 5 and reported in literature [25, 26, 35, 45], the Dzyaloshinskii-Moriya interaction at the interface between the heavy metal and the ferromagnetic layer is responsible for the initial magnetic configuration and in particular for the chirality of the DW [20, 45], which is the second key factor, together with the SHE, governing the DW motion. The interfacial DMI acts on the magnetic texture as a longitudinal DMI effective field, $\mu_0 \mathbf{H}_{DMI} = \frac{D}{M_s \lambda_{DW}} \hat{\mathbf{x}}$ (where $\hat{\mathbf{x}}$ indicate the $+x$ -direction) [45, 138], localized at the domain wall position. Accordingly, the applied external longitudinal field, \mathbf{H}_x , adds up to the DMI field, resulting in a net longitudinal field acting on the DW. The resulting field defines the final DW's magnetic configuration (as explained later, see Fig. 6.11), which in turn defines the strength of the SOT.

As reported in Fig 6.9, the DW velocity is strongly affected by an applied longitudinal magnetic field. Considering $\uparrow\downarrow$ -DWs, a positive H_x slows them down, bringing them in a slow motion regime, while a negative H_x speeds them up. For large enough positive H_x the DWs are also observed to change their direction of motion. However, differently from the case of the Ta/CoFeB/MgO system, it is not possible in this case to access the regime of fast DW motion in the reversed direction. Indeed, for in-plane fields larger than the ones shown in the graphs, local spontaneous magnetization reversal events

[27, 125] start to occur, making the DW motion measurement not possible. The amplitude of \mathbf{H}_x at which domains start to nucleate is observed to decrease with increasing t_{Co} , even if the used current density is actually lower for thicker NWs. This results in a reduction of the range of in-plane fields which can be used for the investigation of each device, moving from D1 to D5.

The reason why the nucleation probability is observed to increase with increasing t_{Co} is not clear. An increasing t_{Co} results, for ultra-thin layers like the ones under investigation, in an increasing conductivity of the ferromagnetic layer [155]. This increases the fraction of the total current actually flowing in the Co layer. Accordingly, the observed increasing nucleation probability could be linked with the increase of the current flowing in the ferromagnetic layer, due to an increasing Joule heating produced directly in the FM [125]. Furthermore, as reported by Pai et al. [95], the increase in t_{Co} generates an increase in the efficiency of the damping-like-SHE-SOT. Since such a torque is considered to be the main driving force for the magnetization reversal in the presence of a longitudinal field, as discussed in Chapter 4, this could explain the observed increasing switching efficiency with an increasing t_{Co} . However, further investigations are needed in order to better understand such observations.

The nucleation process is observed to be particularly strong in the thickest of the investigated devices, where already at applied fields of 10-20 mT reversed domains start to appear in the NWs after the current pulses injection. This results in the impossibility of observing any DW motion's reversal, as reported in Fig. 6.9(e). The lack of data points about reversed DWs' motion will affect the approach for the extraction of the DMI effective fields, as it will be discussed in the next section.

All that has been described above concerning $\uparrow\downarrow$ -DWs is valid for $\downarrow\uparrow$ -DWs too, even if in a symmetric way with respect to H_x . In this case, a positive in-plane field boosts DWs' motion, while a negative field slows them down, bringing them in a slow motion regime (see Fig. 6.9).

6.6 Dzyaloshinskii–Moriya interaction in Pt\Co(t)\AlO_x

According to what has been discussed above for the measurements reported in Fig. 6.9, it is not possible to use the approach by K.-S. Ryu et al. [26] to extract the strength of the DMI in the Pt\Co\AlO_x samples, as done for the Ta\CoFeB\MgO system. The

reason is the lack of high velocity data points for one of the two field polarities (positive, for $\uparrow\downarrow$ -DWs; negative, for $\downarrow\uparrow$ -DWs) in the reported graphs. As already discussed, the lack of those data points is related to the impossibility of measuring DW motion due to the generation of magnetization switching events. Accordingly, it is impossible to proceed with the linear fitting of the high velocity data points in order to extract the stopping fields. As it will be shown clearer in the next section, a linear fitting of the available high velocity data points contained in the graphs in Fig. 6.9, for each DW-type and each current sign, results in the extraction of stopping field values which are outside the observed pinning ranges. This is a clear indication that the 1D-model is sometimes too simple to describe the real systems, since the stopping field has to be contained in the pinning range [139].

For the extraction of the effective DMI in the Pt\Co\AlO_x samples under investigation, the alternative method presented in the previous chapter will be employed. As shown in Chapter 5, such alternative method for the extraction of the effective DMI from CIDWM data (like the ones reported in Fig. 6.9) is a reliable one. As already explained, the method is based on the following observation: the range of in-plane magnetic fields where the DWs are pinned (or move at low velocities) is expected to be centered around the DMI effective field, due to the symmetry of the SHE-SOT [139] (when the STT acting on the DW is much smaller than the SHE-SOT [25, 35]). The pinning range can thus be expressed as: $[H_{DMI}^{\uparrow\downarrow,\downarrow\uparrow} - \Delta H_x^{dep}, H_{DMI}^{\uparrow\downarrow,\downarrow\uparrow} + \Delta H_x^{dep}]$; where $H_{DMI}^{\uparrow\downarrow,\downarrow\uparrow}$ is the DMI effective field for $\uparrow\downarrow, \downarrow\uparrow$ DWs, $2\Delta H_x^{dep}$ the pinning range of longitudinal magnetic fields. Accordingly, the DMI effective field can be extracted as the center of the observed pinning ranges of H_x . Finally the strength of the DMI can be obtained by the equation $D = \mu_0 H_{DMI} M_s \lambda_{DW}$ [45, 138].

The protocol used for the extraction of the two stopping fields, $\mathbf{H}_x^{\uparrow\downarrow}$ and $\mathbf{H}_x^{\downarrow\uparrow}$, is described in the following. This is done for each type of domain wall, for both positive and negative currents. First of all, it is taken note of the magnetic field value, \mathbf{H}_1 , at which corresponds the highest measured v_{DW} in the reversed direction. Such velocity is here assumed to be the threshold velocity, \tilde{v}_{DW} , which defined the boundary between the low velocity regime (pinning regime) and the high velocity regime. Second, it is looked for the data point with the same absolute value of the velocity, but with opposite sign, and the magnetic field at which it occurs, \mathbf{H}_2 . These two values of the applied magnetic field are used as extremes of the pinning range, and the corresponding stopping field, $\mathbf{H}_{stop}^{+,-}$ is

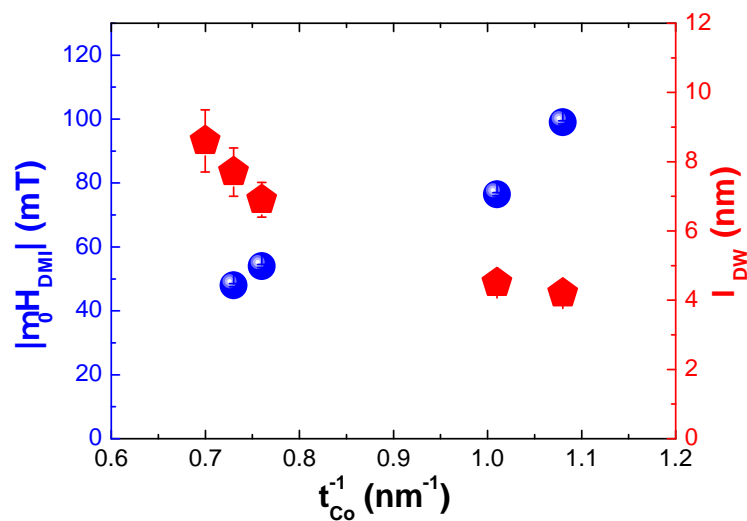
calculated as the arithmetic mean of the two. Two stopping fields are calculated for each type of DW (when this is possible), corresponding to $j_a > 0$ (\mathbf{H}_{stop}^+) and $j_a < 0$ (\mathbf{H}_{stop}^-), and the average stopping field for each DW's type is obtained as $\mathbf{H}_x^{\uparrow,\downarrow} = \frac{\mathbf{H}_{stop}^+ + \mathbf{H}_{stop}^-}{2}$.

Let us consider the case of D1, reported in Fig. 6.9(a). For $\uparrow\downarrow$ -DWs it is obtained: $\mu_0 H_1 = 158.0 \pm 0.5$ mT (the error on the magnetic field comes from the accuracy of the measurement by the Gauss-meter) and $\mu_0 H_2 = 19.5 \pm 0.5$ mT, resulting in $\mu_0 H_{stop}^+ = 89.0 \pm 0.5$ mT for $j_a > 0$; $\mu_0 H_1 = 180.0 \pm 0.5$ mT and $\mu_0 H_2 = 39.0 \pm 0.5$ mT, resulting in $\mu_0 H_{stop}^- = 109.5 \pm 0.5$ mT for $j_a < 0$. As a result, the extracted stopping field for the $\uparrow\downarrow$ -DW is $\mu_0 H_x^{\uparrow\downarrow} = \frac{\mu_0 H_{stop}^+ + \mu_0 H_{stop}^-}{2} = 99.0 \pm 0.5$ mT. On the other hand, for the $\downarrow\uparrow$ -DW it is obtained: $\mu_0 H_1 = -158.0 \pm 0.5$ mT and $\mu_0 H_2 = -19.5 \pm 0.5$ mT, resulting in $\mu_0 H_{stop}^+ = -89.0 \pm 0.5$ mT for $j_a > 0$; $\mu_0 H_1 = -158.0 \pm 0.5$ mT and $\mu_0 H_2 = -58.5 \pm 0.5$ mT, resulting in $\mu_0 H_{stop}^- = -108.5 \pm 0.5$ mT for $j_a < 0$. As a result, the extracted stopping field for the $\downarrow\uparrow$ -DW is $\mu_0 H_x^{\downarrow\uparrow} = \frac{\mu_0 H_{stop}^+ + \mu_0 H_{stop}^-}{2} = -99.0 \pm 0.5$ mT. To these stopping fields correspond: $\mu_0 H_{DMI}^{\uparrow\downarrow} = -99.0 \pm 0.5$ mT and $\mu_0 H_{DMI}^{\downarrow\uparrow} = +99.0 \pm 0.5$ mT; resulting in an effective DMI field for D1 of $\mu_0 H_{DMI}^1 = \frac{\mu_0 H_{DMI}^{\uparrow\downarrow} - \mu_0 H_{DMI}^{\downarrow\uparrow}}{2} = -99.0 \pm 0.5$ mT.

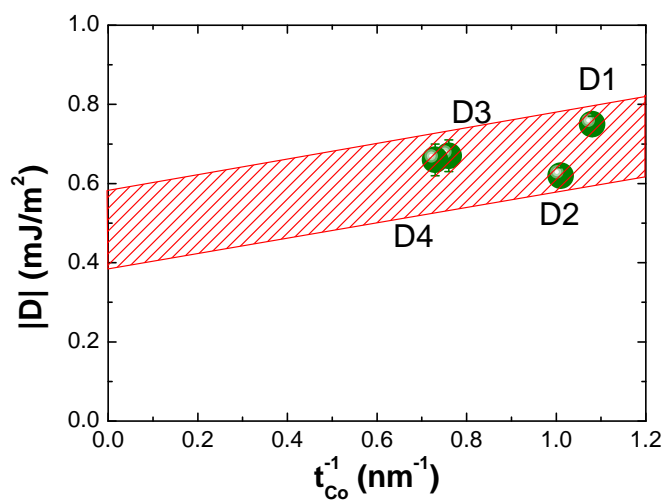
In order to extract the effective DMI coefficient, D , the DW width needs to be calculated first. For D1, $\lambda_{DW} = \sqrt{A/K_{eff}} = 4.2 \pm 0.1$ nm (where the used value for the exchange stiffness of the Co layer, $A = 3.1 * 10^{-11}$ J/m, is taken from [13]). Accordingly, the effective DMI in D1 results to be $D = \mu_0 H_{DMI}^1 M_s \lambda_{DW} = -0.75 \pm 0.02$ mJ/m².

The same process is repeated for D2, D3 and D4, extracting the respective effective DMI field and DMI strength, which are reported in Fig. 6.10(a) and Fig. 6.10(b), respectively. All the data about the five devices are summarized in Tab. 6.2. For D5 it is not possible to extract an effective DMI value. The lack of observations of DW motion in the pinning regime, due to the nucleation issue described above, does not allow to employ the DMI extraction method used for the other four devices.

Looking at Tab. 6.2 and Fig. 6.10(b), it is possible to recognize a clear trend in the changing of the effective DMI coefficient with the Co thickness. The measured effective DMI strength decreases with increasing t_{Co} . This is in qualitative agreement with an interfacial DMI scenario, where the effective DMI strength is expected to be proportional to $1/t_{FM}$: $D \propto \frac{D_{int}}{t_{FM}}$, with D_{int} being the pure interfacial DMI. However, as shown by the dashed area in the graph (which is only a guide to the eye), a hypothetical linear



(a)



(b)

FIGURE 6.10: **Extracted DMI effective values for $\text{Pt}/\text{Co}(t_{\text{Co}})/\text{AlO}_x$.** (a) Extracted DMI effective field, $|\mu_0 H_{\text{DMI}}|$, and DW's width, λ_{DW} , as a function of t_{Co}^{-1} . (b) Absolute value of the extracted DMI coefficients, $|D|$, as a function of t_{Co}^{-1} . Values missing for D5, due to the impossibility of extracting them from the available data points in Fig. 6.9(e). The dashed area is a guide to the eye.

fitting of the data points would not generate a linear curve that crosses the origin of the axes. The crossing for $t_{Co}^{-1} \rightarrow 0$ would happen at a finite value of the ordinate axis.

These observations are in agreement to what observed by Cho et al. [150] for a Pt\Co system, and by Nembach et al. [156] for a Pt\Ni₈₀Fe₂₀ system. Cho and co-authors observed a linear dependence of the effective DMI strength, D , on t_{Co}^{-1} for $t_{Co}^{-1} > 0.5 \text{ nm}^{-1}$ (like in the present study), and a rapid drop of D for $t_{Co}^{-1} < 0.5 \text{ nm}^{-1}$, going to zero at $t_{Co}^{-1} \rightarrow 0$ [150]. Nembach and co-authors obtained similar results and attributed their observations to a non-trivial dependence of the interfacial DMI strength, D_{int} , on t_{FM}^{-1} [156]. These findings give rise to new questions concerning the microscopic origin of the interfacial DMI and on the non-interfacial contributions to it coming from the FM and the HM layers.

Finally, the extracted D for Device 2 is out of the general trend followed by the other data points. It is still not clear why this low value of the DMI is extracted for D2. A possible explanation is the malfunctioning of the patterned device, even if its measured electrical DC resistance (60Ω) is in line with the ones measured for all the other devices. The next step is to measure another device on the sample with the same t_{Co} , and compare again the new results with the actual ones. However, due to lack of time, these measurements could not be carried out before the writing of this thesis.

Device#	λ_{DW} (nm)	$\mu_0 H_{DMI}$ (mT)	D (mJ/m ²)
1	4.2(0.1)	-99(0.5)	-0.75(0.02)
2	4.5(0.2)	-76.5(0.5)	-0.62(0.02)
3	6.9(0.5)	-54(0.5)	-0.67(0.04)
4	7.7(0.7)	-48(0.5)	-0.66(0.04)
5	8.6(0.9)	---	---

TABLE 6.2: **DMI effective values for Pt\Co(t_{Co})\AlO_x.** Values of the DW's width, the effective DMI field, and the effective DMI coefficient for each of the five investigated devices. No H_{DMI} and D values are ported for D5, due to the impossibility of extracting them from the available experimental data. In parentheses are the values of the error.

The extracted DMI coefficients reported in Tab. 6.2 are of negative sign. This means that a negative DMI is observed in this material system, which is in agreement with other observations obtained in material stacks where a bottom Pt layer was in direct contact with a ferromagnetic layer [25, 138, 148, 156]. As a consequence, left-handed homo-chiral DWs are expected to be present in the studied material stack, as illustrated in Fig. 6.11.

<i>Device#</i>	$\mu_0 H_{\perp}$ (mT)	K_{\perp} (J/m ³)	D_c (mJ/m ²)	$ D $ (mJ/m ²)
1	111(3)	$9.9 * 10^4(0.3 * 10^4)$	0.53(0.02)	0.75(0.02)
2	110(5)	$9.9 * 10^4(0.5 * 10^4)$	0.57(0.04)	0.63(0.02)
3	95(7)	$8.5 * 10^4(0.6 * 10^4)$	0.75(0.08)	0.67(0.04)
4	89(8)	$8.0 * 10^4(0.7 * 10^4)$	0.78(0.10)	0.66(0.04)
5	83(9)	$7.5 * 10^4(0.8 * 10^4)$	0.82(0.12)	---

TABLE 6.3: **Critical DMI values for the Pt\Co(*t*_{Co})\AlO_x devices.** Values of the DW's anisotropy field, anisotropy energy density, critical DMI strength and effective DMI strength for each of the five investigated devices. No value for D is ported for D5, due to the impossibility of extracting it from the available experimental data. In parentheses are the values of the error.

As in the previous chapter, also in this case we use the concept of DW's anisotropy [45, 140], which defined the energy needed to change the DW's configuration from Bloch to Néel, by applying an external magnetic field. The effective DW's anisotropy field is defined as $H_{\perp} = N_x M_s = \frac{\ln(2)t_{FM}}{\pi\lambda_{DW}} M_s$. The values of $\mu_0 H_{\perp}$ for the 5 devices are reported in Tab. 6.3. The corresponding anisotropy energy densities are given by $K_{\perp} = \frac{1}{2}\mu_0 H_{\perp} M_s$, and finally the critical DMI constants defined as $D_c = \frac{4\lambda_{DW}K_{\perp}}{\pi}$. All values are reported in Tab. 6.3, where, in order to allow a direct comparison, the absolute values of the extracted DMI coefficients are included as well.

The extracted DMI strengths are very close to the corresponding critical values. However, it is also observed that the extracted D and the calculated D_c have a different trend as a function of the Co layer's thickness. The effective DMI is observed to decrease with increasing t_{Co} , while the critical value D_c is expected to increase with increasing t_{Co} . This results in a particular t_{Co} where D becomes smaller than D_c . In this particular experiment, the cross point is observed to be in between the two thicknesses of the Co layer in D2 and D3. Accordingly, the DW internal configuration is expected to change from a fully Néel configuration (D1, thin Co), to a hybrid configuration with a predominant Néel-component (D5, thick Co). This should influence the dependence of v_{DW} on H_x in the five different devices, due to a different dependence of the DW magnetization's angle on the applied magnetic field. However, as it will be discussed in the next section, no clear evidence of this difference is visible from the experimental results here reported. The homo-chiral Néel DWs stabilized by the DMI are schematically shown in Fig. 6.11(a).

The large effective DMI coefficients here obtained give the possibility to explain one

more observation. As it is possible to see in the Kerr microscopy pictures contained in Fig. 6.4 and Fig. 6.8, the DWs' surface appears to be not orthogonal to the NW's axis. The DWs are visibly tilted away from the expected normal configuration, which would be the energetically most favorable configuration from a magnetostatic point of view, since the DW's energy is proportional to its surface's area. However, this is not the observed situation.

In order to understand such observation, it is necessary to take under consideration the strong DMI characterizing the investigated devices. As explained by Boule et al. [157], DMI in PMA material systems can induce a tilt of the DW's surface when the DW dynamics is driven by an applied easy-axis magnetic field or a spin-polarized current. Furthermore, the tilt of the DW increases with an increasing DMI strength, in a non-trivial way. This explains why such a DW tilt is not observed for the Ta/CoFeB/MgO system in Chapter 5, where the extracted DMI strength is one order of magnitude lower than what is reported here for Pt/Co/AlO_x. A similar tilt of the DW has been observed in another PMA material system with an effective DMI strength similar to what reported here [158]. However, the observed tilting of the DW is a dynamical effect. It is generated by the SHE-SOT acting on the DW's magnetization, resulting in a dynamical tilting angle, χ , which has a non-trivial dependence on the SHE-effective field of the type [157]: $\tan(\chi) \propto \frac{H_{SHE}}{\sigma} \cos(\phi)$, with $\chi(\phi)$ being the DW's tilting angle (DW's magnetization angle) with respect to the longitudinal axis of the NW, and $\sigma = \sigma(D)$ the DMI-dependent DW energy density. The tilt of the DW should be observable only during the injection of the current pulse, when a non-zero torque acts on the DW's magnetization. Instead, such effect is visible in our experiments, where the magnetization configuration is imaged a few seconds after the end of the pulse injection. At the moment of the image's acquisition the DW is stationary, in its final position [157], with no torque acting on it.

The reason why a DW's tilt is present in the images reported in this study is the edge roughness of the nanowires. During the pulse injection, the DW starts to move, and its surface is tilted by the presence of the torque. After the pulse injection, the DW would relax in its minimum energy state, if the system was ideal. However, in a real device the DW is pinned to the edge roughness, which prevents the relaxation of the DW and allows us to image a tilted DW. In turn, the tilting angle observed in our images is expected to be a lower limit for the actual tilt during the DW motion, since the resulting DW's profile is expected to be in between the theoretically predicted dynamical profile

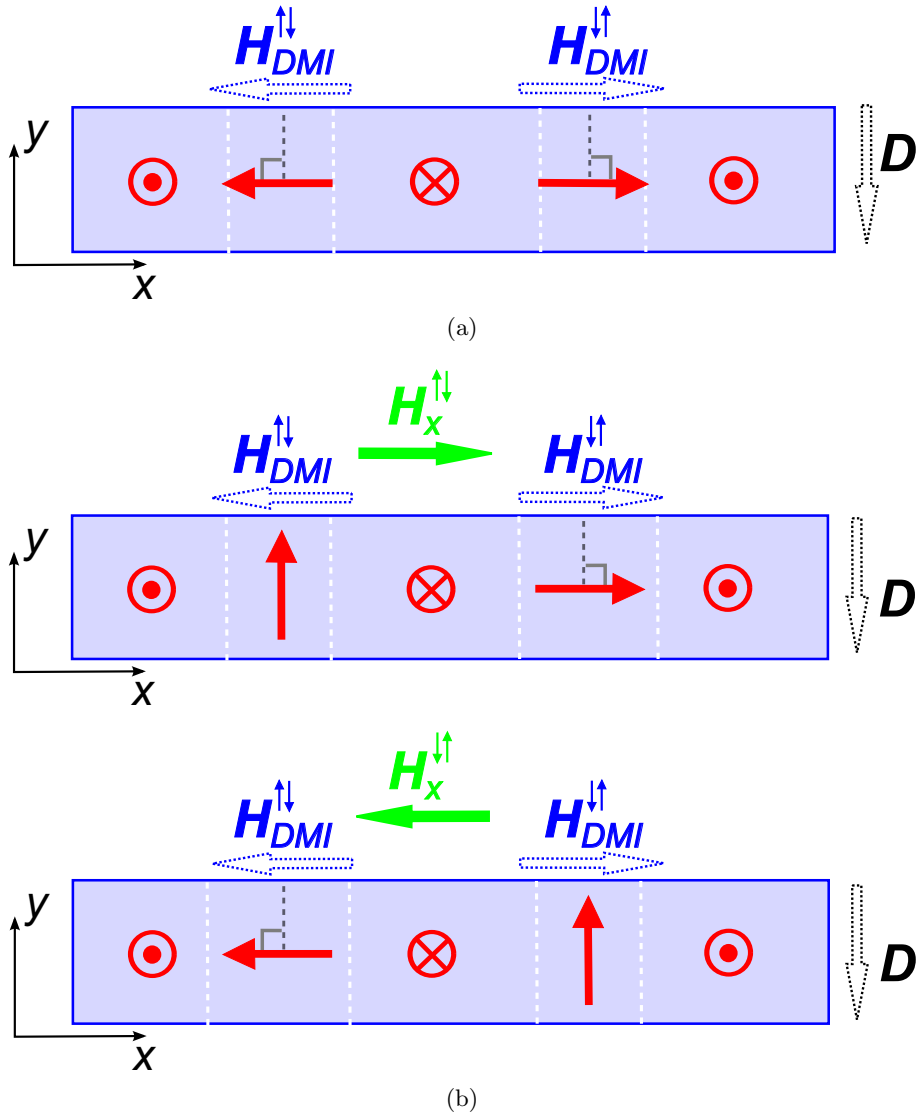


FIGURE 6.11: **Chiral domain walls in $\text{Pt}/\text{Co}(t_{\text{Co}})/\text{AlO}_x$.** (a) $\uparrow\downarrow$ (left) and $\downarrow\uparrow$ (right) chiral DWs stabilized by a negative DMI at the bottom Pt/Co interface. The blue arrows indicate the built-in DMI effective fields at the DWs' location. The case illustrated here is for $D \geq D_c$. (b) Re-orientation of the DWs' magnetization by an external longitudinal field, \mathbf{H}_x . At the top (bottom), the magnetic configuration during the application of the stopping field for the $\uparrow\downarrow$ ($\downarrow\uparrow$) DW is illustrated. The SOT acting on the DW in the Bloch-configuration is expected to be null. When \mathbf{H}_x is applied in the same direction of \mathbf{H}_{DMI} , the Néel wall is enlarged, resulting in a larger DW's width, λ_{DW} .

and the profile with minimum surface (after the relaxation of the DW). The comparison between the observed experimental DW's tilting angle and micromagnetic simulations would give us an alternative way, to what reported above, to estimate the DMI in our systems.

6.7 Chiral DWs in Pt\Co\AlO_x moved by SOT

According to what is reported above, the observed CIDWM in the Pt\Co\AlO_x devices is due to the presence of a negative interfacial DMI and a positive SHE in the investigated material system. This results in the generation of an effective magnetic field, $\mathbf{H}_{SHE} = \frac{\hbar\theta_{SHE}|j_e|}{2\mu_0|e|M_s t_f} \hat{\mathbf{m}} \times (\hat{\mathbf{z}} \times \hat{\mathbf{j}}_e)$, at the DW's location, which is parallel with the magnetization of the domain that the conventional current, j_a , is coming from.

The SHA reported in the previous equation has to be considered as an effective value of the intrinsic SHE efficiency value. As discussed in the previous sections, due to the thin Pt layer present in our devices the effective spin current reaching the Pt\Co interface is expected to be between the 35% and 100% of the bulk spin current which would be generated in a thick Pt layer, with $t_{Co} \gg \lambda_{spin}^{Pt}$. Furthermore, only a fraction of the generated spin current actually crosses the interface, due to the spin-mixing conductance/spin-transparency [95–98] at the Pt\Co interface. As reported by Pai et al. [95] and Zhang et al. [96], the spin-transparency at the Pt\Co interface is around 60% for $t_{Co} > 1$ nm, and is observed to be even smaller for thinner Co layers [95]. Finally, spin-memory loss [99] is also expected to occur at the interface when the spin current generated in the Pt layer enters the Co layer. This would result in an additional reduction of the efficiency of the SHE-SOT, and additional ferromagnetic resonance measurements joined with spin pumping measurements would be necessary to quantify such a reduction in our systems [99].

The SHE-field contributes to the total effective field acting on the DW's magnetic moments, generating an additional precessional torque, $\boldsymbol{\tau}_{SHE,1} \propto -\hat{\mathbf{m}} \times \mathbf{H}_{SHE}$, and an additional dissipative torque, $\boldsymbol{\tau}_{SHE,2} \propto -\hat{\mathbf{m}} \times (\hat{\mathbf{m}} \times \mathbf{H}_{SHE})$, which result in the motion of DWs along the direction of the conventional current, in the zero-field case (see Fig. 6.12(a)). This is all analogous to what is observed in the Ta\CoFeB\MgO NWs. The reason is that both the DMI and the SHE have opposite sign in the two material stacks, resulting in the generation of a \mathbf{H}_{SHE} that has the same symmetry in both systems.

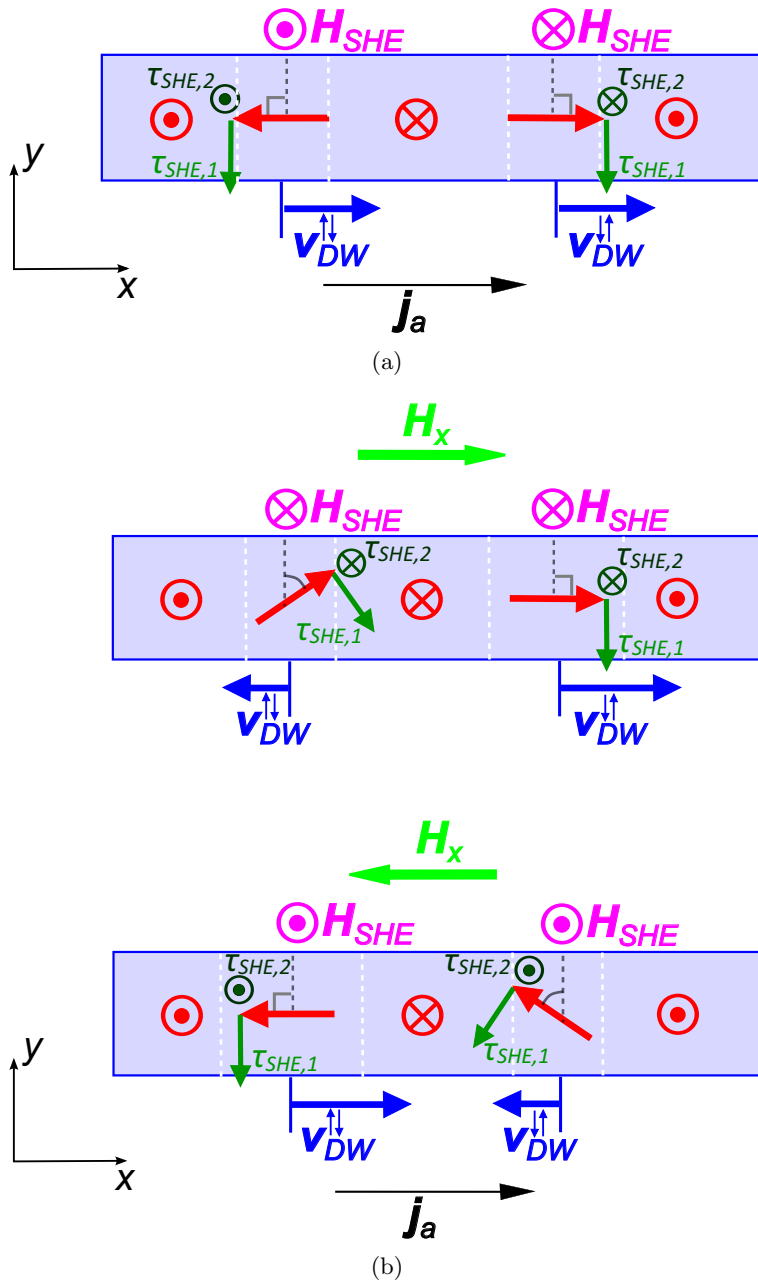


FIGURE 6.12: **Chiral DWs in Pt/Co/AlO_x moved by the SOT.** (a) DW motion driven by SOT in Pt/Co/AlO_x NWs, at zero-field. DWs are stabilized by the DMI in a homo-chiral Néel state. The effective SHE-field acts locally on the DWs, pointing in opposite directions for $\uparrow\downarrow$ and $\downarrow\uparrow$ DWs. The result, due to the action of the precessional torque, $\tau_{SHE,1}$, and of the dissipative torque, $\tau_{SHE,2}$, on the DW's magnetic moments, is the motion of both DWs with \mathbf{j}_a in lock-steps. (b) Applying an external magnetic field, \mathbf{H}_x , along the NW's length, the DW's internal magnetization is rotated (the DW's width is increased) for \mathbf{H}_x anti-parallel to \mathbf{H}_{DMI} (\mathbf{H}_x parallel to \mathbf{H}_{DMI}). The velocity of DWs with intrinsic \mathbf{m}_x parallel to the field is increased, while for DWs with intrinsic \mathbf{m}_x anti-parallel to the field the velocity is reduced. In case the applied field is stronger than the anti-parallel \mathbf{H}_{DMI} , the DW's velocity can be changed in sign. This sketch tries to explain the experimental observations reported in Fig. 6.9.

However, when a finite longitudinal field is applied, the internal magnetic structure of the DW is changed, and different effects are obtained in the two material systems. Indeed, only the DMI defines the chirality of the DWs, and the DMI has been found with opposite sign and with different magnitude in the two material stacks.

Similarly to what reported in Chapter 5, in case the Néel-component of the DW's magnetic moments, \mathbf{m}_x , is initially anti-parallel to the applied field, the magnetization will rotate to the Bloch-configuration and then eventually reverse in the opposite direction along the longitudinal direction. In turn, \mathbf{H}_{SHE} is reduced to zero and then reversed. This results in the stopping and then in the reversal of the DW's velocity for increasing H_x , as reported in Fig. 6.9 and illustrated in Fig. 6.12(b).

On the other hand, when \mathbf{m}_x is parallel to the applied field, the main effect of \mathbf{H}_x is not the increasing of the Néel-component of the DW, or at least not only that. The DWs are expected already to be mainly of the Néel type, due to the strong DMI extracted for the present material stack. As a result, the application of \mathbf{H}_x is expected to increase the width of the Néel DW, as illustrated in Fig. 6.12(b). Accordingly, as suggested by Martinez et al. [139], the increasing of the DW's width is one more ingredient in the description of the final DW's velocity as a function of an applied longitudinal field. Furthermore, the tilting angle of the DW during its motion is also to take into account in the description of the DW's dynamics. Indeed, in the 1D model including the tilting angle of the DW, the final velocity of the DW is expected to be given by the following expression [139] (at high current densities):

$$v_{DW} = \frac{\gamma\lambda_{DW}}{\cos(\chi)} \frac{\pi}{2} (H_{DMI} + H_x) \cos(\phi), \quad (6.1)$$

with χ being the angle between a vector normal to the DW's surface and the NW's axis (defining the DW's tilt), ϕ the DW's magnetization angle with respect to the NW's axis. According to Eq. 6.1, the DW velocity along the NW is expected to be directly proportional not only to H_x , but also to the term $\frac{\lambda_{DW} \cos(\phi)}{\cos(\chi)}$. The experimental results reported in Fig. 6.9, for each device, are qualitatively in agreement with Eq. 6.1, suggesting a constant value for the term $\frac{\lambda_{DW} \cos(\phi)}{\cos(\chi)}$ with respect to the applied \mathbf{H}_x .

In order to understand better the description of the experimental results offered by Eq. 6.1, let us analyze the expected effect of the applied field on the two angles χ and ϕ . Here we focus our attention on the fast DW motion case, with the external magnetic

field being parallel to the intrinsic Néel component of the DW magnetization.

According to the predictions by Martinez et al. [139], an applied in-plane field parallel to the intrinsic Néel-component of the DW's magnetic moments results in the stabilization of such Néel-component. In turn, during the application of a current pulse, the precessional torque, $\tau_{SHE,1}$, rotates the magnetic moments of the DW away from the Néel configuration of a smaller angle, ϕ , than at zero-field. This results in a decreasing ϕ with an increasing H_x , during the DW motion. As a consequence, also χ is expected to decrease with increasing H_x , due to the strong DMI characterizing the investigated samples, resulting in $\frac{\cos(\phi)}{\cos(\chi)}$ being a non-trivial function of H_x .

Experimentally, the reduction of χ with increasing H_x has been actually observed, as reported in Fig. 6.13. The bright and dark areas in the figure indicate the DW displacements in the NWs due to the current pulse injection. The measured final tilting angles, at the end of the CIDWM, are observed to be smaller in presence of \mathbf{H}_x parallel to the intrinsic Néel component of the DW. The tilting angle in the presence of $H_x = 136$ mT, is observed to be reduced of about the 50% compared to the case at zero-field, as shown in Fig. 6.13. This is observed for both $\downarrow\uparrow$ (left side) and $\uparrow\downarrow$ (right side) DWs. Finally, the tilting angle is observed to be positive for the $\uparrow\downarrow$ -DW and negative for the $\downarrow\uparrow$ -DW. This is in agreement with the presence of a SHE-SOT, in a material system with a positive SHA and a negative DMI [139, 157], as here reported.

Concerning the effect of an applied longitudinal field on the DW width, λ_{DW} is expected to increase when an increasing \mathbf{H}_x is applied parallel to the intrinsic Néel-component of the DW's magnetization. In Fig. 6.14 are reported both the DW's width and its normalized value (with respect to the zero-field value), as a function of the applied parallel in-plane field. The values of λ_{DW} as a function of H_x are obtained by micromagnetic simulations⁵. The static magnetic configuration of a DW in a magnetic NW with PMA, characterized by the same magnetic parameters of D1, was micromagnetically simulated. The Thiele definition of DW width, $\frac{2}{(\lambda_{DW})_{Thiele}} = \frac{1}{S} \int (\frac{\partial \mathbf{m}}{\partial x})^2 d^3r$ [48], as been here employed for the extraction of $(\lambda_{DW})_{Thiele}$ from the simulations outcome. In the previous equation, S is the cross section of the NW, \mathbf{m} the normalized magnetization vector in the DW and x the longitudinal direction parallel to the NW axis. In Fig. 6.14 the DW

⁵The DW's magnetization state for a PMA ferromagnetic nanowire with the same magnetic parameters of D1 has been simulated employing the micromagnetic software Micromagn. This was a courtesy of Mr. Andrea De Lucia, a colleague PhD student in Physics at the Johannes Gutenberg Universität Mainz.

width extracted from the micromagnetic simulations is observed to increase monotonically with increasing H_x , reaching a 33% increase for H_x equal to the highest magnetic field experimentally applied. The situation in the real experiments is expected to be in line, at least from a qualitative point of view, with the simulations outcome.

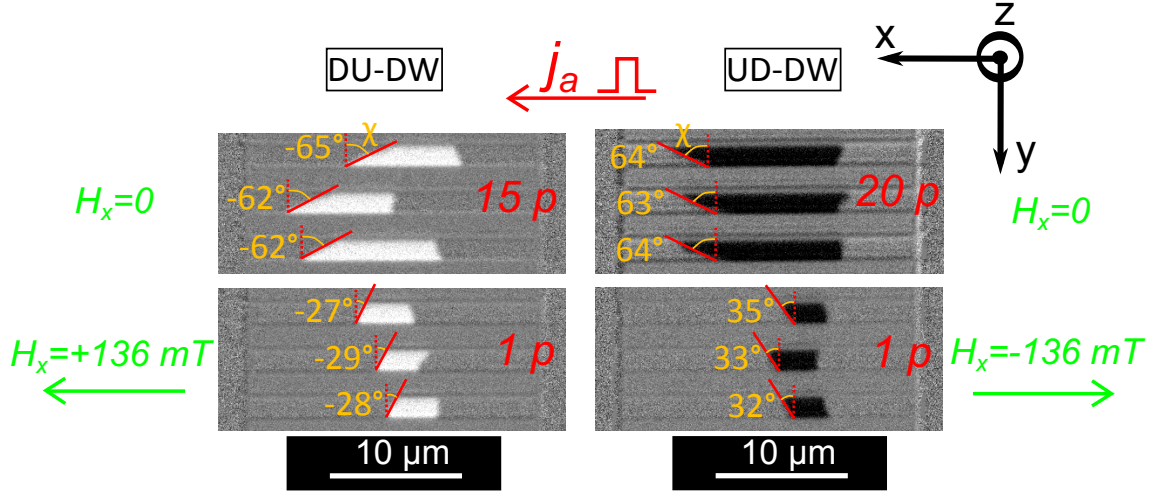


FIGURE 6.13: **Tilting of chiral DWs in Pt/Co/AlO_x NWs in the presence of an in-plane longitudinal field.** Illustration of the DW's tilting angle, at the end of the DW motion (indicated by the bright and dark areas in the NWs). The tilting angle is observed to be reduced in the presence of an applied in-plane field parallel to the intrinsic DW magnetization, for both $\downarrow\uparrow$ (DU) and $\uparrow\downarrow$ (UD) DWs. The injected current density is $j_a = 8.7 \times 10^{11} \text{ A/m}^2$, while the longitudinal field's amplitudes are: $\mu_0 H_x = +136 \text{ mT}$ (DU) and $\mu_0 H_x = -136 \text{ mT}$ (UD). The red numbers indicate how many pulses are used to generate the illustrated DWs' displacements. The gold numbers indicate the tilting angles, χ , of the DWs in the NWs. The angles χ shown in the figure are rotated of -90° with respect to the definition contained in the text. The images refer to Device 1.

According to the discussion above, both the ratio $\frac{\cos(\phi)}{\cos(\chi)}$ and λ_{DW} are expected to be dependent on H_x . Since λ_{DW} increases with an increasing parallel H_x , as observed in micromagnetic simulations, the ratio $\frac{\cos(\phi)}{\cos(\chi)}$ should decrease instead, in order to explain the almost constant slopes, $\frac{\partial v_{DW}}{\partial H_x}$, observable in Fig. 6.9. However, a full micromagnetic simulation of the SHE-SOT-induced DW motion is needed to gain a more detailed understanding of the reported results and to extract the efficiency of the torque producing the DW motion, as explained by Martinez et al. [139].

Observing the results for the different devices, it is possible to see that the slope with which v_{DW} increases as a function of H_x is larger for devices with thicker Co layers. In Fig. 6.15, the data points represent the measured v_{DW} in the 5 devices, for $\downarrow\uparrow$ -DWs and $j_a > 0$, as a function of H_x parallel to the intrinsic Néel-component of the DW's magnetization. The lines are the fitting linear curves of the experimental data, for the

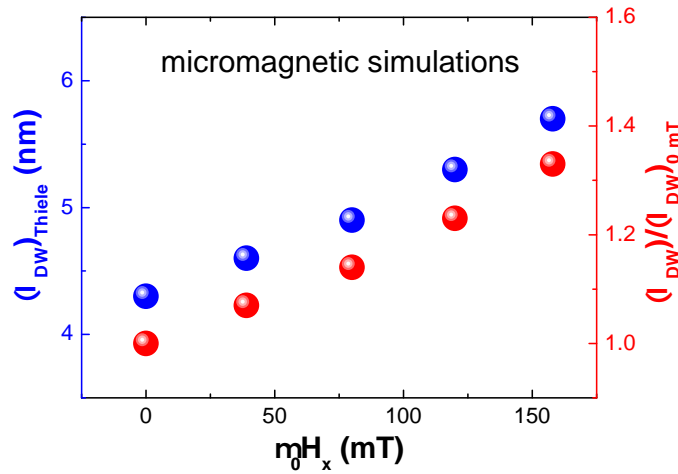


FIGURE 6.14: **DW width in the presence of an in-plane longitudinal field.** Width of the DW and its normalized value (with respect to the width at zero field) as a function of H_x applied parallel to the intrinsic Néel-component of the DW's magnetization. The reported data are the outcome of micromagnetic simulations. The static DW's width of a PMA magnetic nanowire with the same magnetic parameters of D1 is extracted in the presence of an in-plane field, H_x , with different amplitudes. Simulations are a courtesy of Mr. Andrea De Lucia (Johannes Gutenberg Universität Mainz).

five devices. The linearity coefficient of the fitting curves is observed to increase, apart from the case of D2, with increasing t_{Co} (from D1 to D5).

As reported in Tab.s 6.1 and 6.2, the increasing thickness of the ferromagnet results in a smaller PMA, generating wider DWs in the patterned NWs. This suggests that the increase of the DW width with increasing t_{Co} is one of the reasons why the slope $\frac{\partial v_{DW}}{\partial H_x}$ (given by the linearity coefficient of the fitting curve) is observed to increase from D1 to D5. Figure 6.16 reports $\frac{\partial v_{DW}}{\partial H_x}$ and λ_{DW} (at zero-field), normalized to the respective values for D1, as a function of t_{Co} . The relative change of the DW's width and of the linearity coefficient with respect to t_{Co} are very similar, almost the same in the error bars. This seems to indicate that the observed increasing $\frac{\partial v_{DW}}{\partial H_x}$ with an increasing Cobalt thickness is mainly due to an increase of the DW's width, λ_{DW} , as described by Eq. 6.1.

Finally, just a comment about the possibility of using the DMI extraction procedure based on the linear fitting of the high velocity data points. By the linear fitting procedure we extract stopping fields (the value of H_x at which the fitting curves cross the abscissa axis in Fig. 6.15) that are outside the pinning range. Furthermore, the dependence

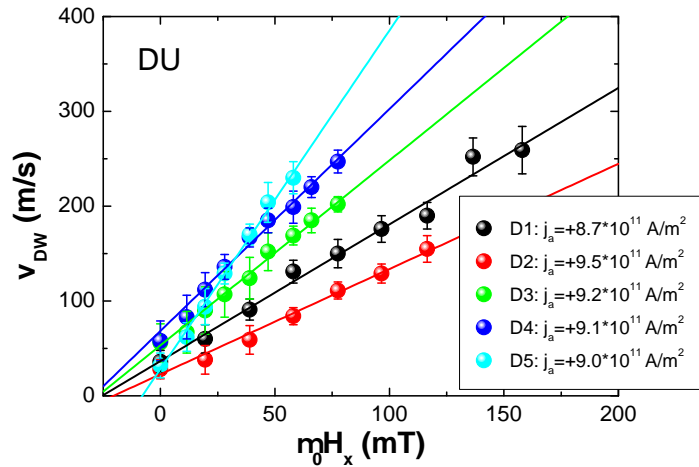


FIGURE 6.15: DW velocity increase in Pt\Co(t_{Co})\AlO_x NWs in the presence of an in-plane longitudinal field. High velocity data points for the $\downarrow\uparrow$ (DU) DW with respect to H_x parallel to the intrinsic Néel-component of the DW's magnetization, for the 5 studied devices. The reported data points refer to measurements with $j_a > 0$. The lines are the linear fitting curves for the 5 different measurements. The linearity coefficient is found to generally increase with increasing t_{Co} (from D1 to D5).

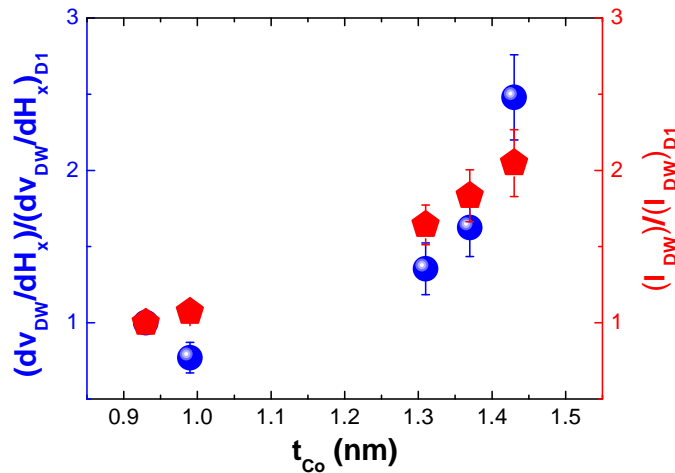


FIGURE 6.16: DW velocity dependence on longitudinal field as a function of the Co thickness in Pt\Co(t_{Co})\AlO_x NWs. The normalized slope, $(\frac{\partial v_{DW}}{\partial H_x})/(\frac{\partial v_{DW}}{\partial H_x})_{D1}$, and DW's width, $(l_{DW})/(l_{DW})_{D1}$, as a function of the Cobalt thickness. The relative changes for the two quantities as a function of t_{Co} are very similar. This suggests that the main origin for the increasing $\frac{\partial v_{DW}}{\partial H_x}$ with increasing t_{Co} is the increase of the DW's width.

of such stopping fields on t_{Co} is not a monotonous decrease with increasing thickness, resulting not in agreement with theoretical predictions [45] and existing experimental observations [148, 150, 156]. Emblematic is the observation, in Fig. 6.15, that the stopping fields for D3 and D4 are larger than the one for D1, which is the device where the largest stopping field is expected to be observed, having the thinnest Co layer among the five devices. All this is in support of the alternative methodology employed in this chapter for the extraction of the DMI strength in the investigated devices, which allows us to extract a dependence of the effective DMI on t_{Co} in line with what is reported in literature [148, 150, 156].

6.8 Conclusion and outlook

In the present chapter, the observed current-induced domain wall motion in magnetic nanowires made of Pt\Co(t_{Co})\AlO_x, for five different Cobalt thicknesses, is reported. First of all, the velocity of the DWs is measured as a function of the current density flowing into the nanostructures. The DWs are observed moving against the direction of motion of the conduction electrons, in all the five investigated devices. Such a DW motion is compatible with an explanation based on a damping-like torque generated by the spin-Hall effect in the bottom Pt layer.

Secondly, the effect of a longitudinal magnetic field on the CIDWM is investigated. The DW's velocity is strongly dependent on the applied magnetic field, and such a dependence is found to be symmetric for $\uparrow\downarrow$ - and $\downarrow\uparrow$ -DWs, with respect to the sign of the applied field: $v_{DW}^{\uparrow\downarrow}(j_a, H_x) = v_{DW}^{\downarrow\uparrow}(j_a, -H_x)$. The observations for the five devices are qualitatively the same. This is interpreted as the presence of an interfacial Dzyaloshinskii-Moriya interaction at the interface between the heavy metal layer and the ferromagnetic layer. The effective DMI is found to range between $D = (-0.75 \pm 0.02)$ mJ/m² and $D = (-0.62 \pm 0.02)$ mJ/m², in general decreasing with increasing t_{Co} , in agreement with the interpretation based on an interfacial origin of the effect. The observed DMI generates left-handed homo-chiral Néel DWs in the investigated NWs.

Furthermore, in agreement with the description of the SHE-SOT-driven DW motion in the 1D model-framework including the DW's tilt, the DW width is found to be one of the key parameters in the definition of the dependence of the observed DW velocity with respect to t_{Co} .

For a more quantitative interpretation of the experimental data, full micromagnetic simulations are required. The strong DMI characterizing the investigated NWs makes the analysis of the DW motion not trivial, due to the strong influence on the DW's geometry, which in turn influences the effective DW speed. Furthermore, the role of the ISGE on the DW motion should also be taken into account [129, 140, 151, 159]. Finally, in order to obtain a better estimation of the intrinsic efficiency of the torques acting on the DW, harmonic voltage measurements, ferromagnetic resonance measurements and spin pumping measurements are necessary to estimate the spin-transparency and the spin-memory loss at the Pt/Co interface in our devices [95, 96, 99].

Chapter 7

General conclusion and outlook

Current-driven magnetization manipulation was studied in magnetic nanostructures made of Ta\CoFeB\MgO and Pt\Co\AlO_x. The two material systems under investigation were characterized by structural inversion asymmetry (SIA) and perpendicular magnetic anisotropy (PMA), resulting in a magnetization pointing out-of-plane. The investigation was carried out employing lithographically patterned nanowires (NWs), whose magnetization state was imaged by Kerr microscopy.

Current-induced magnetization switching was studied in Ta\Co₂₀Fe₆₀B₂₀\MgO NWs [125]. The switching effect was observed for current densities of the order of 10¹¹ A/m², employing 100 ns- and 100 ms-long current pulses. The symmetry of the switching process was found to be consistent with the action of a damping-like spin-orbit torque (SOT) originating from the spin-Hall effect (SHE) in the bottom Ta layer, with a negative spin-Hall angle [68]. Furthermore, the process was found to depend on the length of the pulse, mainly due to thermal effects. The experimental data could be reproduced by employing a generalized Néel-Brown model for thermally-assisted current-induced magnetization switching [65].

Current-induced domain wall motion was also investigated in magnetic nanowires made of Ta\Co₂₀Fe₆₀B₂₀\MgO [128]. The DWs were observed to move against the direction of motion of the conduction electrons, at an increasing velocity with an increasing current density, in agreement with a SHE-SOT-driven DW motion [25, 27, 35]. The effect of a longitudinal magnetic field on the CIDWM was investigated as well. The DW's velocity was found to dependent strongly on the applied magnetic field, in a symmetric way for

$\uparrow\downarrow$ - and $\downarrow\uparrow$ -DWs. Such a dependence of the DW velocity on the longitudinal field can be described as $v_{DW}^{\uparrow\downarrow}(j_a, H_x) = v_{DW}^{\downarrow\uparrow}(j_a, -H_x)$. This was interpreted as due to the presence of an interfacial Dzyaloshinskii–Moriya interaction [45]. An effective DMI with a strength of $D = (+0.06 \pm 0.01)$ mJ/m² was extracted, indicating the presence of homochiral right-handed DWs. Such a positive DMI has been attributed to the presence of a Boron accumulation at the bottom interface in the material stack. Furthermore, reproducing the experimental results by 1D-model simulations, an effective spin–Hall angle value of $\theta_{SHE} = -0.11$ is obtained. The extracted positive DMI together with the negative SHE of Ta emerge as the key factors at the basis of the observed current-induced DW motion.

Finally, current-induced domain wall motion was studied in magnetic nanowires made of Pt\Co(t_{Co})\AlO_x, for five different Cobalt thicknesses ranging from $t_{Co} = 0.93$ nm to $t_{Co} = 1.43$ nm. The DWs were observed to move against the direction of motion of the conduction electrons, in all the five investigated devices. Such a DW motion is compatible with an explanation based on a damping-like SOT generated by the spin–Hall effect in the Pt bottom layer [25, 35]. Furthermore, in analogy to what observed for the Ta\CoFeB\MgO system, the DW velocity was found to depend strongly on an applied longitudinal magnetic field, as described by $v_{DW}^{\uparrow\downarrow}(j_a, H_x) = v_{DW}^{\downarrow\uparrow}(j_a, -H_x)$. A strong effective DMI was found to characterize the investigated devices, with a strength ranging between $D = (-0.75 \pm 0.02)$ mJ/m² and $D = (-0.62 \pm 0.02)$ mJ/m². The magnitude of the effective DMI was observed, in general, to decrease with an increasing t_{Co} , in agreement with the interpretation based on an interfacial origin of the effect [150, 156]. Furthermore, in agreement with the description of the SHE–SOT-driven DW motion in the 1D model-framework including the DW’s tilt [139], the width of the DW was found to be one of the key parameters in the definition of the dependence of the observed DW velocity with respect to t_{Co} .

At the end of this thesis, according to the presented results and the respective discussions, new open questions are left unanswered. Here, possible measurements are proposed that could help with finding an answer to some of them.

Concerning the Ta\CoFeB\MgO system, the observed positive DMI has here been attributed to the accumulation of Boron (B) at the Ta\CoFeB interface, due to the post-growth annealing procedure. The measurement of the effective DMI as a function of the nominal B concentration, in samples undergoing the same annealing process, would

offer a more detailed knowledge on the role of the B concentration on the definition of the DMI at the bottom interface. An alternative approach is to investigate identical as-deposited material stacks, annealed for different times and at different temperatures. This is also expected to generate a different accumulation of Boron at the bottom interface [146], providing the opportunity to study the dependence of the effective DMI on the B concentration at the Ta\CoFeB interface.

Regarding the Pt\Co\AlO_x system, in addition to the damping-like SOT originating from the SHE in Pt, a second torque with a different origin may be contributing to the observed DW motion. Harmonic voltage measurements could add new insight in this direction, since they allow to disentangle SOTs with different symmetry, distinguishing between damping-like and field-like torques [151]. The dependence of the two kind of torques on the Co thickness could reveal how interface-like (generated by the ISGE) or bulk-like (SHE) are the two torques. However, in order to not be misled in the analysis of the data, the spin-transparency and the spin-memory loss at the Pt\Co interface need to be quantified as well, by ferromagnetic resonance and spin-pumping measurements [95, 96, 99]. After that the dependence of the intrinsic torques' efficiencies on the Co thickness is revealed, it will be possible to understand more about the actual origin of the two torques. This, in turn, would also help to gain a better understanding of the DW motion here reported.

Appendix A

Temperature calibration during current pulse injection

In order to calibrate the effective temperature of the Ta\CoFeB\MgO nanowires during the pulse injection, the dependence of the sample resistance R_s on the measured temperature of the sample T_s was measured, with the sample in a cryogenic bath (He-bath). The temperature is swept between 130 K and 278 K, obtaining a change in the sample resistance from 134.2 Ω to 130.7 Ω , as reported in Fig. A.1. R_s is measured by a lock-in technique. A reduction of R_s is observed when the temperature of the sample increases. This indicates [160, 161] that a small part of the MgO tunnel barrier is still present in the location of the electric contacts, underneath the Au pads, despite the milling process carried out in order to remove the insulating layer and obtain a good metallic contact. By fitting the curve in Fig. A.1(a) linearly in the range of T_s 250-278 K, we extract a slope of -0.018 Ω /K (see Fig. A.1(b)).

Once that the trend of the sample resistance as a function of the temperature is obtained, R_s was measured as a function of the current flowing in the nanowires. Limited by the experimental set-up, the measurement of the change in R_s during the injection of ns-long current pulses (the pulse lengths used for the switching experiment reported in the main text in Fig. 4.10) was not possible. However, the resistance change in the nanowires (at a bath temperature T_b of 278 K), during the injection of a much longer 1 ms-long current pulse was measured. This ensured that the temperature in the nanowires reached a quasi-equilibrium value [162].

The experimental results are reported in Fig. A.2 (solid symbols), yielding a linear fitting curve (solid line) described by $R_s = (130.9(\pm 0.2) - 2.0(\pm 0.2) * j) \Omega$. Extrapolating the fitting curve for $j = 7 * 10^{11} \text{ A/m}^2$, a change in the resistance of $\Delta R_s = -(13.9 \pm 1.4) \Omega$ is obtained. Using the calibrated rate of $-0.018 \Omega/\text{K}$ above, the obtained change in temperature is $\Delta T = (770 \pm 80) \text{ K}$. Accordingly, a temperature $T_s(j = 7 * 10^{11} \text{ A/m}^2) \approx (1070 \pm 80) \text{ K}$ was extracted, for a 1 ms-long current pulse with $j = 7 * 10^{11} \text{ A/m}^2$ injected in the sample. The actual temperature in the nanowires during the injection of ns-long current pulses is expected to be much lower than this value [162], for the same current density amplitude.

The equation in [162] was used to determine the temperature rise for the ns-long pulses. This resulted to be less than half of the ΔT_s for the ms-long pulses value. Given that the Curie temperature of the magnetic material in the nanowires (as determined in [134]) is higher than 1000 K, the heating measured in the device here discussed remains far below the Curie temperature.

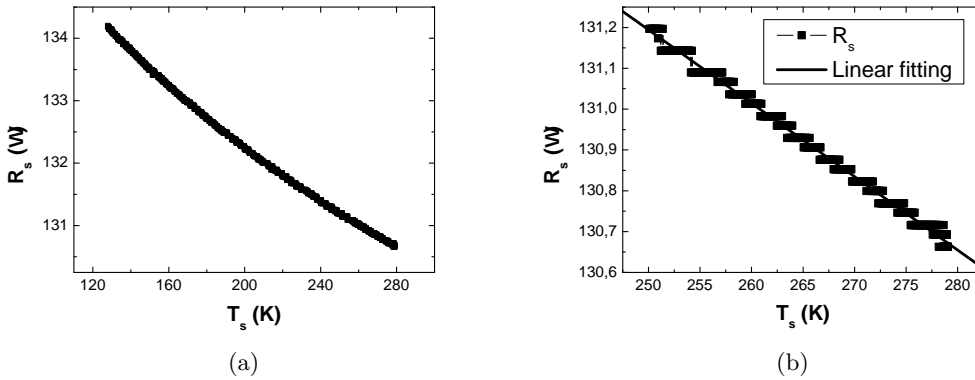


FIGURE A.1: **Sample resistance calibration during current pulse injection.** (a) Sample resistance as a function of the measured sample temperature, in the range 130–278 K. (b) Linear fitting of the resistance values as a function of the sample temperature, for the high temperature range. Such a linear fitting is used for the calculation of the actual temperature of the sample during current injection.

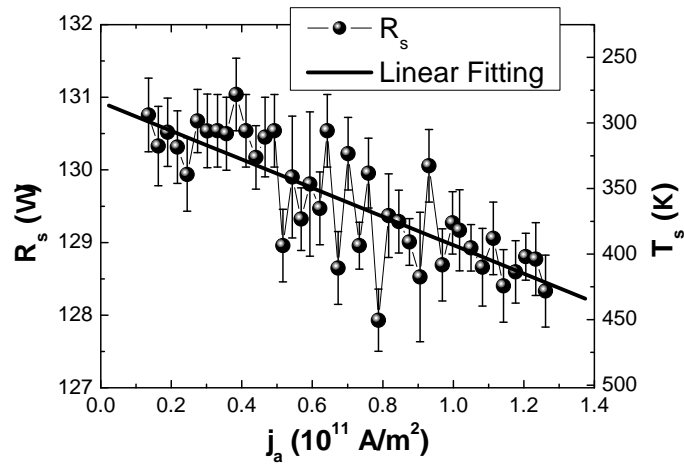


FIGURE A.2: **Sample resistance and temperature as a function of current density.** The solid symbols represent the measured resistance as a function of the injected current density in the NWs. The solid line represents the linear fitting of the measured values. On the right side, the extracted sample temperature. By extrapolation, it is possible to extract the sample temperature for higher current densities.

Appendix B

Current-induced domain wall motion in Pt\CoFeB\MgO nanowires

Current-induced DW motion was also imaged in a Pt(4.5)\Co₆₈Fe₂₂B₁₀(0.6)\MgO(1.5)¹ nanowire (thicknesses in nm) by x-ray magnetic circular dichroism combined with photoemission electron microscopy (XMCD-PEEM) ² [128]. The layout of the sample used for the experiment is shown in Fig. B.1. The magnetic structure (blue area) consisted of a magnetic pad connected to a magnetic nanowire. In this experiment, a magnetic nanowire 500 nm in width was investigated. On the two sides of the magnetic structure there were a ground pad and an Oersted-line (gold areas), which were used for the injection of current pulses through the structure. PEEM imaging was employed due to its higher spatial resolution compared to Kerr microscopy, with the intent of imaging smaller structures and their magnetic texture with a higher resolution.

As shown in Fig. B.2, DWs were observed to move along the electron-flow (indicated by the e-arrows) when a burst of current pulses ($j_a = 5 * 10^{11}$ A/m²) is injected in the nanowire. Reversing the current direction, the DW motion (DW-arrows) was also inverted in its direction.

¹The material stack was grown by Dr. A. P. Mihai, from the *School of Physics and Astronomy of the University of Leeds* (UK).

²The XMCD-PEEM experiments were carried out at the Nanoscience Beamline IO6 of the *DIA-MOND Light Source* synchrotron in Didcot, England (UK), with an ELMITEC microscope.

The observed DW motion with the electron-flow could be easily interpreted in the STT-model [6, 43]. However, this observation is in disagreement with what was observed in Pt/CoFe/MgO nanowires by Emori et al. [25]. They recently observed DWs moving against the electron-flow in their material system. According to the SOT-model, such a movement is due to the presence of a negative DMI at the Pt/CoFe interface (resulting in left-handed chiral Néel-domain walls), jointly with a positive SHE generated in the Pt bottom layer. Following the same interpretation, the experimental observations reported here suggest the presence of right-handed Néel-domain walls ($D > 0$) in the material system here discussed, since the sign of the Pt-SHE is not expected to change, being a bulk property of the heavy metal. This means that in our system D has an opposite sign with respect to the DMI coefficient reported for nanowires made of Pt/CoFe/MgO, corroborating the idea that the B contained in the system can play an important role in the definition of the sign of the DMI at the Pt/CoFeB interface.

However, this result is only a preliminary one. A more detailed study of the DMI in the material stack containing B is needed, in order to clearly identify which is the role (if any) of the B on the definition of the DMI in the multilayer.

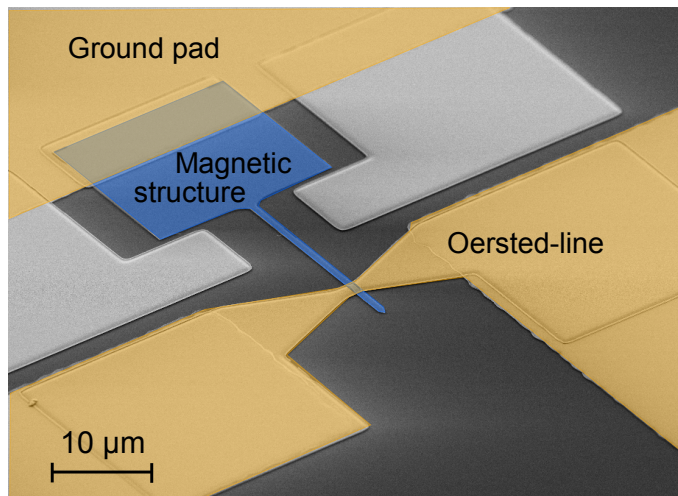


FIGURE B.1: **Layout of the sample used for PEEM imaging.** SEM micrograph of the sample (courtesy of Dr. A. Hrabec, from the *School of Physics and Astronomy of the University of Leeds* (UK)) used for the imaging of CIDWM in Pt/CoFeB/MgO by XMCD-PEEM. The blue area indicate the magnetic structure, consisting of a magnetic pad and a NW with a 500 nm width. On the other hand, the yellow areas indicate the ground pad and the Oersted-line (made both of them of Au), respectively at the top and the bottom of the image. Current pulses through the Oersted-line were used for nucleating DWs in the nanowire; on the other hand, injecting pulses through the NW was possible to displace the nucleated DW along the NW.

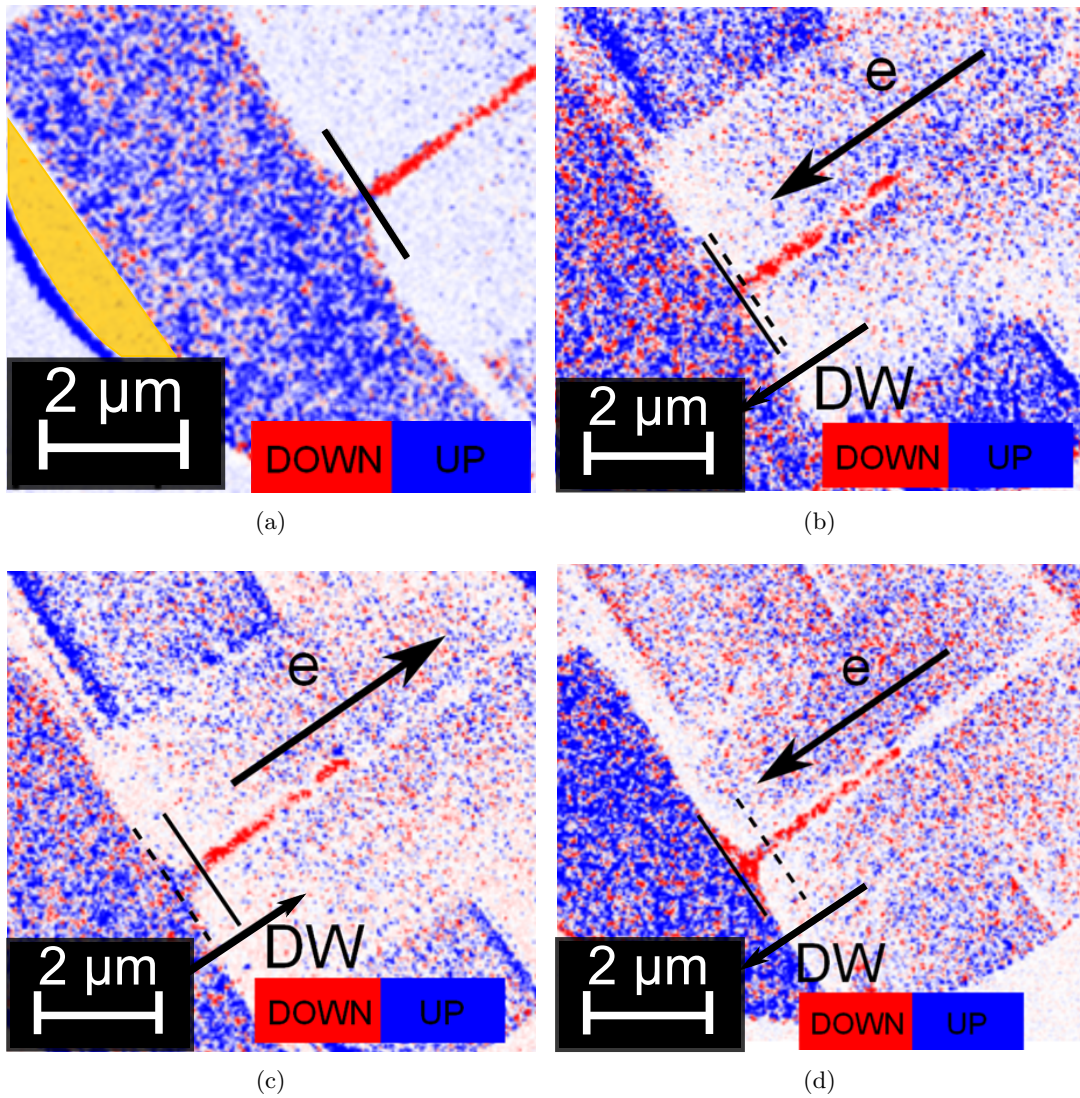


FIGURE B.2: XMCD-PEEM images of current-induced DW motion in Pt/Co₆₈Fe₂₂B₁₀/MgO nanowires. (a) Image of the magnetic structure with a nucleated DW close to the end of the NW. The black line indicates the position of the DW in the nanowire, while red (blue) areas indicate the “down” (“up”) magnetized domains. In (b), (c) and (d) the current-induced DW motion is shown. The dashed (solid) line indicates the initial (final) position of the DW. The DW moves with the electron-flow, as indicated by the arrows. The average measured DW velocity is $v_{DW} \approx 0.5$ m/s, at a $j_a = 5 \times 10^{11}$ A/m². Data from [128].

Bibliography

- [1] S. S. P. Parkin and S.-H. Yang. Memory on the racetrack. *Nat. Nanotech.*, 10:195–198, 2015.
- [2] S. S. P. Parkin, M. Hayashi, and L. Thomas. Magnetic Domain–Wall Racetrack Memory. *Science*, 320(5873):190–194, 2008.
- [3] W. J. Gallagher and S. S. P. Parkin. Development of the magnetic tunnel junction MRAM at IBM: From first junctions to a 16–Mb MRAM demonstrator chip. *IBM J. Res. & Dev.*, 50(1), 2006.
- [4] A. D. Kent and D. C. Worledge. A new spin on magnetic memories. *Nat. Nanotech.*, 10:187–191, 2015.
- [5] S. Ikeda, J. Hayakawa, Y. M. Lee, F. Matzukura, Y. Ohno, T. Hanyu, and H. Ohno. Magnetic Tunnel Junctions for Spintronic Memories and Beyond. *IEEE Trans. Elec. Dev.*, 54(5):991–1002, 2007.
- [6] J. C. Slonczewski. Current–driven excitation of magnetic multilayers. *J. Magn. Magn. Mater.*, 159(1–2):L1–L7, 1996.
- [7] J. C. Slonczewski. Excitation of spin waves by an electric current. *J. Magn. Magn. Mater.*, 195(2):L261–L268, 1999.
- [8] L. Berger. Emission of spin waves by a magnetic multilayer traversed by a current. *Phys. Rev. B*, 54(13):9353, 1996.
- [9] I. M. Miron, T. A. Moore, H. Szambolics, L. D. Buda-Prejbeanu, S. Auffret, B. Rodmacq, S. Pizzini, J. Vogel, M. Bonfim, A. Schuhl, and G. Gaudin. Fast current–induced domain–wall motion controlled by the Rashba effect. *Nat. Mater.*, 10(6):419–423, 2011.

- [10] S.-H. Yang, K.-S. Ryu, and S. S. P. Parkin. Domain–wall velocities of up to 750 m s⁻¹ driven by exchange–coupling torque in synthetic antiferromagnets. *Nat. Nanotech.*, 10:221–226, 2015.
- [11] A. Brataas and K. M. D. Hals. Spin–orbit torques in action. *Nat. Nanotech.*, 9: 86–88, 2014.
- [12] R. Eisberg and R. Resnick. *Quantum Physics: Of Atoms, Molecules, Solids, Nuclei, and Particles*. John Wiley & Sons Inc, 1985.
- [13] J. M. D. Coey. *Magnetism and Magnetic Materials*. Cambridge University Press, 2012.
- [14] I. Dzyaloshinsky. A thermodynamic theory of “weak” ferromagnetism of antiferromagnetics. *J. Phys. Chem. Solids*, 4(4):241–255, 1958.
- [15] T. Moriya. New Mechanism of Anisotropic Superexchange Interaction. *Phys. Rev. Lett.*, 4(5):228–230, 1960.
- [16] T. Moriya. Anisotropic Superexchange Interaction and Weak Ferromagnetism. *Phys. Rev.*, 120(1):91–98, 1960.
- [17] T. Schulz, R. Ritz, A. Bauer, M. Halder, M. Wagner, C. Franz, C. Pfleiderer, K. Everschor, M. Garst, and A. Rosch. Emergent electrodynamics of skyrmions in a chiral magnet. *Nat. Phys.*, 8:301–304, 2012.
- [18] J. Iwasaki, M. Mochizuki, and N. Nagaosa. Universal current–velocity relation of skyrmion motion in chiral magnets. *Nat. Commun.*, 4:1463, 2013.
- [19] S.-G. Je, D.-H. Kim, S.-C. Yoo, B.-C. Min, K.-J. Lee, and S.-B. Choe. Asymmetric magnetic domain–wall motion by the Dzyaloshinskii–Moriya interaction. *Phys. Rev. B*, 88(21):214402, 2013.
- [20] A. Hrabec, N. A. Porter, A. Wells, M. J. Benitez, G. Burnell, S. McVitie, D. McGruther, T. A. Moore, and C. H. Marrows. Measuring and tailoring the Dzyaloshinskii–Moriya interaction in perpendicularly magnetized thin films. *Phys. Rev. B*, 90(2):020402 (R), 2014.
- [21] A. Crepieux and C. Lacroix. Dzyaloshinsky–Moriya interactions induced by symmetry breaking at a surface. *J. Magn. Magn. Mater.*, 182:341–349, 1998.

- [22] H. Yang, A. Thiaville, S. Rohart, A. Fert, and M. Chshiev. Anatomy of Dzyaloshinskii–Moriya interaction at Co/Pt Interfaces. *arXiv*, 1501.05511, 2015.
- [23] N. W. Ashcroft and N. D. Mermin. *Solid State Physics*. Holt Rinehart & Winston, 1976.
- [24] V. Kashid, T. Schena, B. Zimmermann, Y. Mokrousov, S. Blügel, V. Shah, and H. G. Salunke. Dzyaloshinskii–Moriya interaction and chiral magnetism in $3d-5d$ zigzag chains: Tight-binding model and *ab initio* calculations. *Phys. Rev. B*, 90:054412, 2014.
- [25] S. Emori, U. Bauer, S.-M. Ahn, E. Martinez, and G. S. D. Beach. Current-driven dynamics of chiral ferromagnetic domain walls. *Nat. Mater.*, 12(7):611–616, 2013.
- [26] K.-S. Ryu, S.-H. Yang, L. Thomas, and S. S. P. Parkin. Chiral spin torque arising from proximity-induced magnetization. *Nat. Comm.*, 5:3910, 2014.
- [27] J. Torrejon, J. Kim, J. Sinha, S. Mitani, M. Hayashi, M. Yamanouchi, and H. Ohno. Interface control of the magnetic chirality in CoFeB/MgO heterostructures with heavy-metal underlayers. *Nat. Comm.*, 5:4655, 2014.
- [28] *Lexikon der Physik 4*. Spektrum Akademischer Verlag Heidelberg-Berlin, 2000.
- [29] J. W. F. Brown. *Micromagnetism*. Krieger, 1978.
- [30] A. Aharoni. *Introduction to the Theory of Ferromagnetism*. Clarendon Press, 2000.
- [31] S. Finizio. *Field-free Control of Magnetism in Nanostructured Materials Probed with High Resolution X-ray Microscopy*. PhD thesis, Johannes Gutenberg-Universität Mainz, 2015.
- [32] V. Korenivski and J. C. Slonczewski. *Introduction to Spintronics: text reference for the Spin Electronics course at KTH-Physics, Stockholm*. KTH-Stockholm, 2009.
- [33] G. Yu, P. Upadhyaya, Y. Fan, J. G. Alzate, W. Jiang, K. L. Wong, S. Takei, S. A. Bender, L.-T. Chang, Y. Jiang, M. Lang, J. Tang, Y. Wang, Y. Tserkovnyak, P. K. Amiri, and K. L. Wang. Switching of perpendicular magnetization by spin-orbit torques in the absence of external magnetic fields. *Nat. Nanotech.*, 9(7):548–554, 2014.

- [34] L. You, O. Lee, D. Bhowmik, D. Labanowski, J. Hong, J. Bokor, and S. Salahuddin. Switching of Perpendicular Polarized Nanomagnets with Spin Orbit Torque without an External Magnetic Field by Engineering a Tilted Anisotropy. *arXiv:1409.0620*, 2014.
- [35] K.-S. Ryu, L. Thomas, S.-H. Yang, and S. S. P. Parkin. Chiral spin torque at magnetic domain walls. *Nat. Nanotech.*, 8:527–533, 2013.
- [36] I. M. Miron, K. Garello, G. Gaudin, P.-J. Zermatten, M. V. Costache, S. Auffret, S. Bandiera, B. Rodmacq, A. Schuhl, and P. Gambardella. Perpendicular switching of a single ferromagnetic layer induced by in-plane current injection. *Nature*, 476:189–193, 2011.
- [37] N. Nakajima, T. Koide, T. Shidara, H. Miyauchi, H. Fukutani, A. Fujimori, K. Iio, T. Katayama, M. Nývlt, and Y. Suzuki. Perpendicular Magnetic Anisotropy Caused by Interfacial Hybridization via Enhanced Orbital Moment in Co/Pt Multilayers: Magnetic Circular X-ray Dichroism Study. *Phys. Rev. Lett.*, 81:5229–5232, 1998.
- [38] H. X. Yang, M. Chshiev, B. Dieny, J. H. Lee, A. Manchon, and K. H. Shin. First-principles investigation of the very large perpendicular magnetic anisotropy at Fe|MgO and Co|MgO interfaces. *Phys. Rev. B*, 84:054401, 2011.
- [39] N. Miyakawa, D. C. Worledge, and K. Kita. Impact of Ta Diffusion on the Perpendicular Magnetic Anisotropy of Ta/CoFeB/MgO. *IEEE Mag. Lett.*, 4:1000104, 2013.
- [40] L. Néel. Théorie du traînage magnétiques des ferromagnétiques en grains fins avec application aux terres cuites. *Ann. Geophys.*, 5:99–136, 1949.
- [41] W. F. Brown. Thermal fluctuations of a single-domain particle. *Phys. Rev.*, 130:1677, 1963.
- [42] W. Wernsdorfer, E. Bonet Orozco, K. Hasselbach, A. Benoit, B. Barbara, N. Demoncy, A. Loiseau, H. Pascard, and D. Maily. Experimental Evidence of the Néel–Brown Model of Magnetization Reversal. *Phys. Rev. Lett.*, 78(9):1791–1794, 1997.

- [43] O. Boulle, G. Malinowski, and M. Kläui. Current-induced domain wall motion in nanoscale ferromagnetic elements. *Mater. Sci. Eng. R*, 72:159–187, 2011.
- [44] T. A. Moore, I. M. Miron, G. Gaudin, G. Serret, S. Auffret, B. Rodmacq, A. Schuhl, S. Pizzini, and M. Bonfim. High domain wall velocities induced by current in ultrathin Pt/Co/AlOx wires with perpendicular magnetic anisotropy. *Appl. Phys. Lett.*, 93:262504, 2008.
- [45] A. Thiaville, S. Rohart, É. Jué, V. Cros, and A. Fert. Dynamics of Dzyaloshinskii domain walls in ultrathin magnetic films. *Europhys. Lett.*, 100(5):57002, 2012.
- [46] D. C. Ralph and M. D. Stiles. Spin transfer torque. *J. Magn. Magn. Mater.*, 320:1190–1216, 2008.
- [47] T. L. Gilbert. A phenomenological theory of damping in ferromagnetic materials. *IEEE Trans. Mag.*, 40(6):3443–3449, 2004.
- [48] T. Shinjo. *Nanomagnetism and Spintronics*. Elsevier B.V., 2009.
- [49] Z. Jin, A. Tkach, F. Casper, V. Spetter, H. Grimm, A. Thomas, T. Kampfrath, M. Bonn, M. Kläui, and D. Turchinovich. Accessing the fundamentals of magnetotransport in metals with terahertz probes. *Nat. Phys.*, 11:761–766, 2015.
- [50] A. Fert and I. A. Campbell. Electrical resistivity of ferromagnetic nickel and iron based alloys. *J. Phys. F: Metal Phys*, 6(5):849–871, 1976.
- [51] J. C. Slonczewski. Conductance and exchange coupling of two ferromagnets separated by a tunneling barrier. *Phys. Rev. B*, 39(10):6995, 1989.
- [52] L. Berger. Effect of interfaces on Gilbert damping and ferromagnetic resonance linewidth in magnetic multilayers. *J. Appl. Phys.*, 90(9):4632, 2001.
- [53] S. Zhang and Z. Li. Roles of Nonequilibrium Conduction Electrons on the Magnetization Dynamics of Ferromagnets. *Phys. Rev. Lett.*, 93(12):127204, 2004.
- [54] J. Zhang, P. M. Levy, S. Zhang, and V. Antropov. Identification of Transverse Spin Currents in Noncollinear Magnetic Structures. *Phys. Rev. Lett.*, 93:256602, 2004.

- [55] A. Thiaville, Y. Nakatani, J. Miltat, and Y. Suzuki. Micromagnetic understanding of current-induced domain wall motion in patterned nanowires. *Europhys. Lett.*, 69(6):990–996, 2005.
- [56] C. Burrowes, A. P. Mihai, D. Ravelosona, J. V. Kim, C. Chappert, L. Vila, Y. Marty, A. Samson, F. Garsia-Sanchez, L. D. Buda-Prejbeanu, I. Tudosa, E. E. Fullerton, and J.-P. Attané. Non-adiabatic spin-torques in narrow magnetic domain walls. *Nat. Phys.*, 6:17–21, 2010.
- [57] G. Tatara and H. Kohno. Theory of Current-Driven Domain Wall Motion: Spin Transfer versus Momentum Transfer. *Phys. Rev. Lett.*, 92(8):086601, 2004.
- [58] N. L. Schryer and L. R. Walker. The motion of 180° domain walls in uniform dc magnetic fields. *J. Appl. Phys.*, 45:5406, 1974.
- [59] M. Hayashi, L. Thomas, R. Moriya, C. Rettner, and S. S. P. Parkin. Current-Controlled Magnetic Domain-Wall Nanowire Shift Register. *Science*, 320(5873):209–211, 2008.
- [60] B. Dieny. Giant magnetoresistance in spin-valve multilayers. *J. Magn. Magn. Mater.*, 136(3):335–359, 1994.
- [61] R. Jansen. The spin-valve transistor: a review and outlook. *J. Phys. D: Appl. Phys.*, 36:R289–R308, 2003.
- [62] J.-G. Zhu and C. Park. Magnetic tunnel junctions. *Mater. Today*, 9(11):36–45, 2006.
- [63] Y. Zhang, W. Zhao, Y. Lakys, J.-O. Klein, J.-V. Kim, D. Ravelosona, and C. Chappert. Compact Modeling of Perpendicular-Anisotropy CoFeB/MgO Magnetic Tunnel Junctions. *IEEE T. Electron Dev.*, 59(3):819–826, 2012.
- [64] J. Z. Sun and D. C. Ralph. Magnetoresistance and spin-transfer torque in magnetic tunnel junctions. *J. Magn. Magn. Mater.*, 320:1227–1237, 2008.
- [65] Z. Li and S. Zhang. Thermally assisted magnetization reversal in the presence of a spin-transfer torque. *Phys. Rev. B*, 69(13):134416, 2004.
- [66] R. S. Maier and D. L. Stein. Transition-Rate Theory for Nongradient Drift Fields. *Phys. Rev. Lett.*, 69(26):3691–3695, 1992.

- [67] I. M. Miron, G. Gaudin, S. Auffret, B. Rodmacq, A. Schuhl, S. Pizzini, J. Vogel, and P. Gambardella. Current-driven spin torque induced by the Rashba effect in a ferromagnetic metal layer. *Nat. Mater.*, 9(3):230–234, 2010.
- [68] L. Liu, C.-F. Pai, Y. Li, H. W. Tseng, D. C. Ralph, and R. A. Buhrman. Spin-Torque Switching with the Giant Spin Hall Effect of Tantalum. *Science*, 336(6081):555–558, 2012.
- [69] T. D. Skinner, K. Olejnik, L. K. Cunningham, H. Kurebayashi, R. P. Campion, B. L. Gallagher, T. Jungwirth, and A. J. Ferguson. Complementary spin-Hall and inverse spin-galvanic effect torques in a ferromagnet/semiconductor bilayer. *Nat. Commun.*, 6:6730, 2015.
- [70] V. M. Edelstein. Spin polarization of conduction electrons induced by electric current in two-dimensional asymmetric electron systems. *Solid State Commun.*, 73:233–235, 1990.
- [71] P. Gambardella and I. M. Miron. Current-induced spin-orbit torques. *Phil. Trans. R. Soc. A*, 369:3175–3197, 2011.
- [72] A. Manchon, H. C. Koo, J. Nitta, S. M. Frolov, and R. A. Duine. New Perspectives for Rashba spin-orbit coupling. *Nat. Mater.*, 14:871–882, 2015.
- [73] Y. A. Bychkov and E. I. Rashba. Properties of a 2D electron gas with lifted spectral degeneracy. *P. Zh. Eksp. Teor. Fiz.*, 39(2):66–69, 1984.
- [74] M. I. Dyakonov and V. I. Perel. Possibility of orienting electron spins with current. *ZhETF Pis. Red.*, 13(11):657–660, 1971.
- [75] M. I. Dyakonov and V. I. Perel. Current-induced spin orientation of electrons in semiconductors. *Phys. Lett. A*, 35(6):459–460, 1971.
- [76] J. Sinova, D. Culcer, Q. Niu, N. A. Sinitsyn, T. Jungwirth, and A. H. MacDonald. Universal Intrinsic Spin Hall Effect. *Phys. Rev. Lett.*, 92(12):126603, 2004.
- [77] K. Tanaka, H. Kontani, M. Naito, T. Naito, D. S. Hirashima, K. Yamada, and J. Inoue. Intrinsic spin Hall effect and orbital Hall effect in 4d and 5d transition metals. *Phys. Rev. B*, 77:165117, 2008.

- [78] Y. A. Bychkov and E. I. Rashba. Oscillatory effects and the magnetic susceptibility of carriers in inversion layers. *J. Phys. C: Solid State*, 17(33):6039, 1984.
- [79] M. Akyol, J. G. Alzate, G. Yu, P. Upadhyaya, K. L. Wong, A. Ekicibil, P. K. Amiri, and K. L. Wang. Effect of the oxide layer on the current-induced spin-orbit torques in Hf[CoFeB|MgO] and Hf[CoFeB|TaO_x] structures. *Appl. Phys. Lett.*, 106:032406, 2015.
- [80] M. Akyol, G. Yu, J. G. Alzate, P. Upadhyaya, X. Li, K. L. Wong, A. Ekicibil, P. K. Amiri, and K. L. Wang. Current-induced spin-orbit torque switching of perpendicularly magnetized Hf[CoFeB|MgO] and Hf[CoFeB|TaO_x] structures. *Appl. Phys. Lett.*, 106:162409, 2015.
- [81] S. D. Ganichev, E. L. Ivchenko, V. V. Bel'kov, S. A. Tarasenko, M. Sollinger, D. Weiss, W. Wegscheider, and W. Prettl. Spin-galvanic effect. *Nature*, 147:153–156, 2002.
- [82] H. Li, H. Gao, L. V. Zarbo, K. Výborný, X. Wang, I. Garate, F. Dogan, A. Cejchan, J. Sinova, T. Jungwirth, and A. Manchon. Intraband and interband spin-orbit torques in noncentrosymmetric ferromagnets. *Phys. Rev. B*, 91:134402, 2015.
- [83] H. Kurebayashi, J. Sinova, D. Fang, A. C. Irvine, T. D. Skinner, J. Wunderlich, V. Novák, R. P. Campion, B. L. Gallagher, E. K. Vehstedt, L. P. Zarbo, K. Výborný, A. J. Ferguson, and T. Jungwirth. An antidamping spin-orbit torque originating from the Berry curvature. *Nat. Nanotech.*, 9:211–217, 2014.
- [84] M. V. Berry. Quantal Phase Factors Accompanying Adiabatic Changes. *Proc. R. Soc. Lond. A*, 392:45–57, 1984.
- [85] A. Manchon. Spin-orbitronics: A new moment for Berry. *Nat. Phys.*, 10:340–341, 2014.
- [86] J. Sinova, S. O. Valenzuela, J. Wunderlich, C. H. Back, and T. Jungwirth. Spin Hall effect. *arXiv:1411.3249*, 2014.
- [87] S. Murakami, N. Nagaosa, and S.-C. Zhang. Dissipationless Quantum Spin Current at Room Temperature. *Science*, 301:1348–1351, 2003.
- [88] N. Nagaosa, J. Sinova, S. Onoda, A. H. MacDonald, and N. P. Ong. Anomalous Hall effect. *Rev. Mod. Phys.*, 82(2):1539–1592, 2010.

- [89] G. Y. Guo, S. Murakami, T.-W. Chen, and N. Nagaosa. Intrinsic Spin Hall Effect in Pt: First-Principles Calculations. *Phys. Rev. Lett.*, 100:096401, 2008.
- [90] H. L. Wang, C. H. Du, Y. Pu, R. Adur, P. C. Hammel, and F. Y. Yang. Scaling of the Spin Hall Angle in 3d, 4d, and 5d Metals from $Y_3Fe_5O_{12}$ /Metal Spin Pumping. *Phys. Rev. Lett.*, 112:197201, 2014.
- [91] B. Zimmermann, K. Chadova, D. Ködderitzsch, S. Blügel, H. Ebert, D. V. Fedorov, N. H. Long, P. Mavropoulos, I. Mertig, Y. Mokrousov, and M. Gradhand. Skew scattering in dilute ferromagnetic alloys. *Phys. Rev. B*, 90:220403 (R), 2014.
- [92] S. Maekawa, S. O. Valenzuela, E. Saitoh, and T. Kimura. *Spin Current*. Oxford University Press, 2012.
- [93] L. Liu, T. Moriyama, D. C. Ralph, and R. A. Buhrman. Spin-Torque Ferromagnetic Resonance Induced by the Spin Hall Effect. *Phys. Rev. Lett.*, 106:036601, 2011.
- [94] P. C. van Son, K. van Kempen, and P. Wyder. Boundary Resistance of the Ferromagnetic-Nonferromagnetic Metal Interface. *Phys. Rev. Lett.*, 58(21):2271, 1987.
- [95] C.-F. Pai, Y. Ou, D. C. Ralph, and R. A. Buhrman. Dependence of the Efficiency of Spin Hall Torque on the Transparency of Pt-Ferromagnetic Layer Interfaces. *arXiv:1411.3379*, 2014.
- [96] W. Zhang, W. Han, X. Jiang, S.-H. Yang, and S. S. P. Parkin. Role of transparency of platinum-ferromagnet interfaces in determining the intrinsic magnitude of the spin Hall effect. *Nat. Phys.*, 11:496–502, 2015.
- [97] M. Weiler, M. Althammer, M. Schreier, J. Lotze, M. Pernpeintner, S. Meyer, H. Huebl, R. Gross, A. Kamra, J. Xiao, Y.-T. Chen, H. Jiao, G. E. W. Bauer, and S. T. B. Goennenwein. Experimental Test of the Spin Mixing Interface Conductivity Concept. *Phys. Rev. Lett.*, 111:176601, 2013.
- [98] Z. Qiu, K. Ando, K. Uchida, Y. Kajiwara, R. Takahashi, H. Nakayama, T. An, Y. Fujikawa, and E. Saitoh. Spin mixing conductance at a well-controlled platinum/yttrium iron garnet interface. *Appl. Phys. Lett.*, 103:092404, 2013.

- [99] J.-C. Rojas-Sánchez, N. Reyren, P. Laczkowski, W. Savero, J.-P. Attané, C. Deranlot, M. Jamet, J.-M. George, L. Vila, and H. Jaffres. Spin Pumping and Inverse Spin Hall Effect in Platinum: The Essential Role of Spin–Memory Loss at Metallic Interfaces. *Phys. Rev. Lett.*, 112:106602, 2014.
- [100] A. V. Khvalkovskiy, V. Cros, D. Apalkov, V. Nikitin, M. Krounbi, K. A. Zvezdin, A. Anane, J. Grollier, and A. Fert. Matching domain–wall configuration and spin–orbit torques for efficient domain–wall motion. *Phys. Rev. B*, 87:020402 (R), 2013.
- [101] L. Liu, O. J. Lee, T. J. Gudmunsen, D. C. Ralph, and R. A. Buhrman. Current–Induced Switching of Perpendicularly Magnetized Magnetic Layers Using Spin Torque from the Spin Hall Effect. *Phys. Rev. Lett.*, 109:096602, 2012.
- [102] T. Nan, S. Emori, C. T. Boone, X. Wang, T. M. Oxholm, J. G. Jones, B. M. Howe, G. J. Brown, and N. X. Sun. Comparison of spin–orbit torques and spin pumping across NiFe/Pt and NiFe/Cu/Pt interfaces. *Phys. Rev. B*, 91:214416, 2015.
- [103] P. M. Haney, H.-W. Lee, K.-J. Lee, A. Manchon, and M. D. Stiles. Current induced torques and interfacial spin–orbit coupling: Semiclassical modeling. *Phys. Rev. B*, 87:174411, 2013.
- [104] E. Jué, C. K. Safeer, M. Drouard, A. Lopez, P. Balint, L. D. Brude-Prejbeanu, O. Boulle, S. Auffret, A. Schuhl, A. Manchon, I. M. Miron, and G. Gaudin. Chiral damping of magnetic domain walls. *arXiv:1504.04411*, 2015.
- [105] C. S. Akosa, I. M. Miron, G. Gaudin, and A. Manchon. Phenomenology of chiral damping in noncentrosymmetric magnets. *arXiv:1517.07762*, 2015.
- [106] J.-V. Kim. Role of nonlinear anisotropic damping in the magnetization dynamics of topological solitons. *Phys. Rev. B*, 92:014418, 2015.
- [107] D.-Y. Kim, D.-H. Kim, J. Moon, and S.-B. Choe. Determination of magnetic domain–wall types using Dzyaloshinskii–Moriya–interaction–induced domain patterns. *Appl. Phys. Lett.*, 106:262403, 2015.
- [108] H. Ibach and H. Lüth. *Solid-State Physics: An introduction to Principles of Materials Science*. Springer, 1995.
- [109] G. V. Karnad. Current induced magnetization dynamics: Domain walls in motion. Master’s thesis, KU Leuven and TU Dresden, 2014.

- [110] T. Zacke. Spin-transfer torque in high anisotropy nanostructures. Diploma thesis, Johannes Gutenberg-Universität Mainz, 2013.
- [111] M. Altissimo. Electron beam lithography for micro-/nanofabrication. *Biomicrofluidics*, 4(026503), 2010.
- [112] K. Seshan. *Handbook of Thin Film Deposition, Process and Technologies (Second Edition)*. William Andrew, 2002.
- [113] MicroChem Corp. Pmma data sheet. Technical report, MicroChem Corp., 2001. http://www.microchem.com/pdf/PMMA_Data_Sheet.pdf.
- [114] Allresist GmbH. ebeamresists ar-n 7500-7520. Technical report, Allresist GmbH Germany, 2014. <http://www.allresist.com/ebeamresists-ar-n-7500-7520/>.
- [115] Allresist GmbH. Remover ar 300-70, material safety data sheet. Technical report, Allresist GmbH Germany, 2014. <http://www.allresist.com/prozesschemikalien-ar-600-70-600-71-300-70-72-73/>.
- [116] J. Kerr. On rotation of the plane of polarization by reflection from the pole of a magnet. *Phil. Mag. S.5*, 3(19), 1877.
- [117] P. Weinberger. John Kerr and his effects found in 1877 and 1878. *Phil. Mag. Lett.*, pages 1-11, 2008.
- [118] P. N. Argyres. Theory of the Faraday and Kerr effects in ferromagnetics. *Phys. Rev.*, 97(2):334, 1955.
- [119] G. Schönhense. Imaging of magnetic structures by photoemission electron microscopy. *J. Phys.: Condens. Matter.*, 11:9517-9547, 1999.
- [120] U. Tiwari, R. Ghosh, and P. Sen. Theory of magneto-optic Kerr effects. *Phys. Rev. B*, 49(3):2159, 1994.
- [121] R. Schäfer. Investigation of domains and dynamics of domain walls by the magneto-optic Kerr effect. *Handbook of Magn. and Adv. Magn. Mater.*, 3, 2007.
- [122] Z. B. H. Hujan. Magneto-Optical Kerr Effect Microscopy Investigation on Permalloy Nanostructures. Master's thesis, University of York, 2013.

- [123] G. Schütz, W. Wagner, W. Wilhelm, P. Kienle, R. Zeller, R. Frahm, and G. Materlik. Absorption of circularly polarized x rays in iron. *Phys. Rev. Lett.*, 58(7):737, 1987.
- [124] G. Schütz, M. Knülle, R. Wienke, W. Wilhelm, W. Wagner, P. Kienle, and R. Frahm. Spin-dependent photoabsorption at the L-edges of ferromagnetic Gd and Tb metal. *Z. Phys. B – Condensed Matter*, 73:67–75, 1988.
- [125] R. Lo Conte, A. Hrabec, A. P. Mihai, T. Schulz, S.-J. Nho, C. H. Marrows, T. A. Moore, and M. Kläui. Spin-orbit torque-driven magnetization switching and thermal effects studied in Ta/CoFeB/MgO nanowires. *Appl. Phys. Lett.*, 105:122404, 2014.
- [126] Y.-H. Wang, W.-C. Chen, S.-Y. Yang, K.-H. Shen, C. Park, M.-J. Kao, and M.-J. Tsai. Interfacial and annealing effects on magnetic properties of CoFeB thin films. *J. Appl. Phys.*, 99:08M307, 2006.
- [127] M. H. Read and C. Altman. A new structure in Tantalum thin films. *Appl. Phys. Lett.*, 7(3):51–52, 1965.
- [128] R. Lo Conte, E. Martinez, A. Hrabec, A. Lamperti, T. Schulz, L. Nasi, L. Lazarini, R. Mantovan, F. Maccherozzi, S. S. Dhesi, B. Ocker, C. H. Marrows, T. A. Moore, and M. Kläui. Role of B diffusion in the interfacial Dzyaloshinskii–Moriya interaction in Ta/Co₂₀Fe₆₀B₂₀/MgO nanowires. *Phys. Rev. B*, 91:014433, 2015.
- [129] C. O. Avci, K. Garello, C. Nistor, S. Godey, B. Ballesteros, A. Mugarza, A. Barla, M. Valvidares, E. Pellegrin, A. Ghosh, I. M. Miron, O. Boulle, S. Auffret, G. Gaudin, and P. Gambardella. Fieldlike and antidamping spin-orbit torques in as-grown and annealed Ta/CoFeB/MgO layers. *Phys. Rev. B*, 89:214419, 2014.
- [130] C. T. Boone, H. T. Nembach, J. M. Shaw, and T. J. Silva. Spin transport parameters in metallic multilayers determined by ferromagnetic resonance measurements of spin-pumping. *J. Appl. Phys.*, 113:153906, 2013.
- [131] C. O. Avci, K. Garello, A. Ghosh, M. Gabureac, S. F. Alvarado, and P. Gambardella. Unidirectional spin Hall magnetoresistance in ferromagnet/normal metal bilayers. *Nat. Phys.*, 11:570–575, 2015.

- [132] C. Hahn, G. de Loubens, O. Klein, M. Viret, V. V. Naletov, and J. Ben Youssef. Comparative measurements of inverse spin Hall effects and magnetoresistance in YIG/Pt and YIG/Ta. *Phys. Rev. B*, 87:174417, 2013.
- [133] M. Laufenberg, W. Bührer, D. Bedau, P.-E. Melchy, M. Kläui, L. Vila, G. Faini, C. A. F. Vaz, J. A. C. Bland, and U. Rüdiger. Temperature Dependence of the Spin Torque Effect in Current-Induced Domain Wall Motion. *Phys. Rev. Lett.*, 97:046602, 2006.
- [134] M. Yamanouchi, A. Jander, P. Ikeda, S. Matzukur, and H. Ohno. Domain structure in CoFeB thin films with perpendicular magnetic anisotropy. *IEEE Mag. Lett.*, 2:3000304, 2011.
- [135] K. Garello, C. O. Avci, I. M. Miron, M. Baumgartner, A. Ghosh, S. Auffret, O. Boulle, G. Gaudin, and P. Gambardella. Ultrafast magnetization switching by spin-orbit torques. *Appl. Phys. Lett.*, 105(21):212402, 2014.
- [136] A. Fert. Magnetic and transport properties of metallic multilayers. *Mater. Sci. Forum*, 59-60:439-480, 1991.
- [137] K. Gilmore, I. Garate, A. H. MacDonald, and M. D. Stiles. First-principles calculation of the nonadiabatic spin transfer torque in Ni and Fe. *Phys. Rev. B*, 84:224412, 2011.
- [138] S. Emori, E. Martinez, K.-J. Lee, H.-W. Lee, U. Bauer, S.-M. Ahn, P. Agrawal, D. C. Bono, and G. S. D. Beach. Spin Hall torque magnetometry of Dzyaloshinskii domain walls. *Phys. Rev. B*, 90:184427, 2014.
- [139] E. Martinez, S. Emori, N. Perez, L. Torres, and G. S. D. Beach. Current-driven dynamics of Dzyaloshinskii domain walls in the presence of in-plane fields: Full micromagnetic and one-dimensional analysis. *J. Appl. Phys.*, 115:213909, 2014.
- [140] E. Martinez, S. Emori, and G. S. D. Beach. Current-driven domain wall motion along high perpendicular anisotropy multilayers: The role of the Rashba field, the spin Hall effect, and the Dzyaloshinskii-Moriya interaction. *Appl. Phys. Lett.*, 103:072406, 2013.

- [141] J. Kim, J. Sinha, M. Hayashi, M. Yamanouchi, S. Fukami, T. Suzuki, S. Mitani, and H. Ohno. Layer thickness dependence of the current-induced effective field vector in Ta|CoFeB|MgO. *Nat. Mater.*, 12:240–245, 2012.
- [142] E. Martinez. The stochastic nature of the domain wall motion along high perpendicular anisotropy strips with surface roughness. *J. Phys.: Condens. Matter*, 24:024206, 2012.
- [143] X. Qiu, K. Narayanapillai, Y. Wu, P. Deorani, D.-H. Yang, W.-S. Noh, J.-H. Park, K.-J. Lee, H.-W. Lee, and H. Yang. Spin-orbit torque engineering via oxygen manipulation. *Nat. Nanotech.*, 10:333–338, 2015.
- [144] A. Lamperti, E. Cianci, O. Salicio, L. Lamagna, S. Spiga, and M. Fanciulli. Thermal stability of high-k oxides on SiO₂/Si or Si_xN_y/SiO₂/Si for charge-trapping nonvolatile memories. *Surf. Interf. Analys.*, 45:390–393, 2013.
- [145] A. Lamperti, S.-M. Ahn, B. Ocker, R. Mantovan, and D. Ravelosona. Interface width evaluation in thin layered CoFeB/MgO multilayers including Ru or Ta buffer layer by X-ray reflectivity. *Thin Solid Films*, 533:79–82, 2012.
- [146] H. Bouchikhaoui, P. Stender, D. Akemeier, D. Baither, K. Hono, A. Hütten, and G. Schmitz. On the role of Ta cap in the recrystallization process of CoFeB layers. *Appl. Phys. Lett.*, 103(14):142412, 2013.
- [147] G. Yu, P. Upadhyaya, K. L. Wong, W. Jiang, J. G. Alzate, J. Tang, P. K. Amiri, and K. L. Wang. Magnetization switching through spin-Hall-effect-induced chiral domain wall propagation. *Phys. Rev. B*, 89:104421, 2014.
- [148] M. Belmeguenai, J.-P. Adam, Y. Roussigné, S. Eimer, T. Devolder, J.-V. Kim, S. M. Cherif, A. Stashkevich, and A. Thiaville. Interfacial Dzyaloshinskii-Moriya interaction in perpendicularly magnetized Pt/Co/AlO_x ultrathin films measured by Brillouin light spectroscopy. *Phys. Rev. B*, 91:180405, 2015.
- [149] D. Lacour, M. Mehn, M. Alnot, F. Montaigne, F. Greullet, G. Lengaigne, O. Lenoble, S. Robert, and A. Schuhl. Magnetic properties of postoxidized Pt/Co/Al layers with perpendicular anisotropy. *Appl. Phys. Lett.*, 90:192506, 2007.

- [150] J. Cho, N.-H. Kim, S. Lee, J.-S. Kim, R. Lavrijsen, A. Solignac, Y. Yin, D.-S. Han, N. J. J. van Hoof, J. M. Swagten, B. Koopmans, and C.-Y. You. Thickness dependence of the interfacial Dzyaloshinskii–Moriya interaction in inversion symmetry broken systems. *Nat. Commun.*, 6:7635, 2015.
- [151] K. Garello, I. M. Miron, C. O. Avci, F. Freimuth, Y. Mokrousov, S. Blügel, S. Auffret, G. Boule, O. and Gaudin, and P. Gambardella. Symmetry and magnitude of spin–orbit torques in ferromagnetic heterostructures. *Nat. Nanotech.*, 8(6):587–593, 2013.
- [152] Y. Wang, P. Deorani, X. Qiu, J. H. Kwon, and H. Yang. Determination of intrinsic spin Hall angle in Pt. *Appl. Phys. Lett.*, 105:152412, 2014.
- [153] L. M. Loong, P. Deorani, X. Qiu, and H. Yang. Investigating and engineering spin–orbit torques in heavy metal/Co₂FeAl_{0.5}Si_{0.5}/MgO thin film structures. *Appl. Phys. Lett.*, 107:022405, 2015.
- [154] C. O. Avci, K. Garello, A. Ghosh, M. Gabureac, S. F. Alvarado, and P. Gambardella. Interplay of spin–orbit torque and thermoelectric effects in ferromagnet/normal–metal bilayers. *Phys. Rev. B*, 90:224427, 2014.
- [155] M. Li, Y.-P. Zhao, and G.-C. Wang. In situ measurement of thickness dependent electrical resistance of ultrathin Co films on SiO₂/Si(111) substrate. *J. Vac. Sci. Technol. A*, 18:2992, 2000.
- [156] H. T. Nembach, J. M. Shaw, M. Weiler, E. Jué, and T. J. Silva. Linear relation between Heisenberg exchange and interfacial Dzyaloshinskii–Moriya interaction in metal films. *Nat. Phys.*, doi:10.1038/nphys3418, 2015.
- [157] O. Boule, S. Rohart, L. D. Brude-Prejbeanu, E. Jue, I. M. Miron, S. Pizzini, J. Vogel, G. Gaudin, and A. Thiaville. Domain wall tilting in the presence of the Dzyaloshinskii–Moriya interaction in out–of–plane magnetized magnetic nanotracks. *Phys. Rev. Lett.*, 111:217203, 2013.
- [158] K.-S. Ryu, L. Thomas, S.-H. Yang, and S. S. P. Parkin. Current induced tilting of domain walls in high velocity motion along perpendicularly magnetized micron–sized Co/Ni/Co racetracks. *Appl. Phys. Exp.*, 5:093006, 2012.

-
- [159] O. Boulle, L. D. Brude-Prejbeanu, E. Jue, I. M. Miron, and G. Gaudin. Current induced domain wall dynamics in the presence of spin orbit torques. *J. Appl. Phys.*, 115:17D502, 2014.
- [160] C. Kittel. *Festkörperphysik*. Oldenbourg Wissenschaftsverlag GmbH, 2006.
- [161] U. Rüdiger, R. Calarco, U. May, K. Samm, J. Hauch, H. Kittur, M. Sperlich, and G. Güntherodt. Temperature dependent resistance of magnetic tunnel junctions as a quality proof of the barrier. *J. Appl. Phys.*, 89(11):7573–7575, 2001.
- [162] C.-Y. You, I. M. Sung, and B.-K. Joe. Analytic expression for the temperature of the current-heated nanowire for the current-induced domain wall motion. *Appl. Phys. Lett.*, 89:222513, 2006.

Acknowledgements

First of all, I would like to thank my supervisor, Prof. Dr. M. Kläui, who has supported my work with helpful comments and suggestions, and the Graduate School “Materials Science in Mainz”, for giving me the opportunity to do my PhD studies at the University of Mainz.

I would also like to thank my co-supervisor Dr. T. A. Moore from the University of Leeds, who proposed me to join this project. He has been a constant support during all my PhD, and without him I would not have been writing this thesis.

I am very grateful to Dr. A. P. Mihai, who collaborated with me in the initial part of my project, and Dr. A. Hrabec, who introduced me to Kerr microscopy and guided me in my first current-induced domain wall motion experiments. I will be forever thankful to both of them.

I would like to thank all my colleagues from the Kläui-Lab at the University of Mainz. A special thanks goes to T. Schulz, G. V. Karnad, S. Jaiswal, Dr. K. Lee, and K. Litzius for the time spent together working in the Lab and discussing about the exciting and sometimes puzzling results of our experiments. I thank all the office mates I had in these last three years, for the great time spent together. In particular I thank S. Finizio (my first office mate in Mainz), P. Krautscheid, T. Schulz, E. Venzmer, A. Kehlberger, G. V. Karnad, N. Richter, F. Musseau, M. Braatz, A. Pfeiffer, and D. Schönke. I would like to say thank you also to M. König, S. Kauschke and A. Dion for having introduced me to and assisted me with the e-beam lithography technique, making the patterning of my samples possible. A special thanks goes to J. Henrizi and S. Kauschke for their continuous technical support during my experimental work. I also thank I. Berber and S. Duddek for their valuable support with all the bureaucratic aspects concerning my project, and S. Teljega from the International office, who assisted me with my moving to Mainz.

I thank Prof. Dr. J. Sinova, Prof. Dr. G. Jakob, and Dr. M. Jourdan for the many instructive discussions concerning the Physics of my project and not only. I say also thank you to J. Gayles, H. Velkov, and D. Pryshynenko for the many thrilling discussions about the Physics of the SHE and SOTs.

During this project I had the opportunity to carry out experiments also away from Mainz. I am very thankful to all the members of the Condensed Matter Physics group of the University of Leeds, and in particular to Prof. B. J. Hickey and Prof. C. H. Marrows, who allowed me to have access to all the facilities available in their labs. Furthermore, all the members of the group have always been open to help me and I have always felt one of them each time I was there for a new experiment. I also thank the principal scientist of the Nanoscience Beamline IO6 at the DIAMOND Light Source, Dr. S. S. Dhesi, and especially the local support scientist, Dr. F. Maccherozzi, for his

continuous and priceless help during the XMCD-PEEM experiments.

I would also like to thank all the people who are not from Mainz and who collaborated with me in my work. In particular, I thank Prof. E. Martinez (Universidad de Salamanca) for his collaboration with micromagnetic simulations, Dr. A. Lamperti and Dr. R. Mantovan (Laboratorio MDM, IMM-CNR di Agrate Brianza) for the SIMS measurements, Dr. L. Nasi and Dr. L. Lazzarini (IMEM-CNR di Parma) for the support with the TEM imaging, B. Ocker (Singulus Nanotechnologies AG) for the supply of part of the material stacks investigated in this project, N.-H. Kim (Ihna University) for his help during his internship at the Kläui-Lab and for his support to my research with his BLS measurements, Dr. J.-S. Kim and Dr. D.-S. Han (Technische Universität Eindhoven) for the deposition of the Pt\Co\AlO_x material stack used in this work.

I want to thank all the people who made my time in Mainz all the more pleasant. A special thanks goes to T. Schulz, my first German friend, A. De Lucia, who shares with me my endless faith in our favorite football (European football!!!) team, A. Kronenberg, for his constant support, E. Venzmer, M. Emmel, R. Reeve, S. Finizio, N. Richter, P. Krautscheid, S. ten Haaf, C. Euler and all the rest of the Kläui group for the great time had together. A great thanks goes also to L. and R..

I owe a truly special thanks to K., who gave me hope again. Thank you for everything you did.

A great thanks to my everlasting friends from Riccione: S., M. and G.. Even if, in the last years, we have not had as much time to be together as we would have liked to, I have always known that your support was there with me.

Finally, I would like to thank, with all my heart, my parents and my brothers for their immense love and support. You have always believed in me, blindly, and I will be forever indebted to you for this. Cara mamma, caro papà, cari O. e D., tutto questo l'ho ottenuto anche grazie a voi. Senza il vostro immenso amore e sconfinato supporto nulla sarebbe stato possibile. Vi amo.

Curriculum Vitae

Personal Information

Name: Roberto Lo Conte

Address: Mombacher Strasse 85a, 55122 Mainz (Germany)

e-mail: robilochi@libero.it, loconte@uni-mainz.de

Date of birth: February 07, 1987

Nationality: Italian

Education

01.08.2012 – Today: PhD in Physics

School: Johannes Gutenberg-Universität Mainz / Graduate School MAINZ

Title of thesis: *Magnetic nanostructures with structural inversion asymmetry*

Supervisor: Prof. Dr. Mathias Kläui

01.09.2009 – 25.07.2012: M.Sc.Eng. in Physics Engineering

School: Politecnico di Milano

Title of thesis: *Process development for a metallic spin-flip based laser fabrication*
(project done at KTH in Stockholm (Sweden))

Supervisor: Prof. Marco Finazzi

01.08.2010 – 01.06.2012: M.Sc.Eng. in Information Technology (Informationsteknik)

School: Kungliga Tekniska Högskolan (Royal Institute of Technology (KTH)), Stockholm (Sweden)

Title of thesis: *Process development for a metallic spin-flip based laser fabrication*

Supervisor: Dr. Adrian Iovan

01.09.2006 – 22.07.2009: B.Sc.Eng. in Physics Engineering

School: Politecnico di Milano

Title of thesis: *Magnetic force microscopy: characterization of samples with longitudinal and transversal magnetization*

Supervisor: Prof. Marco Finazzi

09.2001 – 06.2006: High School

School: Liceo Scientifico A. Volta, Riccione (Italy)

Teaching

Winter Semester 2013-2014: Organizer and supervisor for exercise lectures

Course: *Materialwissenschaften (A)*

Summer Semester 2014: Supervisor for exercise lectures

Course: *Experimentalphysik I*

Publications List

R. Lo Conte, A. Hrabec, A. P. Mihai, T. Schulz, S.-J. Nho, C. H. Marrows, T. A. Moore, and M. Kläui, *Spin-orbit torque-driven magnetization switching and thermal effects studied in Ta\CoFeB\MgO nanowires*, Appl. Phys. Lett. **105**, 122404 (2014).

R. Lo Conte, E. Martinez, A. Hrabec, A. Lamperti, T. Schulz, L. Nasi, L. Lazarini, R. Mantovan, F. Maccherozzi, S. S. Dhesi, B. Ocker, C. H. Marrows, T. A. Moore, and M. Kläui, *Role of B diffusion in the interfacial Dzyaloshinskii-Moriya interaction in Ta/Co₂₀Fe₆₀B₂₀/MgO nanowires*, Phys. Rev. B **91**, 014433 (2015).

T. Schulz, O. Alejos, E. Martinez, K. M. D. Hals, K. Garcia, L. Vila, K. Lee, **R. Lo Conte**, G. V. Karnad, S. Moretti, B. Ocker, D. Ravelosona, A. Brataas, and M. Kläui, *Spin-orbit torques for current parallel and perpendicular to a domain wall*, Appl. Phys. Lett. **107**, 122405 (2015).